AN ANALYTICAL AND EXPERIMENTAL INVESTIGATION OF CONCRETE-FILLED FIBER REINFORCED PLASTICS (FRP) TUBES

by
MICHEL SABRI SAMAAN
B. S. Civil Engineering, Cairo University, 1987
M.S., Civil Engineering, University of Calgary, 1993

A. dissertation submitted in partial fulfillment of the requirements for the degree of
Doctor of Philosophy
In the Department of Civil and Environmental Engineering
in the College of Engineering
at the University of Central Florida
Orlando, Florida

Fall Term
1997

Major Advisor: Amir Mirmiran

ABSTRACT

Hybrid construction with concrete and fiber composites results in systems with pseudo-ductile characteristics and high stiffness and strength. It also makes optimum use of materials based on their mechanical properties and resistance to corrosive environments. One such application is demonstrated in concrete-filled tubes (CFTs) made of fiber reinforced plastics (FRP). The FRP tube provides the necessary longitudinal and hoop reinforcement, as well as a permanent formwork for the concrete core. In return, the concrete core contributes to the overall stability and stiffness of the composite system. The tube consists of axial and hoop fibers in the form of filament-wound angle plies or axial normal wound plies. The tube also includes internal ribs as shear connectors for beam column applications. As a result, all necessary reinforcement in a conventional RC column can be provided by the tube, thus eliminating the need for reinforcing cage and the pour form. The present study is an analytical and experimental investigation of concrete-filled FRP tubes (CFFT) as structural beam-columns. The focus of this research is on the confinement of concrete with fiber composites, composite action of FRP and concrete in beam-columns, comparing the behavior of CFFTs with conventional RC columns, and the design procedures for the CFFTs.

Experimental results of a series of 6" x 12" circular CFFTs subjected to uniaxial compression were utilized towards the development of a new analytical confinement model. The tested cylinders were composed of a filament-wound fiberglass/polyester tube filled with normal weight medium strength concrete. No bond was provided between FRP and concrete. A mathematical model was developed to generate the complete bilinear stress-strain response of FRP-confined concrete in both axial and lateral directions. The parameters of the model are directly related to the material properties of the FRP tube and the concrete core. The predicted stress-strain curves compared favorably with the available experimental data on uniaxial compression tests of FRP-encased concrete. The model was also shown to provide good estimate for fiber-wrapped columns tested by other investigators.

The tube is intended as both longitudinal and transverse reinforcement for concrete. For the tube to act as longitudinal reinforcement, not only its detailing at the column ends is important, but also its bond with the concrete core is necessary throughout the length of the column. For the tube to act mainly as transverse shear reinforcement, a shear transfer mechanism is still necessary, otherwise the truss analogy will not be applicable. A grid of shear connectors was designed, and a number of specimens were fabricated to study the composite action of the FRP and concrete.

The beam-column behavior of CFFTs was studied by a series of 7" x 7" x 52" square CFFTs that were tested under various combinations of axial-flexural loads. The results of these tests formed the experimental force-moment interaction diagram for square CFFTs. This interaction diagram was compared with theoretical interaction

diagrams of conventional RC sections with variable reinforcement ratios. The comparison revealed a superior load-carrying capacity for the CFFTs. Also, it was shown that the ductility of CUT beam columns is comparable to corresponding RC sections in compression control region of the interaction diagram. The results of the beam column tests were also used to verify the applicability of the beam theory for the design of square bonded CFFTs. Finally, some design issues were discussed for both circular and square CFFTs subjected to either axial or axial-flexural loads.

ACKNOWLEDGMENTS

I would like to express my deepest gratitude to my advisor Dr. Amir Mirmiran. His friendly character, as well as his motivation, advice, and experience greatly contributed to the successful completion of my doctoral studies at UCF.

My deep thanks are also extended to all my committee members, Dr. M. Shahawy, Dr. S. Kunnath, Dr. J. Nayfeh, and Dr. U. O. Onyemelukwe. Their advice, effort and time throughout the course of the study is highly appreciated.

The help provided by the personnel of Florida Department of Transportation, Structural Research Center, as well as the generous support of Marine Muffler Corp., are also appreciated.

My deepest appreciation goes to my wife Magda. Her devoted and dedicated help was a great support. I would also love to thank all the sincere help, advice and moral support I received from my friends: Fady Barsoum, Hazem El Echary, Moheb.Basta, Ashraf Eshak, Ehab Barsoum, Juan-Carlo Mastrapa, Mike Scherer, Mohsen Kargahi, Surami Cabrera. I am also highly indebted to my family and my family in law for their unceasing love and support.

Finally, thank you to all who directly or indirectly contributed in the completion of this work.

TABLE OF CONTENTS

LIST OF TABLES

LIST OF FIGURES

.

LIST OF SYMBOLS

[A]	Laminate extensional stiffness matrix
A_{fr}	Cross-sectional area of one roving
A_g	Gross cross-sectional area of the column
A_{sp}	Cross-sectional area of the steel spirals
b, h	Section dimensions of the column
[B]	Laminate coupling stiffness matrix
C_t	Constant coefficient with units of length in the tension stiffening model Stevens et al. (Chapter 7)
D	Core diameter
[D]	Laminate bending stiffness matrix
d_b	bar diameter
D;	Parameter controlling the descending portion of the f_i- ϵ_i curve in and Shah's confinement model (Chapter 2)
E	Young's modulus
E_1, E_{1r}	First slope of the stress-strain response in the axial and lateral directions
E_2, E_{2r}	Second slope of the stress-strain response in the axial and lateral
E_c	Initial tangent modulus of concrete
E_{el}	Elastic energy released at failure (Chapter 7)
E_i	Initial slope of the f_i - ϵ_i curve
E_j	Modulus of elasticity of the FRP jacket in the hoop direction
E_{sec}	Secant modulus of concrete
E_{tot}	Total absorbed energy (Chapter 7)
F'_{cc}	Compressive strength of confined concrete
F'_{co}	Compressive strength of unconfined concrete
f_{cr}	Cracking stress of concrete
F'_{cu}	Ultimate compressive stress of confined concrete
F_j	Hoop tensile strength of the FRP jacket
F_{jc}	Compressive stress in the FRP tube (Chapter 7)
F_{jt}	Tensile stress in the FRP tube (Chapter 7)
f_o, f_{or}	Reference stress in the axial and lateral directions
F_r	Confining pressure
F_{sv}	Yield stress of the steel spirals
F_y	Yield stress of steel

f_{yj}	Yield stress of the steel jacket
E_{1peak}	Main principal strength
G_{ij}	Shear modulus associated with the ij-plane
K	Parameter function of f'_{co} (Chapter 2)
k_1	Constant varying between 1 and 1.5 (Chapter 2)
K_c	Confinement coefficient
M_1	Primary moment
M_{1peak}	Primary peak moment
M_2	Secondary moment
M_{TOT}	Total moment
n	Parameter function of f'_{co} (Chapter 2)
n	Total number of laminae in a laminate (Chapter 4)
n, n,	Curve-shape parameter in the axial and lateral directions (Chapter 5)
n_{fr}	Number of rovings per unit length
P_A	Axial force
P_o	Axial capacity of the column
[Q]	Lamina stiffness matrix
[Q]	Transformed lamina stiffness matrix
R	Corner radius of the square tube
R^2	Coefficient of correlation
s	Ultimate stress of FRP (Chapter 4)
s	Elastic slope of the load-deflection curve at the failure point (Chapter 7)
s_1, s_2	Initial slopes of the load-deflection curve (Chapter 7)
S_{sp}	Pitch of the steel spirals
t_j	Thickness of FPR jacket
v	Volume fraction
V	Volume
V_c	Natural capillary porosity of the paste
V_P	Volume fraction of paste in concrete
w_{fr}	Weight of fiber per unit length of roving
w_o	Water-cement ratio in the concrete mix
α	Parameter accounting for the effect of bar diameter and distribution in the tension stiffening model by Stevens et al. (Chapter 7)
α_x	Terminal degree of hydration
β	Function of the concrete type (Chapter 2)
Δ_{fr}, Δ_{fr}	Deflection at yield and ultimate capacity
ϵ	Average strain (Chapter 4)
ϵ_c	Axial strain in concrete
ϵ_{cc}	Strain in concrete at peak confined stress
ϵ_{cm}	Maximum compressive strain at potential plastic hinge regions (Chapter
ϵ_{co}	Peak strain of unconfined concrete
ϵ_{cr}	Cracking strain of concrete

ϵ_{cu}	Ultimate axial strain of confined concrete
ϵ_{1peak}	Strain in the i direction at f_{1peak}
ϵ_{ju}	Ultimate strain of the FRP jacket
ϵ_r	Lateral strain in concrete
ϵ_{ru}	Ultimate lateral strain of confined concrete
ϵ_{sm}	Maximum stress in the steel jacket (Chapter 2)
ϵ_v	Volumetric strain in concrete
$\varepsilon_x^o, \varepsilon_y^o, \varepsilon_{xy}^o$	Strains at the middle surface of the laminate
Φ	Strength reduction factor (chapter 7)
$\Phi_v\, \Phi_v$	Curvature at yield and ultimate capacity
γ	Unit weight
K_x, K_y, K_{Xy}	Curvatures at the middle surface of a laminate
λ	Parameter function of a in the tension stiffening model by Stevens et (Chapter 7)
μ	Dilation rate
μ_D	Ductility index (Chapter 7)
μ^*_D	Energy-based ductility index (Chapter 7)
μ_o	Initial dilation rate
v	Poisson's ratio
v_o	Initial value of v
V_{ij}	Poisson's ratio of the strain in the j-th direction due to loading in the i direction
θ	Inclination angle of the fiber orientation with respect to principal axis
θ_y, θ_u	Rotation at yield and ultimate capacity
ρ_g	Gross reinforcement ratio
ρ_{gg}	Gross reinforcement ratio of glass
ρ_{gs}	Equivalent steel reinforcement ratio
$\underline{P_s}$	Reinforcement ratio
σ	Average stress (Chapter 4)

Subscripts

a	Axial direction (Chapter 5)
f	Fiber
L	Longitudinal direction
In	Matrix (resin)
max	Maximum
r	Radial direction
T	Transversal direction
u	Ultimate
v	Void

Superscripts

(+) Tension

(-) Compression

1.

INTRODUCTION

\

1.1 BACKGROUND

Since ancient times humans used fibrous composites in different forms, e.g. straw-reinforced clay, timber and paper. By the beginning of this century steel-reinforced concrete evolved as a different form of structural composites. The middle of the century saw the development of fiber composite plastics as a new and effective form of fibrous composites also referred to as FRP, which stands for fiber reinforced plastics. This newly developed material is predominantly characterized by high strength-to-weight ratio and durability in corrosive environments, which made it especially attractive for aerospace and marine industry. Over the last two decades, the application of FRP has become increasingly popular in civil infrastructure.

FRP provides an effective solution for the chloride induced deterioration of reinforced and prestressed concrete bridges. Therefore, it has emerged as a successful means of structural repair (Meier 1996). Another attractive characteristic of FRP is its orthotropic behavior, which

but recent advances in new and automated manufacturing processes have made it more affordable and competitive with other materials (Seible 1996).

During the present decade intensive research has been conducted in order to investigate the properties of FRP as a new construction material. The effect of corrosive environment, i.e. salt spray, humidity, and high temperature, on concrete cylinders jacketed with S-glass and Kevlar were investigated by Bavarian et al. (1996). No loss of strength or ductility was reported. Effects of more severe environmental effects like low temperatures, freeze-thaw cycles, and sea water on FRP have also been investigated (Soudki and Green 1996, Karbhari and Eckel 1993). Degradation of strength was shown not to be substantial. Properties of carbon fibers have proven most stable in such environments. As far as long term behavior of FRP is concerned, it has been established that external carbon fiber wrap on concrete beams can significantly decrease the creep strains in concrete (Ligday et al. 1996, Pelvris and Triantafillou 1994).

Current applications of FRP in infrastructure could be divided into two main categories; either structural repair and retrofitting, or new structures. The first category includes the strengthening of concrete columns, beams, and slabs by means of FRP laminates, either prestressed or nonprestressed (Meier 1996, Fyfe 1995, Saadatmanesh 1994). The second category includes the pultruded shapes used as structural beams or trusses (Liskey 1991), the reinforcing rebars, the prestressing tendons, and the concrete filled tubes.

1.2 PROPOSED HYBRID SYSTEM

The main focus of the present study is on the concrete-filled FRP tubes, which were proposed by Mirmiran and Shahawy (1995; US Patent 5, 599, 599). It basically consists of a filament-wound FRP tube filled with concrete. This concrete-filled FRP tube (CFFT) is comparable to the concrete-filled steel tube (CFST) (Figure 1.1).

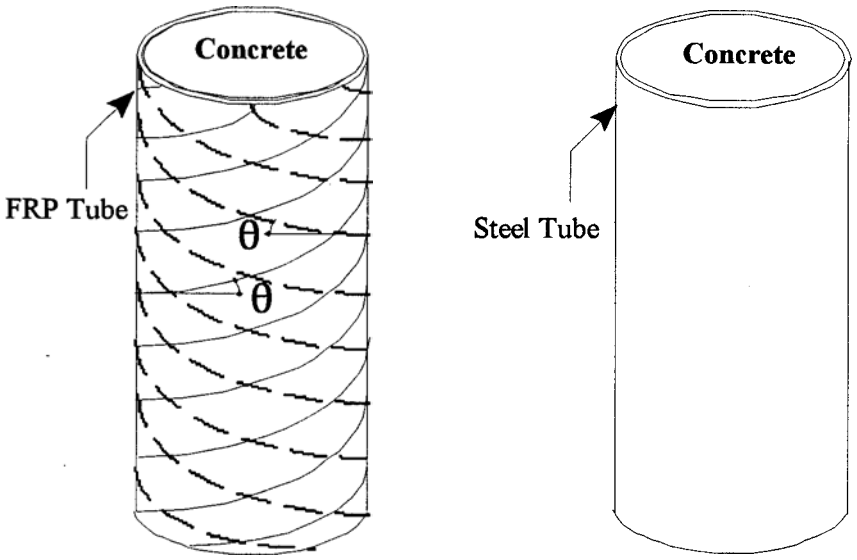

Concrete-filled FRP tube Concrete-filled steel tube

Figure 1.1 Concrete-filled tubes

In both composite columns, the tube acts as: formwork for the encased concrete; longitudinal and lateral reinforcement; protective jacket; and a continuous confining jacket. Due to the confinement of the concrete core, an enhancement in strength and ductility results. The core, in return, adds to the stability of the tube and prevents its

buckling (Daniali 1992). However, due to the light weight, strength, and durability of FRP, CFFT shows superior behavior over CFST.

1.3 PROBLEM STATEMENT

The scope of the present study is primarily focused on the structural feasibility of CFFT. The following issues are examined:

1) Confinement of concrete with fiber composites;
2) Composite action of FRP and concrete in beam columns;
3) Comparison of its behavior with conventional RC columns;
4) Design issues such as reliability and safety factors.

1.4 OBJECTIVES

The main objectives of this research are formulated as follows:

1) Develop an analytical confinement model for concrete columns confined by FRP;
2) Investigate the beam-column behavior of CFFTs under axial, axial-flexural, and flexural loading systems;
3) Compare the behavior of CFFTs with conventional RC columns; and
4) Develop a design methodology for CFFTs, comparable with existing methods.

1.5 OUTLINE OF THESIS

The present study embraces two major aspects of hybrid FRP-concrete columns; modeling of FRP-confined concrete, and the beam-column behavior of CFFTs. Both

analytical and experimental techniques were employed in this research. This thesis consists of seven chapters beside this introductory chapter. A brief overview of the contents of each chapter follows.

Chapter 2 presents an up-to-date survey of available confinement models used for steel and FRP confined concrete. Chapter 3 reviews the experimental study of CFFTs under uniaxial compression. The first step in modeling is the study of the mechanics of fiber composite, which in turn facilitates calculation of the properties of the FRP tube. This issue is discussed in detail in Chapter 4. A new confinement model is developed and verified against the test results of previous studies in Chapter 5. A second series of experiments is presented in Chapter 6, which deals with the beam-column behavior of CFFTs. In Chapter 7, test results of beam-columns were compared with equivalent conventional RC columns in regard to the strength and ductility. In the same chapter, analytical modeling of the square CFFT is discussed, along with some design guidelines. The conclusions of the present study and recommendations for further research are summarized in Chapter 8.

Finally, it should be noted that the abbreviation CFFT is used for both circular and square concrete-filled FRP tubes.

2.

CONFINEMENT OF CONCRETE

2.1 INTRODUCTION

It is well known that confinement improves the strength and ductility of concrete. Concrete can be confined by: 1) lateral reinforcement in the form of steel ties or spirals; 2) encasing concrete in steel tubes; 3) external fiber composite wraps; or 4) encasing concrete in fiber composite tubes. All these means of confinement produce a so-called `passive' state of confinement, in which the confining effect is a function of the lateral expansion of the concrete core.

The effect of confinement has been recognized since the early days of structural concrete. Many confinement models have been developed in order to predict the response of confined concrete. Concrete is often said to be "pressure- sensitive,: while it is perhaps better characterized as "restraint-sensitive" (Panatazapolou 1995). This clarifies why the stiffness of confining member has such a determining effect on the behavior of confined concrete (Mirmiran and Shahaway 1997). Also, the geometry of the cross-section and the state of loading are both factors limiting the applicability of each confinement model.

In this chapter, a literature review is presented of the research performed in the area of confinement of concrete structures, with a special emphasis on the commonly used confinement models. The confinement of concrete columns is reviewed in the first part of the chapter, followed by the confinement of beam-columns in the second part.

2.2 CONFINEMENT OF CONCRETE COLUMNS

2.2.1 Confinement by Lateral Steel Reinforcement

By the beginning of the century some research was conducted in order to evaluate the enhanced strength of concrete due to confinement. The early tests mainly considered the `active' state of confinement, in which the confining pressure was kept constant during the entire loading process. Considere *(1903)* tested the triaxial behavior of *3.15" x 11.8"* mortar cylinders, in which the lateral confinement was provided by constant hydraulic pressure. From the test results, he proposed the following relationship to predict the compressive strength of confined concrete:

$$f_{cc} = k_l f'_{co} + k_c f_v \qquad (2.1)$$

where, f'_{cc} and f'_{co} are the compressive peak stress of the confined and unconfined concrete, respectively, k_l is a constant varying between 1 and *1.5,* k_c is the confinement coefficient equal to *4.8,* and f, is the lateral confining pressure.

Considere's findings were further investigated by Richart, Brandtzaeg, and Brown *(1928)* for concrete cylinders. They subjected *4"x 8"* normal-weight concrete cylinders to

constant hydraulic pressure while applying the axial compressive load until failure. The unconfined strength of the concrete varied from 1 to 3.8 ksi, while the applied lateral pressure varied from 550 and 4090 psi. They defined the confined strength of concrete as:

$$f_{cc} = f'_{co} + k_c f_r \tag{2.2}$$

where the average value of k_c for the tests they conducted was 4.1.

Balmer (1949) tested 6" x 12" concrete cylinders under triaxial compression. A maximum confining ratio $\left(\frac{f_r}{f'_{co}}\right)$ of 6.8 was applied. Later, Chinn and Zimmerman (1965) found out that for high confining pressures ($\left(\frac{f_r}{f'_{co}}\right) \leq 17$) the confinement coefficient k, is a function of the lateral pressure. They proposed the following formula for k_c:

$$k, = 3.65\ f_r^{-0.117} \qquad (f_r \text{ in ksi}) \tag{2.3}$$

Newman and Newman (1972) compiled the test results of Richart et al. (1928), Balmer (1949), and Chinn and Zimmerman (1965) and came up with the following form for the confinement coefficient:

$$k_c = 3.7\left(\frac{f_r}{f'_{co}}\right)^{-0.14} \tag{2.4}$$

Their proposed equation implied a reducing effect of confinement at higher levels of confining pressures. Similarly, Saatcioglu and Razvi (1992) suggested the following form for k_c by fitting the test data of Richart et al. (1928):

$$k_c = 4.825\ f,^{-0.17} \qquad \text{(f, in ksi)} \tag{2.5}$$

As far as passive confinement is concerned, Richart, Brandtzaeg, and Brown (1929) also conducted a series of tests on `passively' confined concrete. A series of 23 short circular concrete columns, 10" x 40", were tested under concentric compression. The columns were externally wrapped by mild steel spirals at 1" pitch. The diameters of the spirals varied from 1/8" to 3/8". They found that the confined compressive peak stress f_{CC} could be expressed by the same equation developed for active confinement (Equation 2.2) and using the same confinement coefficient of 4.1. The confinement pressure f_r was calculated based on the maximum stress in the steel spirals using the hoop tension formula, given by:

$$fr = \frac{2 f_{sy} d_s}{D} \tag{2.6}$$

where f_s,, and d., are the yield stress and the diameter of the confining spirals, and D the inside diameter of the column. Yet, the effect of spiral spacing was not taken into account.

Iyengar et al. (1972) investigated effect of spiral spacing. They tested a series of spiral-reinforced normal-weight concrete cylinders under concentric compression. The

specimens were of two sizes: 4" x 8" with spiral pitches ranging from 1.18" to 3.86", and 6" x 12" with pitches ranging from 1.18" to 4.65". They concluded that the strength enhancement due to the spiral confinement could still be represented by the expression of Richart et al. (1928), yet with a confinement coefficient of 4.6 instead of 4.1. They suggested a modified expression for the confining pressure f_r, as:

$$f_r = \frac{2A_{sp}f_{sy}}{DS_{sp}} \tag{2.7}$$

where A_{sp}, f_{sy}, S_{ap} are the cross-sectional area, yielding stress, and pitch of the spiral, respectively, and D is the inside diameter of the column.

Ahmad and Shah (1982a) developed a constitutive relationship for plain concrete subjected to triaxial compressive stresses. They proposed a fractional equation to predict the complete stress-strain curve of `actively' confined concrete in the following form:

$$Y = \frac{A_i X + (D_1 - 1)X_i^2}{1 + (A_i - 2)X_i + D_i X_i^2} \tag{2.8}$$

in which $\mathbf{Y} = \frac{f_1}{f_{1peak}}$ $\mathbf{X} = \frac{\varepsilon_1}{\varepsilon_{1peak}}$, f_1 is the main principal compressive stress, f_{1peak} is the main principal strength, ϵ_1 is the strain in the principal direction (**i** = 1, 2, or 3), ε_{1peak} the strain at f_{1peak} ,A=$\frac{Ei}{E_{ipeak}}$ is the initial slope of the f_1-ϵ curve $E_{ipeak} = \frac{f_{1peak}}{\varepsilon_{1peak}}$ and D_i is a parameter controlling the descending portion of the f_1-ϵ_i curve. Thus, the equation

is valid in the principal axial direction (i =1) as well as in the lateral direction (**i** = 2, $f_2 = f_3 = f_r$). The calculation of the peak strength f_{1peak} (=f'_{cc}) and the peak strain f_{1peak} (=ϵ_{cc}) Was based on the octahedral theory. They arrived at a bilinear relationship in lieu of the linear equation of Richart et al. (1928). According to their procedure, the confined compressive strength was expressed as follows:

$$f'_{cc}=f'_{cc}+4.256f_r \qquad (for\ f_r \leq 0.679 f'_{co})$$
$$f'_{cc}=1.776f'_{co}+3.117 f_r \qquad (for\ f_r \leq 0.679 f'_{co}) \tag{2.9}$$

They also established an incremental iterative procedure to predict the behavior of `passively' confined concrete using their model for 'active' confinement (Ahmad and Shah 1982b). The procedure is summarized as follows: For a certain axial strain ϵ_{1i}, a confining pressure f_r is assumed. The f_c-ϵ_e, and f_c-ϵ_r curves are developed for the assumed value of f_r, using Equations. 2.8 and 2.9. The values of f_{ci}, ϵ_{ri}, and f_{si} are obtained, where f_{si} is the stress in the steel spirals (see Figure 2.1). A new value of f_r is then calculated using the obtained hoop steel stress f_{si}. The new value of f_r is compared with the old one. The procedure is repeated till convergence takes place. Then, the same steps are repeated for the next strain increment.

Experimental data of their own (Ahmad and Shah 1982 a&b), of Iyengar et al. (1970), and of Burdette et al. (1971) on short concrete columns confined by steel stirrups, were used to verify the above model. Experimental and predicted results compared favorably. Here, it should be noted that Ahmad and Shah's model is best suited for circular

concrete columns confined by steel stirrups or steel tube, since the calibration of the parameter D_1 (Equation 2.8) was based on the test results of uniaxial compressive testing of concrete-filled steel cylinders (Ahmad 1981).

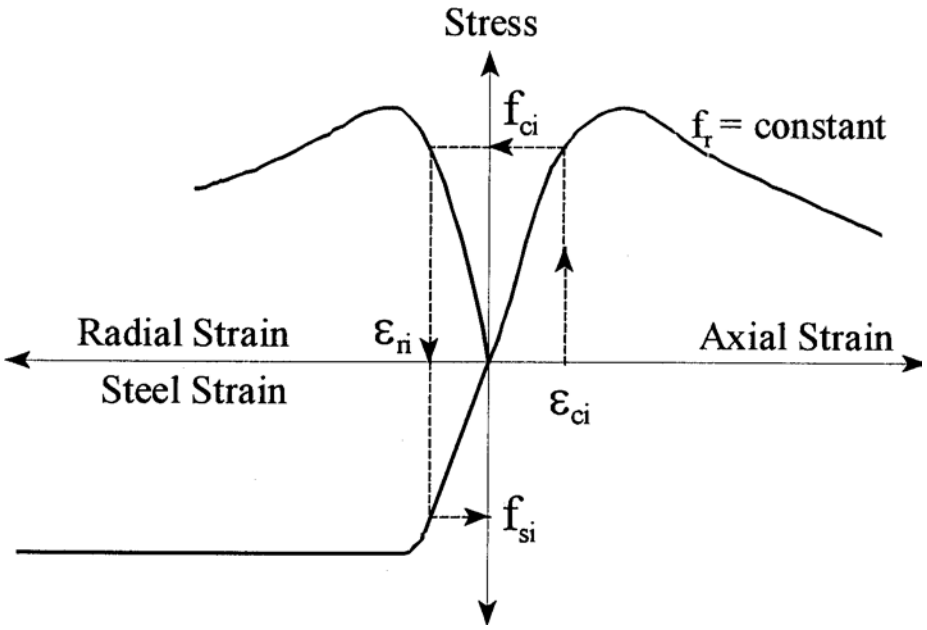

Figure 2.1 Schematic of the confinement model of Ahmad and Shah (1982b)

Mander, Priestley, and Park (1988) developed a more simplified confinement model applicable to concrete confined by circular or rectangular transverse reinforcement. The proposed stress-strain model is based on an equation proposed by Popovics (1973) for plain concrete. The axial compressive stress in concrete f_c is expressed in terms of the axial strain ϵ_c, the peak strength f'_{cc} and the corresponding strain Ecc as follows:

$$f_c = \frac{f'_{cc} \times r}{r - 1 + x^r} \tag{2.10}$$

where $x = \frac{\varepsilon_c}{\varepsilon_{cc}}$, $r = \frac{E_c}{E_c - E_{\sec}}$, E_c is the tangent modulus of elasticity of concrete, and E_{sec} $= \frac{f'_{cc}}{\varepsilon_{cc}}$. The value of f'_{cc} is determined based on the multi-axial failure surface by William SIC and Warnke (1975) and for circular sections it is given by:

$$f'_{cc} = f'_{co}\left(-1.254 + 2.254\sqrt{1 + \frac{7.94 f_r}{f'_{co}}} - 2\frac{fr}{f'_{co}}\right) \tag{2.11}$$

And the value of $\epsilon_{cc}$is given by:

$$\varepsilon_{cc} = \varepsilon_{co}\left[1 + 5\left(\frac{f'_{cc}}{f'_{co}} - 1\right)\right] \tag{2.12}$$

The ultimate axial strain s_c,, is determined based on an energy balance approach, which assumes that the additional ductility in the confined member is due to the energy stored in the transverse reinforcement.

The model assumes a constant confining pressure throughout the loading history and it is insensitive to variation of the Poisson's ratio of concrete, and thus it does not satisfy the strain compatibility condition at peak stress (Mirmiran and Shahawy 1997a). In other words, it presents a solution for the active confinement problem rather than the passive confinement. Studies by Chai (1991) have shown that the model underestimates the ultimate compressive strains of conventional RC columns by as much as 85%.

Madas and Elnashai (1992) developed a passive confinement model for reinforced concrete columns subjected to cyclic or transient loading. Their model was an improvement over the model of Mander et al., and at the same time a simplification of the Ahmad and Shah's model. In their procedure, they expressed the lateral strain in concrete ϵ_r as a cubic polynomial function of the longitudinal strain ϵ_c. The derivation is based on a correlation of the Poisson's ratio v and ϵ_c proposed by Elwi and Murray (1979) as:

$$v = v_o \left[1.0 + 1.3763 \left(\frac{\varepsilon_c}{\varepsilon_{co}} \right) - 5.36 \left(\frac{\varepsilon_c}{\varepsilon_{co}} \right)^2 + 8.586 \left(\frac{\varepsilon_c}{\varepsilon_{co}} \right)^3 \right] \tag{2.13}$$

where v_o is the initial value of v, and ϵ_{co} is the longitudinal strain at f'_{co}. Thus, for a certain axial strain ϵ_c the corresponding value of ϵ_r is determined, which is equal to the hoop strain in steel, by strain compatibility. Thus, the stress in steel is determined, and the f_r value is calculated using the hoop tension formula. The axial stress f_c is then calculated using the corresponding stress-strain curve, developed by any active confinement model such as that of Ahmad and Shah (1982a). The model proved to give better predictions of the experimental results in comparison to the model of Mander et al. for RC columns, by taking into consideration the strain compatibility in the lateral direction.

All the previously mentioned models were mainly applicable to circular columns, except for the model by Mander et al. (1988), who included a certain formula for lateral pressure developed by rectilinear hoops. Many other models are available in the literature and were summarized by Sheikh (1982). For example, El-Dash and Ahmad (1994)

modified Ahmad and Shah's confinement model in order to predict the complete stress-strain relationship for short normal and high strength concrete columns confined by rectilinear steel hoops.

2.2.2 Confinement by Steel Tubes

Another form of concrete confinement is by encasing concrete in a steel tube (Kloppel and Goder 1957). The steel tube acts as longitudinal, transversal, and shear reinforcement; formwork; and as a continuous confining jacket for the encased concrete. In return, concrete delays local buckling of the tube (Gardner and Jacobson 1967). Knowles and Park (1969, 1970) conducted a series of tests on concrete-filled steel tubes of different slenderness ratios, and concluded that in most cases buckling of the tube dictated the overall failure of the composite column before the activation of confinement. They recommended to avoid loading the steel tube in the longitudinal direction in order to achieve its full utilization in the circumferential direction. This was later confirmed by Orito et al. (1987), who determined that unbonded concrete-filled steel tubes had higher axial compressive strength in comparison with the bonded tubes.

Prion and Boehme (1994) performed a series of tests on concrete-filled circular steel tubes. They reported that the confinement effect is noticeable for a slenderness ratio, L/D, less than 15, where L and D are the height and diameter of the column, respectively. The failure mode for short columns ($L/D < 15$) was a shear failure of the concrete core.

2.2.3 Confinement by FRP Wraps

Since early 1980's, fiber composites have been used for confinement of concrete. Fardis and Khafh (1981) wrapped bi-directional FRP fabrics on 3"x 6" and 4"x 8" concrete cylinders. Four different types of FRP fabrics were used: 10 oz/ sq yd fiberglass cloth; 13, 15, and 24 oz/ sq yd unbalanced woven rovings. The specimens were tested under uniaxial compression. They concluded that confinement by FRP not only increases concrete strength, but enhances its ductility, as well. They also developed an analytical model describing the performance enhancement using a hyperbolic equation (Fardis and Khalili 1982), as follows:

$$f_c = \frac{E_c \varepsilon_c}{1 + \varepsilon_c \left(\frac{E_c}{f'_{cu}} - \frac{1}{\varepsilon_{cu}} \right)} \tag{2.14}$$

where, E_c is the initial tangent modulus of unconfined concrete, f'_{cu} is the ultimate strength of confined concrete, which is determined by either the expression of Richart et al. (1928) or by the one by Newman and Newman (1972), Equations 2.2 and 2.4, respectively, and E,,,, is the ultimate axial strain of confined concrete, which is given by:

$$\varepsilon_{cc} = 0.002 + 0.001 \frac{E_j t_j}{D f'_{co}} \tag{2.15}$$

where, E; and tj are the modulus and the thickness of the FRP jacket, respectively.

Ahmad, Khaloo, and Irshaid (1991) conducted an investigation of the confinement effectiveness of fiberglass spirals as transverse reinforcement of concrete columns. They tested 33 FRP-confined 4"x 8" concrete cylinders under axial compression. The test results were used to modify the confinement model of Ahmad and Shah (1982b), in order to predict the response of concrete confined by FRP spirals. They proposed the following expression for the peak stress of confined concrete, f'_{cc}:

$$f'_{cc} = f'_{co}\left(1 + \frac{k}{4^{ns_{sp}}}\right) \tag{2.16}$$

where k and n are functions of f'_{co} and S_{sp} is the spacing of the spirals. An expression for the peak strain of confined concrete was also proposed in a similar form:

$$\varepsilon_{cc} = \varepsilon_{co}\left(1 + \frac{k}{4^{ns_{sp}}}\right) \tag{2.17}$$

Saadatmanesh et al. (1994) proposed the use of precured E-glass or carbon thin straps to wrap around existing concrete columns. The straps can be wrapped in a continuous spiral and/or in separate rings. A parametric study was conducted on the behavior of circular and rectangular columns strengthened with composite straps. Four parameters were considered in their study: the concrete strength, the FRP strap thickness, the strap clear spacings, and the material of the straps. For the analysis they used the confinement model of Mander et al. (1988). Yet, the analytical results were not verified by experiments.

Nanni and Bradford (1995) investigated the behavior of 6" x 12" concrete cylinders confined by three types of fiber-wraps: pretensioned braided aramid cables, precured hybrid glass-aramid shells, and glass filament-winding. For the first series, they tested 16 specimens with variable diameter and spacing of the cables. Four specimens were tested in the second series, and 15 in the third series. The cylinders of the third series were made with a central rod, which was then placed on a filament-winding machine, and wrapped with 1, 2, 4, or 8 plies of E-glass fibers and vinylester resin (or polyester for some of the specimens). The strength of concrete core was reported as: 5.2, 6.6, and 5.3 ksi for the three series, respectively. They concluded that the stress-strain response of FRP-encased concrete, in general, could be modeled by a simple bilinear curve with a bend-over point at the peak stress of unconfined concrete, which corresponds to a strain of 0.003. They, however, did not develop a confinement model. Test results were also compared with the confinement models by Mander et al. (1988) and Fardis and Khalili (1982), both of which grossly underestimated the ultimate strain of encased concrete, but compared reasonably well for strength of confined concrete.

Picher (1995) tested a total of 44 6" x 12" concrete cylinders wrapped in 2, 3, 4, or 5 layers of carbon fibers with different orientation angles. Most specimens, however, were made with three layers of carbon fibers. Fiber orientations of 0°, +6°, +9°, +12°, +18°, and ±24°, or a combination of these were used. Two different types of unidirectional carbon fabrics, namely Mitsubishi and Autocon, were used. The unconfined strength of concrete for all specimens was 5.8 ksi. He further performed an incremental nonlinear finite element analysis. The Drucker-Prager failure criterion was implemented in the

analysis. Two models were incorporated for the concrete: elastic-perfectly plastic, and elastic-plastic with strain hardening. The second model resulted in more accurate predictions.

As an extension of Picher's work, Rochette (1996) tested a series of 33 fiber-wrapped specimens in uniaxial compression. The parameters studied included cross-sectional shape (circular, square, and rectangular), fiber type (carbon and aramid), comer radius, and number of composite layers or wraps (2 to 5 layers for carbon, and 3 to 12 layers for aramid). The concrete strength ranged between 4.2 to 6.4 ksi. The same analytical approach used by Picher (1995) was carried out for this study. The model compared favorably with the experimental results. However, it was concluded that a more complex elasto-plastic formulation of concrete behavior is needed to enhance the model for various cross sections, fiber orientations, and load combinations (Rochette and Labossiere 1996).

Recently, Monti and Spoelstra (1997) proposed a confinement model for circular columns wrapped with fiber-reinforced plastics. The procedure is basically the same as the model of Ahmad and Shah(1982). For a certain axial strain ϵ_{ci}, a value f_{ri} is assumed. The axial stress f_{ci} is then calculated using the confinement model of Mander et al. (1988) as an active confinement model. The lateral strain ϵ_r is then calculated using the expression developed by Pantazopoulou (1995). Knowing ϵ_r and the constitutive relationship of the jacket, a new value of f_r is calculated and compared with the previous value. The procedure is repeated until f_r converges to a stable value. The expression of the lateral strain ϵ_r is given by:

$$\varepsilon_r = 0.5\beta \frac{E_c - E_{\sec}}{E_{\sec}} \tag{2.18}$$

where, E_c is the initial tangent modulus of concrete, Esec is the current secant modulus and is equal to $\frac{f_c}{\varepsilon_c}$, and β is a function of the concrete type, as below:

$$\beta = -\frac{V_p^3 v_c}{3} \tag{2.19}$$

where V_P is the volume fraction of paste in concrete, and v_c is the natural capillary porosity of the paste, which depends on the water-cement ratio w_o and the terminal degree of hydration α_x, as:

$$v_c = 3.22 \frac{w_o - 0.3064\alpha_x}{1 + 3.22 w_o} \tag{2.20}$$

$$\alpha_x = \frac{1.031 w_o}{0.194 + w_0} \tag{2.21}$$

The model compared favorably with the experimental results of Picher et al. (1996).

2.2.4 Confinement by FRP Tubes

In the late 1970's Kurt (1978) suggested using commercially available plastic pipes (PVC) filled with concrete. For a slenderness ratio of less than 20, plastic-encased concrete showed a 45° shear failure, both in the concrete core and in the plastic pipe,

resulting from the combination of axial compression and hoop tension in the pipe. Since the plastic material used by Kurt was weak, the enhancement in the strength of concrete was not significant.

In early 1990's, as part of an investigation on the effect of confinement on high-strength concrete, Lahlou et al. (1992) tested two 2" x 4" glass fiber tubes filled with concrete. However, since the fibers were axially oriented (pultruted), they did not observe any significant enhancement in the strength of concrete.

Harmon et al. (1995) tested small scale FRP tubes filled with concrete under axial compression. Glass/epoxy and carbon/epoxy circular 2" x 4" tubes were produced by filament winding and filled with high strength concrete (f'_{co} = 9.3 ksi). Fiber to concrete volume ratios ranging from 0 to 0.06 were used. Bi-linear stress-strain responses resulted for all the glass and carbon specimens. The following observations were reported:

- The second slope of the axial stress-strain curves was proportional to the tube stiffness.
- The axial stress at the bend-point of the bilinear stress-strain curve is proportional to the tube stiffness.
- The dilatancy is inversely proportional to the tube stiffness.

They also modeled the nonlinear behavior of confined concrete using a mechanistic crack model based on shear slip on oblique fracture planes. Reasonable results were obtained.

Mirmiran and Shahawy (1995) proposed a concrete-filled FRP tube (CFFT), in which the tube acts as: formwork for the encased concrete, hoop and longitudinal

reinforcement, and corrosion-resistant casing for the concrete. The CFFT was proposed for bridge columns as well as for pile splicing. The Florida Department of Transportation (FDOT) sponsored a series of projects in order to investigate the behavior of the proposed CFFT. Several parameters were considered in these studies, e.g. the type of loading, the cross-section, the bond, and the length effect. Kargahi (1995) investigated the strength of CUT under uniaxial compression. A total of 12 circular specimens were tested, 9 CFFTs and 3 6" x 12" plain concrete cylinders. Filament-wound E-glass/polyester tubes were used, with winding angle of ±75° with respect to the longitudinal axis of the tube. Three different tube thicknesses were included, namely, 0.074", 0.13", and 0.237". An enhancement in the concrete strength, in the order of 2.5-3.5 times the unconfined strength, was reported. He also performed a series of split-cylinder tests, in order to investigate the improvement of the tensile strength of the FRP-confined concrete. It was concluded that the FRP tube improves the behavior of the concrete section in tension by containing the cracked concrete rather than confining it. A parametric study was also performed on the effect of ply thickness, winding angle, and the composite action on the confined strength of the column. The analysis was based on the confinement model of Mander et al. (1988). It was concluded that the thickness of the tube increases the pure axial strength. The presence of full composite action does not significantly improve the axial capacity of the column but rather the flexural capacity. Moreover, an increase in the fiber winding angle will decrease the pure axial strength. The pure flexural capacity is maximum at a winding angle of ±45*.

Scherer (1996) extended the study of Kargahi and investigated the shape of the stress-strain curve and also the dilatancy properties of the same type of tubes under the same type of loading (this is explained in detail in Chapter 3). He further studied the cost optimization of the proposed composite structure.

The bond effect was investigated by Mastrapa (1997). He tested a total of 32 6" x 12" composite cylinders, half of which were wrapped in 1, 3, 5, or 7 layers of S-glass fabric, while for the other half concrete of the same batch was poured in tubes made of the same S-glass fabric and with the same number of layers. Tests were done in two series. In Series 1, multi-layer jackets were made layer-by-layer with a splice of about 17% of the perimeter of the cylinders, while in Series 2, the jacket was made of a continuous wrap of the fabric with an overlap of about 32% of the perimeter of the cylinder. The average unconfined strength of concrete for specimens of Series 1 was 5.4 ksi. The hoop strength and modulus of the FRP jacket were 85 ksi and 2,984 ksi, respectively. It was concluded that the effect of construction bond on axially loaded confined concrete is not significant.

Pico (1997) tested a total of 9 6" x 6" x 12" square concrete-filled FRP tubes under axial compression, in order to study the effect of cross section of the CFFT. No bond was provided between the concrete core and the FRP tube. A marginal increase in strength was observed independent of the jacket thickness. The over-riding parameter in controlling the confinement was shown to be the product of the corner radius and the confining pressure.

El Echary (1997) evaluated the effects of length-to-diameter (L/D) and diameter - to-thickness (D/t) ratios on the behavior of the CFFT. A total of 24 circular CFFTs

(D_{inner}=5.71") with three different tube thicknesses (6, 10, and 14 layers) and four different lengths (12", 18", 24", and 30") were tested. No buckling was observed during the tests. The analysis of the test results indicated that the maximum eccentricity was within 10-12% of the section width. The reduction in strength was not significant. It was concluded that up to a ratio L/D of 5:1, slenderness effects are negligible.

2.3 CONFINEMENT OF CONCRETE BEAM-COLUMNS

2.3.1 Confinement by Lateral Steel Reinforcement

The confinement improves both strength and ductility of concrete columns under axial loads, while a different scenario is observed for beam columns. Sheikh and Yeh (1986,1992) stated that in presence of strain gradient the confinement mainly improves the ductility of the section, while the enhancement in the strength is not noticeable. They modified the confinement model by Sheikh and Uzumeri (1980) for concentric f compression to include the effect of strain gradient. They used a modified concrete compression block to determine the flexural capacity of structural concrete members.

Ziara et al. (1995) tested 12 under-reinforced and 4 over-reinforced beams in flexure in order to investigate the confining effect of the stirrups in the compression zone. Test results showed that over-reinforced beams with confinement can be designed to fail in a ductile manner and reach their full flexural capacity. They defined a new maximum reinforcement ratio taking into consideration the confinement characteristics.

2.3.2 Confinement by Steel Tubes

Large-scale columns were tested at the University of California at San Diego, in order to investigate the performance of columns retrofitted with steel jackets (Chai et al. 1991). The columns were 0.4-scale models of a prototype 60"-diameter bridge column. The test columns were constructed with a footing to allow foundation interaction to be monitored. The tests included models with the pre-1971 reinforcing details without retrofitting, columns retrofitted with steel jackets, and a post-damage retrofitted column to determine whether a damaged column can be salvaged after an earthquake. A'¼"-gap was provided between the column and jacket. The gap was pressure-injected with water/cement grout. From the test results, it was concluded that the confinement provided by a fully grouted steel jacket could completely contain the cover concrete to eliminate bond failure. Moreover, a ductile mode of flexural failure with good energy dissipation could be achieved.

Chai, Priestley, and Seible (1994) developed an analytical model for the first-yield limit state and the ultimate limit state of flexurally dominated steel jacketed circular bridge columns. An expression was derived for the maximum compressive strain at potential plastic hinge regions s_{cm} as follows:

$$\varepsilon_{cm} = 0.004 + \frac{5.6 t_j f_{yj} \varepsilon_{sm}}{D f'_{cc}} \tag{2.22}$$

where t_j is the thickness of the steel tube, f_{yj} and ϵ_{sm} are the yield stress and the maximum strain of the steel jacket, D is the concrete core diameter, and f'_{cc} is the peak confined

concrete stress according to the model of Mander et al. (1988). Equation 2.22 can be solved for the jacket thickness t_j as:

$$t_j = \frac{0.18(\varepsilon_{cm} - 0.004)Df'_{cc}}{f_{yj}\varepsilon_{sm}} \quad (2.23)$$

The increase in lateral stiffness of circular bridge columns due to steel jacketing and the ultimate displacement ductility capacity of the steel jacketed columns were assessed.

The beam column behavior of concrete-filled steel tubes has been studied by Prion and Boehme (1994). They tested a total of 26 circular steel tubes with a 6" outside diameter, a ⅛" wall thickness and variable lengths filled with high strength concrete (10-13 ksi), under different load combinations ranging from pure axial compression, through various combinations of axial-flexure, to pure flexure. They reported that the beam column specimens failed by tension failure of the steel tube accompanied by buckling of the steel in the compression zone, whereas eccentric loading caused an abrupt failure along with lateral buckling of the tube. Significant slippage between steel and concrete was observed in pure flexure tests. It was also noticed that the secondary moments, due to the P-Δ effects, constituted 20% of the total ultimate moment. This was a result of the large deformations prior to failure.

Hajjar et al. (1996) developed a polynomial equation to represent the three-dimensional cross-section strength of square or rectangular concrete-filled steel tube CFT beam-columns. The parameters of their model is the width-to-thickness ratio of the steel tube, and the ratio of the concrete compressive strength to the yield stress of the steel

tube. They also verified their model against experimental results of short CFT in the literature.

2.3.3 Confinement by FRP Wraps

Fardis and Khaff (1981&1982) tested a concrete-filled FRP box in pure flexure. The cross-section of the box was 3" wide x 6" deep with a total length of 48". The bottom, sides, and ends of the FRP box consisted of two layers of 24 oz. fiberglass bi-directional woven roving. In addition, reinforcing unidirectional plies were provided at the bottom. After pouring concrete in the FRP box, the top and the sides were covered with two layers of 10 oz. fiberglass cloth. Five specimens with different number of reinforcing layers were tested under four point flexure loading. No mechanical interlocking was provided between concrete and FRP, which caused some slippage to take place. The failure was mainly due to crushing of the concrete followed by bursting of the FRP layers in the compression zone. They also tested four reinforced concrete beams with different reinforcement ratios for comparison. An equivalent FRP reinforcement ratio was proposed, which resulted in the same flexural capacity as that of RC beams. That ratio was calculated by dividing the total area of the axial FRP within the bottom quarter of the section by the gross cross-sectional area and then multiplying that number by the ratio of the strength of FRP and the yield strength of steel. However, the deflection of the FRP-encased concrete beams was higher than the corresponding RC beams, due to the low stiffness of fiberglass as compared to steel.

Nanni and Norris (1995) performed a series of flexural and axial-flexural tests on circular and rectangular FRP-wrapped reinforced concrete beams. They tested 19 circular 6" diameter and 7 rectangular (6"x 8") specimens. Two types of FRP jackets were used; braided aramid/epoxy tapes spirally wound at 0" and 1" pitches; and precured glass-aramid/epoxy shells. The specimens were 60" long and were loaded under cyclic flexure. The concentric axial loads on some of the specimens was applied via prestressing bars. It was concluded that the FRP jacketing increased the ductility of the specimens in comparison to typical unconfined beams. This was more apparent for specimens with higher axial loads.

Researchers at the University of California, San Diego proposed a design criteria for circular concrete column retrofitted by FRP jackets (Priestley et al. 1995). They adopted the confinement model of Mander et al. (1988), yet with a different expression for the ultimate compressive strain of confined concrete ϵ_{cu} given by:

$$\varepsilon_r = 0.5\beta \frac{E_c - E_{\text{sec}}}{E_{\text{sec}}} \tag{2.24}$$

where ρ is the volumetric ratio of confinement and is equal to $\frac{4t_c}{D}$, $f_{j \text{ and }} \epsilon_{ju}$ are the ultimate stress and strain of the FRP jacket, and f'_{cc}. is the peak confined concrete stress according to the model of Mander et al. (1988). Equation 2.24 is also applicable to rectangular jackets using the following expression for p as:

$$\rho = 2t_j \left[\frac{b+h}{bh} \right] \qquad (2.25)$$

where b and h are the section dimensions of the column.

Based on tests on circular concrete columns retrofitted with FRP jackets to improve ductility, they reported that the confinement effectiveness for FRP jackets is more efficient than steel jackets (Priestley et al. *1995)*. This is mainly attributed to the elastic nature of FRP.

2.3.4 Confinement by FRP Tube

Carbrera (1996) tested two series of short square concrete-filled FRP tubes in pure flexure. The first series of test consisted of 8, 6" x 6" x *22"* concrete beams, 6 of which were encased in fiberglass tubes, and 2 were control specimens. The beams were loaded to failure under a four-point loading test. Test results indicated that while the shear strength of the beams was increased by up to 133 percent, excessive slippage at the concrete jacket interface inhibited development of full shear strength by the jacket. A second series of tests was conducted with shear connectors on all interior faces of the FRP tube. Results of these tests demonstrated that slippage was completely arrested by the shear connectors. The FRP tube was able to increase the shear strength beyond the flexural capacity of the members. She also conducted a study on the seismic performance of concrete-filled FRP tubes based on a cyclic stress-strain model. The parameters of the study were the reinforcement index, the confinement ratio, the axial loads, and the eccentricities. The effects of these parameters on hysteretic loops and cumulative energy absorption of FRP-

concrete columns were studied. Results indicated that the effect of confinement ratio on the energy absorption of the member is more than the effect of reinforcement ratios. Currently, there are two other on-going projects at the University of Central Florida. Under the first project, beam-column behavior of sixteen 10' long, 14" diameter pipes filled with concrete is being investigated. Half of the pipes are made by the filament-winding method, while the other half are made by the centrifuge technique. The pipes are intended for use as piles which will be driven in the field. The second project, evaluates the long-term behavior of concrete-filled FRP tubes, and examines the issues of creep, shrinkage, and fatigue.

In the last two years, and upon promising results from the work at UCF, research on CFFT has received attention in the US and overseas. Researchers at the University of California, San Diego have conducted experiments with carbon shells for bridge piers. Some work is also in progress in India and Hong Kong.

3.

UNIAXIAL, COMPRESSION TESTS

3.1 INTRODUCTION

Uniaxial compression tests were conducted on three different series of concretefilled fiberglass circular tubes. The purpose of these tests was primarily to determine the confinement effectiveness of the proposed composite column. The main purpose of the first series (Series A) was to investigate the feasibility of the proposed confinement system, and to quantify the strength enhancement for different tube thicknesses. The results of the second and third Series (C and D) allowed for studying the behavior of the confined composite column under pure axial compression. The results of Series D were further investigated and used for the calibration of the proposed confinement model (see Chapter 5).

In the following sections, a brief explanation of the tests is presented. A detailed description of Series A may be found in Kargahi (1995), and of Series D in Scherer (1996).

3.2 TEST PROGRAM

A summary of the test program is presented in Table 3.1. A total of 42 concrete-filled fiberglass tubes and 12 control cylinders were tested (Kargahi 1995, Sherer 1996, present study). The fiberglass tubes were all of 12" length and 5.71" inside diameter, while the outer diameter was variable according to the tube thickness. The control plain concrete cylinders, however, were all 6" x 12". Each of the three series included three concrete batches and three different tube thicknesses (Table 3.1). The fiberglass tubes consisted of filament-wound E-glass/polyester angle plies with a ply angle of ±75° with respect to the axis of the tube and were manufactured by Marine Muffler Corp., Apopka, FL. The glass rovings were Vetrotex CertainTeed 67B R099, 450 yield, and the polyester resin was Reichhold Dion FR 6692T (33-611). The material properties are presented later in Chapter 4.

All concrete batches for the three series were manually mixed and cast at the University of Central Florida. As for curing the concrete inside the FRP tubes, only the top exposed surface was wetted for 3-4 days after casting.

At the onset of the project, it was not known how much bond stress would be developed at the interface of concrete and tube. Therefore, in order to force the tube to act as a hoop tension band and not to carry any axial load, the concrete-filled tubes were grooved at both ends. The circumferential grooves were 3/16" thick at about 3/4" from the end surfaces, and were cut through the thickness of the tube. Additional grooves at the end surfaces were cut for the specimens of Series C. Later it was found out that the actual

Table 3.1 Uniaxial compression test

Series No.	Batch No.	Concrete strength (ksi)	No. of composite specimens	No. of control cylinders	Tube thickness (in)			No. of plies		
					Tube 1	Tube 2	Tube 3	Tube 1	Tube 2	Tube 3
	1	3	3	1						
A	2	6.8	3	1	0.074	0.13	0.237	9	16	28
	3	5.9	3	1						
	1	5.3	3	1						
C	2	4.5	3	1	0.074	0.13	0.237	9	16	28
	3	6.6	3	1						
	A	4.5	9	2						
D	B	4.3	9	2	0.051	0.083	0.118	6	10	14
	C	4.6	6	2						
Total			42	12						

mechanical bond at the interface of concrete and tube is almost non-existent due to the smooth internal surface of the tubes. As for the instrumentation, only the specimens of Series C and D were strain gaged in order to record the stress-strain response of FRPconfined concrete in both axial and hoop directions. Specimens of Series C were mainly instrumented with 2 foil stain gages in the hoop direction except for 3 specimens (2 composites and 1 control), for which 4 bi-directional rossettes were used. The rosettes were of TML strain gages PFC-10 with a gage length of 10 mm, gage width of 0.9 mm, and gage factor of about 2.1. The gages were attached with a two part epoxy adhesive at the mid-height of each specimen at 2 or 4 locations evenly distributed around the specimen. The bi-directional rossettes allowed monitoring the axial and hoop strains on the surface of the tube. In addition, all specimens were instrumented with an embedded gage (PML-30) with 30 mm gage length and 1 mm gage width at the mid-height of specimen to measure the axial strains in concrete. Additionally, 3 Linear Variable Differential Transducers (LVDT) were placed at 120° apart around the specimen to measure the axial displacements and average axial stains.

Specimens of Series D were instrumented with two 60-mm surface gages (TML gage PL-60) in order to measure the hoop strains at the mid-height of each specimen. The surface gages were superglued to the specimens after sanding and cleaning the contact surface of the specimens. In addition to surface gages, three of the specimens (one of each thickness in Batch A, DA12, DA22, and DA32) were fitted with a 30-mm. embedded strain gage (TML gage PML-30) inside concrete at the mid height of specimen to measure the axial strains in concrete. Moreover, for measurements of average axial strains, three

LVDTs were placed at 120° apart around the specimen. The results from the LVDTs were compared with those of the embedded gages. It was observed that for all practical purposes, the average axial strains measured by LVDTs were as accurate as the measurements made with the embedded gages, especially since the embedded gages reached their readability limit at 2% strain levels, which proved too low for all jacket thicknesses.

All specimens were capped with sulfur mortar except for two specimens of Series A, for which neoprene pads were used instead. The specimens of Series A were tested by a 600-kip Forney compression machine at a loading rate of 60 kip/min. While specimens of Series C and D were tested by a 550-kip MTS machine in a displacement control mode at a rate of 0.22 in/min.

3.3 TEST OBSERVATIONS

All specimens behaved more or less in the same manner during the loading process. Cracking noises were heard during the early to middle stages of loading revealing the fracture of the concrete core. It was also observed that the failure of the FRP tube was preceded by flow of resin which manifested itself by white patches at highly stressed sections (Figure 3.1). The principal failure mode was a typical shear failure of the FRP tube towards the mid-height and along the fiber direction. This was followed by fiber fracture and delamitation of the tube. Figures 3.2 and 3.3 display the failure modes of Specimens A32 and DB22 of Series A and D, respectively. Shear failure of the tube along

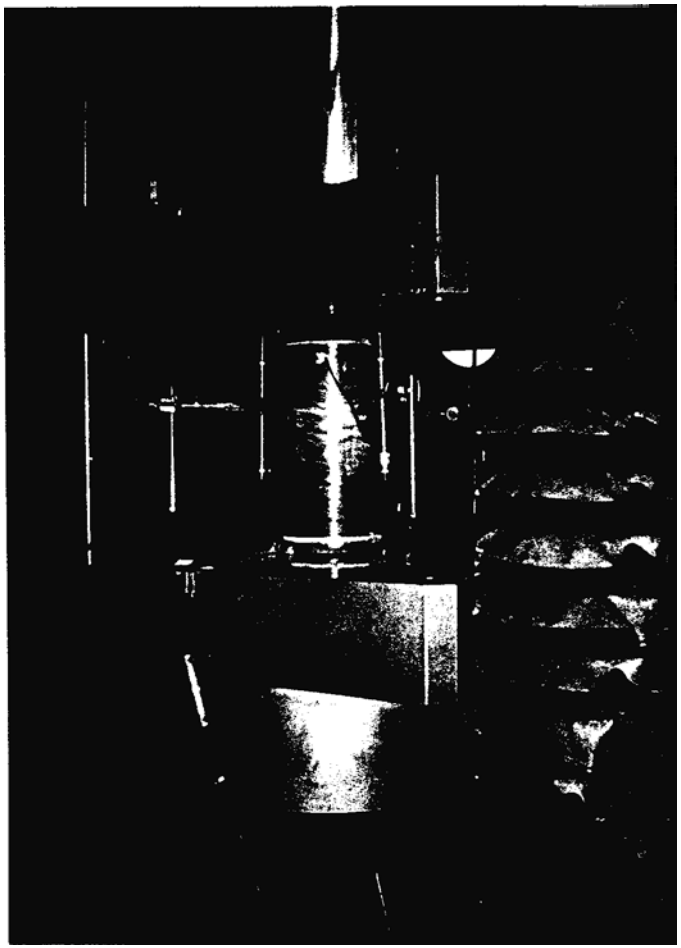

Figure 3.1 White patches at stressed zones prior to failure

Figure 3.2 Failure of Specimen A32 of Series

with fiber fracture and delamination are apparent. At this stage the encased concrete is totally crushed and even pulverized. Figure 3.4 shows the state of the concrete core at failure. It was also noticed that the encased crushed concrete is usually moist due to poor aeration. As far as bond is concerned, it was observed that no concrete was attached to the remainder of the tube, and a smooth interface was discovered (Figure 3.4). This led to the conclusion that no bond is developed between concrete and FRP tube.

For most specimens, the first failure occurred within the middle third of the specimen height, while a failure towards the top and bottom edges characterized some specimens of Series C (Figure 3.5). This raised a concern that the capping may have not been completely level with respect to the vertical axis of the specimens, which resulted in an undesired eccentricity of the applied load. Consequentially, the ultimate strains and stresses were generally low in comparison to the values obtained for Series D.

Three specimens of Series D (Batch B) failed at higher than the anticipated loads. This was attributed to higher unconfined strength of the concrete core due to the variation of the curing process. Two observations supported this assumption, the high bend point of the stress-strain curve, and also high initial modulus of the concrete core.

3.4 TEST RESULTS

The test results are summarized in Table 3.2 for Series A and C, and in Table 3.3 for Series D. The stress-strain curves of Series C and D were corrected by the so-called

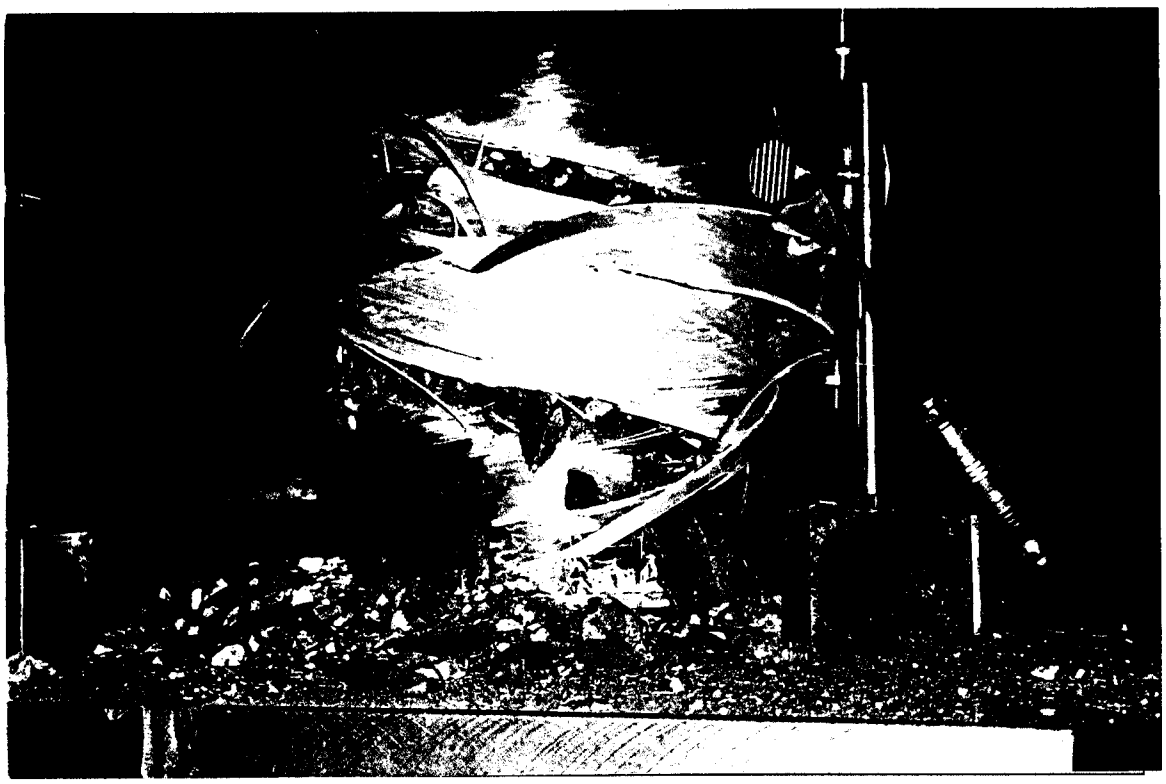

Figure 3.3 Typical shear failure of FRP tube along with fiber fracture and delamination

Figure 3.4 State of encased concrete at failure, no concrete attached to the tube 38

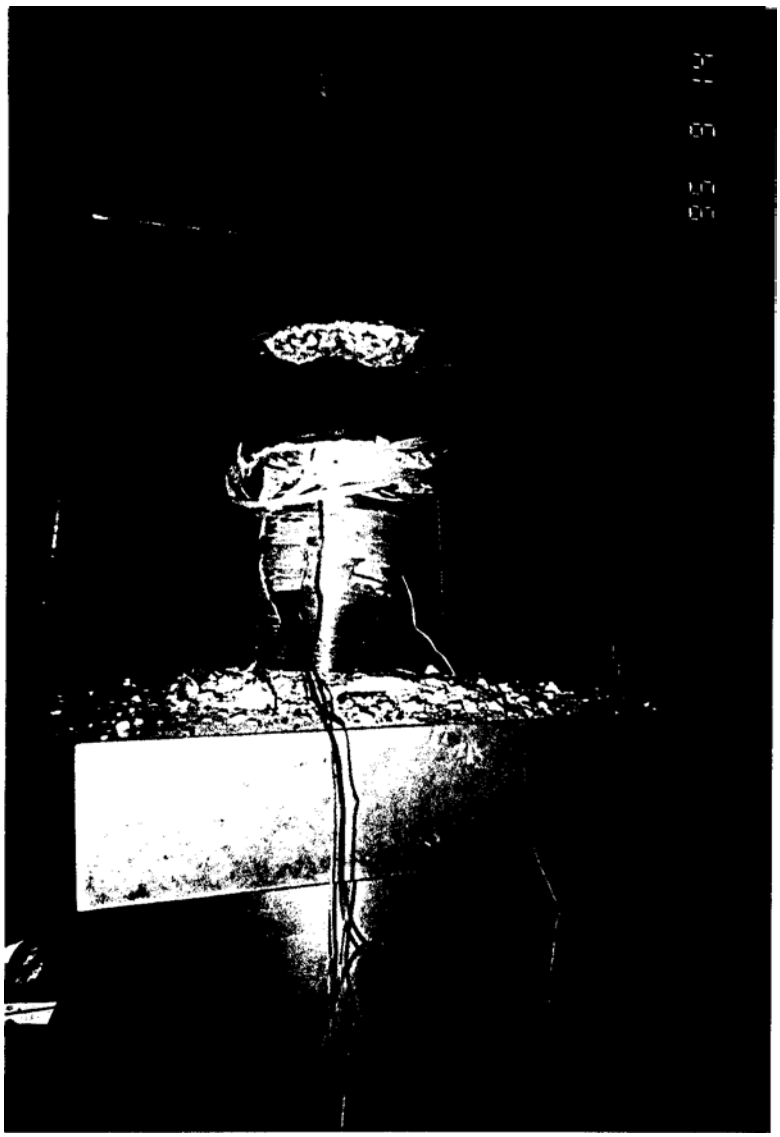

Figure 3.5 Failure towards top edge (Specimen C33 of Series C)

toe compensation procedure, which makes up for the initial softer response (ASTM D69591).

The axial stress-strain plots for the tested specimens of Series C are presented in Figure 3.6. Here, it should be mentioned that the capacity of the specimens of Series A

Table 3.2 Test results for specimens of Series A and

Specimen	**t_j (in)**	**P,at (kip)**	**f'_{cu} (ksi)**	**Specimen**	**tj (in)**	**P,at (kip)**	**f'_{cu} (ksi)**	**ϵ_{cu}**
A11*	0.074	204	8.00	C11**	0.074	186	7.20	-
A21	0.074	287	11.25	C21	0.074	237	9.16	0.0153
A31	0.074	327	12.76	C31	0.074	230	8.86	0.0149
A12	0.130	470	18.40	C12	0.130	377	14.73	0.0261
A22	0.130	464	18.13	C22	0.130	331	12.85	0.0235
A32	0.130	451	17.63	C32	0.130	385	14.80	0.0268
A13	0.237	not tested	-	C13	0.237	462	18.15	0.0345
A23	0.237	not tested	-	C23**	0.237	505	19.72	-
A33	0.237	>572	>22.4	C33	0.237	464	18.27	0.0404

* Premature failure due to mis-alignment of the testing machine

** Neither strains nor deflections were recorded for this

Table 3.3 Test results for specimens of Series D

Specimen	t_i (in)	P_{ult} (kip)	f'_{cu} (ksi)	ϵ_{cu}
DAI1	0.0568	207.28	7.78	0.0306
DA12	0.0568	not tested		
DA13	0.0568	218.26	8.19	0.0327
DB 11	0.0568	259.31	9.74	0.0290
DB 12	0.0568	213.60	8.02	0.0376
DB13	0.0568	232.68	8.74	0.0380
DC 11	0.0568	228.18	8.57	0.0343
DC 12	0.0568	234.84	8.82	0.0343
DA21	0.0868	287.29	10.57	0.0407
DA22	0.0868	258.97	9.53	0.0294
DA23	0.0868	307.53	11.31	0.0441
DB21	0.0868	293.98	10.81	0.0431
DB22	0.0868	366.79	13.49	0.0428
DB23	0.0868	282.88	10.40	0.0392
DC21	0.0868	305.01	11.22	0.0379
DC22	0.0868	303.93	11.18	0.0377
DA31	0.1168	344.92	12.43	0.0435
DA32	0.1168	subjected to cyclic compressive loading		
DA33	0.1168	349.13	12.58	0.0469
DB31	0.1168	346.95	12.50	0.0460
DB32	0.1168	461.37	16.63	0.0533
DB33	0.1168	351.85	12.68	0.0414
DC31	0.1168	346.52	12.49	0.0422
DC32	0.1168	338.00	12.18	0.0430

and C with the largest wall thickness (t_j = 0.237in) was apparently higher than the usable capacity of the compression machines. Therefore those specimens were fractured by sustaining a load close to the machine capacity up to failure. This resulted in a constant stress plateau prior to failure (Figure 3.6).

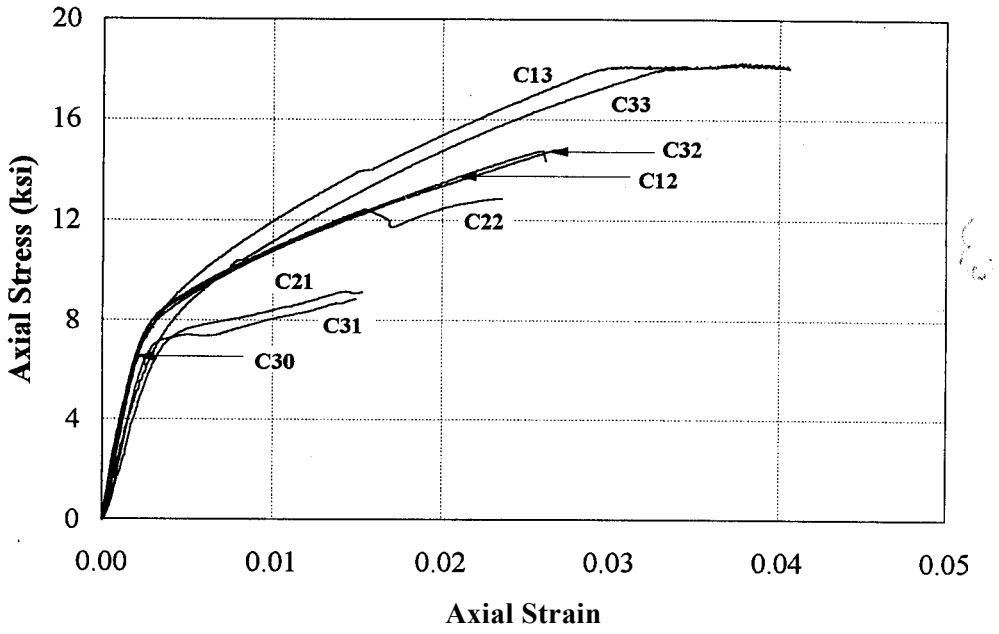

Figure 3.6 Stress-strain curves for specimens of Series C

For Series D, a more thorough study was performed. Figures 3.7 -3.9 show axial stress versus radial and axial strains for all specimens of Series D along with the unconfined axial stress-strain curve for each set. The following are some general observations:

1. The stress-strain curves in both the axial and lateral directions are bilinear with a connecting transition curve.
2. The first slope of the axial response almost coincides with the initial slope of the unconfined concrete core.
3. The second slope of the axial response as well as the ultimate strain and stress are all proportional to the tube thickness.

4. The enhancement in strength and ultimate strain due to confinement of circular columns is substantial. Depending on the level of confinement, strength is increased anywhere from 1.5 to 2.5 times the unconfined strength. While the ultimate strain is increased by 10 to 15 times the unconfined strain.

The test results of Series D were further investigated for better understanding of the mechanics of confinement by fiber composites. The radial strain-axial strain relationship has been plotted for all specimens as well as for the control cylinders corresponding to each set. These plots are presented in Figures 3.10 - 3.12. The unconfined specimens had the following trend: a mild initial slope up to the axial strain that corresponds to the concrete strength, where the radial strain increases rapidly till failure. The general shape of the curves was characterized by three distinct regions:

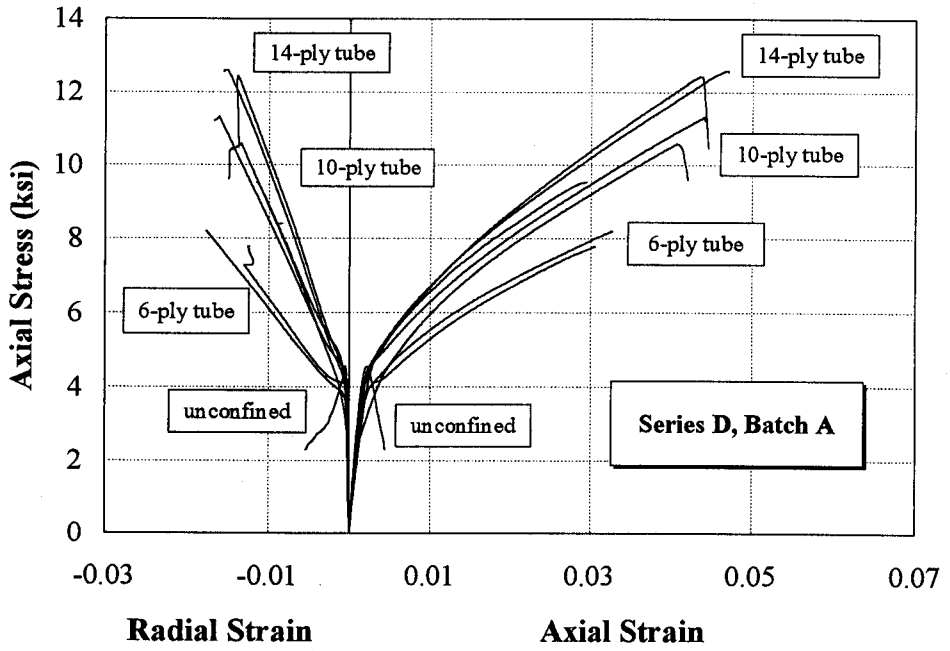

Figure 3.7. Stress-strain curves for Series D, Batch A 43

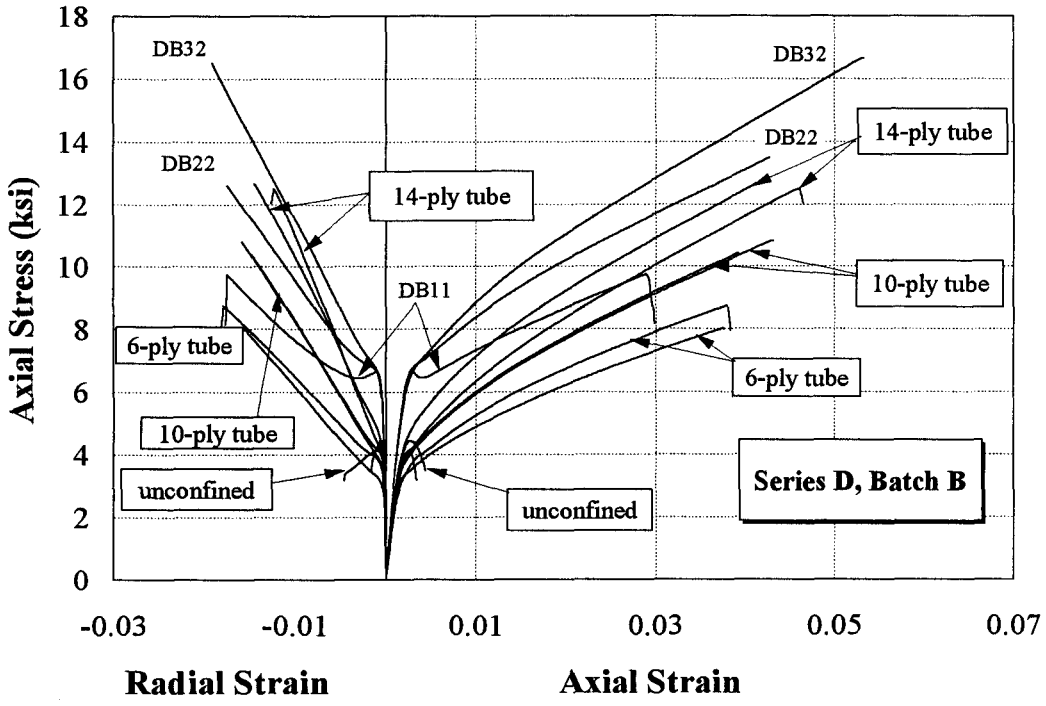

Figure 3.8 Stress-strain curves for Series D, Batch B

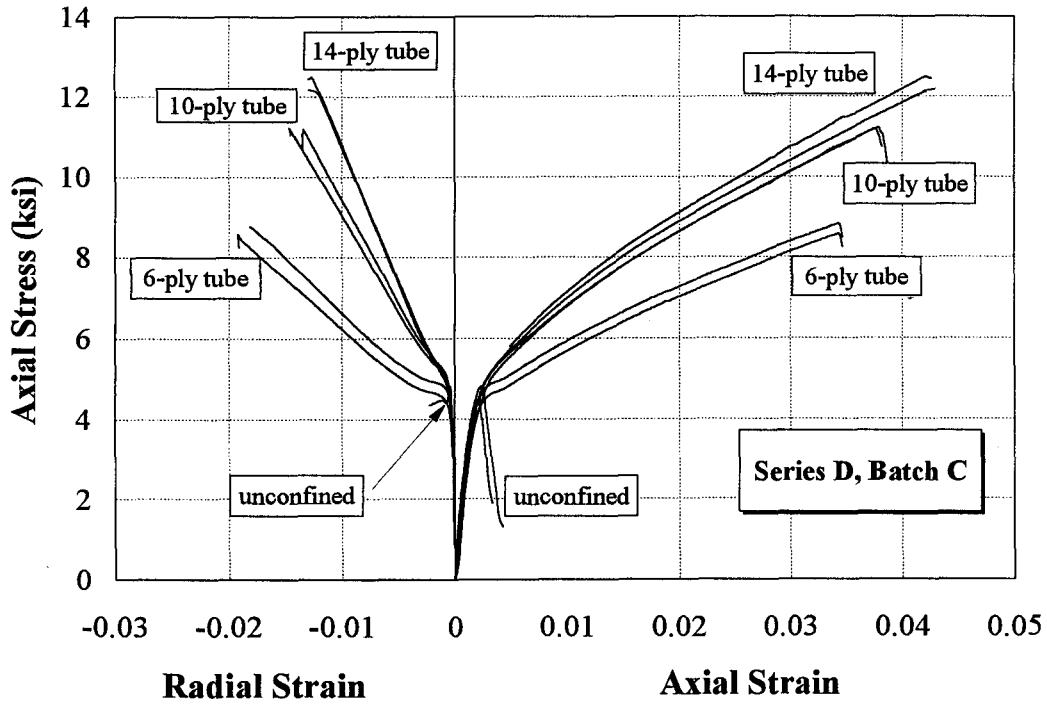

Figure 3.9 Stress-strain curves for Series D, Batch C 44

The first region has a mild slope up to ε_r =0.002-0.0035, where the second regions starts and is characterized by a steep slope. Then the third region starts, where the slope starts to decrease and eventually stabilizes at a constant value up till failure (refer to Chapter 5). As the tube thickness increases, the radial strains are generally decreased, indicating the effect of confinement on the lateral expansion of concrete core.

These observations lead to the idea of introducing the rate of change of the lateral strain with respect to the axial strain, which may shed more light on the behavior of the column under study. This ratio is also called the dilation rate p and is defined as:

$$\mu = \frac{d\varepsilon_r}{d\varepsilon_c} \qquad (3.1)$$

The typical shape of the dilation curve is shown in Figure 3.13.

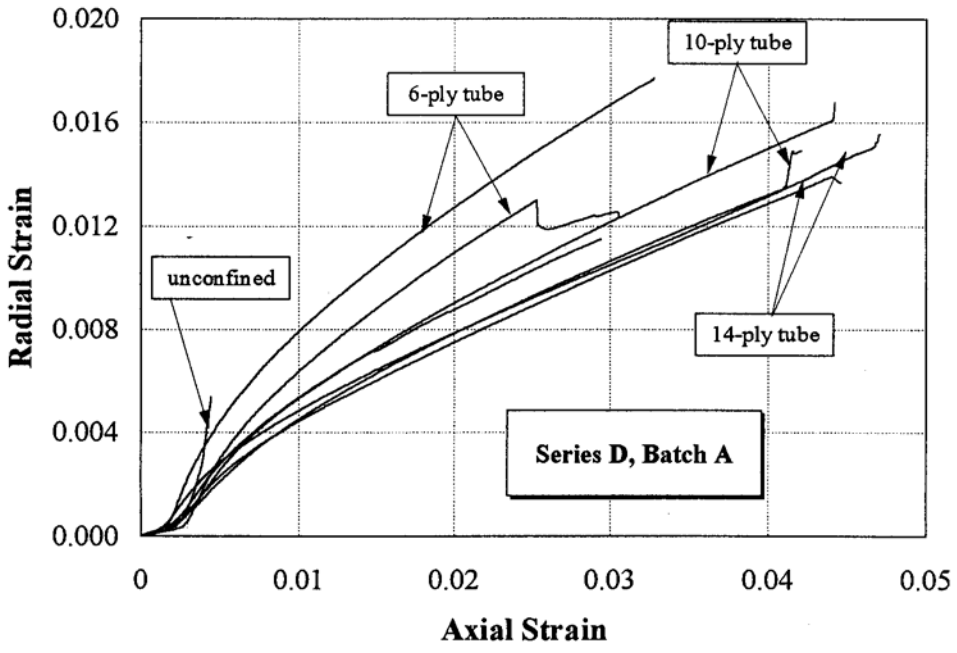

Figure 3.10 Radial versus axial strains for Series D, Batch A

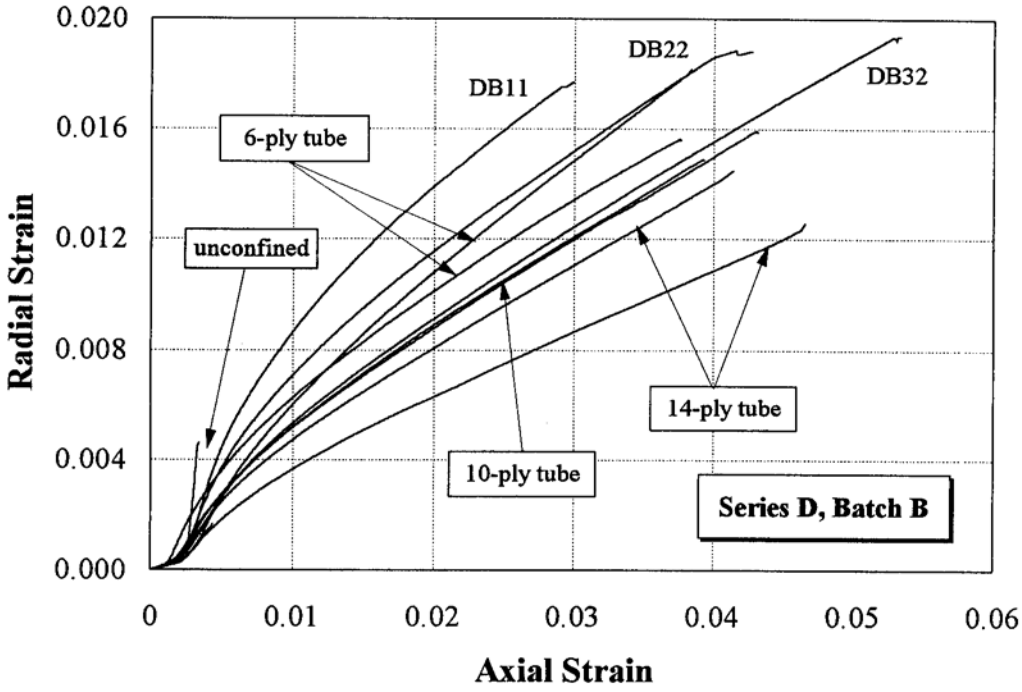

Figure 3.11 Radial versus axial strains for Series D, Batch B

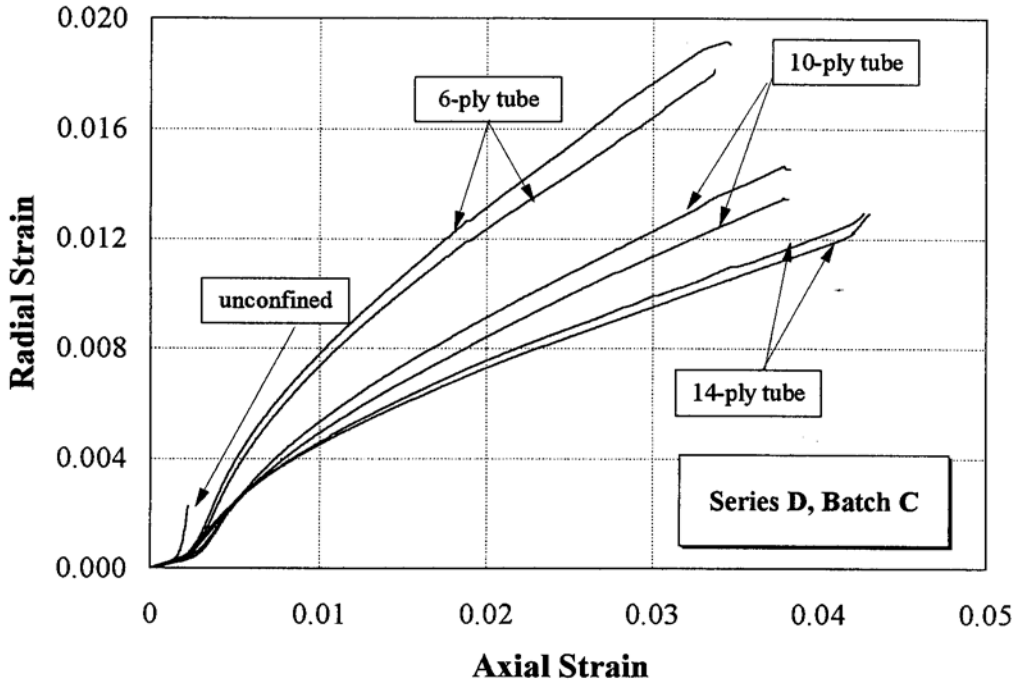

Figure 3.12 Radial versus axial strains for Series D, Batch C 46

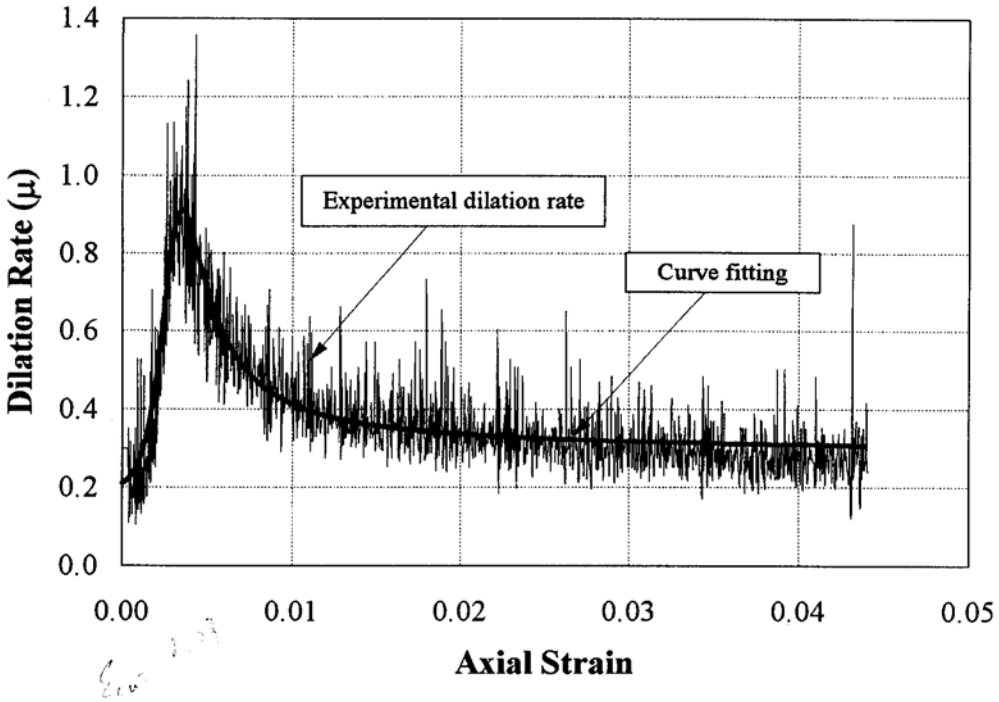

Figure 3.13 Typical shape of dilation rate for FRP-confined concrete

The curve starts with a gradual increase from a starting value, which is the same as the Poisson's ratio for concrete (0.15-0.22). A rapid increase follows the first region up to a peak value at a strain of ϵ, = 0.003-0.004, which appears to coincide with the ultimate failure strain of unconfined concrete. Beyond that peak a drop in the dilation rate takes place till it reaches an asymptotic constant value before failure.

A fractional four-parameter equation was chosen to curve-fit the experimental relationship using the method of the least square error. The following equation was used:

$$\mu = \frac{\mu_o + a + x + bx^2}{1 + cx + dx^2} \qquad (3.2)$$

where μ_o is the initial dilation rate and is equal to the Poisson's ratio of concrete, $x = \frac{\varepsilon_c}{\varepsilon_{co}}$

where ϵ_{co} is the strain at the peak stress of unconfined concrete, and a, b, c, and d are the four parameters of the equation.

The curve-fitted dilation rates were plotted for all specimens and for the control cylinders as well, as it is presented in Figures 3.14-3.16. The peak values for these curves ranges from 0.6 to 2.0 according to thickness of the jacket; the thinner the jacket the higher the peak. The ultimate dilation value ranges from 0.3 to 0.6, inversely proportional to the jacket thickness. Use of dilation curves for the confinement effectiveness will be 1 discussed in Chapter 5.

Plots of volumetric strain for specimens of Series D (Figures 3.17-3.19) further demonstrate the confining effect of the FRP tube. The initial portions of the curves for the confined and unconfined concrete are generally the same, in that they both experience a volume reduction up to a stress level in the vicinity of f'_{co}. At that point, the plain concrete dilates and loses its strength, which is a volume reduction up to a stress level in the vicinity of f'_{co}. At that point, the plain concrete dilates and loses its strength, which is revealed in the continuous volume expansion till failure. However, the confined concrete behaves similarly to a certain variable level of volume expansion, at which point containment of encased concrete takes place. This is demonstrated in the strain reversal towards volume reduction. This containment effect is proportional to the jacket stiffness, as it is evident from the curves.

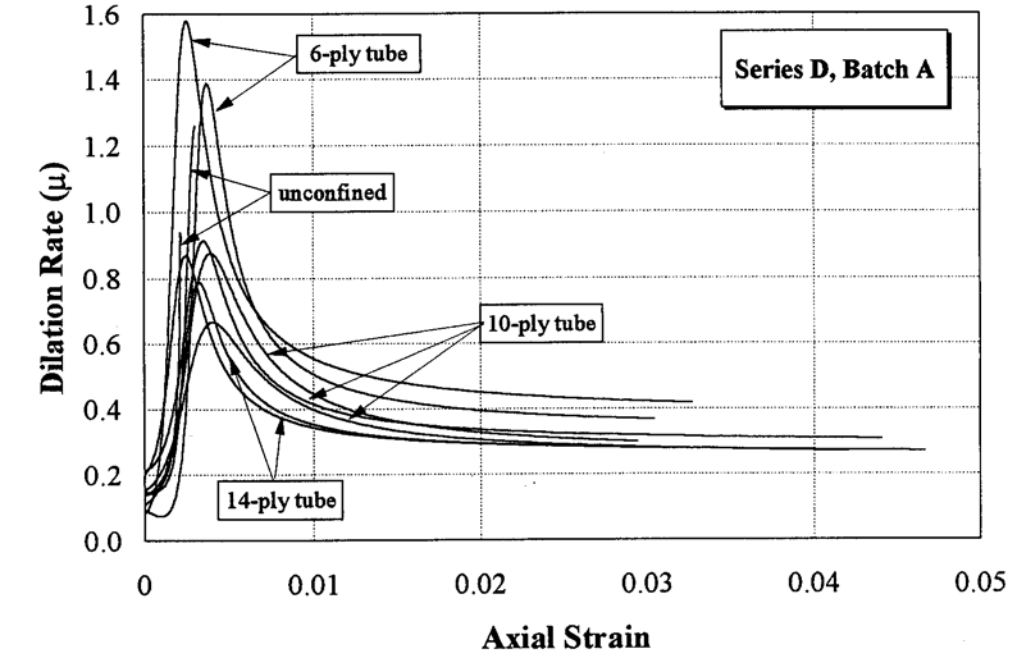

Figure 3.14 Dilation rate versus axial strain for Series D, Batch A

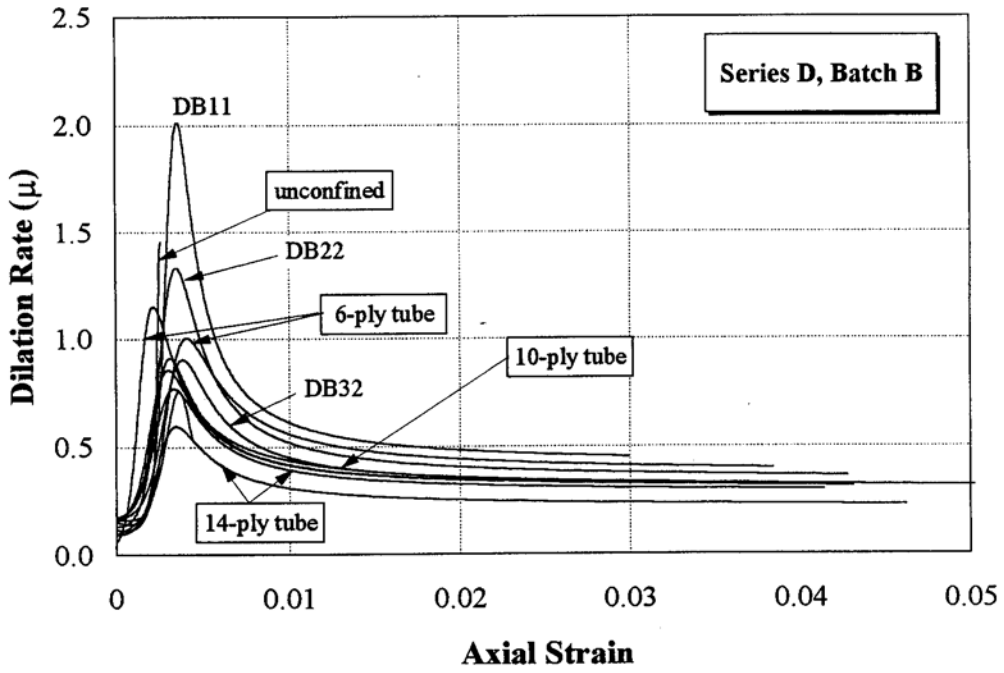

Figure 3.15 Dilation rate versus axial strain for Series D, Batch B

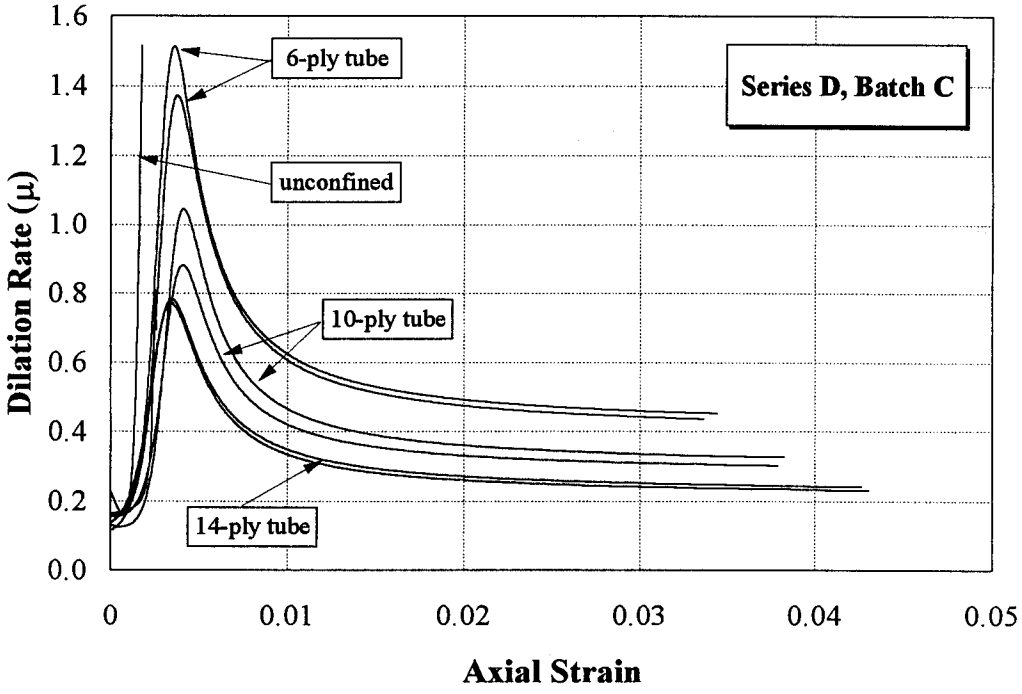

Figure 3.16 Dilation rate versus axial strain for Series D, Batch C

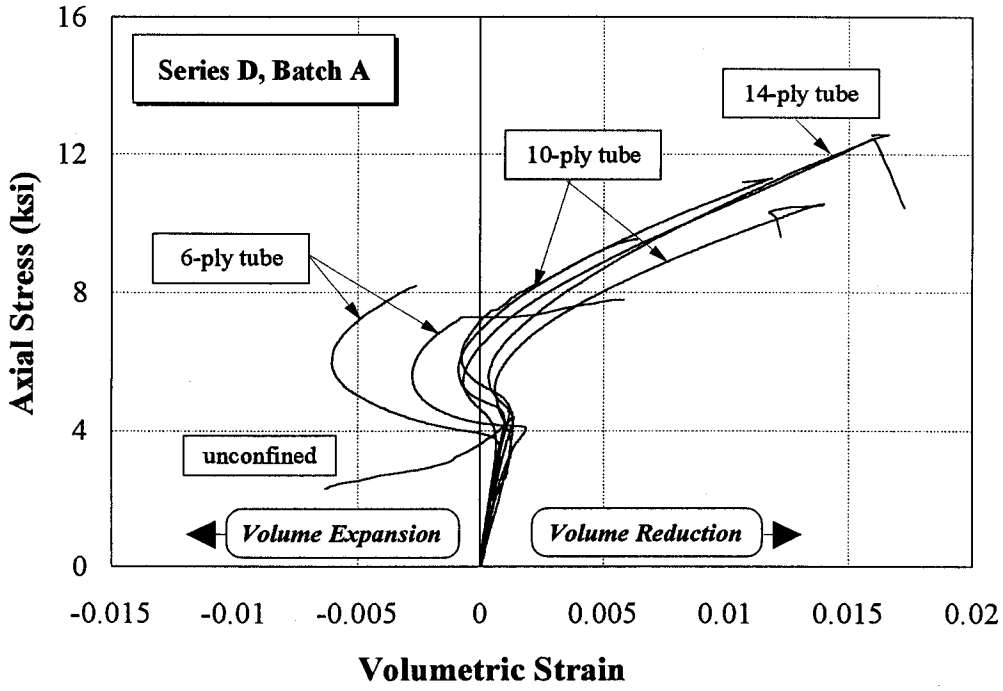

Figure 3.17 Axial stress versus volumetric strain for Series D, Batch

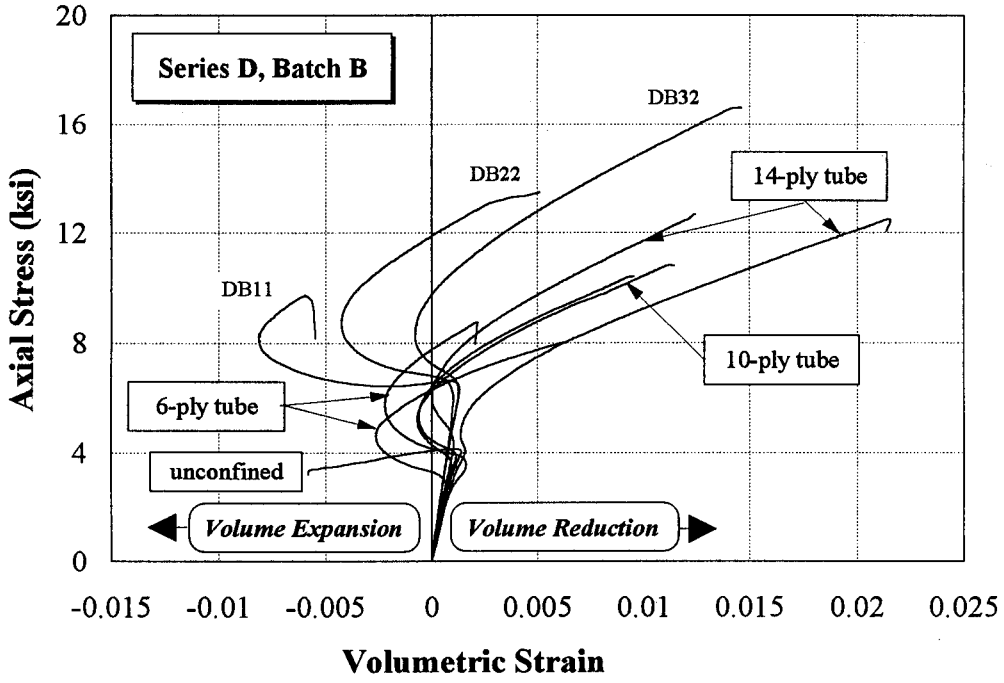

Figure 3.18 Axial stress versus volumetric strain for Series D, Batch B

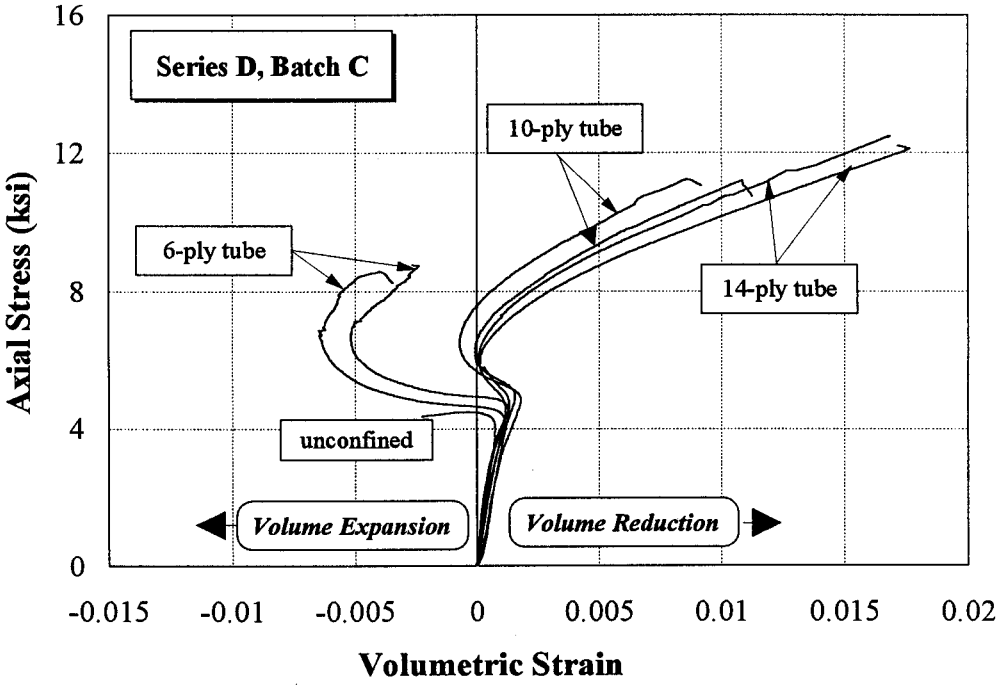

Figure 3.19 Axial stress versus volumetric strain for Series D, Batch C

3.5 CONCLUSION

The uniaxial compression tests were presented in this chapter, along with a discussion of the test results. Some behavioral aspects have also been investigated in order to understand the behavior of FRP-confined concrete. The next step is to model the behavior in order to predict the stress-strain response. The model will be presented in Chapter 5, after the properties of FRP are discussed.

4.

MECHANICS OF FIBER COMPOSITES

4.1 INTRODUCTION

The CUT is composed of a concrete core and an FRP tube, as it was described earlier. In order to model the confining effect of the FRP tube on the concrete core, the mechanical properties of both materials need to be determined. A close estimate of the strength of the concrete core is easily obtained by performing the traditional compression test on unconfined cylinder made of the same batch. Yet, a much more complicated testing procedure is required for the FRP tube, due to the orthotropic nature of the material. Tensile, compressive, and shear properties need to be determined separately in the longitudinal and transverse directions with respect to the fiber orientation. In order to avoid the complicated experimental procedure, a two-step mechanical analysis can be performed. The first step is the micro-mechanical analysis, which is concerned with the mechanical interaction of the constituent materials, i.e., the fibers and the matrix. The second step is the macro-mechanical analysis, which deals with the gross mechanical behavior of the composite lay-up (Gibson 1994).

In the first part of this chapter, the mechanical analysis of fiber composites is reviewed. This is followed by a detailed mechanical analysis of the filament-wound FRP tube used in this study.

As an introduction to the mechanical analysis of fiber composites, a brief glossary of terms is presented next (from Engineered Materials Handbook 1987).

4.1.1 Glossary of Terms

Anisotropic	Properties are different in all directions, so that the material contains no planes of material property symmetry.
Fiber direction	The orientation of the longitudinal axis of the fiber with respect to reference axis.
Hand lay-up	The process of placing successive plies in position on a mold by hand.
Heterogeneous	Properties changing from point to point in the material.
Hygrothermal effects	Change in properties due to moisture absorption and temperature change.
Lamina	A single layer in a laminate.
Laminate	A layered sheet composed of multiple laminae.
Laminate lay-up	A geometrical description of the laminae in a laminate.
Matrix	The homogeneous resin or polymer material, in which the fiber system is embedded.

Stacking sequence	A description of a laminate that details the ply orientations and their sequence in the laminate.
Unidirectional lamina	A fiber reinforced plastic lamina, in which all fibers are oriented in the same direction, usually in the direction of the major principal axis of the lamina.
Volume fraction	Fraction of a constituent material based on its volume.
Woven roving	A heavy glass fiber fabric made by weaving roving or yarn bundles.

4.2 PRINCIPLES OF MECHANICS OF COMPOSITE MATERIAL

Composite materials are considered heterogeneous at the constituent material level, with properties possibly varying spatially. As a reasonable approximation, the stressstrain relationships of the lamina will be expressed in terms of the average stresses and strains and effective properties of an equivalent homogeneous material (Gibson 1994). Using the average stresses ($\overline{\sigma}$) and strains($\overline{\varepsilon}$) the generalized Hooke's law can be written as follows:

$$\overline{\sigma}_i = Q_{ij}\overline{\varepsilon}_j \tag{4.1}$$

where Q;; is the effective modulus.

The general composite lay-up is usually considered anisotropic. Yet, a unidirectional lamina is considered an orthotropic material, that is constant properties along the principal lamina coordinates. If the principal lamina coordinates are identical to

the fiber orientation, the lamina is called specially orthotropic. Otherwise, if the fiber orientation is inclined by an angle, the lamina is called generally orthotropic (see Figure 4.1). On the other hand, laminae are often assumed to be in a state of plane stress, for which $\sigma_3 = \tau_{23} = \tau_{31} = 0$. The three-dimensional stress notations are given in Figure 4.2.

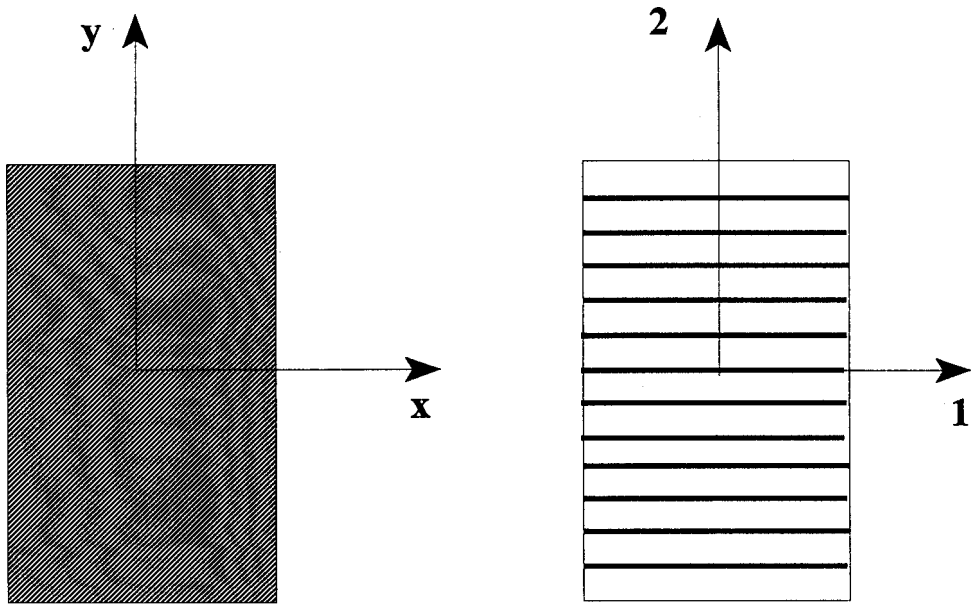

generally orthotropic specially orthotropic

Figure 4.1 Generally and specially orthotropic laminae

The constitutive relationship for a specially orthotropic lamina is given by (Gibson1994):

$$\begin{Bmatrix} \sigma_1 \\ \sigma_2 \\ \tau_{12} \end{Bmatrix} = \begin{bmatrix} Q_{11} & Q_{12} & 0 \\ Q_{21} & Q_{22} & 0 \\ 0 & 0 & Q_{66} \end{bmatrix} = \begin{Bmatrix} \varepsilon_1 \\ \varepsilon_2 \\ \gamma_{12} \end{Bmatrix} \tag{4.2}$$

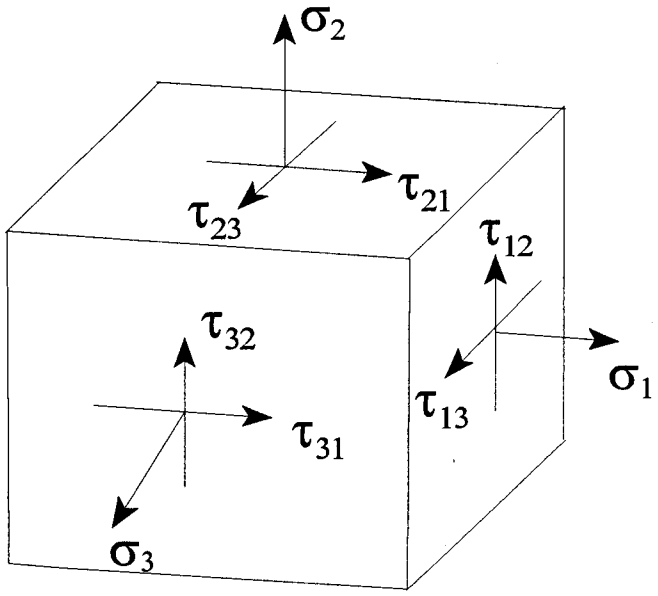

Figure 4.2 General three-dimensional stress notation

where,

$$Q_{11} = \frac{E_1}{1 - v_{12}v_{21}} \tag{4.3}$$

$$Q_{12} = \frac{v_{12}E_1}{1 - v_{12}v_{21}} = Q_{21} \tag{4.4}$$

$$Q_{22} = \frac{E_2}{1 - v_{12}v_{21}} \tag{4.5}$$

$$Q_{66} = G_{12} \tag{4.6}$$

(4.7)

where, Q_{ij} are the components of the lamina stiffness, E_i is the Young's modulus in the i-th direction, G_{ij} is the shear modulus associated with the ij-plane, and v_{ij} is the Poisson's ratio, the ratio of the strain in the j-th direction due to loading in the i-th direction.

The relationships for a generally orthotropic lamina are given by:

$$\begin{Bmatrix} \sigma_x \\ \sigma_y \\ \tau_{xy} \end{Bmatrix} = \begin{bmatrix} \overline{Q}_{11} & \overline{Q}_{12} & \overline{Q}_{16} \\ \overline{Q}_{12} & \overline{Q}_{22} & \overline{Q}_{26} \\ \overline{Q}_{16} & \overline{Q}_{26} & \overline{Q}_{66} \end{bmatrix} \begin{Bmatrix} \varepsilon_x \\ \varepsilon_y \\ \gamma_{xy} \end{Bmatrix} \tag{4.8}$$

where,

$$\overline{Q}_{11} = Q_{11} \cos^4\theta + Q_{22} \sin^4\theta + 2(Q_{12} + 2Q_{66}) \sin^e\theta \cos^2\theta \tag{4.9}$$

$$\overline{Q}_{12} = (Q_{11} + Q_{22} - 4Q_{66}) \sin^2\theta \cos^2\theta + Q_{12}(\cos^4\theta + \mathrm{Sin}^4\theta) \tag{4.10}$$

$$\overline{Q}_{22} = Q_{11} \mathrm{Sin}^4\theta + Q_{22} \cos^4\theta + 2(Q_{12} + {}^2Q_{66}) \sin^2\theta \cos^2\theta \tag{4.11}$$

$$\overline{Q}_{16} = (Q_{11} - Q_{12} - 2Q_{66}) \cos^3\theta \sin\theta - (Q_{22} - Q_{12} - 2Q_{66}) \cos\theta \sin^3\theta \tag{4.12}$$

$$\overline{Q}_{26} \quad (Q_{11} - Q_{12} - 2Q_{66}) \cos\theta \sin^3\theta - (Q_{22} - Q_{12} - 2Q_{66}) \cos^3\theta \sin\theta \tag{4.13}$$

$$\overline{Q}_{66} - (Q_{11} + Q_{22} - {}^2Q_{12} - 2Q_{66}) \sin^2\theta \cos^2\theta + Q_{66}(\sin^4\theta + \cos^4\theta) \tag{4.14}$$

where, $\overline{Q}_{if}$ are the Components of the transformed lamina stiffness, and θ is the inclination angle of the fiber orientation with respect to the principal axis (see Figure 4.3).

Thus, in order to develop the lamina stiffness matrix, 5 independent constants need to be determined first: E_l, E_2, G_{t2}, v_{12}, and θ. This is the first step in calculating the laminate stiffness matrix, as it will be discussed in Section 4.4.

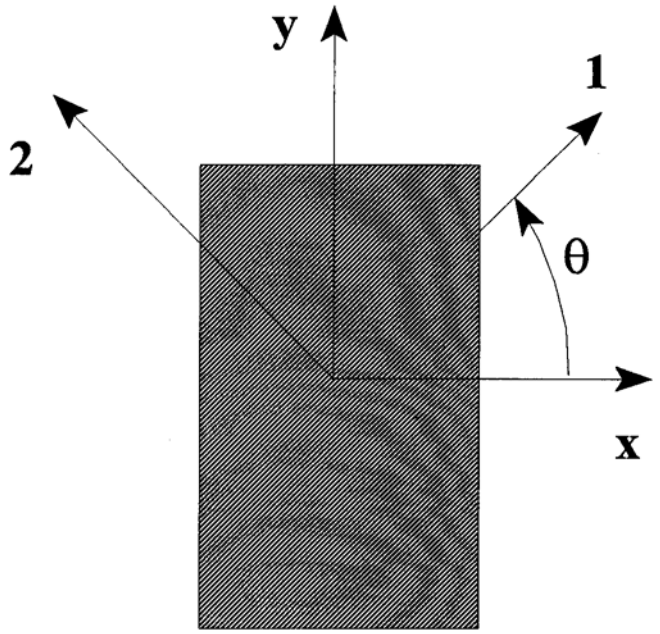

Figure 4.3 Coordinates of a generally orthotropic lamina

4.3 MICRO-MECHANICS OF A UNIDHIECTIONAL LAMINA

Micro-mechanics is the analysis of effective composite properties in terms of constituent material properties (Gibson 1994). In other words, it is the first step of analysis, through which the properties of the lamina are determined.

A fiber composite lamina is composed mainly of fibers and matrix, in addition to a certain amount of voids. The total volume V is the summation of the volumes of each individual constituent, as follows:

$V^{=}V_f+V_m+V_v$ (4.15)

where the subscripts f, m, and v stand for fibers, matrix, and void, respectively. By dividing both sides of Equation 4.15 by the total volume V, one can get the volume fractions of the constituents as follows,

$1^{=}v_f+v_m+v_v$ (4.16)

where *vf,* v_m, and $v_{,,}$ are the volume fractions of the three components; fibers, matrix, and the voids, respectively. The fiber volume fraction (v_f) is one of the main variables in the micro-mechanic analysis. Other variables are mainly the mechanical properties of the fiber and the matrix, which may be provided by the manufacturer, supporting test data or available tables in the literature. Here, it should be noted that the fiber properties should be determined according to the resin-impregnated fiber test (ASTM D-2343), which provides a realistic estimate of the properties of the fiber system embedded in the matrix. The following is a summary of the main micro-mechanic equations for the calculation of the elastic constants and the in-plane strengths of a unidirectional lamina (Chamis 1987):

$E_L = v_f E_f + v_m E_m$ (4.17)

$$E_r = \frac{E_m}{1-\sqrt{v_f}\left(1-E_m/E_{ft}\right)} \quad (4.18)$$

$$G_{lt} = \frac{Gm}{1 - \sqrt{v_f}\left(1 - G_m / G_{flt}\right)} \quad (4.19)$$

$v_{lt}=v_f v_{flt}+v_m v_m$ (4.20)

$$S_L^{(+)} = v_f s_f^{(+)} \quad (4.21)$$

$$S_L^{(-)} = v_f s_f^{(-)} \quad (4.21)$$

$$S_T^{(+)} = s_m^{(+)}\left[1-\left(\sqrt{v_f} - v_f\right)\left(1 - E_m / E_{fr}\right)\right] \quad (4.22$$

$$S_T^{(-)} = s_m^{(-)}\left[1-\left(\sqrt{v_f} - v_f\right)\left(1 - E_m / E_{fr}\right)\right] \quad (4.23)$$

$$S_{LT} = s_{mLT}\left[1-\left(\sqrt{v_f} - v_f\right)\left(1 - G_m / G_{fLr}\right)\right] \quad (4.24)$$

where v, E, G, v, and s stand for volume fraction, Young's modulus, shear modulus, Poisson's ratio, and stress, respectively. The subscripts f, m, L, and T denote fibers, matrix (resin), longitudinal direction (i.e. fiber direction), and transverse direction (perpendicular to the fiber direction), respectively. The superscripts (+) and (-) denote tension and compression, respectively.

4.4 MACRO-MECHANICS OF A LAMINATE

Composite structures are usually in the form of laminates consisting of multiple laminae, or plies, oriented in the desired directions and bonded together in a structural unit (Gibson *1994)*. The general Classical Lamination Theory (CLT) enables the laminate analysis for any arbitrary fiber orientation and under any combination of in-plane loads and

edge moments. The CLT is a generalized form of the classical theory of plates which takes into account the coupling effects due to the directionality of the material properties of the different laminae. The general assumptions of the CLT are as follows (Gibson 1994):

1) The plate consists of orthotropic laminae perfectly bonded together, therefore no interface slippage is allowed.
2) Thickness of the plate is much smaller than the lengths along the plate edges.
3) The plate thickness is constant.
4) In-plane displacements u, v, and out-of-plane displacement w are small compared to the plate thickness.
5) In-plane displacements u and v are linear functions of the normal z-coordinate.
6) Transverse shear strains y_{xz} and y_y, and normal strain ϵ_Z are negligible.
7) Each ply follows the Hooke's law.

According to assumptions 1, 5 and 6, the following constitutive relationship of the generally orthotropic lamina applies for the 0 lamina (Gibson 1994):

$$\begin{Bmatrix} \sigma_x \\ \sigma_y \\ \tau_{xy} \end{Bmatrix}_k = \begin{bmatrix} \overline{Q_{11}} & \overline{Q_{12}} & \overline{Q_{16}} \\ \overline{Q_{12}} & \overline{Q_{22}} & \overline{Q_{26}} \\ \overline{Q_{16}} & \overline{Q_{26}} & \overline{Q_{66}} \end{bmatrix}_k \begin{Bmatrix} \varepsilon_x^0 + z\kappa_x \\ \varepsilon_y^0 + z\kappa_y \\ \gamma_{xy}^0 + z\kappa_{xy} \end{Bmatrix} \qquad (4.25)$$

where the $\overline{Q}$ -matrix is the transformed lamina stiffness matrix, $\varepsilon_x^0, \varepsilon_y^0, \gamma_{xy}^0$ are the strains at the middle surface, and $\kappa_x, \kappa_y, \kappa_{xy}$ and 1% are the curvatures at the middle surface, and z is the distance of the k^{th} lamina from the middle surface (see Figure 4.4).

In order to express the above equation in a more useful form, the middle surface strains and curvatures are related to the applied forces and moments. The total force and moment per unit length in a certain direction i can be written in terms of the laminae stresses in the following form:

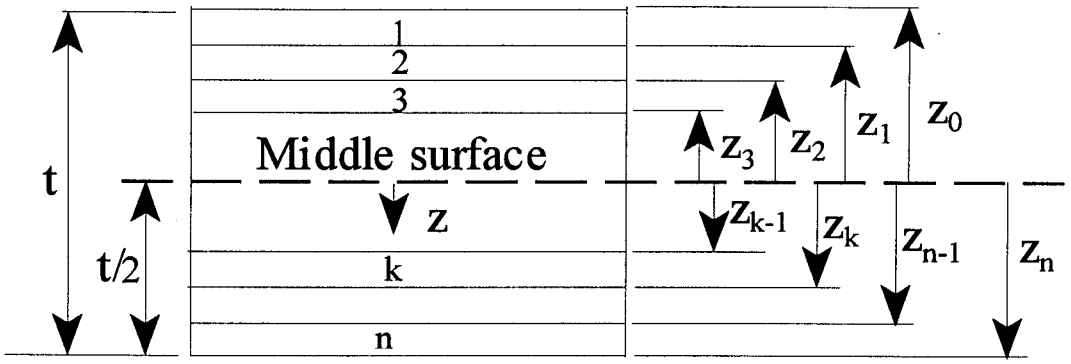

Figure 4.4 Laminate geometry and ply numbering system

$$N_i = \sum_{k=1}^{n} \left\{ \int_{z_{k-1}}^{z_k} (\sigma_i)_k \, dz \right\} \tag{4.26}$$

$$M_i = \sum_{k=1}^{n} \left\{ \int_{z_{k-1}}^{z_k} (\sigma_i)_k \, z dz \right\} \tag{4.27}$$

where n is the total number of laminae.

By substituting the stresses from Equation *4.25* into Equations *4.26* and *4.27* and by rearranging, the following relationship results:

$$\begin{Bmatrix} N_x \\ N_y \\ N_{xy} \\ M_x \\ M_y \\ M_{xy} \end{Bmatrix} = \begin{bmatrix} [A]_{3x3} & [B]_{3x3} \\ [B]_{3x3} & [D]_{3x3} \end{bmatrix} \begin{Bmatrix} \varepsilon_x^0 \\ \varepsilon_y^0 \\ \gamma_{xy}^0 \\ \kappa_x \\ \kappa_y \\ \kappa_{xy} \end{Bmatrix} \quad (4.28)$$

where,

[A] = the laminate extensional stiffness matrix, which relates the in-plane forces to the middle surface strains as follows:

- *i(''–Y)k (Zk -Zk-1)*

(4.29

) [B] = the laminate coupling stiffness matrix, which couples the in-plane forces with the middle surface curvatures, and the moments with the middle surface strains, as follows:

$$N_i = \sum_{k=1}^{n} \left\{ \int_{z_{k-1}}^{z_k} (\sigma_i)_k \, dz \right\} \quad (4.26)$$

$$M_i = \sum_{k=1}^{n} \left\{ \int_{z_{k-1}}^{z_k} (\sigma_i)_k \, z dz \right\} \quad (4.27)$$

–

1 *k=1* (Q

where n is the total number of laminae.

By 2 \-~) *k (" k Z k 1 l*

/ (4.30)

By substituting the stresses from Equation *4.25* into Equations *4.26* and *4.27* and by rearranging, the following relationship results:

Where it is clear that matrix B;; is a zero matrix for perfectly symmetrical laminates with respect to the middle surface, and finally;

[D] = the laminate bending stiffness matrix, which relates the moments to the middle surface curvatures, as follows,

$$D_{if} = \frac{1}{3}\sum_{k=1}^{n}\left(\overline{Q}_{if}\right)_k \left(z_k^3 - z_{k-1}^3\right) \tag{4.31}$$

Equation 4.28 is called the laminate force-deformation relation. This could be inverted in order to express the middle surface strains and curvatures in terms of the forces:

$$\left\{\begin{matrix}\varepsilon^0 \\ \kappa\end{matrix}\right\} = \left[\begin{matrix}A & B \\ B & D\end{matrix}\right]^{-1}\left\{\begin{matrix}N \\ M\end{matrix}\right\} = \left[\begin{matrix}A' & B' \\ C' & D'\end{matrix}\right]\left\{\begin{matrix}N \\ M\end{matrix}\right\} \tag{4.32}$$

Using this form, the laminae strains could be obtained from known laminate forces and moments. Hence, the laminae stresses could also be calculated by using Equation 4.25.On the other hand, Equation 4.32 is also used to determine the laminate moduli for symmetric laminates. This is done by applying a single load in the direction of the required modulus and by dividing the resulting stress by the middle surface strain. Thus:

$$\left\{\begin{matrix}E_x \\ E_y \\ G_{xy}\end{matrix}\right\} = \frac{1}{t}\left\{\begin{matrix}\dfrac{1}{A'_{11}} \\ \dfrac{1}{A'_{22}} \\ \dfrac{1}{A'_{66}}\end{matrix}\right\} \tag{4.33}$$

The laminate analysis can be performed using the computer program GENLAM (GENeral purpose LAMinate program, Tsai 1988), which incorporates the above explained Classical Lamination Theory. For a certain ply stacking sequence and a certain

load combination, the program calculates the ply stresses and strains at the top and bottom of each ply. It also provides the effective engineering constants.

In order to define the failure for off axis and multi-axial loading, the quadratic failure criterion is incorporated. This criteria defines a quadratic failure surface for anisotropic materials (Tsai and Wu 1971). For the case of plane, stress the following form applies:

$$F_{11}\sigma_{12}+F_{22}\,\sigma_2^{2}+F_{22}\,\sigma_6^{2}+F_1\sigma_1+F_2\sigma_2+2F_{12}\sigma_1\sigma_2\leq 1 \tag{4.34}$$

where,

$$F_{11}=\frac{1}{s_L^{(+)}s_L^{(-)}} \tag{4.35}$$

$$F_1=\frac{1}{s_L^{(+)}}-\frac{1}{s_L^{(-)}} \tag{4.36}$$

$$F_{22}=\frac{1}{s_T^{(+)}s_T^{(-)}} \tag{4.37}$$

$$F_1=\frac{1}{s_T^{(+)}}-\frac{1}{s_T^{(-)}} \tag{4.38}$$

$$F_{66}=\frac{1}{s_{LT}^{2}} \tag{4.39}$$

$$F_1=\frac{1}{s_L^{(+)}}-\frac{1}{s_L^{(-)}} \tag{4.40}$$

This concludes the first part of the chapter dealing with the mechanics of fiber composites, which is further applied to filament-wound tubes in the second part. Here, it should be mentioned that there are numerous fabrication processes for fiber composites, e.g. filament winding, pultrusion, hand lay-up, open mold process, autoclave molding, and many others. Yet, the CLT applies to laminates produced by any of these different fabrication processes.

4.5 MECHANICAL ANALYSIS OF FILAMENT-WOUND FRP TUBES

In this section, the analysis of the FRP tubes of the present study is discussed. First, the fabrication technique is explained, followed by the description of the methods used to determine the fiber volume fraction. The mechanical properties are then presented.

4.5.1 Filament Winding Technique

In the filament winding process, a band of continuous resin-impregnated rovings or filaments is wrapped around a mandrel and cured to produce axi-symmetric hollow parts. The advantage of this procedure is that it uses continuous lengths of fibers. Hence, sections with very high strength-to-weight and stiffness-to-weight ratios can be manufactured (Mallick 1988).

A schematic drawing of a basic filament winding process is shown in Figure 4.5. A large number of fiber rovings are pulled from a series of creels into a liquid resin bath. Just before entering the resin bath, the rovings are gathered into a band by passing through a textile thread board or a stainless steel comb. After the rovings are immersed into the

resin, they are pulled through a wiping device that removes the excess resin and controls the resin coating thickness around each roving. Once the rovings have been impregnated and wiped, they are gathered together in a flat band by using a straight bar, a ring or a comb. The band former is usually located in a carriage, which traverses back and forth parallel to the mandrel. The traversing speed of the carriage and the winding speed of the mandrel are controlled to create the desired winding angle patterns. Each time the carriage returns, it starts the next lamina.

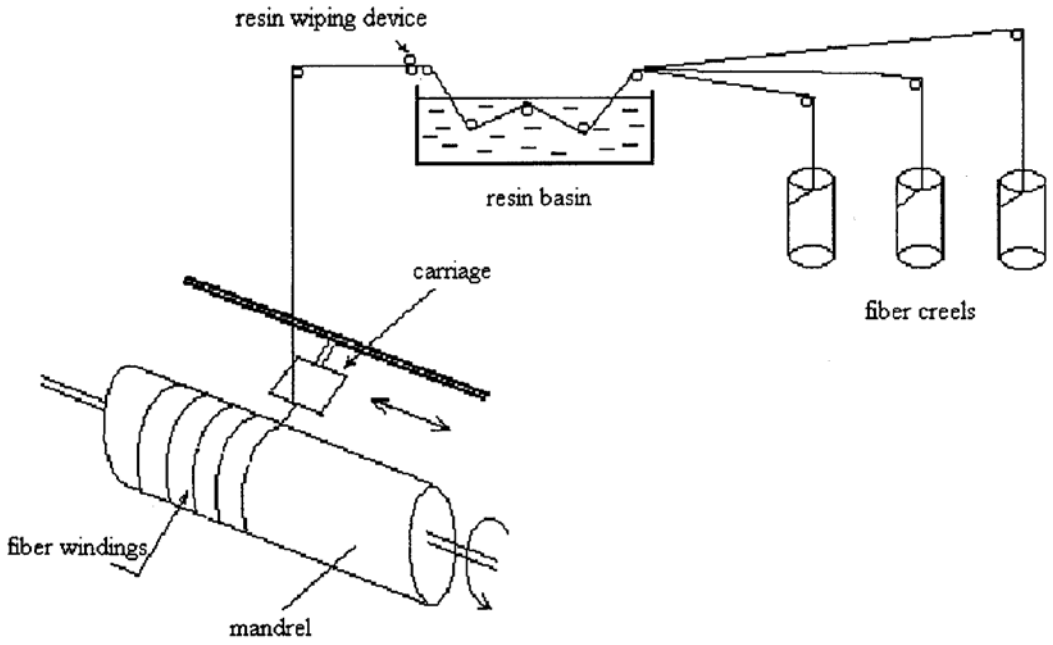

Figure 4.5 Filament Winding Process (Mallick 1988)

4.5.2 Determination of Fiber Volume Fraction

In order to perform a mechanical analysis of a filament-wound fiberglass tube, the glass fiber volume fraction should be estimated first. This task was carried out by the following methods:

1) Band Width Method

In this method, the intensity of windings per unit length of the tube is used to determine the fiber volume fraction, as follows:

$$v_f = \frac{n_{fr} A_{fr}}{t_{fp}} \qquad (4.41)$$

where n& is the number of rovings per unit length, tfp is the ply thickness, and Af, is the cross-sectional area of one roving and is calculated as:

$$A_{fr} = \frac{1}{\gamma_f} \qquad (4.42)$$

where Wf, is the weight of fiber per unit length of roving, and y_f is the unit weight of the fibers. The weight of unit length of fibers is equal to the inverse of the yield number, given by the manufacturer in lb/yd. According to the properties mentioned in Chapter 3, A_f, for the glass fibers used in this study is calculated as 0.00066 in^2, which agrees with the typical values reported in Peters et al. *(1991).* The ply thickness was then determined by dividing the total tube thickness by the number of plies, which resulted in *0.000947* in for the *6* plies, and 0.00851in for the 10 and 14 plies. The difference was attributed to higher

amounts of resin for the 6-ply tubes. Using Equation 4.41, the following values of fiber volume fraction results: of = 0.43 for 6-ply tubes, and 0.48 for the 10 and 14-ply tube, respectively.

2) Weight Method

The weight method calculates an overall average volume fraction of the laminate. The fiber volume fraction is calculated using the following formula, in which the densities of the fibers and the resin are provided as:

$$v_f = \frac{\gamma_e - \gamma_m}{\gamma_f - \gamma_m} \tag{4.43}$$

where γ_c, γ_m, and γ_f are the unit weights of the composite, matrix (resin), and fibers, respectively. The values of γ_m and γ_f were provided by the manufacturer, while γc, was determined experimentally. For each tube thickness, five one-inch-wide rings were cut and weighed. By knowing the volume and weight, γ_c was calculated. Substituting an average value of γ_c for each thickness in Equation 4.43, the following values of fiber volume fractions were computed: 0.323 for the 6-ply tubes, and 0.413 for the 10- and 14- ply tubes.

3) Microscopic Method

In this method, representative samples of FRP cross sections are placed under a microscope, and the areas of fibers and resin are measured, thus identifying the volume fractions. This task was performed at the Florida State University Center for Materials

Research and Technology. The average volume fractions were determined to be 0.445 for the 6-ply tubes and 0.530 for the 10- and 14-ply tubes. However, the standard deviations of the results were considerably high.

4) Burning Method

In this method, the fiber volume fraction is determined by burning the resin out of the laminate, and measuring the weight of the remaining material. However, this method was not utilized for this project.

The results of the first two methods were combined and used in the study. The third method was not included due to its rather high variations. The average values for the fiber volume fraction are: 0.37 for the 6-ply tubes; and 0.44 for the 10-and 14-ply tubes.

4.5.3 Micro-Mechanical Analysis

A micro-mechanical analysis of an E-glass/polyester lamina was performed using the material properties provided by the manufacturer (Table 4.1) in addition to the calculated fiber volume fractions. The results of the analysis for of = 0.37 and 0.44 are presented in Table 4.2 for both the longitudinal and the transversal directions.

4.5.4 Macro-Mechanical Analysis

The laminate analysis was performed using the computer program GENLAM, which incorporates the Classical Lamination Theory. The analysis was carried out for the ply stacking sequences of $[\pm 75^{\circ}]3$, $[\pm 75^{\circ}]5$, and $[\pm 75^{\circ}]_7$, for the 6, 10 and 14 plies, respectively. For each lay-up, a unit load is applied in the global X-direction of the

Table 4.1 Mechanical properties of resin-impregnated glass fibers and polyester resin

Property	450-Yield E-Glass	Polyester Resin
Specific Gravity	2.58	1.41
Tensile Strength, ksi	317	10.4
Tensile Modulus, ksi	10,100	630
Shear Modulus, ksi	4,370	232
Poisson's Ratio	0.22	0.36

Table 4.2 Mechanical properties of unidirectional E-glass/polyester lamina

Property	Fiber Volume Fraction	
	0.37	**0.44**
Longitudinal Modulus, ksi	4,134	4,800
Transversal Modulus, ksi	1,466	1,666
Shear Modulus, ksi	546	623
Poisson's Ratio, ν_{LT}	0.31	0.3
Longitudinal Tensile Strength, ksi	117.29	139.48
Longitudinal Compressive Strength, ksi	70.18	83.46
Transversal Tensile Strength, ksi	8.08	8.22
Transversal Compressive Strength, ksi	12.43	12.65
Shear Strength, ksi	6.19	6.31

laminate, which represents the circumferential (hoop) direction for the tube. The ultimate stresses and strains are then determined (see Table 4.3).

Here, it should be mentioned that for asymmetrical lay-ups, such as the laminates under study, the coupling effects are usually substantial and cause complex deformations as explained before. Effective engineering constants (i.e., $\mathbf{E}_L$, $\mathbf{E}_T$, $\mathbf{G}_{LT}$, $\mathbf{V}_{LT}$) are not defined for such lay-ups, and usually constants of corresponding symmetrical lay-ups are used as an approximation. Therefore, the same analysis was performed for the 7-, 11-, and 15-ply lay-ups in order to determine the engineering constants. The analytical results were further experimentally verified using the split-disk method, as it is explained in the following section.

Table 4.3 Mechanical properties of the FRP tube according to the macro-mechanical analysis

Property	6 Plies ksi	10 Plies ksi	14 Plies ksi
Hoop tensile strength ϵ_L^+	80	95	100
Ultimate hoop tensile strain ϵ_L^+	0.0222	0.0220	0.0225
Effective hoop modulus $\mathbf{E}_L$	3,575	4,115	4,115
Effective longitudinal modulus $\mathbf{E}_T$	939	1,043	1,043
Effective shear modulus $\mathbf{G}_{LT}$	552	630	630

4.5.5 Split-Disk Tests

Split-disk method (ASTM D2290-92) is used for filament-wound FRP tubes in order to determine their hoop tensile strength, since it is not feasible to use flat specimens to measure the properties of such tubes (Bert 1975). In this test method a ring specimen is loaded in hoop tension through a split-disk loading device, as shown in Figure 4.7. An apparent (rather than a true) tensile strength is obtained because of the bending stresses developed at the split area between the two half disks (see ASTM D2290-92). However, these effects may be reduced by minimizing the spacing between the disks of the test fixture. The other alternatives were the burst pressure test, segmented cylinder loading, bladder loading with axial constraint (Bert 1975), which would provide more accurate properties, yet much more complicated, than the basic split-disk test. Furthermore, the actual internal pressure produced by the lateral expansion of concrete unto the FRP tube is barely uniform, and some bending stresses are expected to develop.

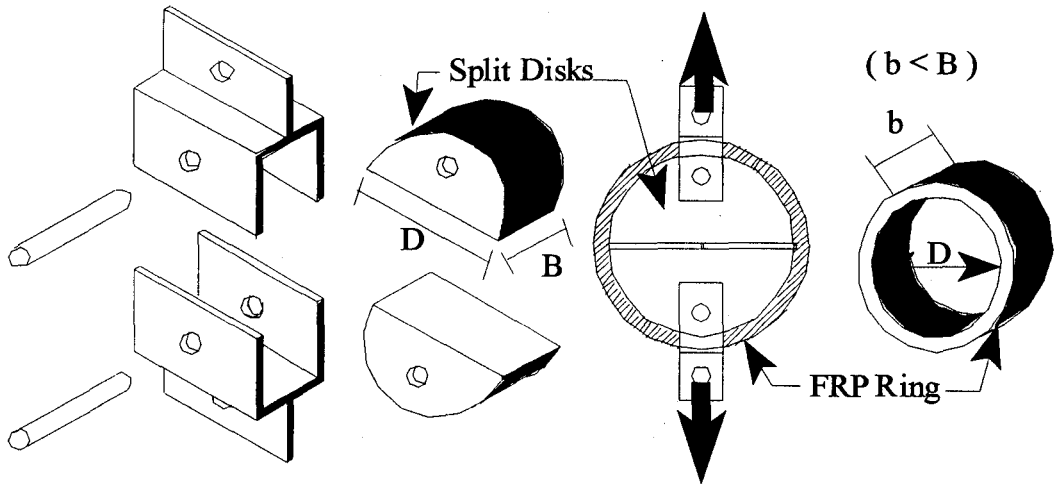

Figure 4.6 Split-disk test fixture

The test fixture was designed and manufactured at UCF. Two series of split disk tests were conducted. Series 1 corresponded to the FRP tubes of Series A and C (see Chapter 3) and included 11 rings. Series 2 corresponded to the FRP tubes of Series D and included 14 rings.

Series 1

The width and thickness of all ring specimens are listed in Table 4.4. The loading was controlled by a displacement rate of 0.01 in/min. The typical primary failure mode was the shear failure along the fiber direction. The expected point of first failure is at the gap between the two half discs, where the ring is not supported. Yet, the first failure in most of the specimens occurred at different locations, which indicated the presence of some warping stresses. For that reason, the results were not further considered in the analysis. Test results are summarized in Table 4.4.

Series 2

All specimens had a nominal width of 1 in and a variable thickness according to the number of plies (refer to Chapter 3). For each thickness, three rings were strain-gauged, and for the remainders only the load-deflection was monitored. The specimens failed primarily in shear around the expected points of failure, namely at the gap between the two half disks. The actual measurements of all specimens along with the measured strengths and moduli are listed in Table 4.5. The stress-strain curves for all specimens are included in Appendix B.

By comparing the analytical results of Table 4.3 and the experimental results of Table 4.5, the following could be inferred:

1) The analytical values of the tensile strengths are slightly higher than those obtained by the experiments. This was in fact expected due to the bending stresses as discussed above.

2) The experimental values of the moduli are much lower than the analytical values. This is mainly attributed to the coupling effects of asymmetrical laminates, which were neglected in the analysis.

Therefore, the results of the split-disk test were considered for the calibration of the confinement model.

Table 4.4 Split-disk results for Series 1

Specimen	t_{ave} **(in)**	W_{ave} **(in)**	A_{ave} **(in2)**	p_{max} **(lb)**	f_{jmax}. **(ksi)**
All	0.072	0.577	0.0415	6.90	83.04
A12	0.075	0.580	0.0435	7.30	83.91
A13	0.076	0.606	0.0461	7.60	82.51
A21	0.071	1.057	0.0750	13.66	91.01
A22	0.075	1.076	0.0807	11.97	74.14
A23	0.075	1.135	0.0851	13.80	81.06
Average					**82.61**
B 12	0.134	0.546	0.0732	15.40	105.24
B13	0.129	0.600	0.0774	15.40	99.48
B21	0.142	1.025	0.1456	23.00	79.01
B22	0.136	1.018	0.1384	25.40	91.73
B23	0.125	0.955	0.1194	25.00	104.71
Average					**96.04**

Table 4.5 Split-disk results for Series 2

SPECIMEN	t_1 (in)	t_2 (in)	t_{2V9} (in)	W_1 (in)	W_2 (in)	W_{avg} (in)	P_{max} (kip)	S_L^+ (ksi)	ϵ_L^+	E_L (ksi)
SD61	0.0562	0.058	0.0571	1.058'	1.133	1.095	9.960	83.31	0.01426	2921.11
SD62	0.0571	0.0572	0.05715	1.040	1.050	1.045	9.280	76.62	0.0152	2520.39
SD63	0.0579	0.057	0.05745	1.052	1.083	1.068	8.555	70.20	0.01364	2573.31
SD64	0.0572	0.0561	0.05665	1.086	1.090	1.088	8.385	66.76	0.01276	2615.99
SD65	0.0556	0.0559	0.05575	1.080	1.059	1.070	9.895	82.77	0.01439	2875.96
Average								**75.93**		**2701.35**
Std. Dev.								**7.40**		**368.00**
SD101	0.0865	0.0883	0.0874	0.949	1.044	0.996	13.795	83.68	0.01287	3250.97
SD102	0.0857	0.086	0.08585	1.011	1.048	1.030	15.363	88.65	0.01615	2744.5
SD103	0.0846	0.0867	0.08565	0.990	1.022	1.006	15.825	94.13	0.01422	3309.77
SD104	0.0909	0.0867	0.0888	0.994	1.050	1.022	13.440	73.75	0.015	2458.33
SD105	0.0885	0.0843	0.0864	1.016	1.000	1.008	14.835	81.98	0.01432	2862.43
Average								**84.44**		**2925.22**
Std. Dev.								**7.60**		**714.00**
SD142	0.1169	0.1151	0.116	1.042	1.070	1.056	22.640	91.13	0.01583	2878.40
SD143	0.1149	0.1173	0.1161	0.989	1.058	1.024	22.405	98.03	0.01691	2898.58
SD144	0.1148	0.1191	0.11695	0.987	1.019	1.003	22.175	97.43	0.01603	3038.99
SD145	0.1154	0.1252	0.1203	1.061	1.018	1.040	21.025	85.39	0.01421	3004.57
Average								**93.00**		**2955.13**
Std. Dev.								**6.00**		**157.00**

5.

MODELING OF AXIALLY LOADED FRP/CONCRETE COLUMNS

5.1 INTRODUCTION

Most of the confinement models presented in Chapter 2 were originally proposed in order to predict the response of concrete confined by steel stirrups or continuous sleeves (or tubes). However, these models when applied to concrete confined by fiber

I composite wraps or tubes can not predict the experimental results. This is mainly attributed to the behavioral difference between steel and FRP, since steel is an elasto-plastic material, while FRP is a linearly elastic material. In the first part of this chapter, A four of the existing confinement models are discussed in view of the present experimental P i results presented in Chapter 3. The need for an appropriate confinement model is deliberated. A new model is proposed for circular concrete columns confined by FRP wraps or tube. As a verification, the model is then applied to the test results of the present study as well as the work of other researchers.

5.2 APPLICATION OF EXISTING CONFINEMENT MODELS

In general, the behavior of confined concrete varies according to the characteristics of the confining material. In case of elasto-plastic material, such as steel,

a state of pseudo-active confinement is developed. As soon as the confining jacket yields, a constant confining pressure is applied, and the section starts to gradually lose its strength. Yet, a different scenario takes place for linearly elastic confining materials, such as fiber composites. The confining effect of the FRP jacket increases proportionally with the increase of axial strain to the point of jacket hoop fracture, which marks the ultimate failure of the composite column. This is one of the main reasons why the confinement models for steel-confined concrete are not applicable to confinement with FRP. In Figure 5.1, the prediction of the ultimate confined stress f'_{cu} according to the existing models is compared with the experimental values of the present study, as well as other studies on FRP-confined concrete. In Figure 5.2, the stress-strain prediction of the existing models are plotted versus the experimental results for Specimen DA13 of the present study (refer to Chapter 3).

One of the most rational confinement models is the one by Ahmad and Shah (1982 a&b), which was originally calibrated for steel-confined concrete. The model uses an incremental iterative procedure to trace the passive response of the confining jacket and its impact on the encased concrete, as it was discussed in Chapter 2. The used formula for the peak strength f'_{cc}, which was based on the octahedral theory, highly overestimates the experimental values for larger values of f_r (Figure 5.1). In Figure 5.2, the model grossly overestimates the strength of the section.

The confinement model by Mander, Priestley and Park (1988) was originally proposed for steel-confined concrete. One of the main shortcomings of the model is its insensitivity to the variation of the Poisson's ratio of concrete (Mirmiran and Shahawy

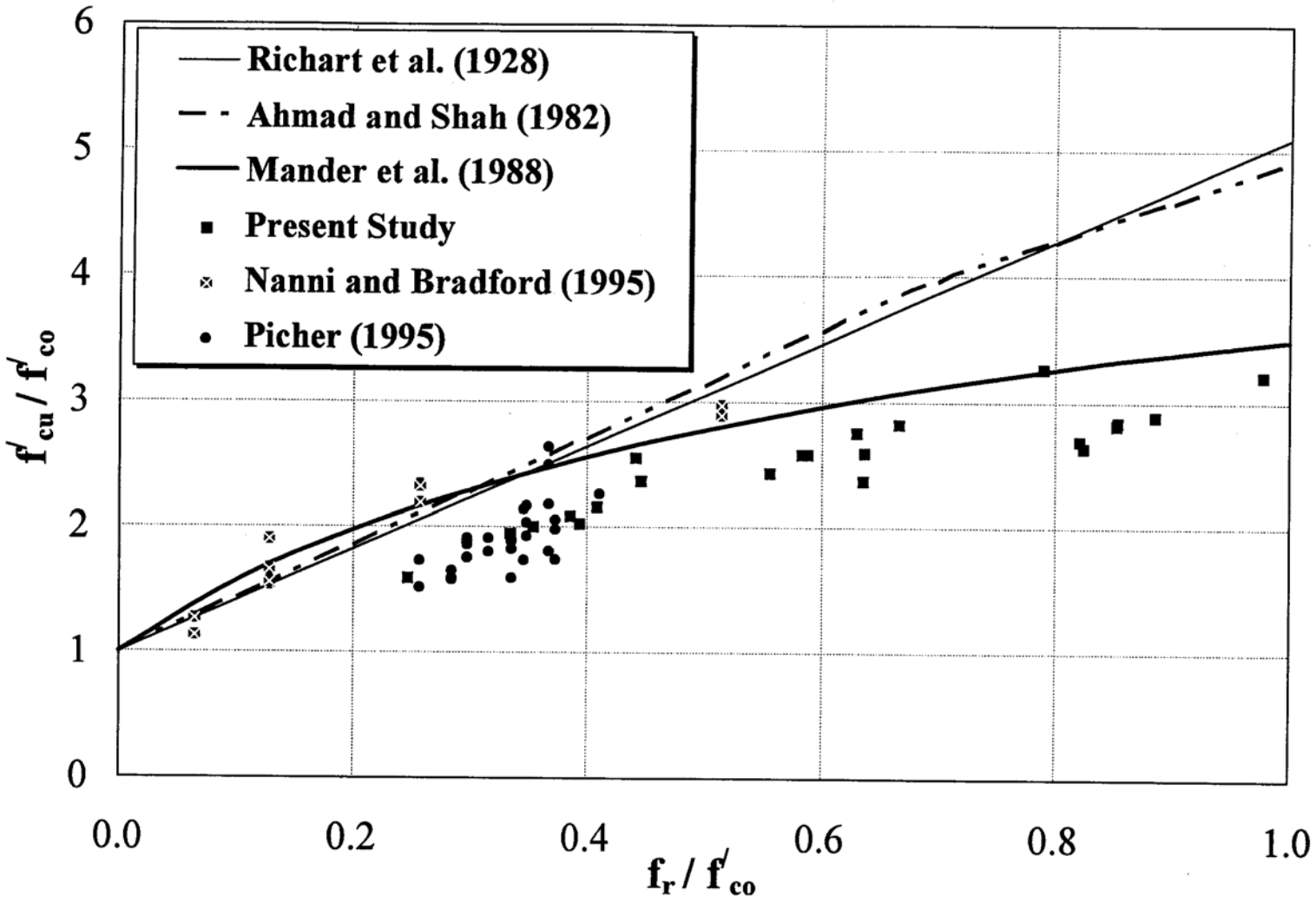

Figure 5.1 Predictions of f'_{cu} according to different models in comparison to test results of FRP-confined concrete

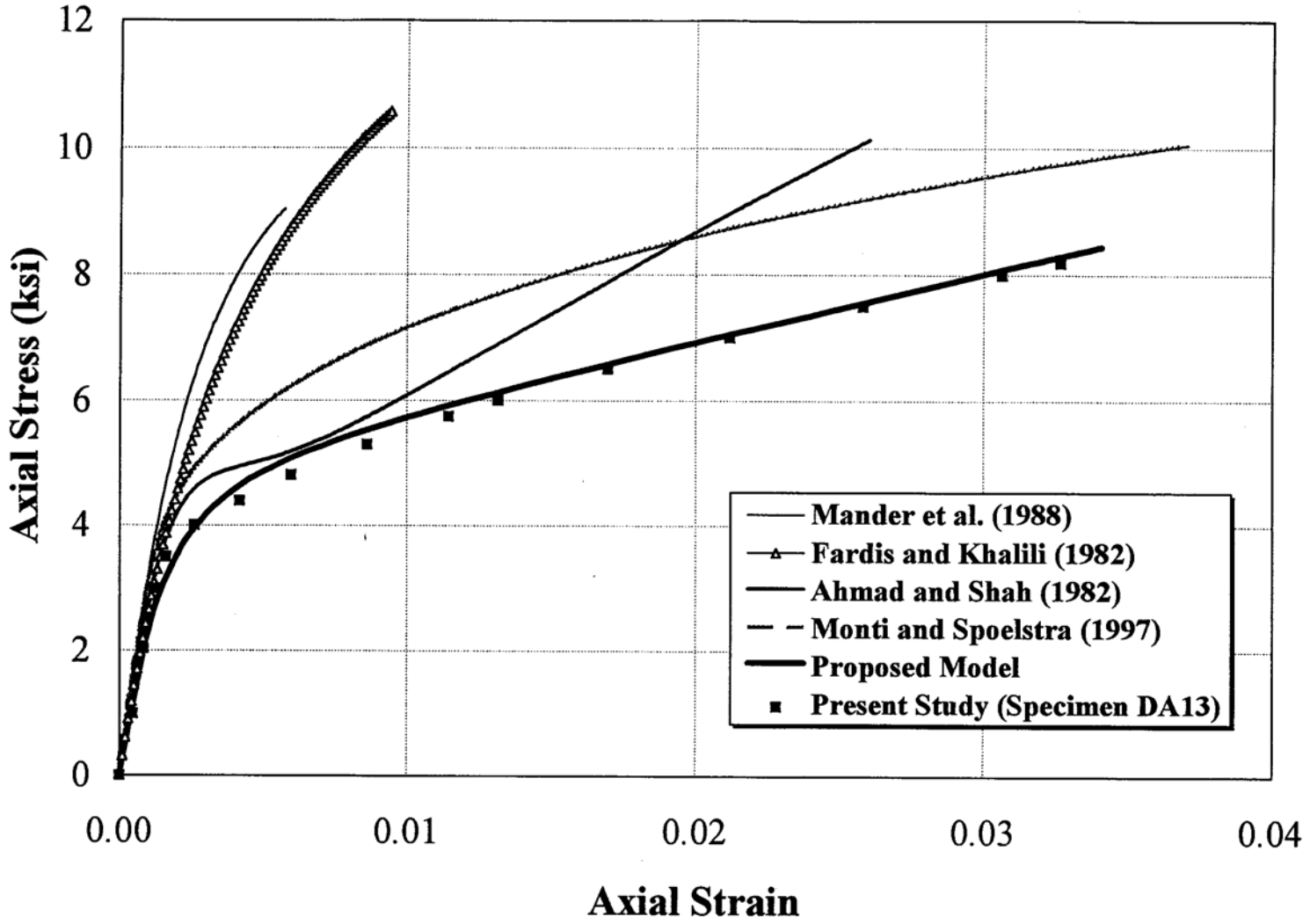

Figure 5.2 Comparison of different confinement models for Specimen DA13

1997a). In other words, it presents a solution for the active rather than the passive confinement problem. However, for confinement by steel stirrups this approximation is acceptable due to the constant confining pressure beyond the yield strain. Another problem with the model is the determination of the ultimate axial compressive strain ϵ_{cu} using the energy balance approach. When applying the model for fiber-wrapped columns, the ultimate strain is highly underestimated (Demers and Neale 1994, Mirmiran 1997a). This is attributed to considering the energy stored in the confining steel and neglecting the internal energy of the concrete core in calculation of the total strain energy. Harmon and Wang (1996) estimate the energy stored in the concrete core as 80% of the total strain energy for FRP-confined concrete.

Fardis and Khalili (1981 and 1982) tested a series of concrete cylinder confined by bi-directional fiberglass woven roving in pure axial compression. The experimental stress strain curves of those specimens had a hyperbolic shape, which conflicts with the test results of Nanni and Bradford (1995), Picher (1995), Scherer (1996), and the present study, all of which reported a bilinear response. The different shape may be attributed to the presence of axial fibers in FRP jackets in their tests. Therefore, the hyperbolic equation proposed by Fardis and Khafli does not apply to the present experimental results. The ultimate stress $f'_{cu}$is also overestimated, while the predicted ultimate strain $s,_u$ is much lower than the experimental values (Figure 5.2).

The confinement model proposed recently by Monti and Spoelstra (1997) is considered an applicable model for FRP-confined concrete. The procedure was presented previously in Chapter 2. The quality of the model is a result of a good estimate of the

lateral radial strain in concrete, which is equal to the hoop strain in the jacket by way of strain compatibility. The model is a simplified version of the model by Ahmad and Shah (1982b) with a different formula for the ultimate strength f. - . and the lateral strain s,, as it was explained in Chapter 2. The application of their model to the present experimental results is depicted in Figure 5.2. The model predicts the lateral strain according to the equation proposed by Pantazopoulou (1995), as a function of the capillary porosity and the volume of the paste in concrete (1mran 1994, Panatazopoulou and Mills 1995). Although the model presents a reasonable prediction for FRP-confined concrete, it involves a complicated procedure.

As a conclusion of this discussion, it is obvious that the confinement models established for steel-confined concrete are not applicable to FRP-confined concrete. This is attributed to their inability in estimating the dilatancy of FRP-confined concrete. A simple and powerful confinement model for FRP-confined concrete, is presented in the following section.

5.3 PROPOSED CONFINEMENT MODEL

5.3.1 Behavioral Characteristics of FRP-Confined Concrete

As shown in Chapter 3, the typical stress-strain curves of FRP-encased concrete is characterized by a bilinear ascending response in both the axial and lateral directions with no descending branch (see also Picher et al. 1996). This form of response is valid for all

confining materials with linear elastic behavior, as it was reported by Nanni and Bradford (1995), who tested short concrete columns wrapped by different fiber composite materials such as glass, carbon, and kevlar fibers.

This typical response consists of three distinct regions. In the first region, the behavior of confined concrete is similar to that of plain concrete, since the confining effect of the jacket is still not activated by the lateral expansion of the concrete core. Here, it is noteworthy that a similar behavior is reported for the initial response of steel-confined concrete (Ahmad 1981). In the vicinity of the peak stress of unconfined concrete f'_{co} the confined concrete reaches a state of unstable volumetric growth caused by excessive cracking. At this point, the confining jacket is activated, and starts to gradually restrain the rapid growth of the lateral strains. This region of the response is characterized by a transitional curve in the vicinity of the unconfined strength f'_{co}. Finally, a third region is recognized in which the confining jacket is fully activated, and the stiffness is generally stabilized around a constant rate. The response in this region is mainly dependent on the linear elastic response of the confining jacket.

To shed more light on the subject, the behavior of an FRP-confined -concrete cylinder is compared with that of a steel-confined concrete cylinder in a simple case study. A steel-confined concrete cylinder, Specimen CS in a series of tests by Orito et al. (1987), is compared with an FRP-confined concrete, Specimen DB21 of the present study (see Chapter 3). Table 5.1 presents the properties of the two specimens. The confinement ratio is defined as the ratio of confinement pressure to the unconfined strength of concrete core.

As clear from Table 5.1, both tubes provide the same level of confinement ratio (about 0.65), which is in fact why they were chosen for this comparison.

Table 5.1 Properties of concrete-filled steel and FRP tubes

Properties	**Specimen CS**	**SpecimenDB21**
Core diameter (D)	4.50 in	5.71 in
Tube thickness (t_j)	0.20 in	0.087 in
Unconfined concrete strength *(f'co)*	7.60 ksi	3.83 ksi
Confined concrete strength *(f'cc)*	24.95 ksi	10.81 ksi
Confinement effectiveness $\left(\frac{f'_{cc}}{f'_{co}}\right)$	3.28	2.83
Ultimate strain (ϵ_{cu})	0.036	0.043
Tube's hoop strength(f_j)	54.6 ksi	84.0 ksi
Confinement pressure (f_r)	4.97 ksi	2.55 ksi
Confinement ratio $\left(\frac{f_r}{f'_{co}}\right)$	0.65	0.66

Figure 5.3 shows the axial stress-strain curves for the two confinement mechanisms. The axial stresses are normalized with respect to the unconfined strength of their respective concrete cores. The figure also shows a typical response of plain (unconfined) concrete for comparison. It can be seen from the figure that the steelconfined concrete experiences only a mild softening before it reaches a

of f'_{cc}, after which it follows a gradual-post peak descending branch. It is generally accepted that the peak strength of confined concrete (f'_{cc}) occurs as soon as the steel tube

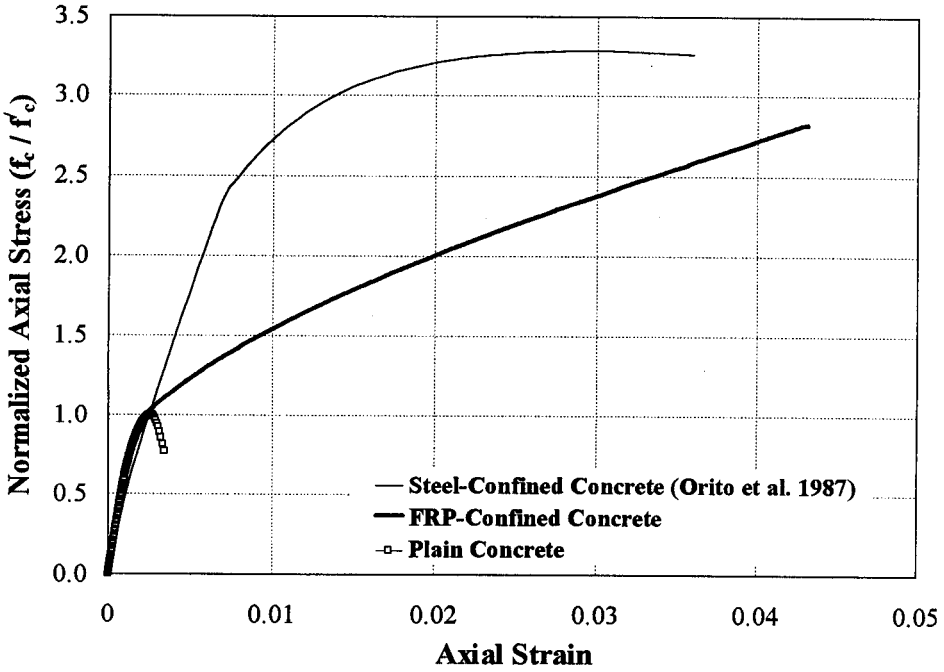

Figure 5.3 Stress-strain response of FRP-confined concrete versus steel-confined concrete

yields. On the other hand, the FRP-confined concrete displays a distinct bilinear response with a sharp softening and a transition zone at the level of its unconfined strength f'_{co}) after which the stiffness stabilizes at a constant slope until reaching the failure strength (f'_{cu}).

It is obvious from the areas under the stress-strain curves that the steel-confined concrete provides a larger energy absorption capacity than its FRP-confined counterpart. It is also noteworthy that while the two confinement mechanisms provide the same level of

confinement pressure, the degree of lateral restraints is not the same. The FRP tube applies a continuously increasing pressure on the concrete core until the tube reaches its first-ply failure. On the other hand, the confining pressure of the steel tube becomes constant once the tube yields under hoop tension.

A more elucidating approach to examine the behavior of confined concrete is to look at its volumetric response. Figure 5.4 shows the axial stress-volumetric strain curves for the two confinement mechanisms. In the figure, a typical response of plain (unconfined) concrete is also shown for comparison.

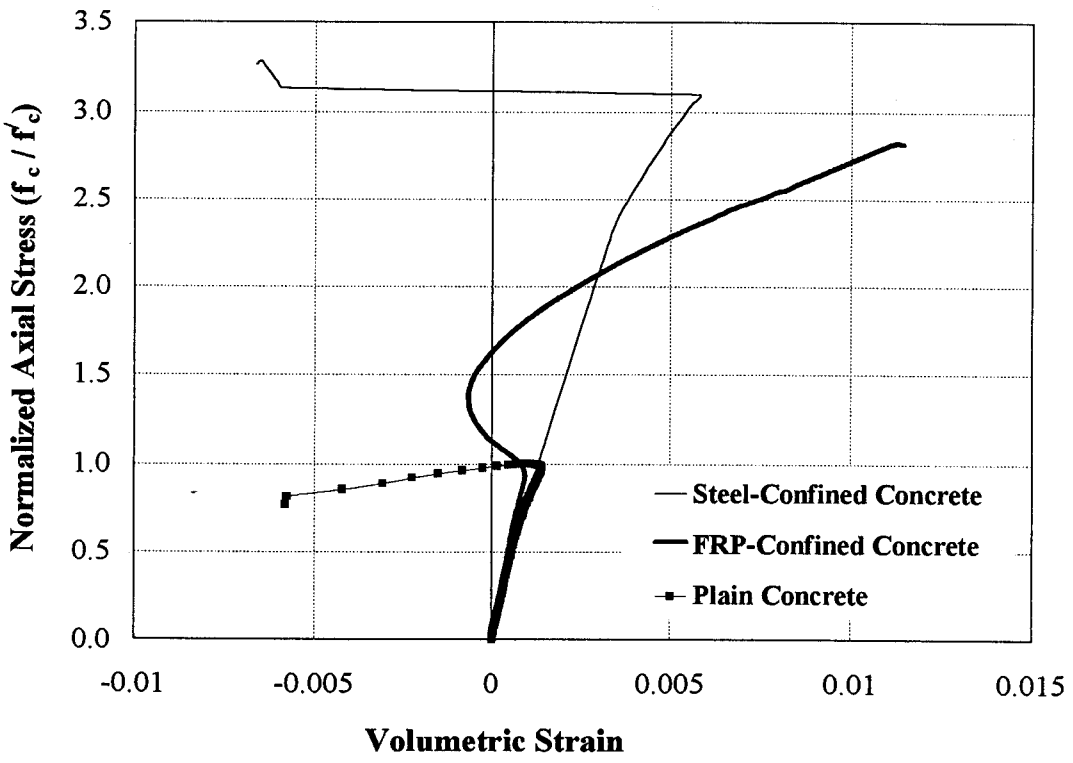

Figure 5.4 Volumetric response of FRP-confined concrete versus steel-confined concrete

The unconfined concrete curve has an initial portion, where a volume reduction is observed. As soon as the critical stress, which ranges from 0.7-0.95f'$_{co}$, is reached, a volume expansion, also called dilation, starts to take place up to failure (Chen 1982). For steel-confined concrete a similar behavior is observed with a higher critical stress than plain concrete, due to the confining effect of the steel jacket up to its yield point. After yielding, dilation takes place till failure. Yet, for FRP-confined concrete a quite different scenario is evident. The first region is similar to plain concrete, the critical stress is however higher due to the effect of confinement. Beyond the critical stress, dilation takes place up to a point of maximum dilation, when the second strain reversal occurs, and the dilatancy of concrete becomes contained. That containment effect is a function of the stiffness of the jacket as shown earlier in Figures 3.17-3.19. Picher (1995) also studied the volumetric change of FRP-confined concrete. However, the containment effect was not captured due to the small jacket thickness (3 layers). Harmon et al. (1995) found out that in case of very stiff FRP tubes, no dilation ever takes place

This behavioral difference is more pronounced in the dilation response of the two confinement mechanisms. The dilation rate ~t is defined as (also refer to Chapter3):

$$\mu = \frac{d\varepsilon_r}{d\varepsilon_c} \tag{5.1}$$

In Figure 5.5, the dilation curves of concrete for the two confinement mechanisms, as well as a typical dilation curve for an unconfined concrete cylinder, are displayed. All three curves begin at a dilation rate of equal to the Poisson's ratio of concrete. The dilation rate

for unconfined concrete increases drastically with the growth of micro-cracks, and becomes unstable near the its peak strength. Dilation of the steel-confined concrete, on the other hand, is effectively contained by the tube until the steel yields, after which the confined concrete behaves much in the same way as the unconfined concrete. Dilation of FRP-confined concrete, however, displays a unique response. Once the tube becomes fully activated, it not only contains the dilation of concrete core, but also reduces it to an asymptotic value.

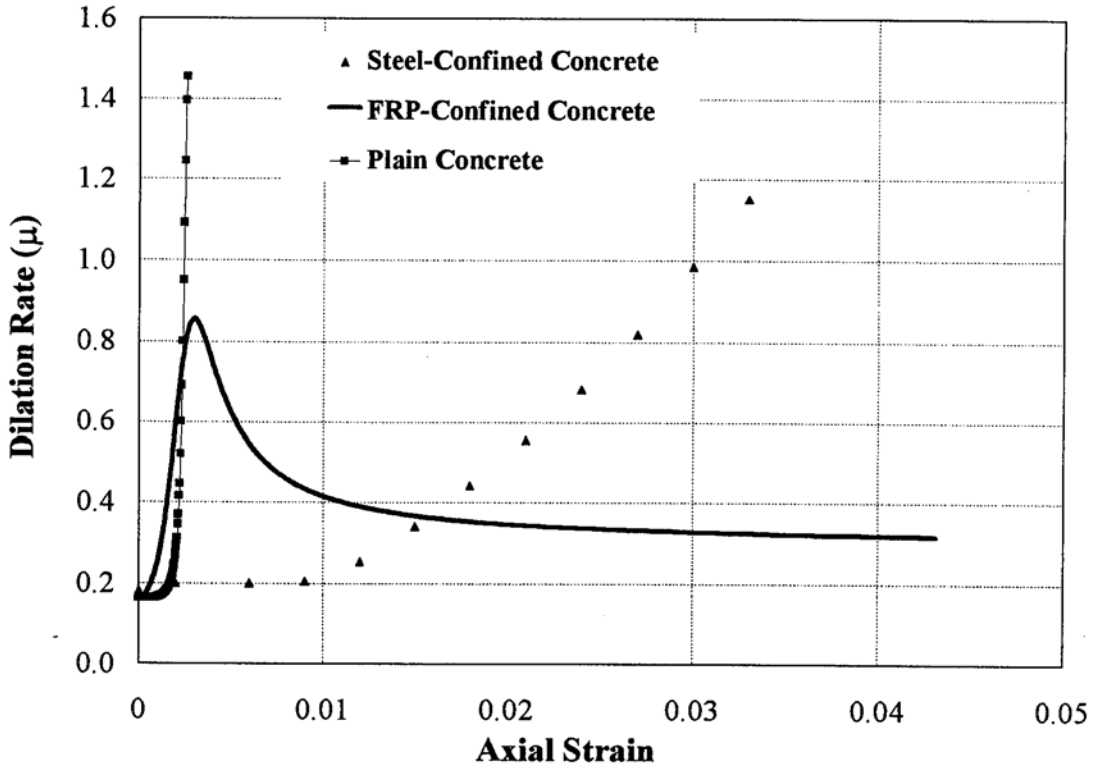

Figure 5.5 Dilation curve of FRP-confined concrete

The values of the peak dilation rate μ_{max} and the ultimate asymptotic dilation rate μ_u were calibrated as:

$$\mu_{\max} = -0.977 In\left(\frac{2E_j t_j}{f'_{co} D}\right) + 3.938 \qquad R^Z = 89.80\ \% \tag{5.2}$$

$$\mu_u = -0.187 In\left(\frac{2E_j t_j}{f'_{co} D}\right) + 0.881 \qquad R^Z = 87.00\ \%$$

It is noted that the proposed equations of Amax and pu are basically functions of the physical properties of both the jacket and the concrete.

As a conclusion of the above discussion, the models for FRP-confined concrete should account for the stiffness of the tube. Moreover, any attempt at developing a unified t 1 confinement model has to include the effect of restraint mechanism on the dilation tendency of the concrete core

5.3.2 Mathematical Model

One of the major aims of this research was to study the behavior of concrete-filled FRP tubes and to model the response of FRP-confined concrete. The proposed procedure was to find a suitable equation producing the characteristic bilinear stress-strain curve of FRP-confined concrete. The equation should be easy to use and to calibrate its parameters as functions of the physical properties of both the concrete core and the confining FRP jacket. Several square-root models were attempted with three, four, or five parameters as follows:

$$f_c = A + B\varepsilon_c - \sqrt{C^2\varepsilon_c^2 + A^2}$$

$$f_c = A + B\varepsilon_c - \sqrt{C^2\varepsilon_c^2 + 2D\varepsilon_c + A^2} \qquad (5.3)$$

$$f_c = A + B(\varepsilon_c - C) - D\sqrt{(\varepsilon_c - C)^2 + E^2}$$

The four and five parameter models were calibrated efficiently, yet the parameters were not directly related to the physical and geometrical properties. Another fractional polynomial equation, similar to the one used by Ahmad and Shah (1982a), yet with different powers was used, in the following form:

$$f_c = \frac{A\varepsilon_c + (D-1)\varepsilon_c^B}{1 + (A-2)\varepsilon_c + D\varepsilon_c^D} \qquad (5.4)$$

Very good correlation with the experimental results was obtained, however, the relevance of the parameters to the physical and geometrical properties were complicated. Finally, a versatile formula was used, which satisfied the above requirements. The formula was first proposed by Richard and Abbot (1975); a general stress-strain equation applicable to normal weight concrete as well as triaxially confined soils. The same formula was later successfully utilized by Almusallam and Alsayed (1995) to model the stress-strain response of normal and light weight concrete, as well as high-strength concrete. The fourparameter formula is given as follows:

$$f_c = \frac{(E_1 - E_2)\varepsilon_c}{\left[1 + \left(\frac{(E_1 - E_2)\varepsilon_c}{f_o}\right)^n\right]^{\frac{1}{n}}} + E_2\varepsilon_c \tag{5.5}$$

where E_1 and E_2 are the first and second slopes of the stress-strain response, respectively, ϵ_c and f_c are the concrete strain and stress, respectively, f_o is the reference stress at the intercept of the second slope with the stress axis, and *n* is a curve-shape parameter which controls the curvature in the transition zone (Figure 5.6).

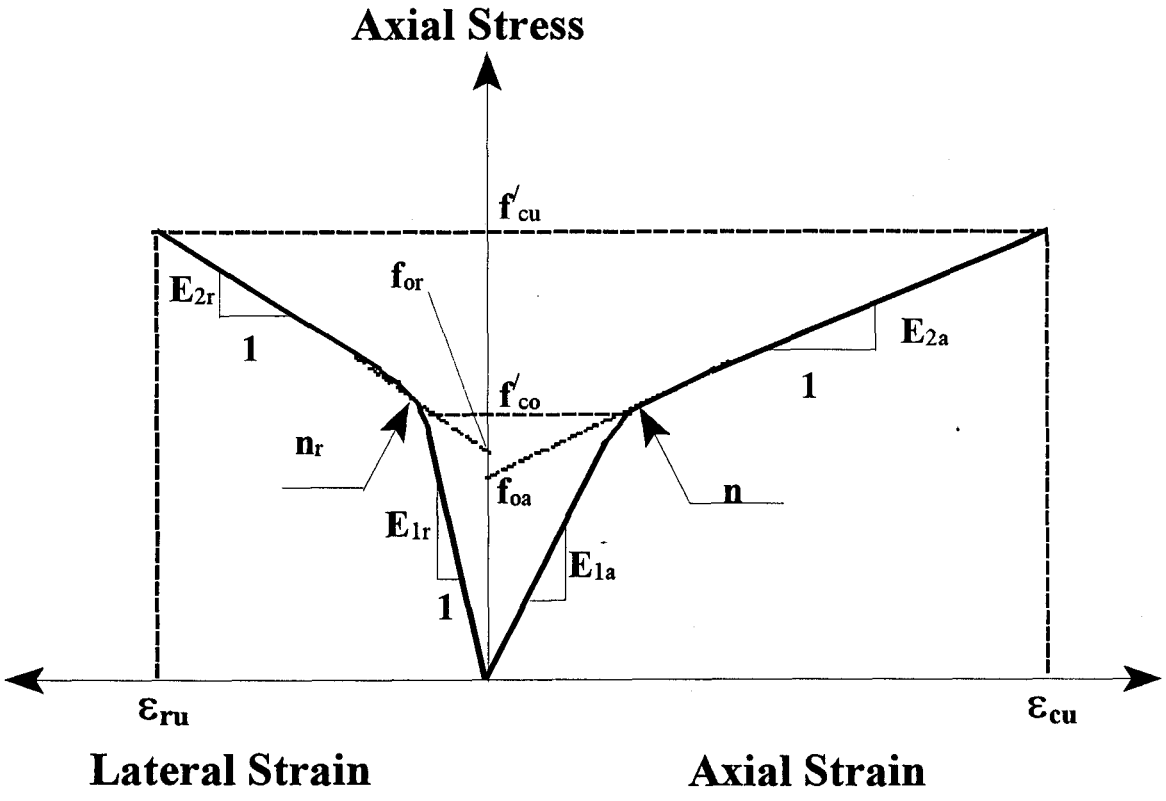

Figure 5.6 Parameters of bilinear confinement model

5.3.3 Correlation of Model Parameters in the Axial Direction

In order to evaluate the first slope E_l, the following formula for the secant modulus as proposed by Ahmad and Shah (1982a) was adopted since the ACI equation proved to overestimate the elastic modulus:

$$E_{1a} = 47.586\sqrt{1000 f'_{co}} \quad \text{[ksi]}$$

$$= 3950\sqrt{f'_{co}} \quad \text{[MPa]} \tag{5.6}$$

where subscript a denotes the axial direction, and f'_{co} is the unconfined strength of the encased concrete.

According to the previous discussion, concerning the behavior of the FRP-confined concrete, it is expected that the transition from the first into the second slope of the stress-strain response takes place at an axial stress in the vicinity of f'_{co}. Yet, by further examining the stresses at the bend point in the transition zone, and comparing them with the strengths of the control specimens, some variations were observed. These variations directly corresponded to the difference between the first slope of the confined concrete and that of the control specimens. This observation triggered the assumption that control specimens may not truly represent the strength of concrete core. This may be attributed to different curing conditions in that the concrete core would not lose its moisture at the same rate as the control specimens. For this reason, f'_{co} was taken as the stress at the bend point for each confined specimen.

In order to model the second slope in the axial direction, E_{Za}, it is noted that as concrete core approaches its unconfined strength, micro-cracks grow to the extent that the Poisson's ratio can no longer describe the relation between the lateral and axial strains, and the jacket becomes the sole restraining device against catastrophic failure. Therefore, the second slope (E2) is a function of the stiffness of the confining tube, and to a lesser extent a function of the unconfined strength of concrete core as below:

$$E_{2a} = 52.411 f'^{0.2}_{co} + 1.3456 \frac{E_j t_j}{D} \quad \text{(ksi)}$$

$$R^Z = 90.0\% \qquad (5.7)$$

$$= 245.61 f'^{0.2}_{co} + 1.3456 \frac{E_j t_j}{D} \quad \text{(MPa)}$$

where E_j is the effective modulus of elasticity of the FRP tube in the hoop direction, t; is the tube thickness, D is the core diameter, and R^Z represents the coefficient of correlation. The intercept stress L is a function of both the strength of the concrete core, and the ultimate hoop pressure of the tube, f_r (see Figure 5.7):

$$f_{oa} = 0.872\ f'_{co} + 0.371\ f_r + 0.908 \qquad R^2 = 93.0\% \qquad (5.8)$$

where,

$$f_r = \frac{2 f_j t_j}{D} \qquad (5.9)$$

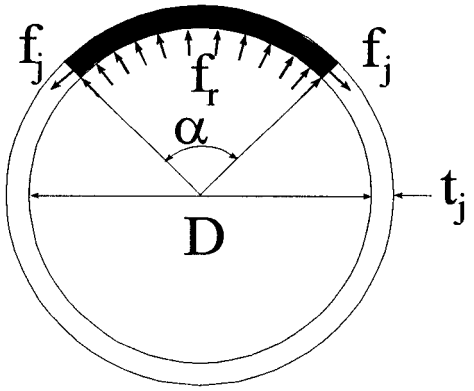

Figure 5.7 Confining pressure f_r

The correlation of the predicted and the experimental values of E_2 and f_{oa} are depicted in Figures 5.8 and 5.9, respectively.

At the beginning of this chapter, the confined strength of concrete f'_{cu} was compared with existing confinement models (see Figure 5.1). It was noted that the models of Richart et al. (1928) and of Ahmad and Shah (1982a) both overestimate the value of f'_{cu} for higher values of lateral pressure f_r. This fact was also realized by Saatcioglu and Razvi (1992), as they proposed a nonlinear relationship by and f_r given by:

$$f'_{co} = f'co + 4.825 f_r^{0.83} \qquad \text{[ksi]} \qquad (5.10)$$

Yet, their proposed equation still overestimates the peak stress of FRP- confined concrete, as shown in Figure 5.10 for the test results of the present study as well as of Nanni and Bradford (1995) and of Picher (1995). Therefore, a new nonlinear equation is calibrated using the test data in Chapter 3 in the following form:

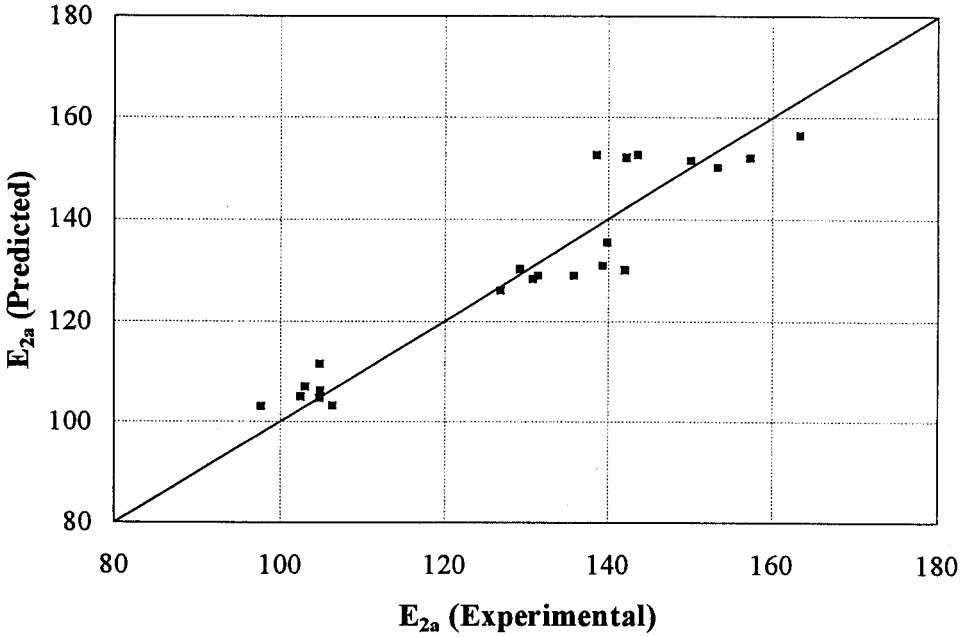

Figure 5.8 Correlation of experimental and predicted values of E_{2a}

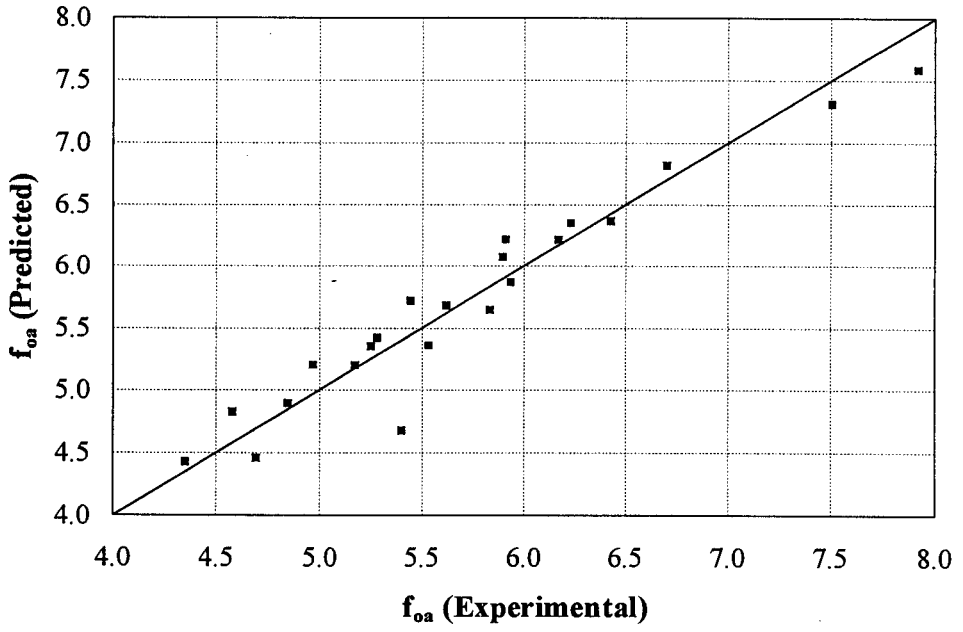

Figure 5.9 Correlation of experimental and predicted values of f_{oa}

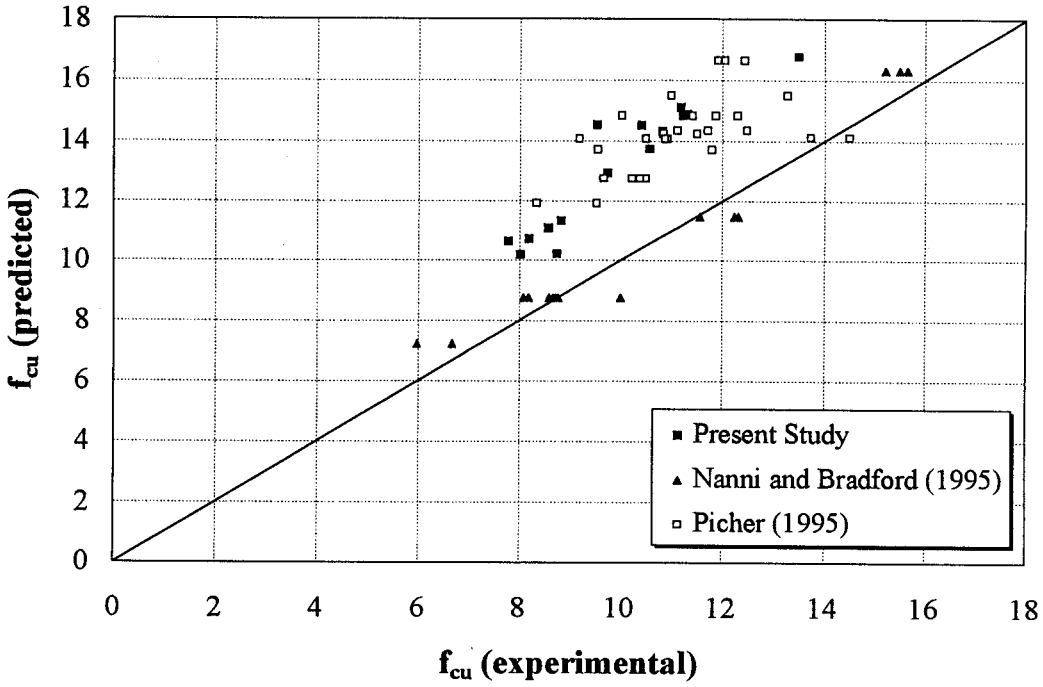

Figure 5.10 Experimental versus predicted values off using the equation by Saatcioglu and Razvi (1992)

$$f'_{cu} = f'_{co} + 3.38\, f_r^{0.7} \quad \text{(ksi)}$$

$$R^2 = 88.9\ \% \qquad (5.11)$$

$$= f'_{co} + 6.0 f_r^{0.7} \quad \text{(MPa)}$$

where f'_{cu} is the ultimate compressive strength, and is also the peak (or maximum) compressive strength f'_{cu} in the case of FRP-confined concrete. This equation was also applied to the test data of Nanni and Bradford (1995) and of Picher (1995), and a good correlation resulted as shown in Figure 5.11.

The ultimate strain ϵ_{cu} is determined from the second slope of the curve as below:

$$\varepsilon_{cu} = \frac{f'_{cu} - f_c}{E_2} \qquad (5.12)$$

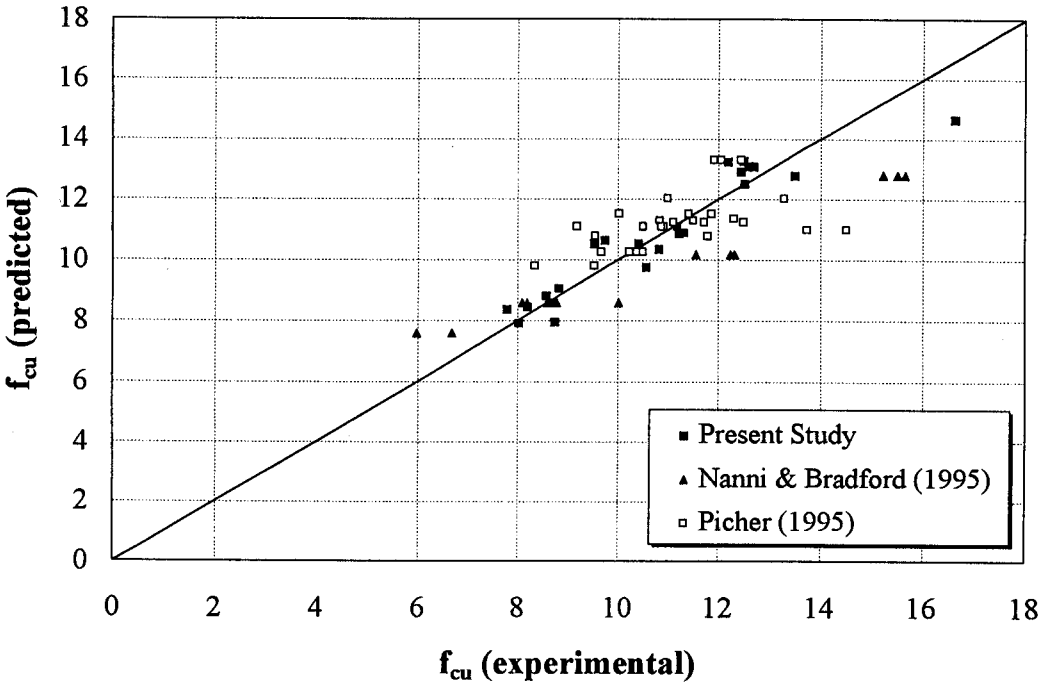

Figure 5.11 Correlation of experimental and predicted values of f'_{cu}

The model is not very sensitive to the curve-shape parameter n (Figure 5.6). A constant value of 1.5 was found appropriate for the present application.

5.3.4 Correlation of Model Parameters in the Lateral Direction

Since the axial stress-lateral strain curve is also bilinear, and the transition zone occurs at the same axial stress level as for the axial direction (refer to Chapter 3), the model can be generalized for the lateral direction, as below:

$$f_c = \frac{(E_{1r} - E_{2r})\varepsilon_r}{\left[1 + \left(\frac{E_{1r} - E_{2r}\varepsilon_r}{f_{0r}}\right)^{n_r}\right]^{\frac{1}{n_r}}} + E_{2r}\varepsilon_r \qquad (5.13)$$

where subscript r denotes the lateral (radial) direction.

The first slope El, is simply obtained by dividing the initial slope in the axial direction by the Poisson's ratio of concrete vo (typically 0.15-0.22) as follows (Ahmad 1981):

$$E_{1r} = \frac{E_{1a}}{V_o} \tag{5.14}$$

The remaining parameters are calibrated using the dilation parameters discussed earlier in this chapter. Using Equation 5.2, E_2, and n_r are correlated as:

$$E_{2r} = \frac{E_{2a}}{\mu_u} \qquad R^2 = 82.60\% \tag{5.15}$$

$$n_r = \frac{n}{\mu_u} \tag{5.16}$$

The reference plastic stress, f_{or}, is calibrated in a form similar to L_a as:

$$f_{or} = 0.636\ f'co + 0.233\ f_r + 0.661 \quad \text{(ksi)}$$

$$R^Z = 79.9\ \% \tag{5.17}$$

$$= 0.636\ f'_{co} + 0.233\ f_r + 4.561 \quad \text{(MPa)}$$

Finally, the ultimate radial strain is calculated as

$$\varepsilon_{ru} = \frac{f'_{ca} - f_{0r}}{E_{2r}} \tag{5.18}$$

5.4 COMPARISON WITH TEST RESULTS

The proposed confinement model was applied to four sets of experimental results: test results of Series D (Chapter 3), test results of Picher (1995), test results of Nanni and Bradford (1995), and those of Mastrapa (1997). Good correlation was obtained.

Here, it should be mentioned, that one major difference between steel and fiber jackets is the material properties. Steel, in general, is a homogeneous isotropic material, while FRP is a composite orthotropic material. The mechanical properties of composite materials is highly sensitive to the properties of its constituents. The uniformity of the layup as well as its stacking sequence, play a big role especially if the hand lay-up manufacturing technique is used. Even for the filament winding technique, the uniformity of the tube along its length is of concern, since amount of resin may vary, unless fully automated control mechanisms are employed. In short, FRP tube may have some imperfections and consequently non-homogenous properties. Moreover, since FRP is an orthotropic material, its in-plane properties are function of the loading pattern. All these factors complicate the prediction of experimental results, especially the true failure point.

5.4.1 Present Study

The model was applied to the experimental results, which were previously discussed in Chapter 3. The input for each specimen composed of the following five values: D, t_i, f'_{co}, f_j, and E_j, which simply represent the geometrical and mechanical properties for both the concrete core and the FRP jacket. Here, it is noted that f'_{co}, is not the average strength of the control unconfined specimens, but rather the stress at the bend

point, which occurs at an axial strain in the range of ϵ_c = 0.0025-0.0035, as it was discussed earlier in this chapter. Figures 5.12-5.14 show the application of the model to three specimens of different jacket thicknesses for each of the three Series, DA, DB, and DC. The specimens plotted are: DA13, DA23, and DA31 of Series DA; DB 12, DB23, and DB33 of Series DB, DC12, DC22, and DC31 of Series DC. The experimental results are shown by markers, while solid lines represent the model prediction. The experiment and the model compare favorably in both the axial and the lateral directions. The application of the model to all specimens of series D is presented in Appendix A.

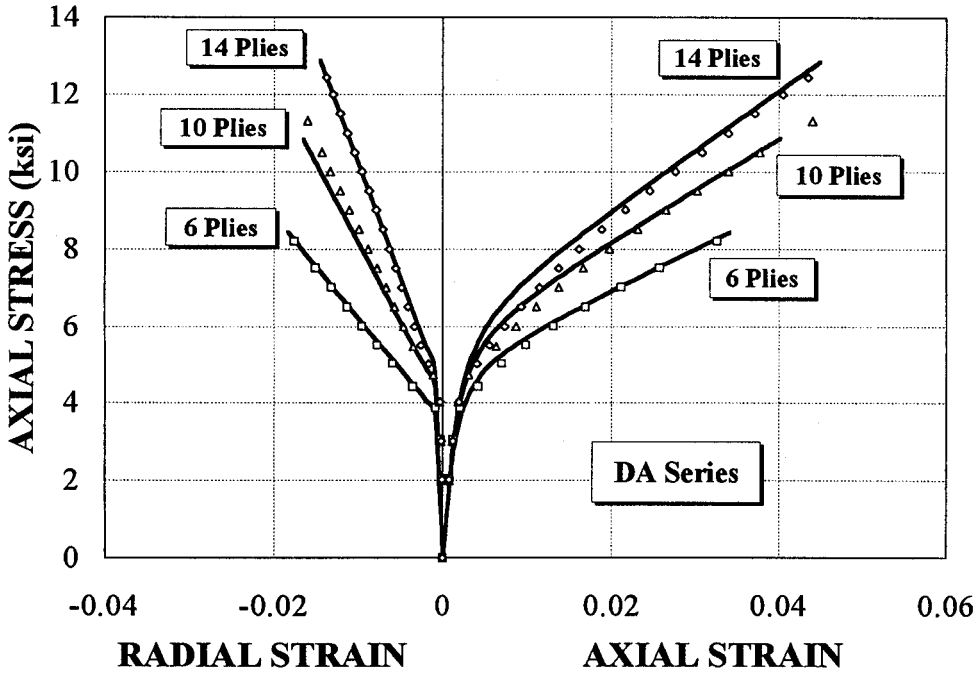

Figure 5.12 Application of confinement model to specimens of Series DA 101

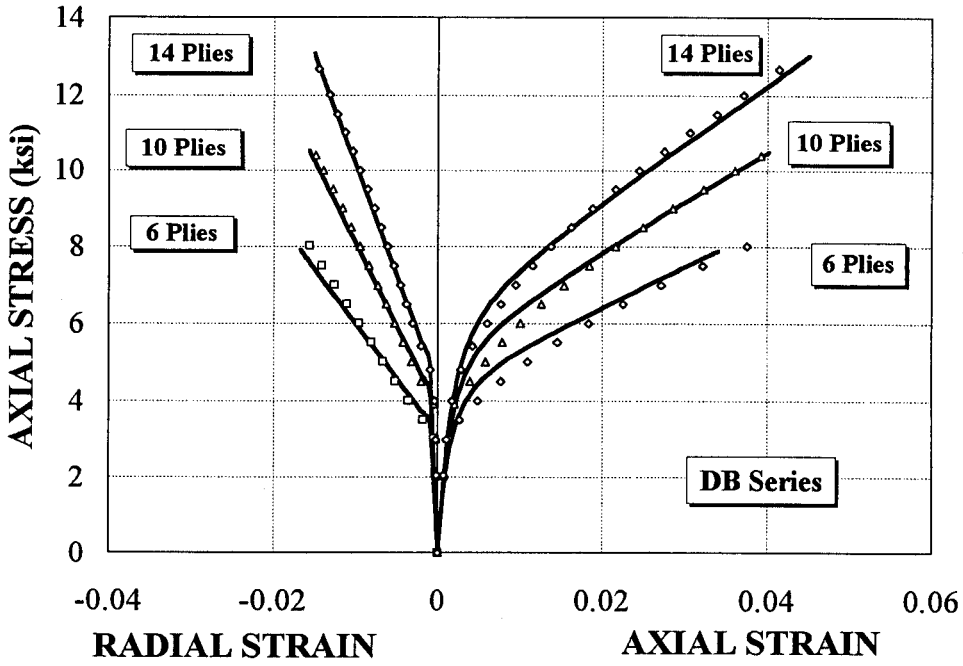

Figure 5.13 Application of confinement model to specimens of Series DB

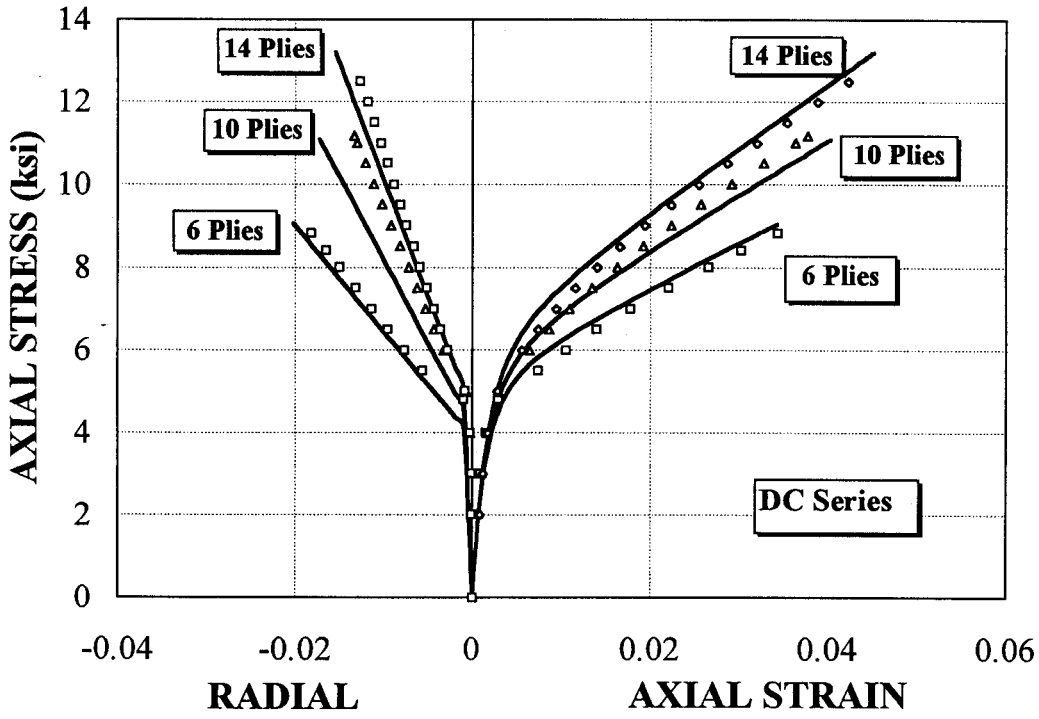

Figure 5.14 Application of confinement model to specimens of Series DC

5.4.2 E-Glass Filament-Wound Concrete Cylinders

To further confirm the validity of the model, it was applied to one of the fiber-wrapped specimens of Nanni and Bradford (1995). In their experiment, E-glass fibers were filament-wound around 6". x 12" concrete cylinders (refer to Chapter 2 for a detailed description of the tests). The reported hoop strength and effective modulus of the FRP jacket were 84.6 ksi and 7,542 ksi, respectively. They tested specimens with 1, 2, 4, and 8 plies with a nominal thickness of 0.0118 inch per ply. The strength of concrete core was reported as 5.26 ksi. Figure 5.15 shows the test results and the predicted stress-strain curve using the present model for a 4-ply specimen. Reasonable agreement is observed for the shape of the curve and the second slope. Yet, the ultimate failure point is underestimated for both strain and stress. As it was mentioned before, the manufacturer's data may be too conservative.

5.4.3 Carbon Fiber-Wrapped Concrete Cylinders

Picher (1995) tested a series of 6 in x 12 in concrete cylinders wrapped by two different types of unidirectional carbon fabrics and subjected to uniaxial compression (refer to Chapter 2). The stiffness of the carbon jacket was varied by using different fiber orientation in order to optimize the confinement configuration. The reported unconfined concrete strength for all specimens was 5.76 ksi . He provided a detailed mechanical analysis of the jacketing material in his report using the Classical Lamination Theory for the different fiber orientations taking into account the effect of biaxial loading of the jacket (refer to Chapter 4). The present confinement model was applied to two of his specimens

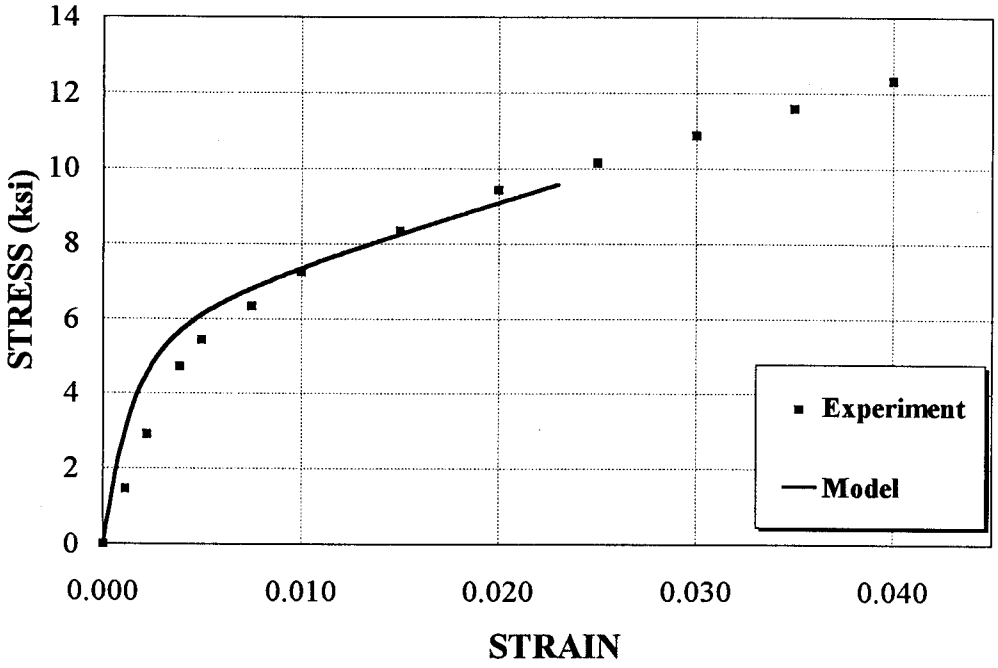

Figure 5.15 Application of confinement model to test results of Nanni and Bradford (1995)

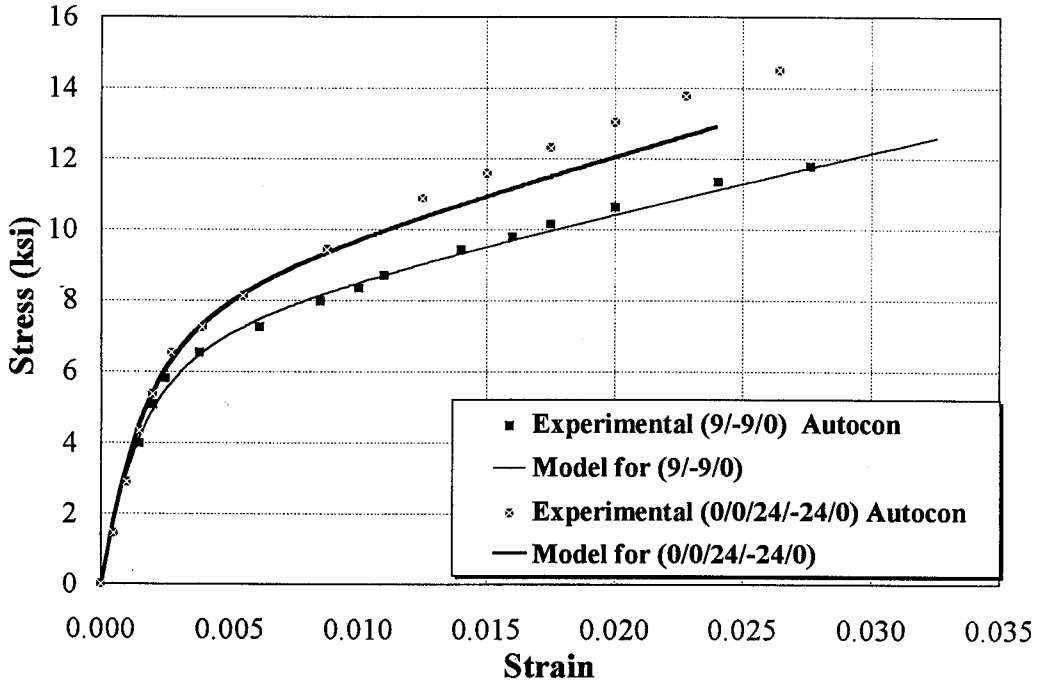

Figure 5.16 Application of present model to test results of Picher (1995)

as shown in Figure 5.16. The numbers inside the brackets are the fiber orientation angles for each layer. The reported ultimate hoop strains of the jackets for these two specimens were close to the analytical results, which indicated a mature failure.

An excellent comparison is realized for the 3-layer (9/-9/0) specimen with Autocon carbon, except for the failure point, which is slightly overestimated. A good comparison is also obtained for the 5-layer (0/0/24/-24/0) specimen with Autocon carbon. The ultimate axial strain is predicted reasonably well, while the ultimate stress is slightly underestimated.

5.4.4 S-Glass Fiber-Wrapped Concrete Cylinders

Mastrapa (1997) tested a series of 6" x 12" concrete cylinders confined by 1, 3, 5, or 7 plies of unidirectional S-glass fabric (refer to Chapter 2). For half of the specimens the fabric was wrapped around the cured concrete cylinders, while for the other half concrete was poured inside tubes made of the same S-glass fabric. Concrete of the same batch was used for all specimens with an average unconfined strength of 5.4 ksi. The average hoop strength and effective modulus of the FRP jacket were 85 ksi and 2,984 ksi, respectively. The results of the two construction methods were very similar. The confinement model was applied to one unbonded 3-ply specimen (3UBA), and one bonded 5-ply specimen (5BC). An excellent comparison is evident, as shown in Figure 5.17, especially for the 5-layer specimen. Yet, the failure point was overestimated for the 3-layer specimen. This, however, is attributed to premature failure of the specimen due to debonding at the splice (Mastrapa 1997).

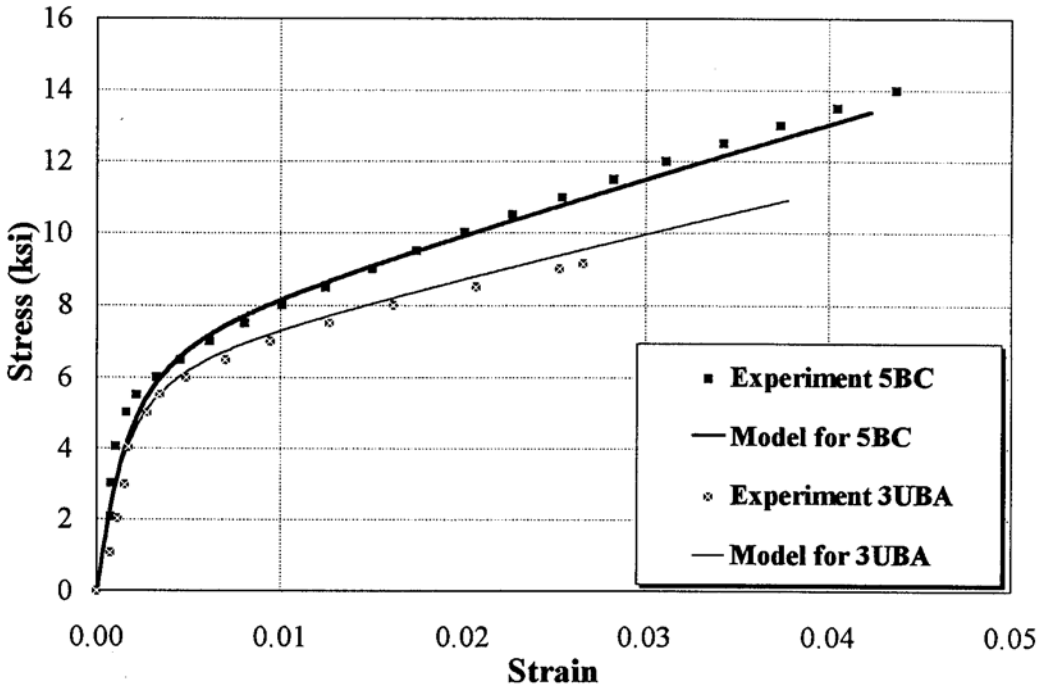

Figure 5.17 Application of confinement model to test results of Mastrapa (1997)

As a conclusion, the proposed confinement model is proved applicable to different types of FRP used for the confinement of concrete columns.

6.

AXIAL-FLEXURAL TESTING

OF CONCRETE-FILLED FRP TUBES

6.1 INTRODUCTION

The previous chapters were mainly focusing on the confinement of circular concrete sections by FRP composites. A confinement model was proposed enabling the prediction of the stress-strain response of circular FRP-confined concrete sections, subjected to concentric compression loading. In the remainder of this thesis, the study is expanded to cover the case of concrete-filled square FRP sections subjected to axial and flexural loads. The beam-column tests are covered in this chapter along with a description of the fabrication procedure. Five 7" x 7" x 52" specimens were tested under various combinations of axial and lateral loads in order to establish an experimental force-moment interaction diagram for the proposed column.

6.2 MANUFACTURE OF SQUARE FRP TUBES

The FRP tube in the case of concentrically loaded column merely provides hoop confinement, and therefore, the mechanical bond between FRP and concrete is not of

importance. Yet, for flexural loads the FRP tube plays an important role. It confines the concrete in the compression zone and acts as the flexural and shear reinforcement both at the same time. This requires the development of the full composite action between FRP and concrete. Since no natural bond exists between FRP and concrete, a mechanical bond is necessary. Therefore, the required tube should accommodate axial and hoop fibers in addition to a series of interior shear connectors.

The FRP tube used in this study consisted of one interior ply of unidirectional 24 oz E-glass woven roving and 15 E-glass filament-wound angle plies with a winding angle of ±75° with respect to the longitudinal axis of the tube. In addition, a series of longitudinal and transversal internal ribs are provided to serve as shear connectors and the load distribution mechanism (Figure 6.1).

6.2.1 Collapsible Mandrel

In order to fabricate the square tube with projected internal ribs, a collapsible mandrel was designed and manufactured to facilitate the filament winding process. The mandrel was made of 4 aluminum angles 2 1/2" x 2 1/2" x 3/8" with a length of 5 1/2 feet (66"). The angles were mounted on two 11" x 11" x I/2" aluminum end plates with a 1" gap in between to form a 6" x 6" square section with an outer comer radius of $^{1}/4$" (Figure 6.2). The mandrel was designed to be driven by a 1" diameter central driving shaft. On each face of the aluminum angles a series of 2" x 1 13/16" x $^{1}/4$" maple wood plates were mounted with $^{1}/2$" spacing in between, in order to form the ribs. The sides of the wood plates were wedged at 45° angle to facilitate the dismantling of the tube.

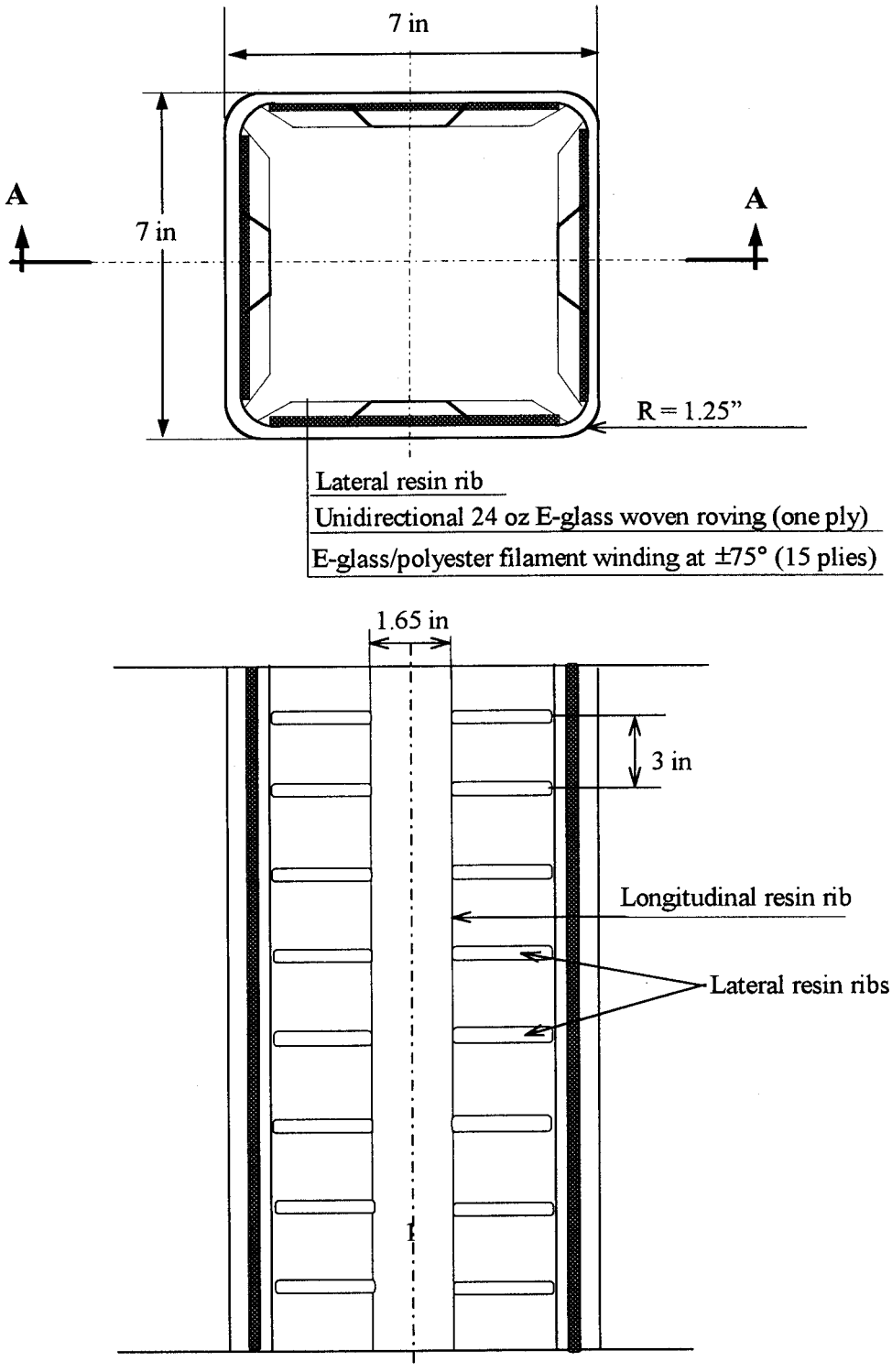

Figure 6.1 Cross-section of the square CFFT

6.2.2 Fabrication Procedure

After assembling the aluminum mandrel, the gaps between the aluminum angles were covered by masking tapes. Liquid wax was then applied on the wood plates to avoid adhesion to the resin (Figure 6.3). This was followed by filling the spaces between the wood plates with polyester paste (Figure 6.4). The paste consisted of Ashland Chemicals polyester resin (Dion 33-611), silica fume, PPG chopped glass fibers (6.4 mm length), and MEKP (methyl ethyl ketone peroxide) as a catalyst. The amounts of the chopped glass and MEKP were about 1% and 1.5% by volume, respectively. After application of the polyester paste, it was left for about 30 minutes to cure. The curing process was accompanied by some heat dissipation, discoloration and shrinkage. A unidirectional 24 oz glass woven roving made by Knytex was then placed over the cured paste by applying liquid resin polyester (Figure 6.5). The liquid resin composed of polyester and 1.5% MEKP catalyst. The fiber-to-resin ratio was 30/70 %. Upon completion of this phase at UCF, the mandrel was taken to Marine Muffler Corp., Apopka, FL to perform the regular filament winding process. The same filament winding machine for the circular tubes as described in Chapter 3 was used with the same winding angle of ±75° to add 15 plies of Eglass/polyester (Figure 6.6). The curing process was speeded up by placing the mandrel on a revolving system with hot air blowing by a fan from underneath for 30 minutes (Figure 6.7). The mandrel was then placed in room temperature for about 12 hours for the tube to completely cure. After curing, the two end plates were dismantled and the four angles

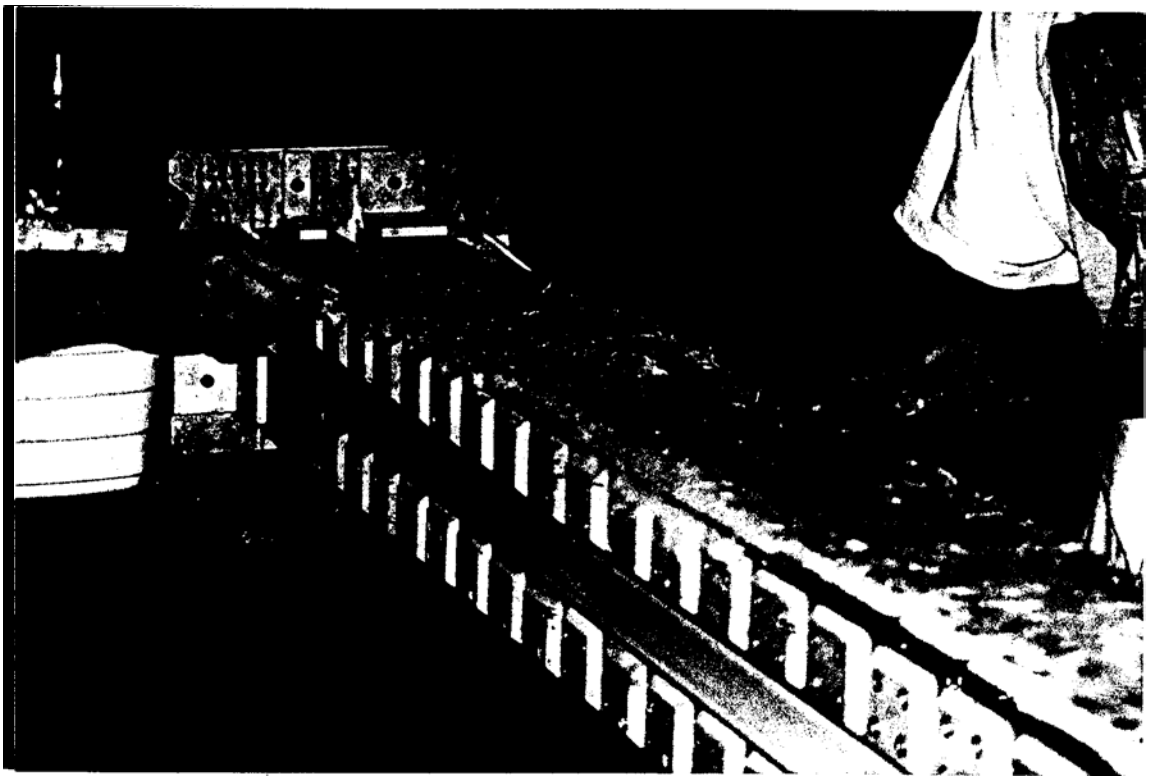

Figure 6.4 Application of the polyester paste to the spaces in between wood plates

Figure 6.2 Collapsible square mandrel

Figure 6.5 Placement of the glass woven roving and application of polyester resin

Figure 6.3 Wrapping of wood plates

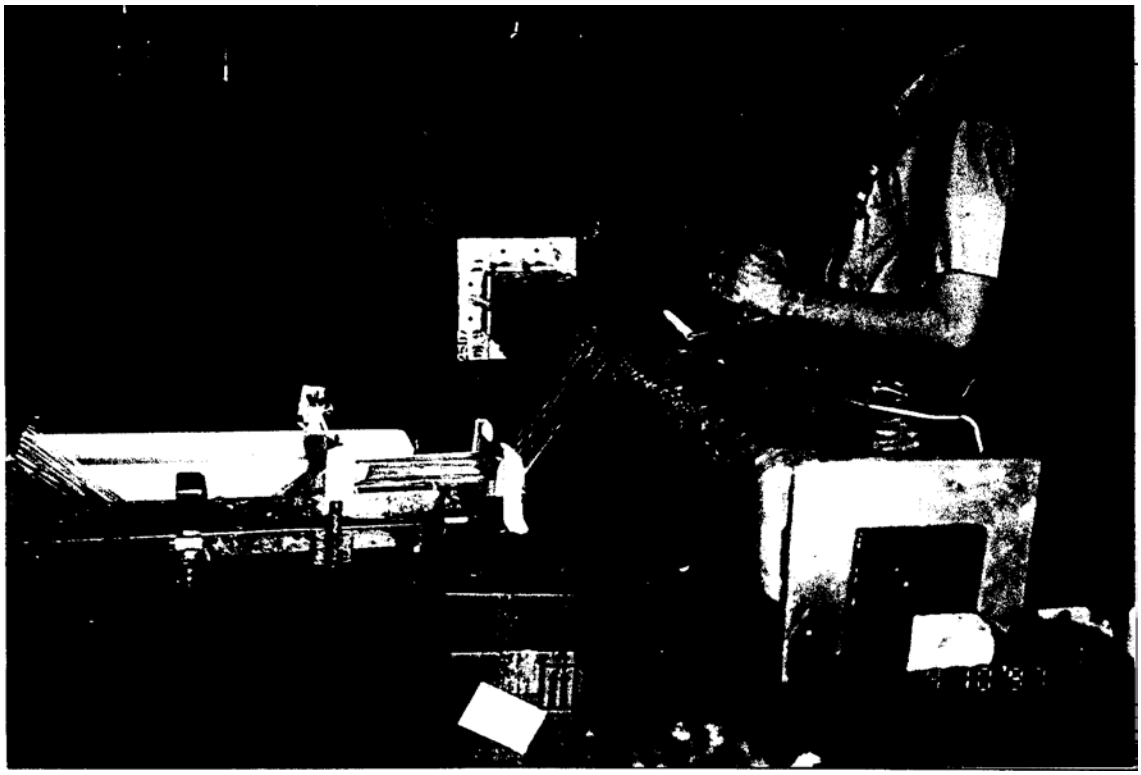

Figure 6.6 Filament winding of the square tube

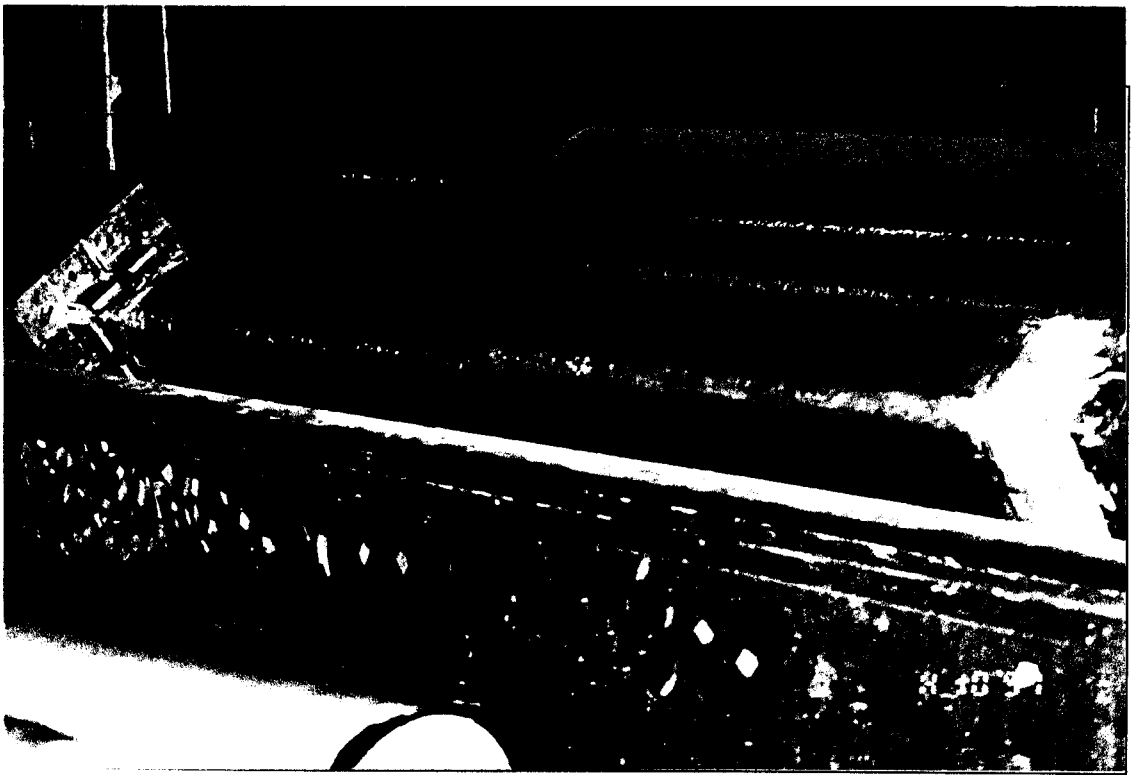

Figure 6.7 Curing of the square filament-wound tube

were collapsed inward in order to remove the finished tube. In Figure 6.8, a finished tube is shown.

The above procedure was followed to fabricate seven 52" long tubes. One of these tubes did not include the glass woven roving fabric. This tube was cut into 3 segments of 12" length, while five of the tubes were trimmed to 52" length. The seventh tube was used for the coupon testing, as it will be discussed in the next chapter. The average dimensions of the finished square FRP tube were 7" x 7" outer dimensions, $^{1}/4$" wall thickness, $^{1}/4$" rib thickness, and an average outer corner radius of 1.25" (see Figure 6.1).

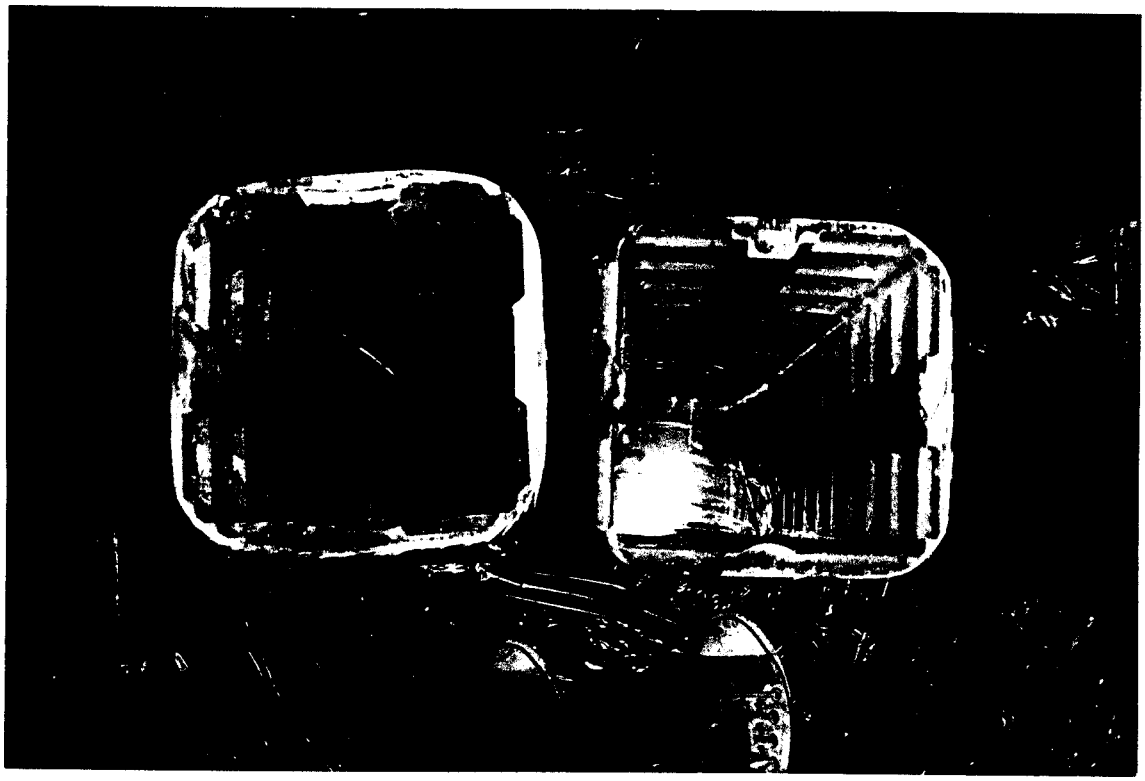

Figure 6.8 The cured square tube before casting concrete

6.3 TEST PROCEDURE

The manufactured FRP tubes were filled with ready mix concrete of 3,000 psi target strength. In addition, three control 6" x 12" cylinders were cast to measure the concrete strength. The tests were conducted after 31 days from casting at the Florida Department of Transportation Structures Lab. The five long specimens were tested as follows:

- one specimen under uniaxial compression;
- one specimen under pure flexure; and
- three specimens under combined axial-flexural loads at different levels of axial loads

The three short specimens along with the three control cylinders were tested vertically under axial compression using the 550-kip NITS machine. The control cylinders were sulfur-capped and tested in compression. The load readings at failure were 76.5, 76.4, and 76.4 kip. This resulted in an average concrete strength of 2.7 ksi.

All long and short specimens were grinded at the end sections to ensure plane and smooth loading surfaces. The strain gages were then glued to the specimens. Instrumentation, test procedure, and results are explained below for each specimen.

6.3.1 Short Columns Under Axial Compression

The specimens were instrumented with four PFC rosettes on the four sides at the mid-height. In addition, four LVDT's were used, one on each side, to measure average strains. All specimens were capped by a 3/16" lead plate covering the entire cross-section,

except for SC3, for which the cap only covered the concrete core. The general test setup is shown in Figure 6.9. The loading rate was 0.22 in/min. Concrete cracking could be heard at about 30% of the ultimate load. Resin flow at the comers indicated stress concentration at a load level of about 60-70% of ultimate load. The white bands originated at the comers and propagated towards the sides at a load level of 75-80% of ultimate load. The primary failure mode was in shear. The failed specimens are displayed in Figure 6.10 and Figure 6.11, while the test results are shown in Table 6.1. It is noticed that Specimen SC3 failed at a higher load which may be attributed to the fact that the axial load was not directly applied to the jacket, but rather indirectly through the

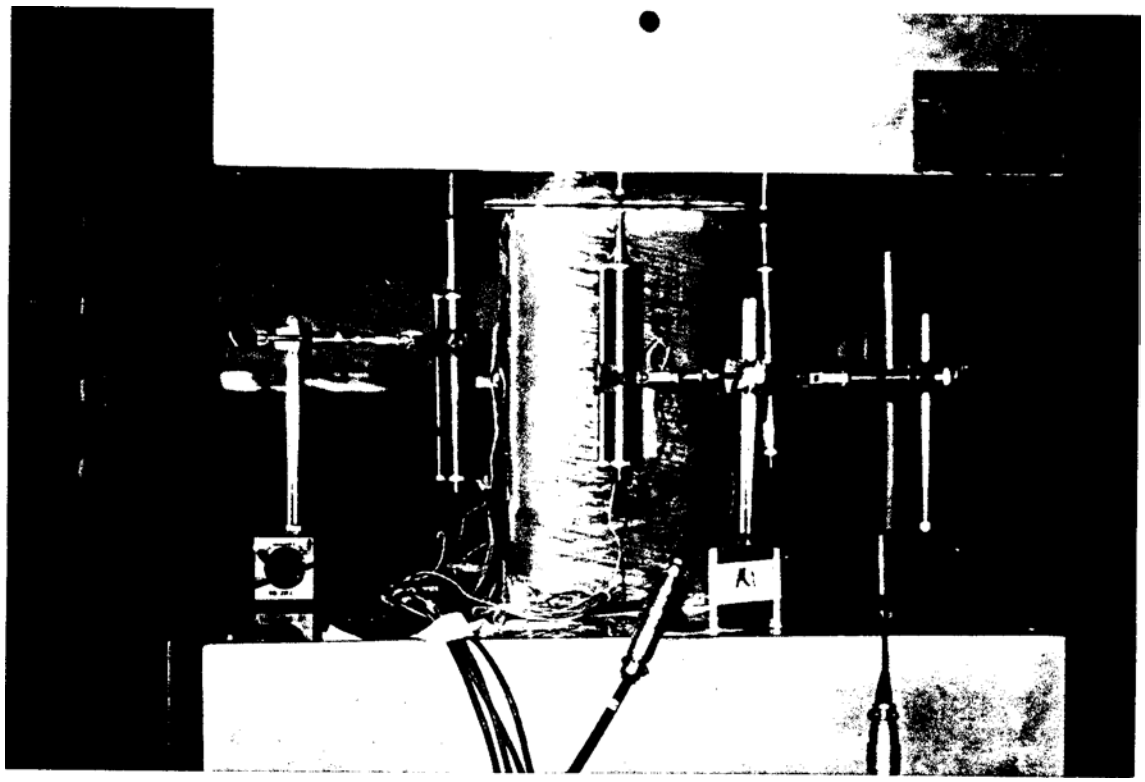

Figure 6.9 Test setup for short columns

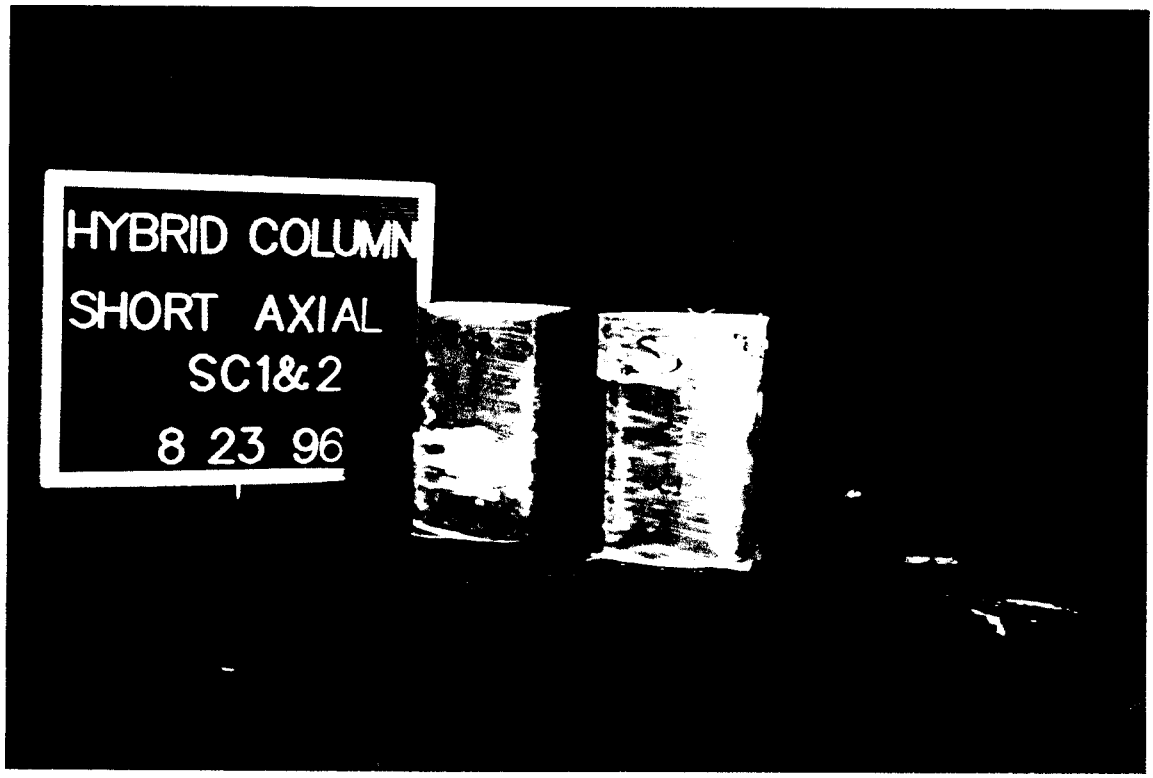

Figure 6.10 Short columns SC1 and SC2 after failure

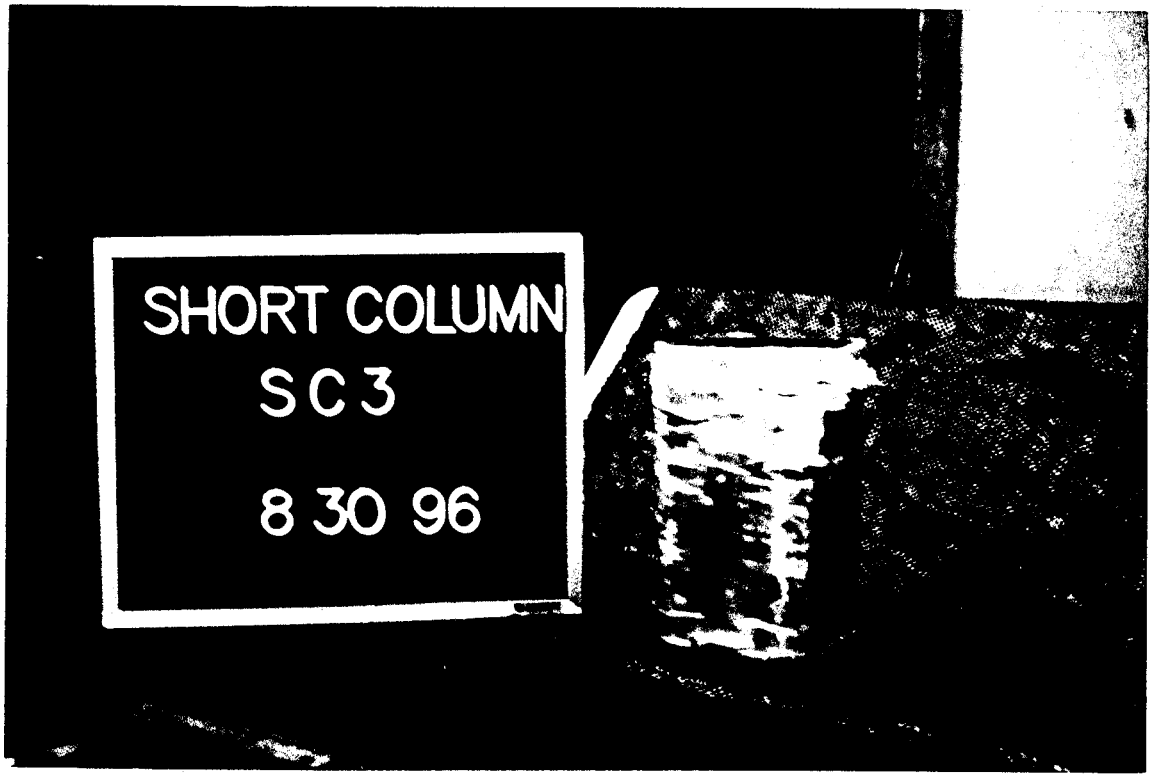

Figure 6.11 Short column SC3 after failure

Table 6.1 Test results for the short columns

Specimen	Height (in)	P_{ult} (kip)	Δ_{ult} (in)	f''_{cu} (ksi)	ϵ_{cu}	Failure Mode
SCI	12.00	278	0.68	5.67	0.053	Shear
SC2	11.75	252	0.57	5.13	0.047	Shear
SC3	12.00	294	0.69	6.00	0.051	Shear
Average		275	0.65	5.60	0.050	

6.3.2 Long Column Under Uniaxial Compression (Specimen C)

The specimen was instrumented by a total of 24 strain gages and two LVDT's. The strain gages were provided at three rings located at the quarter points. Each ring consisted of two 60-mm foil gages (PL-60), longitudinal and transversal, on each of the four sides of the column. Two LVDT's were also positioned at the two ends to monitor the axial shortening of the specimen. Lead plates, $^1/4$" thick, were provided at the two ends to ensure flat loading surfaces. The end pin conditions were simulated with 2" rollers between the end plates. A hydraulic jack was used for applying the axial load along with a 400-kip load cell to monitor the applied load. The specimen was supported on two smooth half-cylinders 48" apart (Figure 6.12).

At an axial load of 109 kip, cracking of the encased concrete could be heard. An uplift at the south support was noticed at 200 kip. This was attributed to possible eccentricity of the applied load. The load was then sustained in order to observe behavior

under sustained high axial loads. By further increasing the load, flow of resin was observed at 205 kip around the mid-span area. At 220 kip, the central longitudinal strain gage at bottom failed and transversal hoop cracks developed starting at the south side. The load reading reached its peak at 230 kip, when it started to drop, indicating loss of strength and an increasing rate of crack opening. The specimen failed with considerable lifting at the south support and noticeable central downward deflection (Figure 6.13). The ultimate axial shortening measured was equal to 1.19". By investigating the failed specimen, it was found that the intensity of the lateral cracks was mainly towards the south end. The major tube fracture was located on the top surface at 21.75" from south end of the specimen (Figure 6.14).

6.3.3 Long Specimen in Pure Flexure (Specimen B)

The specimen was instrumented with a total of nine strain gages (PL-60), which were distributed at the midspan as follows:

- two at the top, one longitudinal and one transversal;
- one longitudinal at the bottom; and
- three longitudinal on each side evenly distributed across the depth.

The specimen was tested under four-point loading with no axial load applied. The span length was 48" and the loading points were at the third points. A hydraulic jack was used to apply the lateral load along with a 50-kip load cell to monitor the applied load. The load was transferred through a 20"-long steel I-beam to the 2"-diameter rollers resting on the top surface of the beam. Epoxy putty was used to level the beam on top of

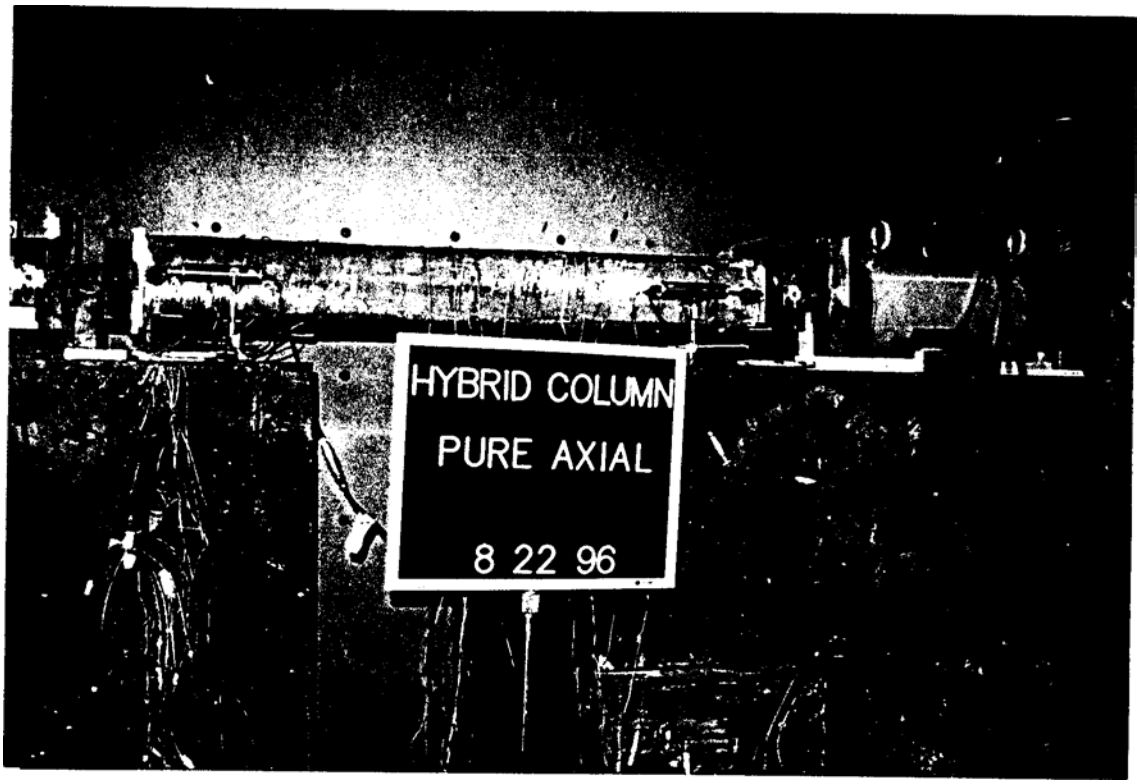

Figure 6.12 Test setup for Specimen C

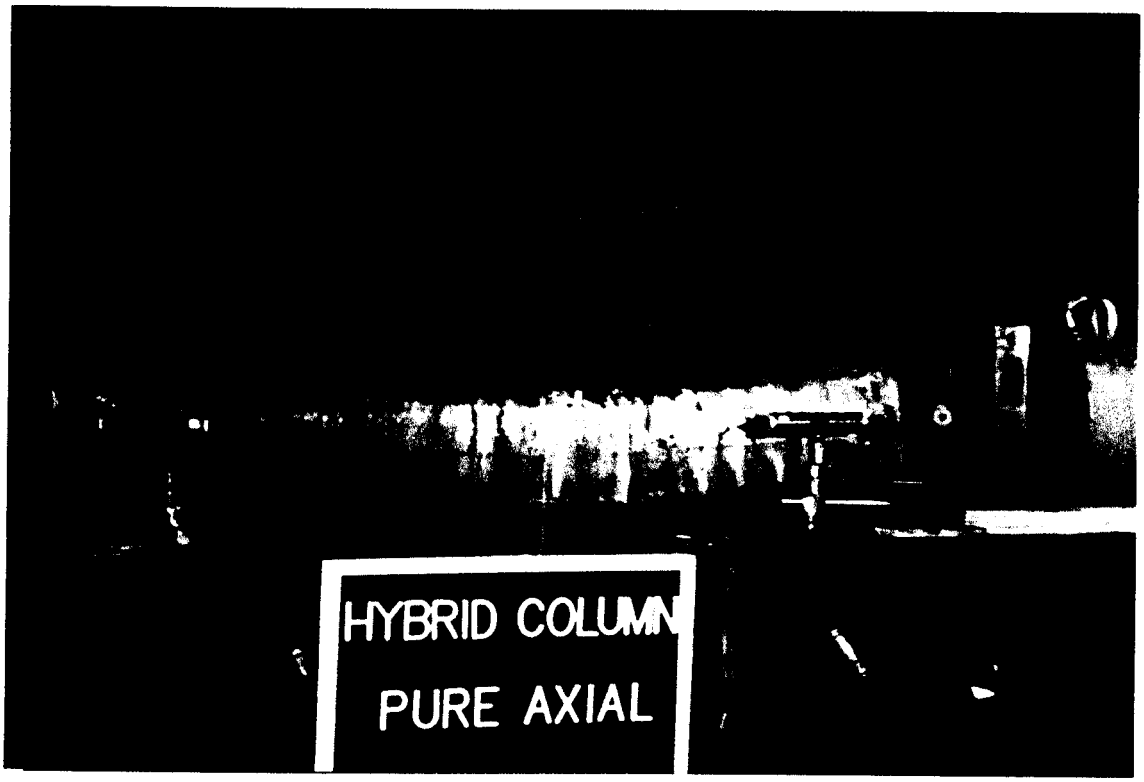

Figure 6.13 Specimen C at failure

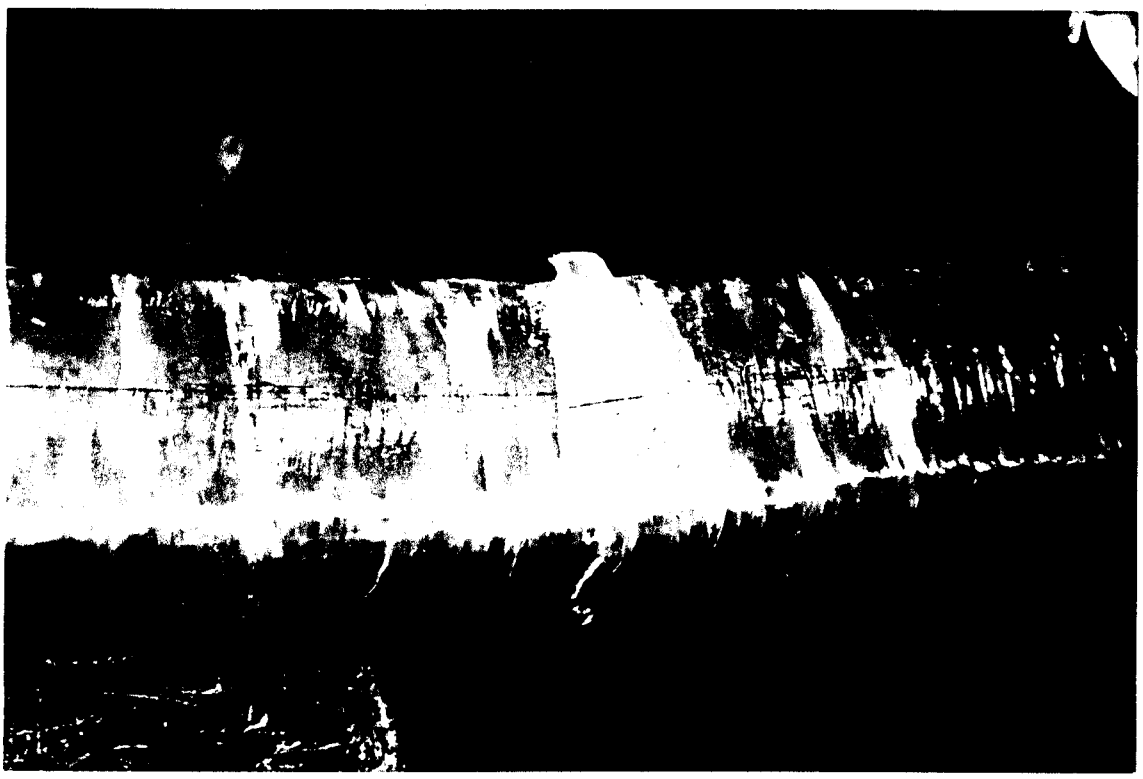

Figure 6.14 Tube fracture on the top surface of Specimen C

the supports and the rollers on top of the beam surface. Vertical deflections were"~ measured at the bottom surface of the beam by means of three LVDT's located underneath the loading points and at the mid-span. A fourth LVDT was used to monitor any vertical movement at the south support. Figure 6.15 displays the above explained test setup. The lateral load was increased gradually. Transverse cracking started to take place at the bottom side of the beam towards the mid-span, and then spread longitudinally. The total lateral load reached a value of 11.6 kip, when a major tension crack took place at mid-span and the load readings started to drop revealing loss of strength. As soon as the load dropped the loading was stopped. The major crack took place at the mid-span on the

bottom side, as it was expected (Figure 6.16). A maximum deflection of 0.8" was recorded at the mid-span.

6.3.4 Beam-Column Tests

According to the previous test results, the axial load capacity, P_o of the CFFT was estimated as 270 kip. Three combined axial-flexural tests were conducted at three different axial load level corresponding to 1/8, $^1/2$, and $^3/0$ of the axial capacity. Each specimen was first loaded axially to the desired load level, which was then maintained while applying a gradually increasing transverse load. Epoxy putty was used to level the beam on top of the supports and the rollers on top of the beam surface, the same way as for Specimen B. The distribution of the strain gages was similar to the pure flexure specimen in addition to 2 longitudinal strain gages at the bottom side at the quarter-span points. A total number of 7 LVDT's were also used as follows:

- three to measure vertical deflection in the region of the middle third similar to the pure flexure test;
- two to measure the axial deformation similar to the case of pure axial; and
- two to measure any uplift at the supports.

The general test setup for the axial-flexural tests is displayed in Figure 6.17.

6.3.4.1 Specimen BC1 (PA =1/8 P.)

The first stage was the gradual application of the axial load. At a load of 22 kip a 0.1" rise at the north support was noticed. Upon reaching the required load of 33.75 kip,

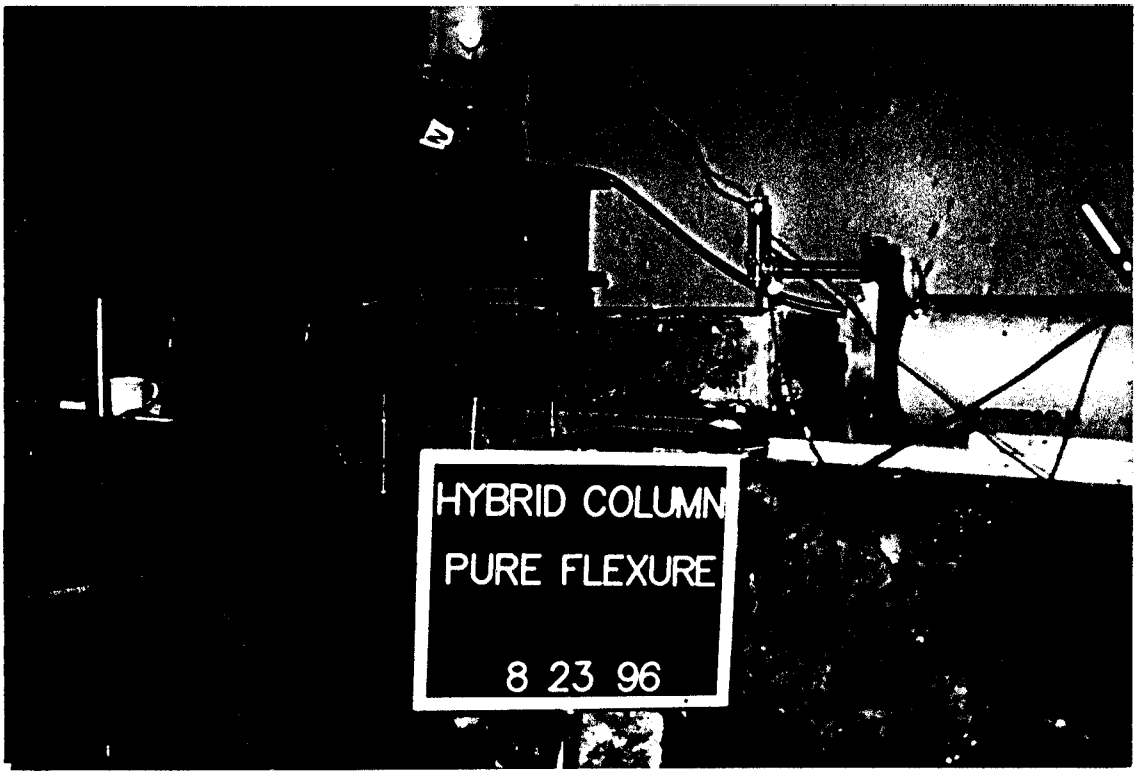

Figure 6.15 Test setup for Specimen B

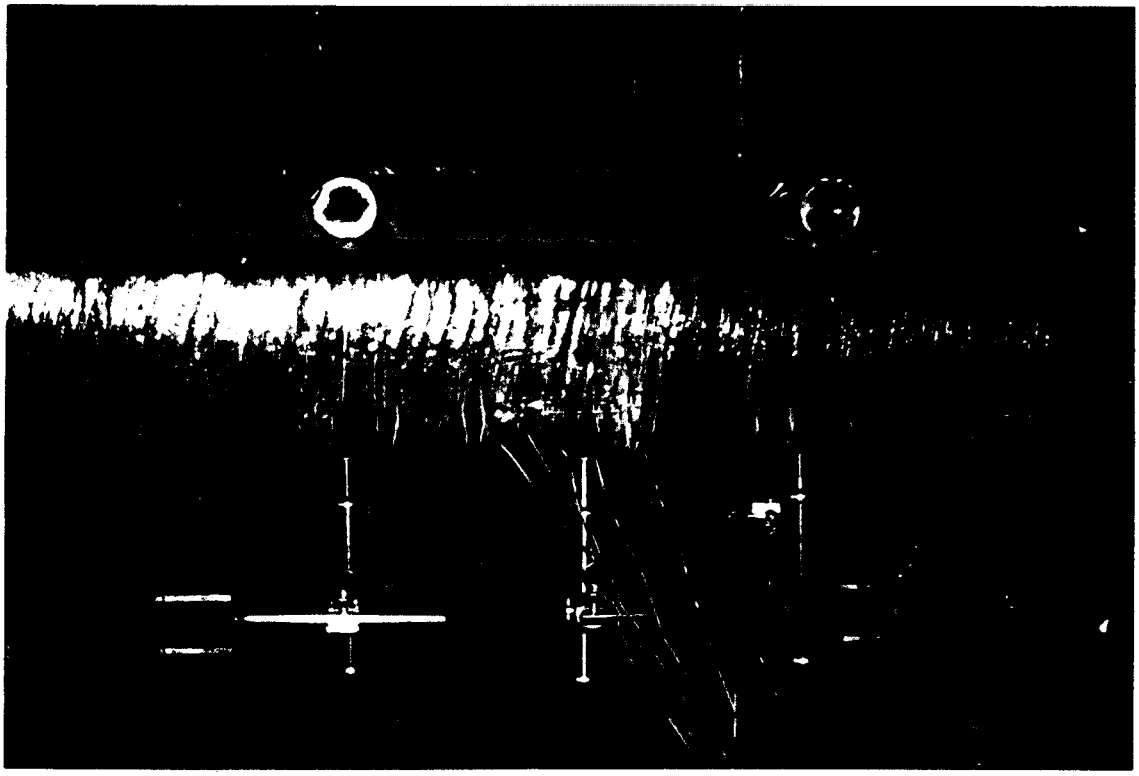

Figure 6.16 Specimen B at failure

the axial load was maintained, after which the transverse load was applied gradually. At a total transverse load of 11.4 kip, concrete cracking could be heard. Tension cracks in the FRP tube at the bottom side were noticed at a load of 17.5 kip. The tension cracks were progressively increasing in intensity and in depth and were manifested by white patches on the tube surface. The maximum lateral load was equal to 23 kip, at which time the load readings started to drop, indicating loss of strength. It was apparent that the failure was attributed to the fracture of the FRP tube in tension. A progressive plastic failure was observed and a maximum mid-span deflection of 1.1" was recorded. A major compression crack took place prior to collapse. Figure 6.18 shows the specimen at failure. The west side of the FRP tube was cut and removed in order to examine the encased concrete after failure. As shown in Figure 6.19, the concrete inside was still intact except for a single major crack across the height at mid-span. This observation revealed the following:

1) The section is under-reinforced in tension;
2) The shear ribs prevented any relative slippage between the tube and the concrete; and
3) The shear ribs contained the concrete in tension and controlled the opening of cracks.

6.3.4.2 **Specimen BC2 (P_A= 1/2 P.)**

During the application of the axial load, some rise at both supports was noticed but no cracking was heard nor observed. The concrete cracking was first heard at a transverse load of 13 kip. At 22 kip, some tension cracks started to show at the bottom side towards the mid-span of the FRP tube. These tension cracks started to increase in depth and in intensity with the increase of load. At a load of 26 kip the transverse load reading began to

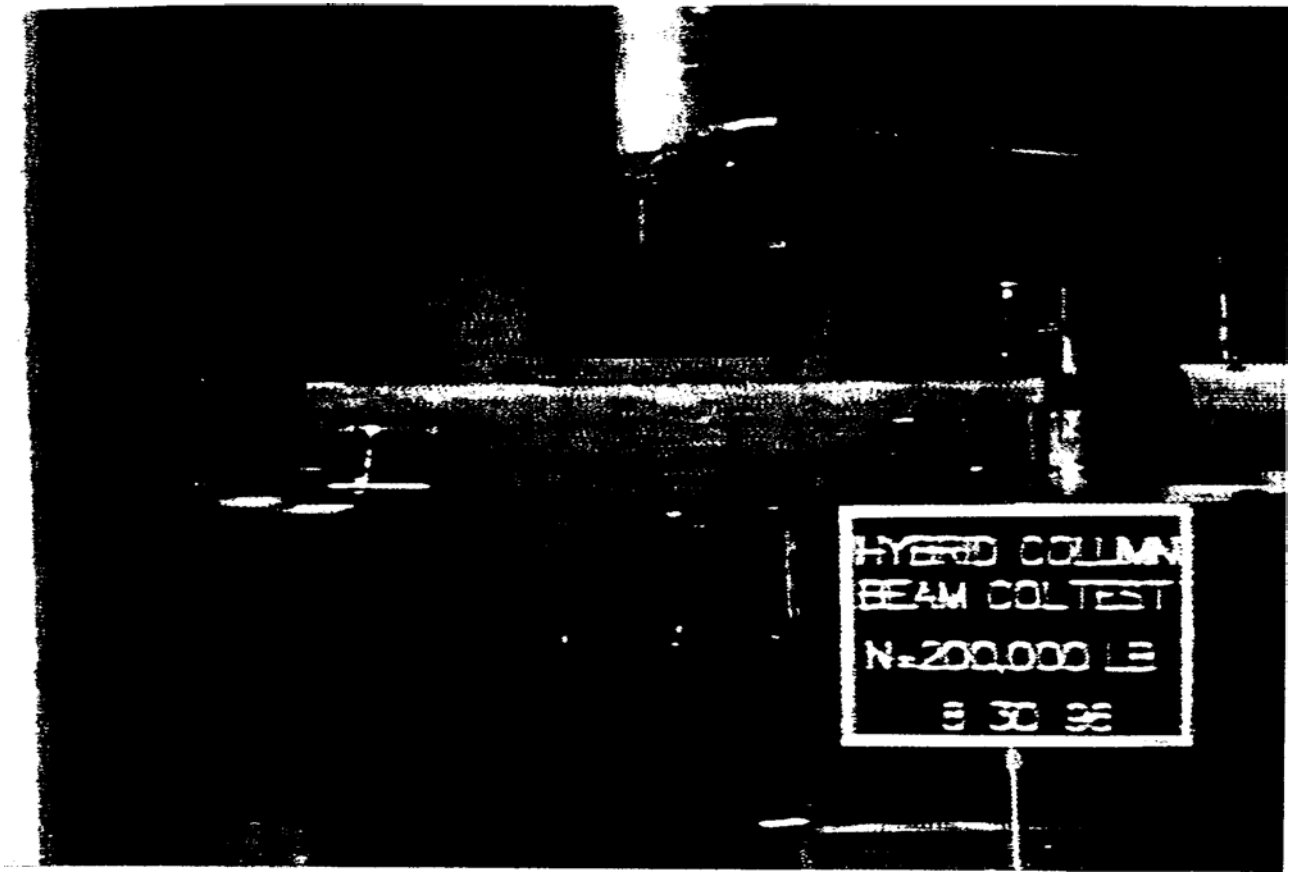

Figure 6.17 General test setup for axial-flexural tests

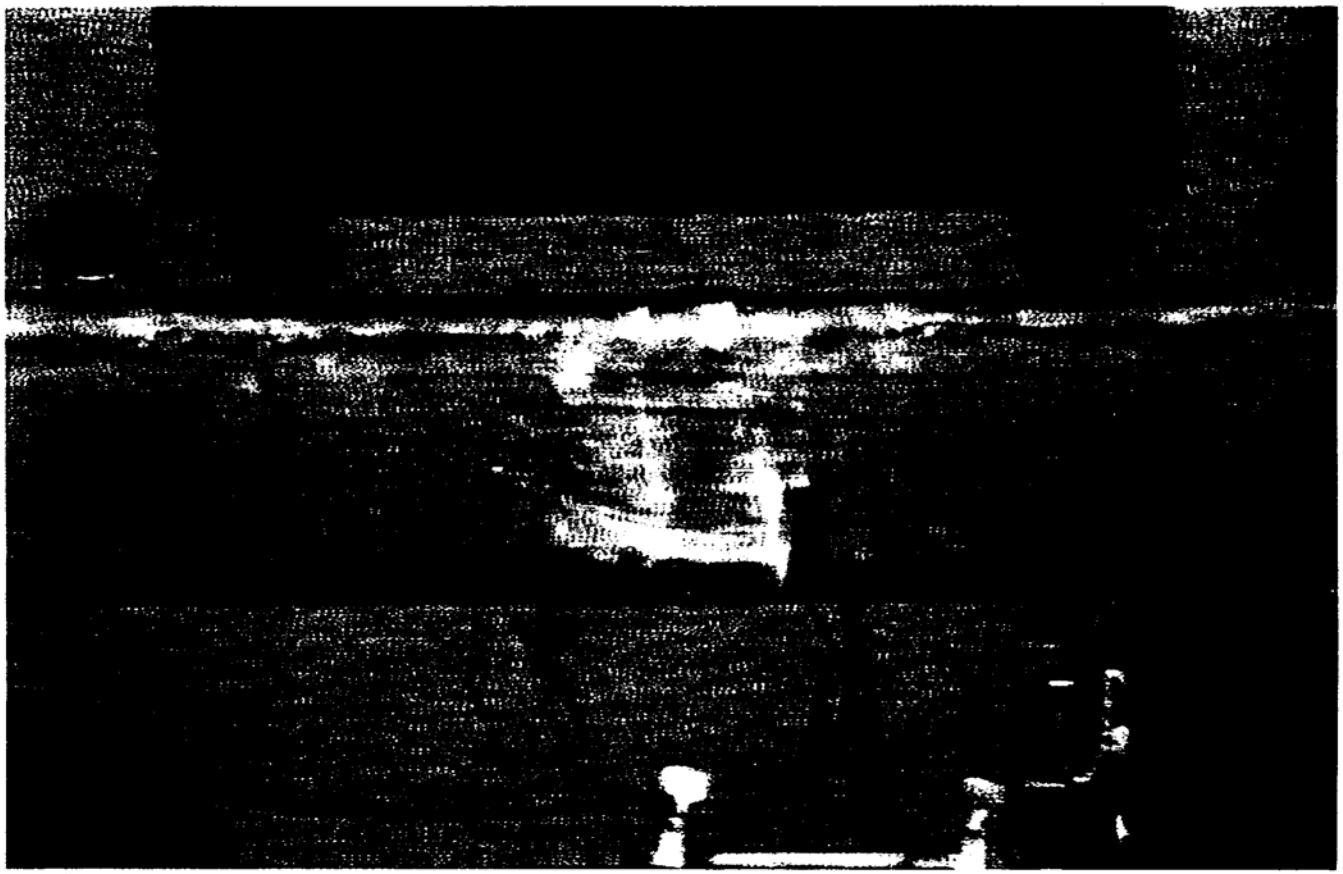

Figure 6.18 Specimen BC1 at failure

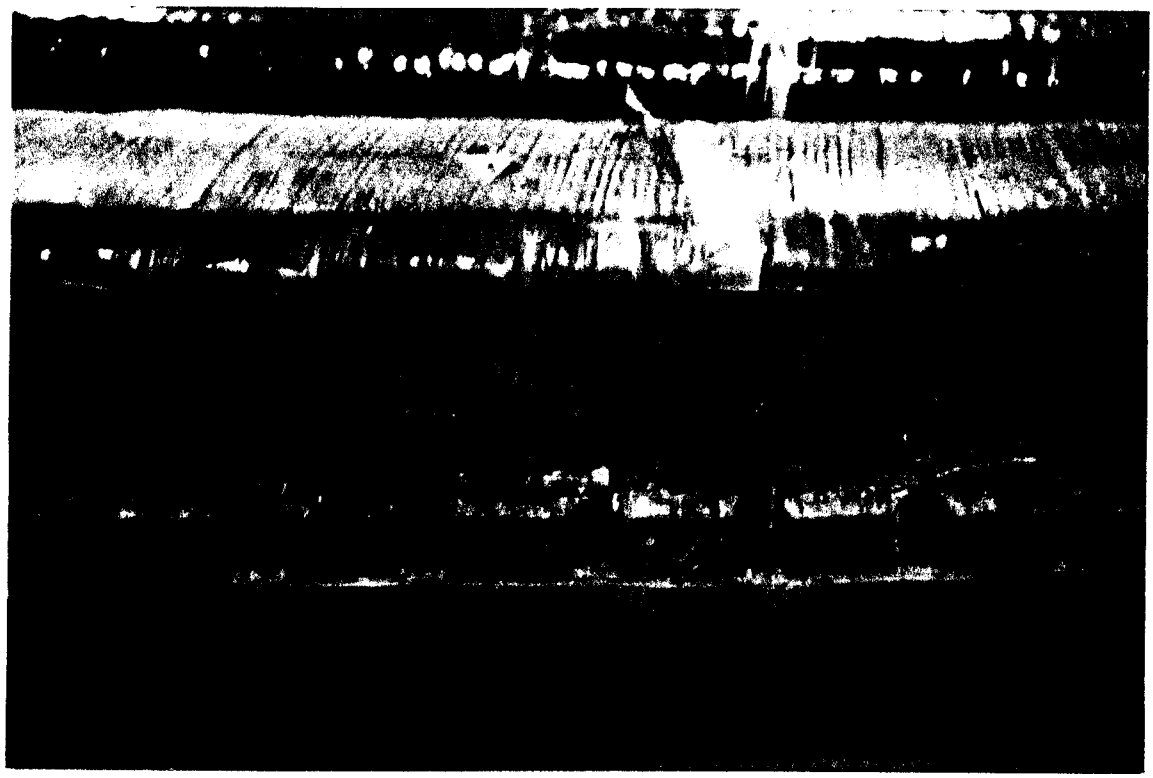

Figure 6.19 Cracking of encased concrete of Specimen BC I

drop, revealing loss of strength. By further increasing the transverse load, cracking of the compression side (top side) started to take place rapidly. As the load reading dropped to 22 kip, three major compressive cracks were already formed. The failure of the specimen was gradual and ductile, even though it was considered a compression failure. The ultimate measured lateral deflection was 1.51", and the uplift at the supports was negligible. Figure 6.20 displays the specimen at failure.

6.3.4.3 Specimen BC3 (P_A = 3/4 P.)

The test procedure was similar to the previous two tests, however due to the high initial compression concrete cracking took place during the first phase at an axial load of

107 kip. The cracking of the FRP tube was initiated on the compression side (top side) at a transverse load of 10 kip.At a load of 11 kip, the section began to lose its strength, and compression cracks began to spread towards the tension side. A progressive and ductile compression failure took place along with an ultimate recorded lateral deflection of 2.1". The measured rise at the south support at failure was 0.7". Figure 6.21 displays the specimen at failure.

A summary of the test results of the long specimens is presented in Table 6.2.

6.4 DISCUSSION OF TEST RESULTS

6.4.1 Short Columns Under Axial Compression

The stress-strain plots for the three short specimens are plotted in Figure 6.22. The curves start with a linear portion up to a stress in the vicinity of f'_{co}, where some softening takes place. For two of the three specimens, a short descending branch exists prior to the failure point. It is apparent that the second slope for Specimen SC3 is larger compared to the other two specimens. This may be attributed to the fact that the load was mainly applied to the concrete core, which is much *stiffer* than the FRP tube in the longitudinal direction. However, this *stiffer* response softens due to the excessive cracking of the concrete core near the failure point.

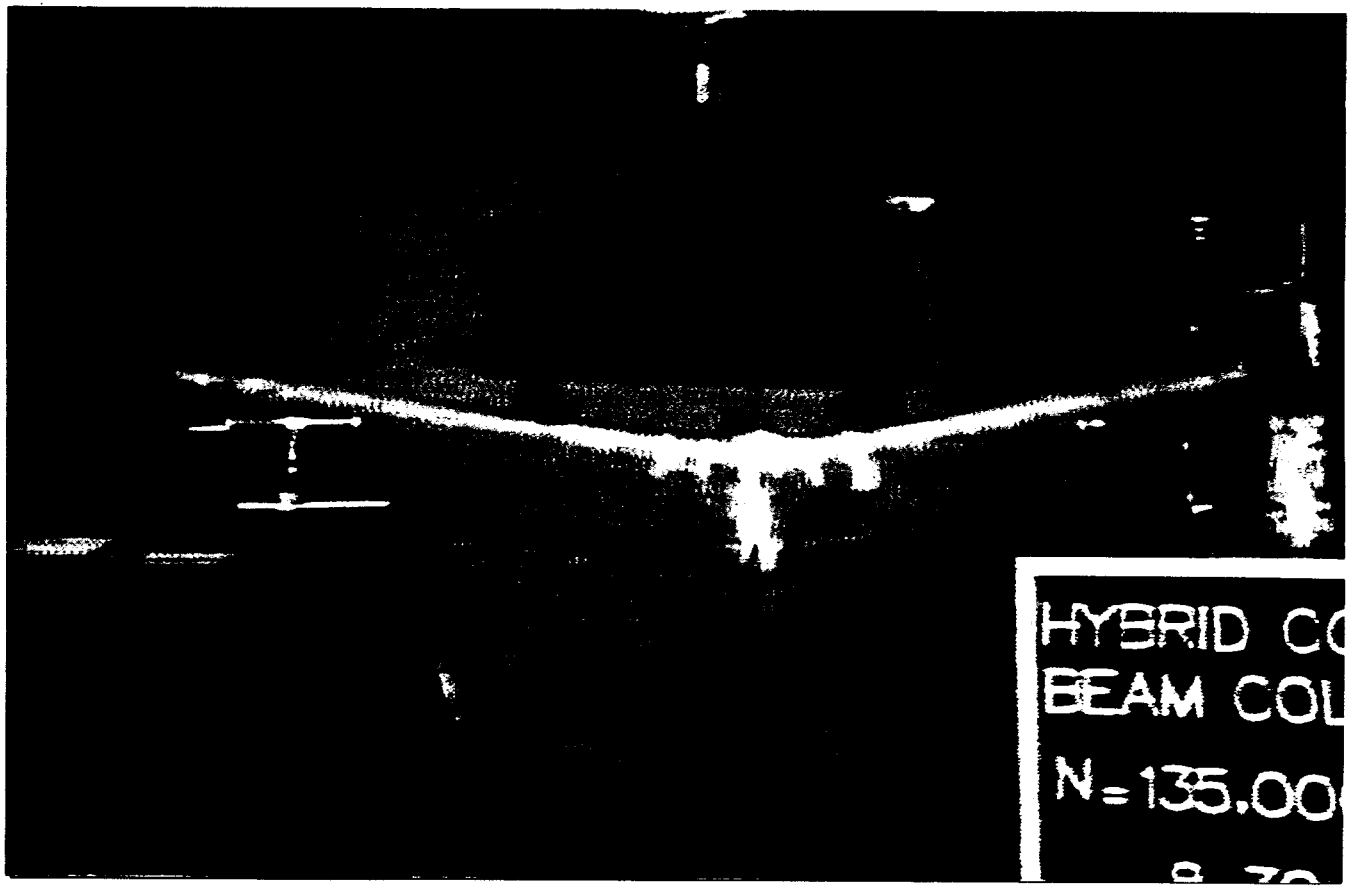

Figure 6.20 Specimen BC2 at failure

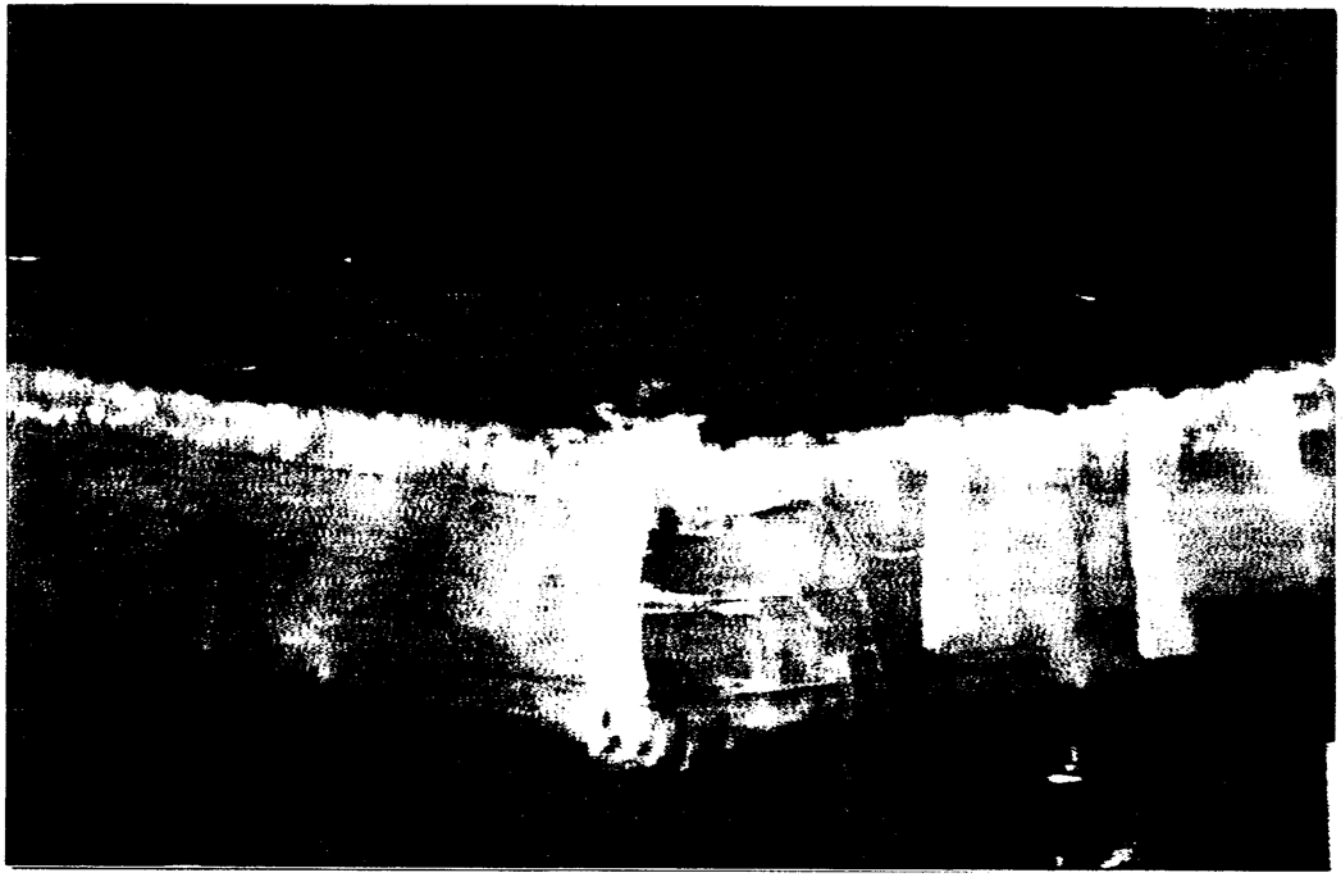

Figure 6.21 Specimen BC3 at failure

Table 6.2 Test results for the long specimens

Specimen	Length	Axial Load* (kip)	Max Lateral Load. (kip)	Axial** Deflection (in)	Lateral** Deflection. (in)
C	51.88	230.62	-	1.19	-
B	-	-	11.58	-	0.80
BC1	51.94	29.77	23.11	0.13	1.10
BC2	51.13	131.96	26.29	0.90	1.51
BC3	52.06	198.23	12.32	1.30	2.10

This value represents the actual axial load (P_A).,,,,, at the peak lateral load (PL),,,ak At ultimate

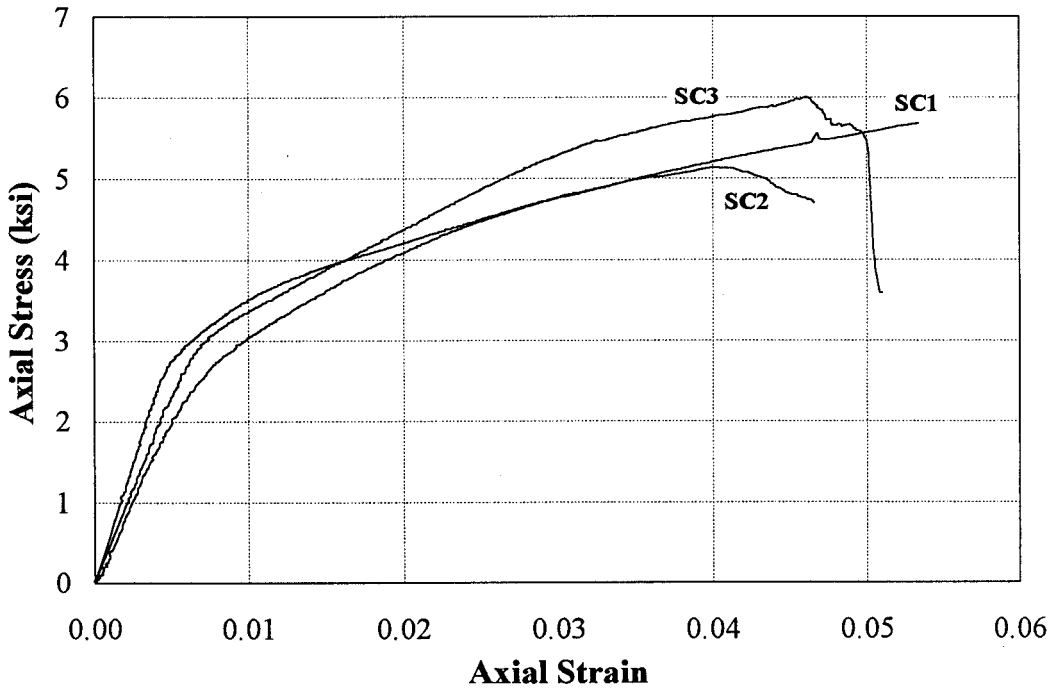

Figure 6.22 Stress-strain curves for the short columns

An interesting comparison is presented in Figure 6.23 between the normalized stress-strain responses of the circular and the square CFFT. For this comparison, the stress-strain curves of Specimens DB31 and SCI were chosen, to represent the circular and the square CFFT, respectively. Table 6.3 summarizes the description of the two specimens. Both responses are bilinear with a transitional curvature connecting the two lines. It is apparent that the slopes of the square specimen are lower than their circular

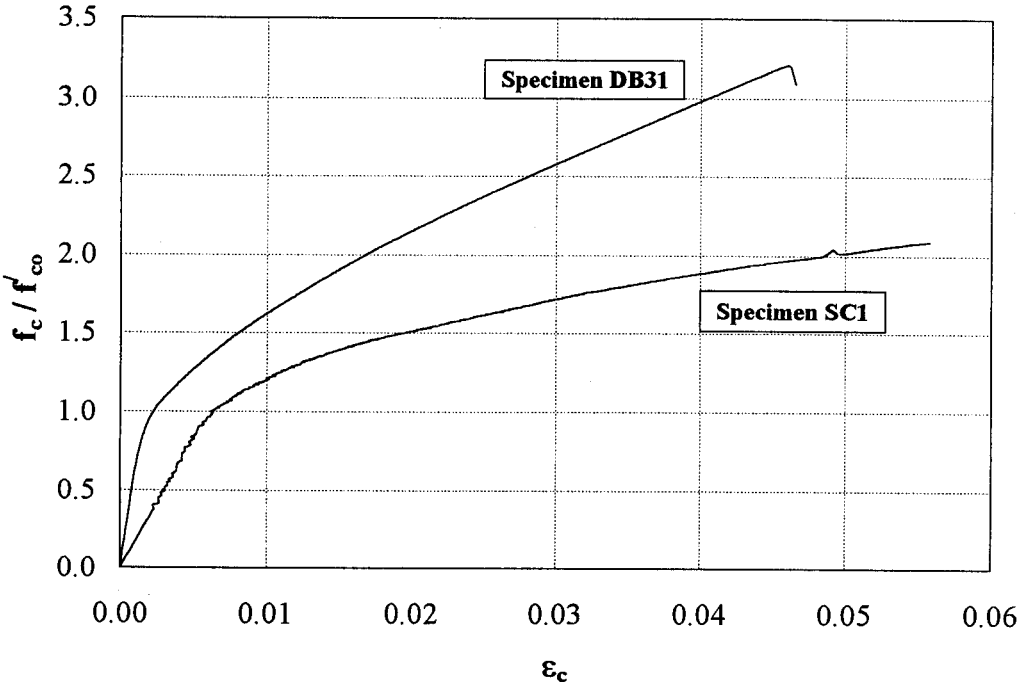

Figure 6.23 Comparison of the stress-strain responses of the circular and square CFFT

counterparts. The main reason for the lower first slope for square tubes is the low longitudinal stiffness of the tube. Due to the existing bond between concrete and FRP,

both components take the axial loads. This results in a slope lower than the initial modulus of concrete, unlike the circular unbonded specimen, for which the first slope is equivalent to the initial modulus of concrete core.

Table 6.3 Descriptions of Specimens DB31 and SCI.

	Specimen DB31	**Specimen SCI**
Shape	circular	square
Size	6" x 12"	7" x 7" x 12"
No of FRP plies	14	15
Winding angle	±75°	±75°
f'_{co}	3.9	2.72
Bond	unbonded	bonded

Moreover, the lower second slope of the square specimen is mainly attributed to the low confinement effectiveness of square FRP-confined concrete cross-sections. This topic was investigated by Rochette (1996), who indicated that the corner radius plays a significant role in the confinement of non-circular cross-sections, along with the tube wall thickness. His findings were further developed by Mirmiran (1997b) and Pico (1997), who expressed the confinement effectiveness of both circular and square sections as a function of the following parameter: $\frac{2R}{D} = \frac{f_r}{f'_{co}}$; where, R is the comer radius, D is the inside

dimension of the tube, f,', is the compressive strength of the concrete core, and f is the ultimate confining pressure given by:

$$f_r = \frac{2 f_j t_j}{D} \tag{6.1}$$

where, f; and t; are the hoop strength and the thickness of the FRP jacket, respectively. They proposed a logarithmic relationship for the ratio of the ultimate and the peak stress levels $\left(\frac{f'_{cu}}{f'_{cc}}\right)$ as a measure of the confinement effectiveness, in the following form:

$$\frac{f'_{cu}}{f'_{cc}} = 0.1693 Ln\left[\left(\frac{2R}{D}\right)\frac{f_r}{f'_{co}}\right] + 1.2855 \tag{6.2}$$

where $\left(\frac{f'_{cu}}{f'_{cc}}\right)$ is equal to unity for responses with ascending second slope, as it is the case for the specimens tested in this study.

Furthermore, another reason for the lower second slope of the square specimen is the bi-axial state of stress, which the FRP tube is subjected to. Since the tube participates in carrying the axial load, it is subjected to compressive longitudinal stresses. In addition, the tube undergoes lateral tensile strains due to expansion of the encased concrete. This state of stress results in a reduced hoop strength and a lower confinement effectiveness for square sections.

6.4.2 Specimen C

The load readings are plotted versus the various longitudinal and transversal strain readings in order to investigate the behavior of the hybrid column under study. In Figures 6.24-6.26 the axial load is plotted versus longitudinal strains at north, mid-span, and south sides, respectively. The trend is mainly bi-linear up to the peak load. The repetitive drops in the load is mainly due to sustaining the applied load pressure. Some load eccentricity is evident in the plots at the north and south sides. In order to further investigate the deformations of the column, the load-axial strain relations were plotted on all four sides (Figures 6.27-6.30). These plots further indicate the presence of some eccentricity, which explains the bending occurred at failure (see Figure 6.13).

In Figure 6.31, the load-deformation curve of the column is shown. By dividing the ultimate deformation by the total length it results in an ultimate strain of about 2.3% compared to 5.6% for the short columns. Thus, it is clear that a premature failure took place due to some eccentricity of the load, which in turn generated some bending. Moreover, reviewing the hoop strain readings at the top surface, it became clear that the maximum ultimate tensile hoop strain is equal to 0.072 as compared to 0.12 for the cylindrical specimens. This shows that the cylindrical specimens have larger expansion in the hoop direction, and hence activate a higher level of confinement.

6.4.3 Specimen B

One of the main observations is the large deflections at failure, as it is apparent from the load-deflection plot (Figure 6.32). This issue is discussed in detail in Chapter 7.

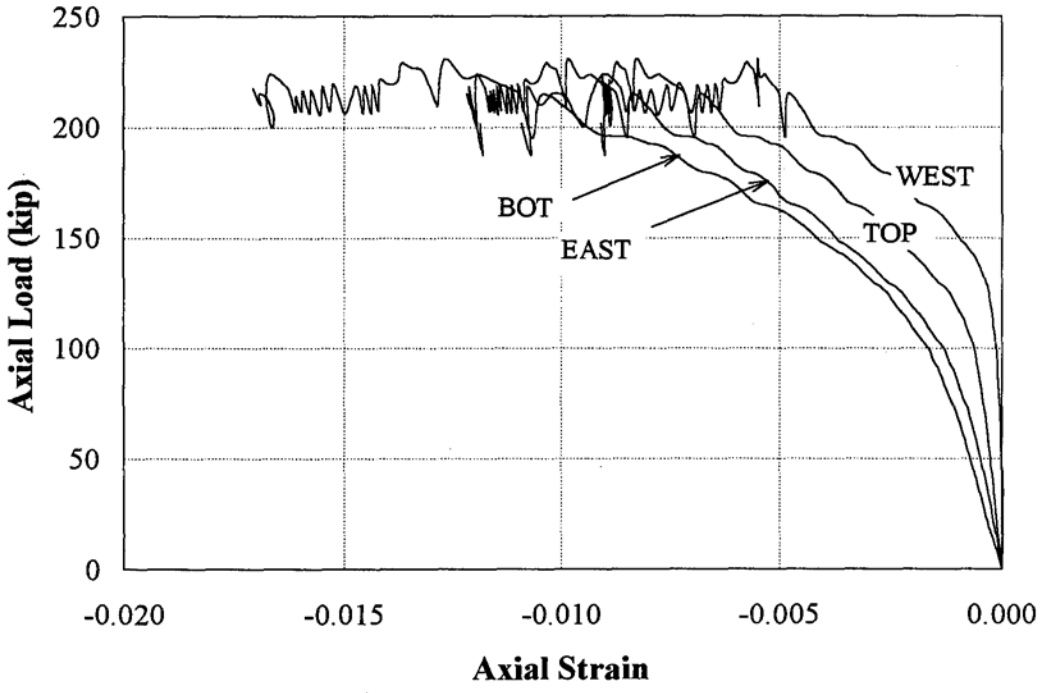

Figure 6.24 Load-strain plots for strain gage readings at north side of Specimen C

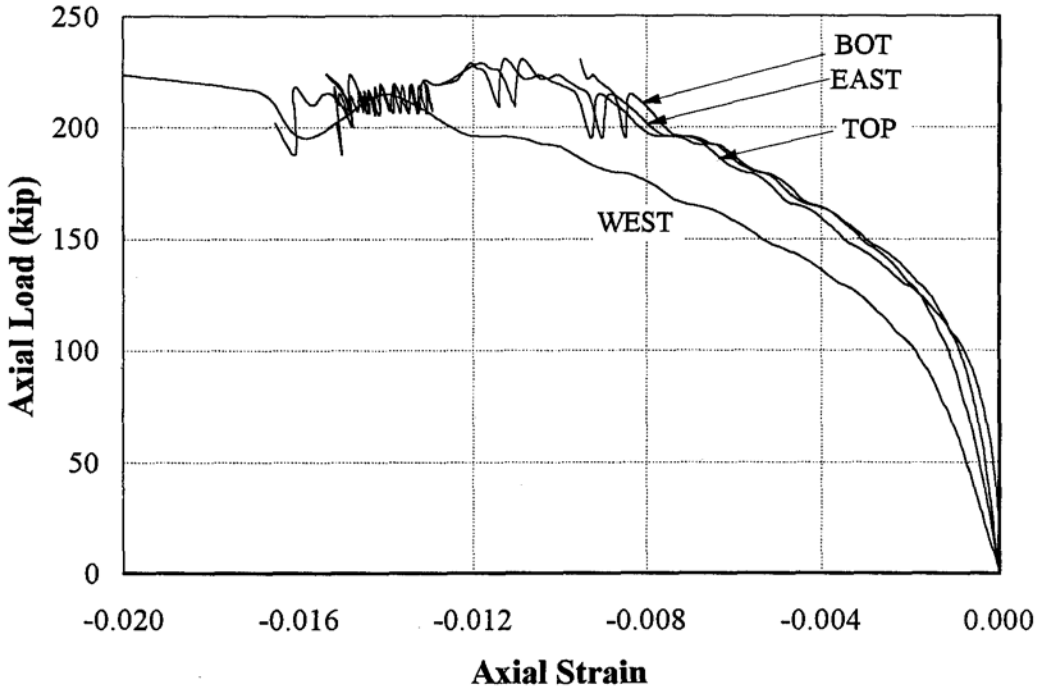

Figure 6.25 Load-strain plots for strain gage readings at mid-span of Specimen C

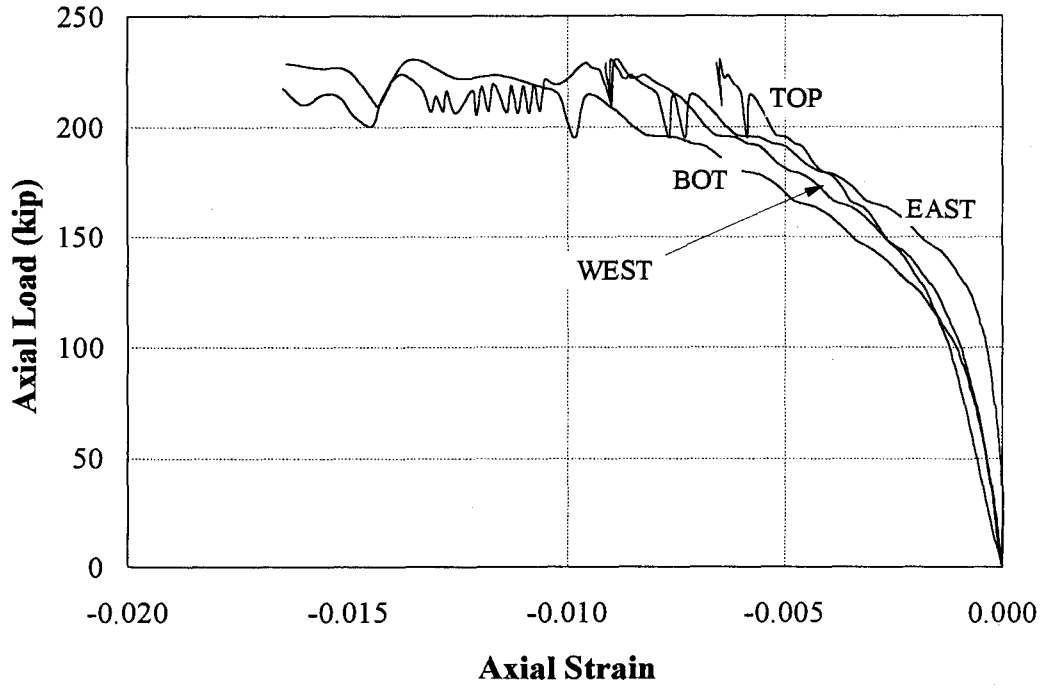

Figure 6.26 Load-strain plots for strain gage readings at south side of Specimen C

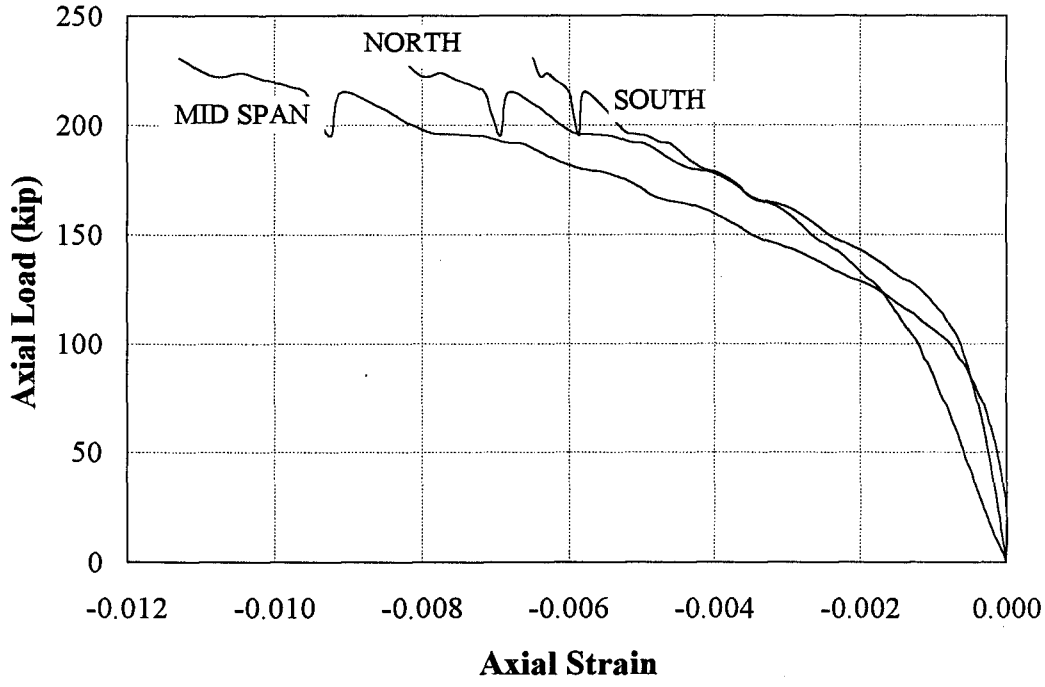

Figure 6.27 Load-strain plots for strain gage readings along top side of Specimen C

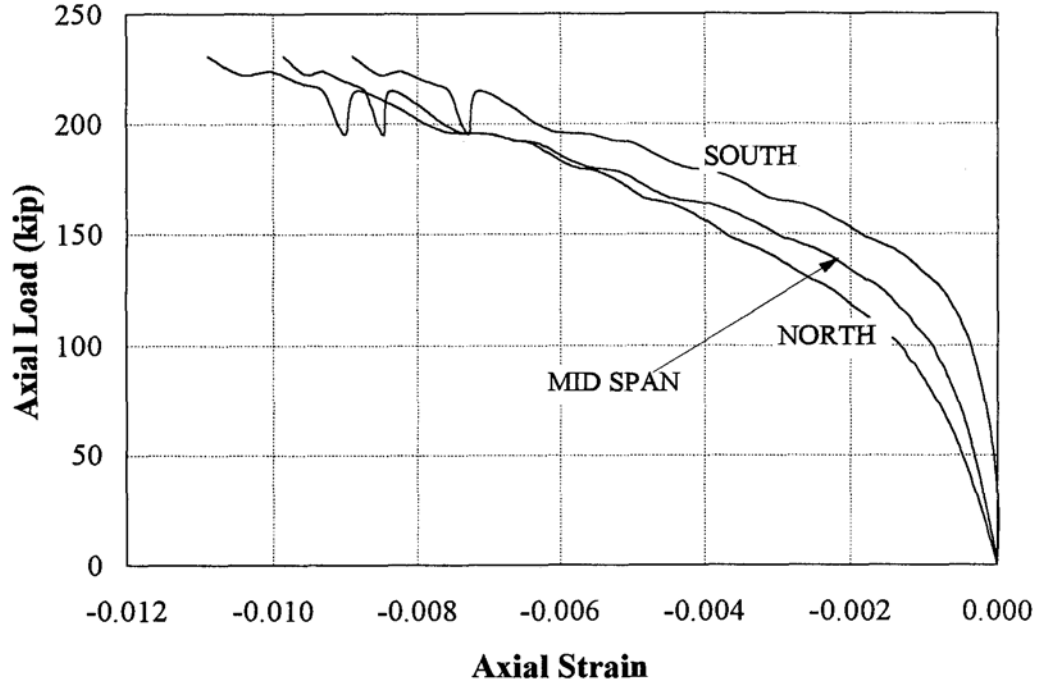

Figure 6.28 Load-strain plots for strain gage readings along east side of Specimen C

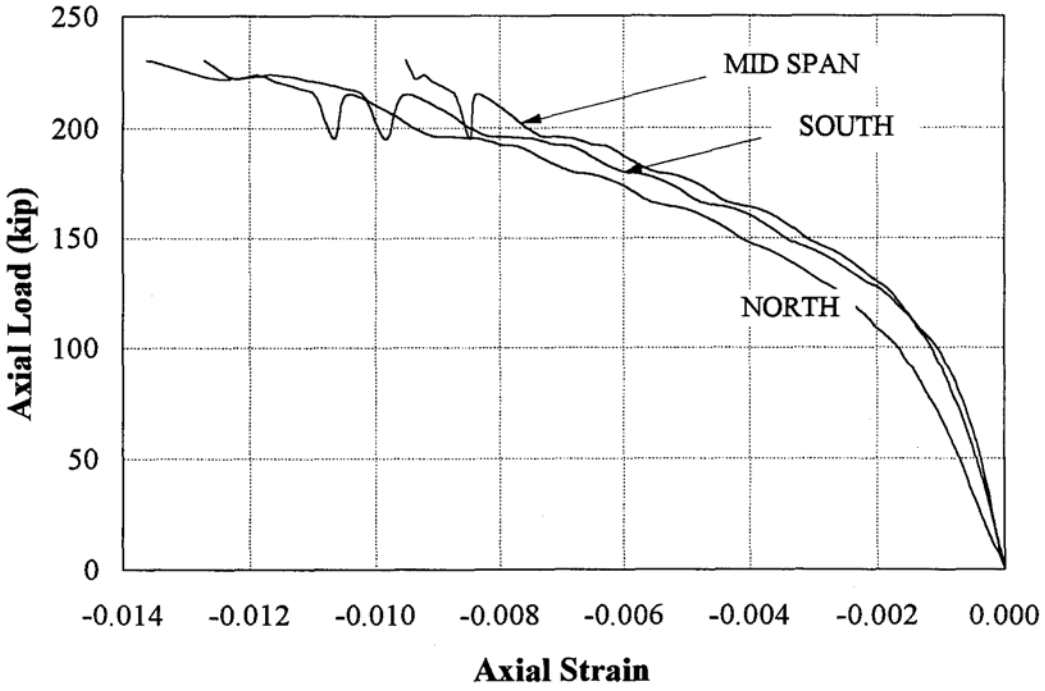

Figure 6.29 Load-strain plots for strain gage readings along bottom side of Specimen C

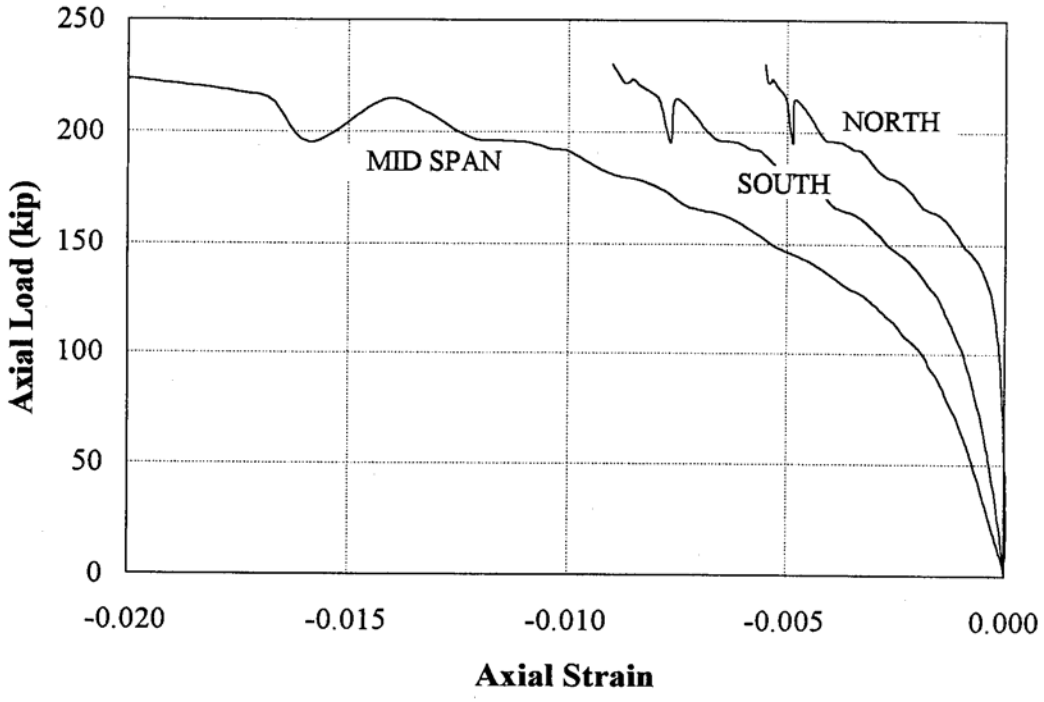

Figure 6.30 Load-strain plots for strain gage readings along west side of Specimen C

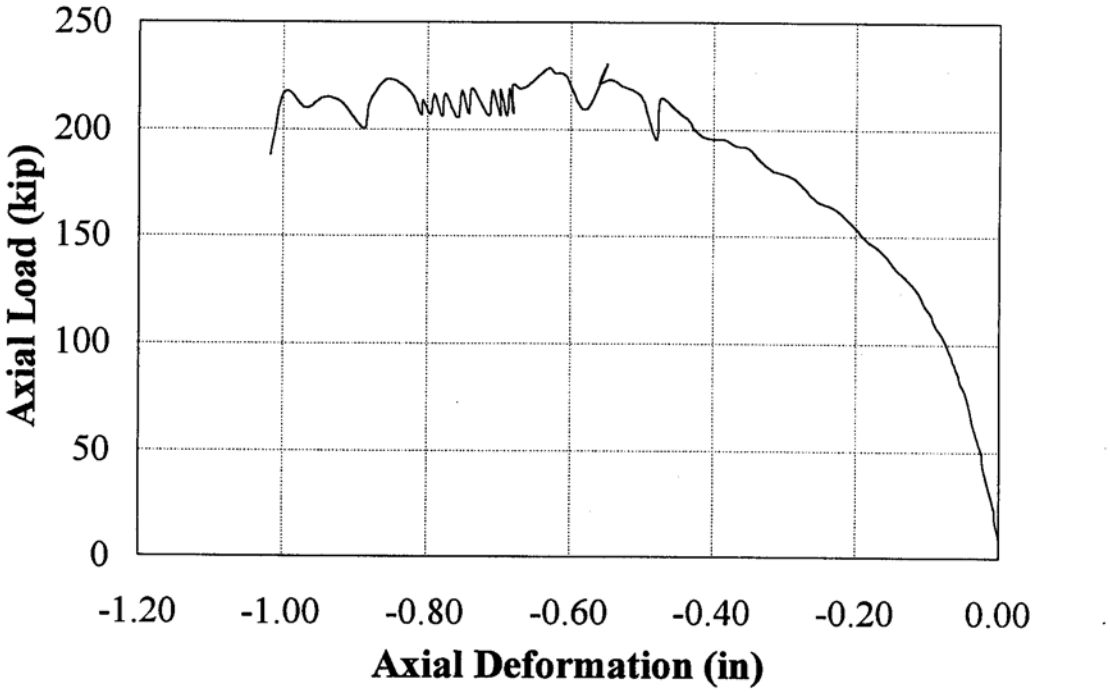

Figure 6.31 Axial deformations of Specimen C

The moment-curvature relationship is plotted in Figure 6.33, in which the curvatures are calculated simply by dividing the difference between the top and bottom strains by the depth of the section. The plot is discontinued at the failure point of the bottom strain gage.

The load-strain plot is displayed in Figure 6.34. The strain values are consistent and show good correlation between the readings of both the western and eastern side of the section. The top strain at peak load is equal to 0.00344, which is approximately equal to the ultimate compressive strain of plain concrete. Thus, the developed compressive force in the section insufficient to activate the hoop confinement. This is further verified

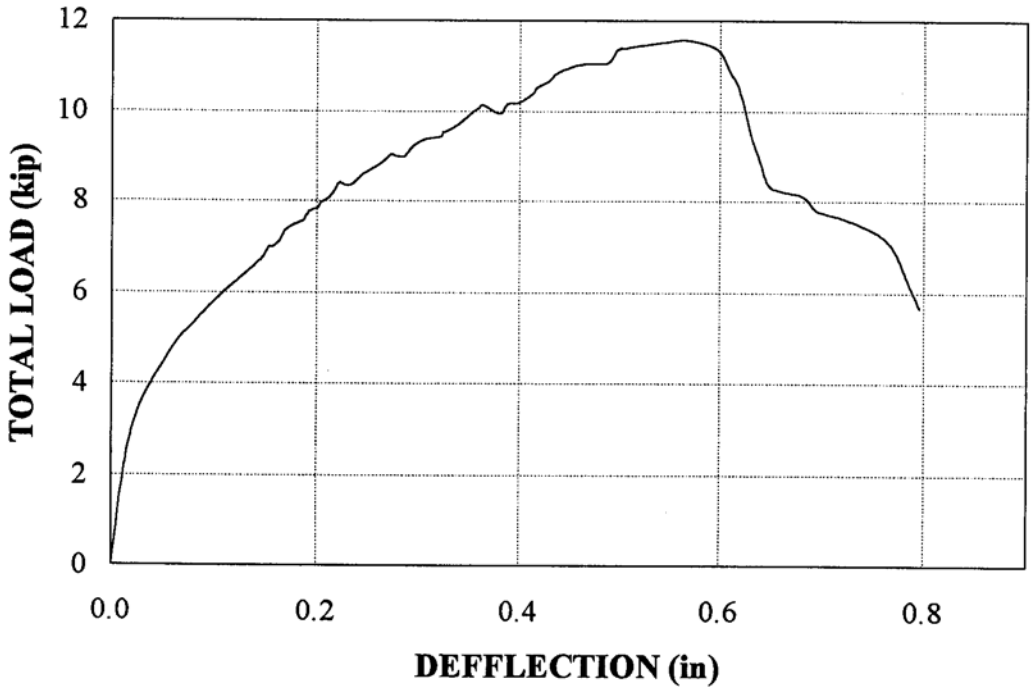

Figure 6.32 Load-deflection plot for Specimen B

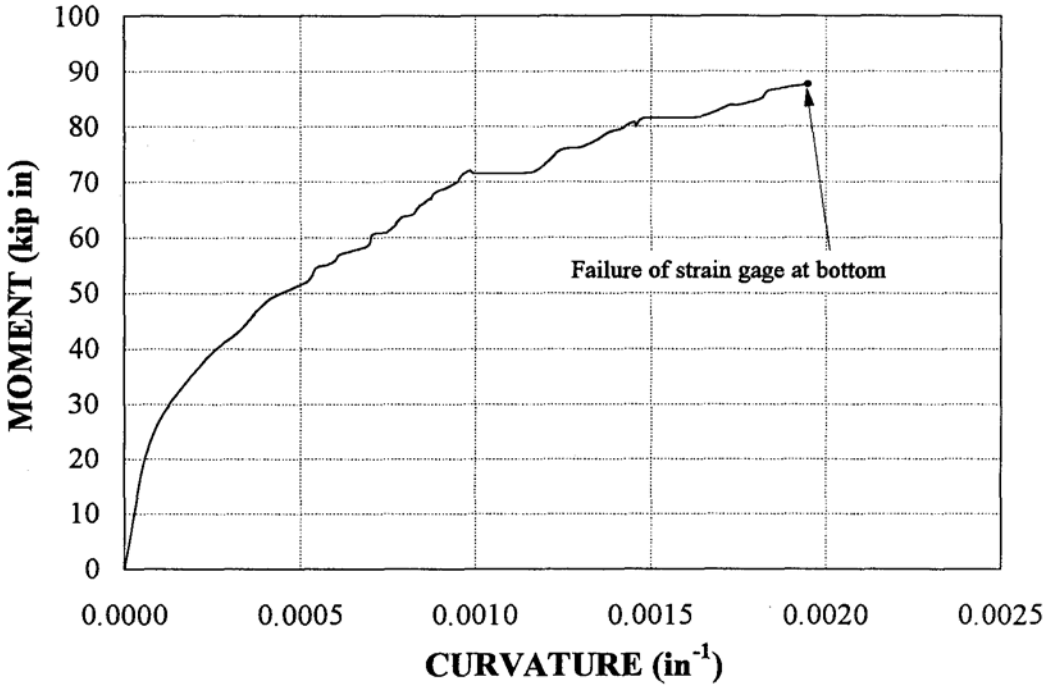

Figure 6.33 Moment-curvature plot for Specimen B

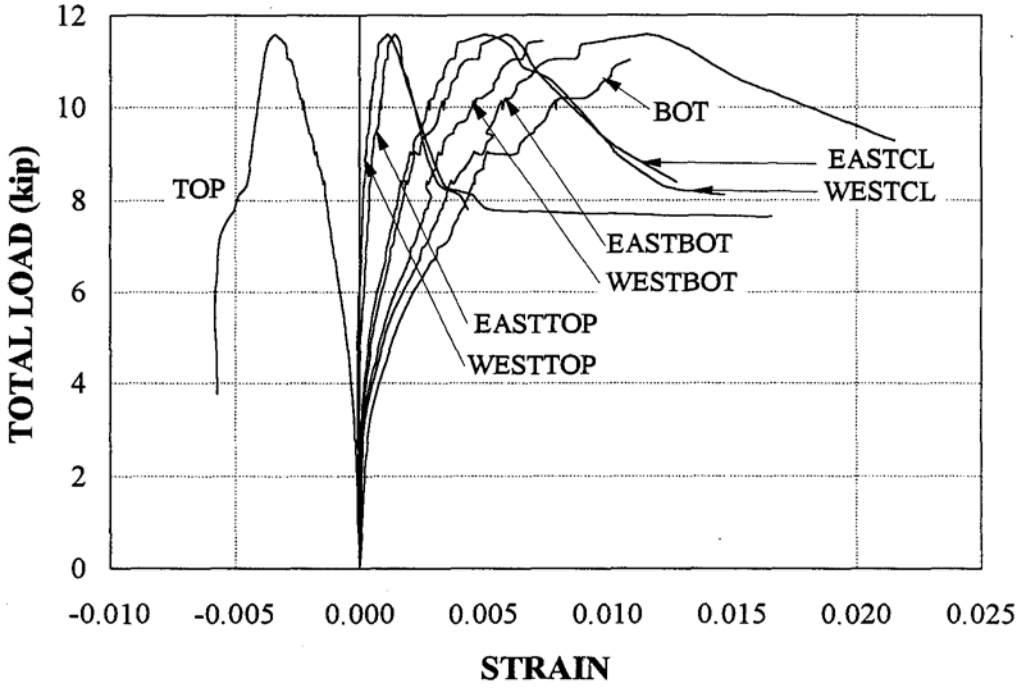

Figure 6.34 Load-strain plots for Specimen B

6.4.4 Specimen BC1

As it was explained earlier, the specimen was subjected to a gradually increasing axial load before applying the lateral load. In Figure 6.35, the axial load is plotted against the longitudinal strains at the mid-span section. By studying the plot, it could be inferred that while applying the axial load some bending took place about the vertical axis, which resulted in higher compressive strains on the east side as compared to the west side. On the other hand, the difference between the top and bottom strain readings is not significant, indicating negligible initial bending about the horizontal axis.

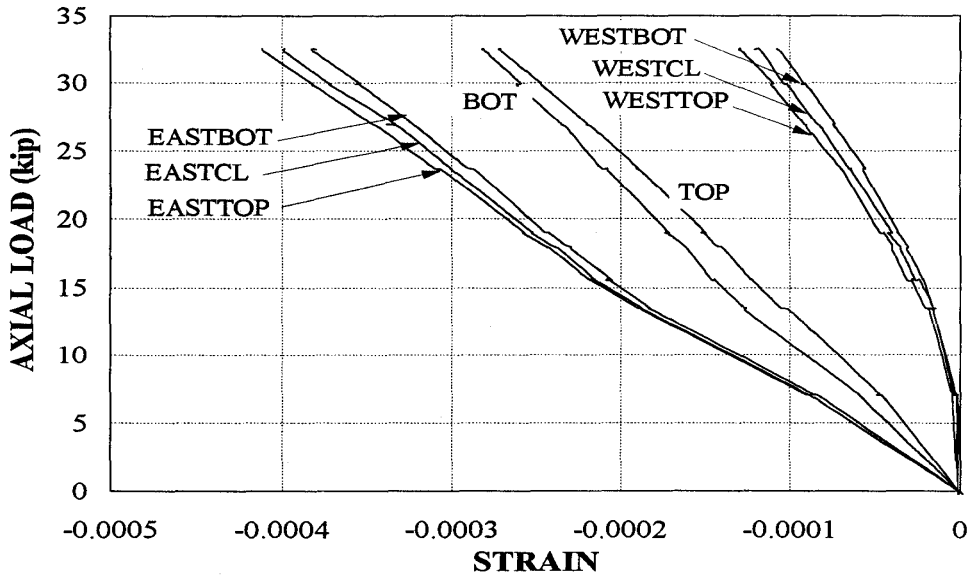

Figure 6.35 Axial load-strain plots for Specimen BC1

The lateral load-deflection relationship is plotted in Figure 6.36. Gradual post peak drop in the load, and the large ultimate deflections are evident. In Figure 6.37, the lateral

load is plotted versus the longitudinal strains at the mid-span section. An ultimate compressive strain of 0.0176 at the top surface is recorded. Since this strain value is much higher than the ultimate compressive strain of plain concrete, some confinement and crack containment are present. However, the hoop strain on the top surface is 0.0034 at failure, indicating little expansion in that direction. Therefore, for this specimen crack containment rather than confinement can be assumed.

The bending moment is plotted versus the vertical deflection as well as the vertical curvature at the mid-span, as shown in Figure 6.38. Three curves are plotted:

- The primary moment M_1 produced by the lateral loads;
- The secondary moment M_2, which represents the P-Δ effect due to the large transverse deformations at the mid-span; and
- The total moment MTOT, which is the actual moment capacity of the section.

The ratio of M_2 to MTOT is almost 12% for this case of loading.

6.4.5 Specimen BC2

The variation of the longitudinal strains at the mid-span due to the application of the axial load is presented in Figure 6.39. It is evident that a certain diagonal eccentricity of the axial load took place due to the variability of the sectional dimensions along the length of the member. This resulted in a higher compression towards the west-top corner and a low compression at the opposite east-bottom corner. Figure 6.40 shows the lateral load-strain curves. Again, the effect of the initial bi-axial bending is apparent.

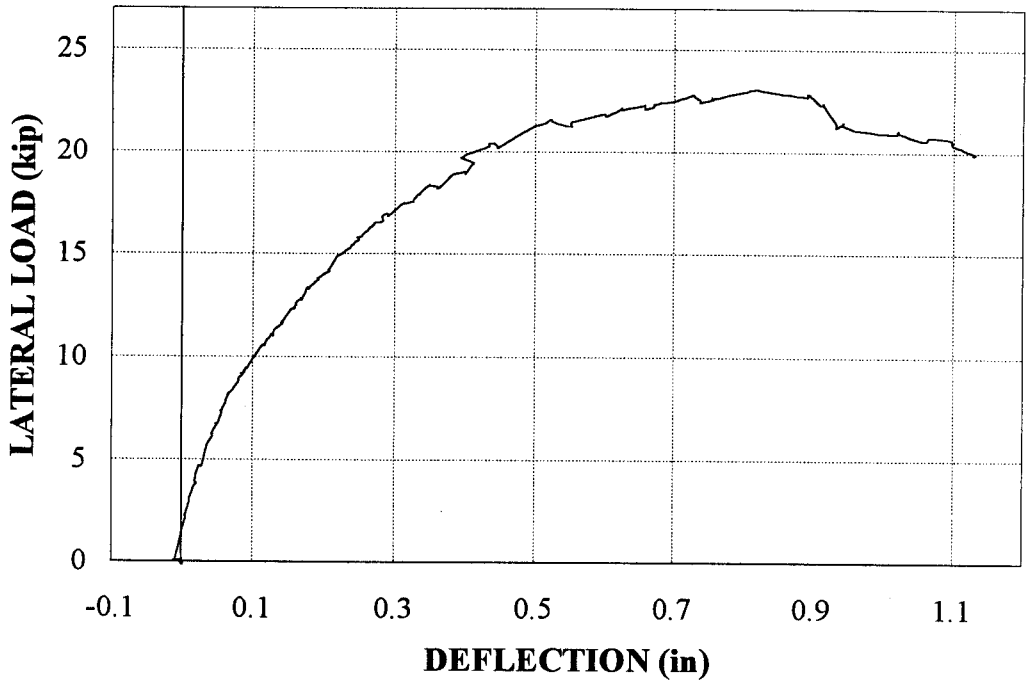

Figure 6.36 Load-deflection plot for Specimen BC1

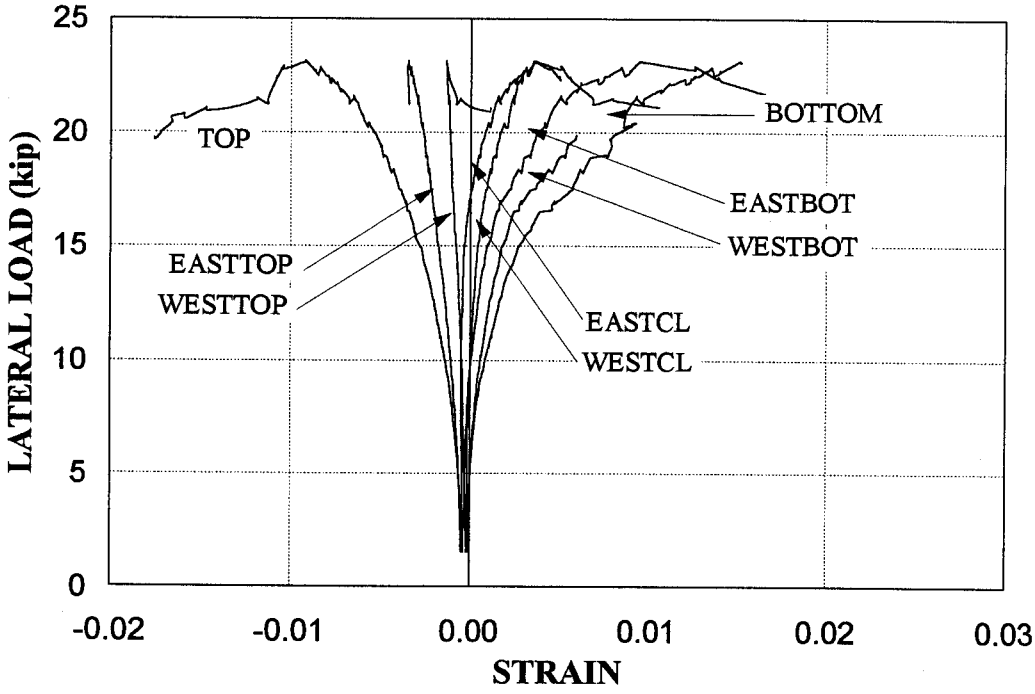

Figure 6.37 Lateral load-strain plots for Specimen BC1

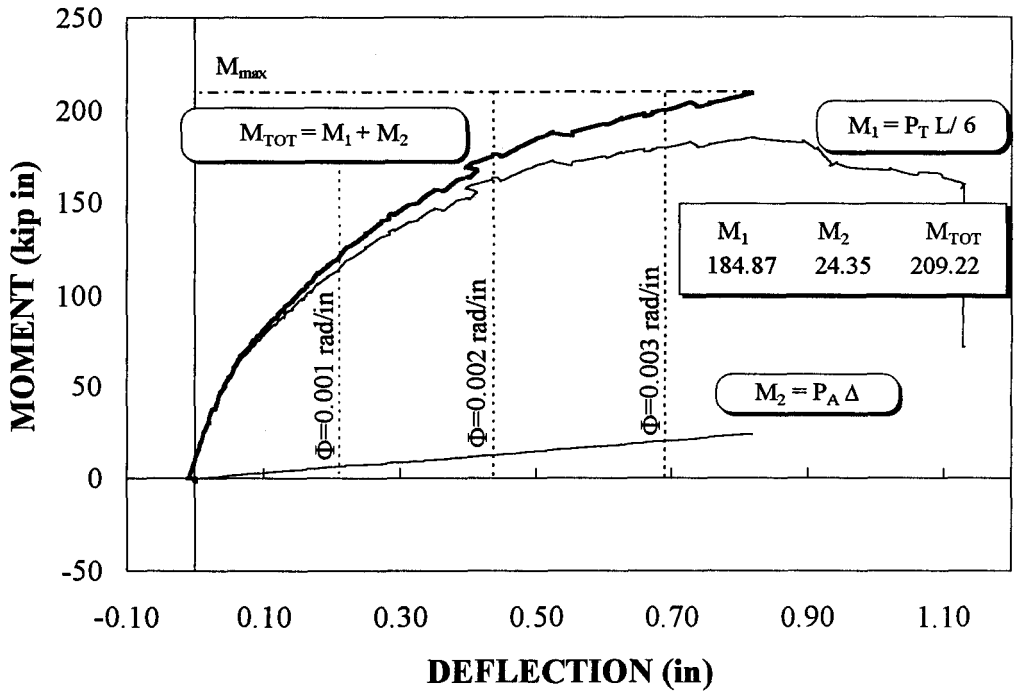

Figure 6.38 Moment-deflection-curvature plots for Specimen BC1

In Figure 6.41, the load-deflection curves are plotted according to the readings of the north, south, and mid-span LVDTs. The plot shows an initial vertical camber at the onset of the lateral load. The moment-deflection-curvature plot is presented in Figure 6.42. The percentage of the secondary moment M_2 to the total moment M_{tot} is equal to 30.5%.

6.4.6 Specimen BC3

Similar to the previous cases, the axial load-strain curves are plotted, as shown in Figure 6.43, to detect any initial imperfections. It is evident that a lateral eccentricity took place resulting in higher compression at the west side of the member in comparison with the east side. This was also accompanied by some vertical eccentricity resulting in higher

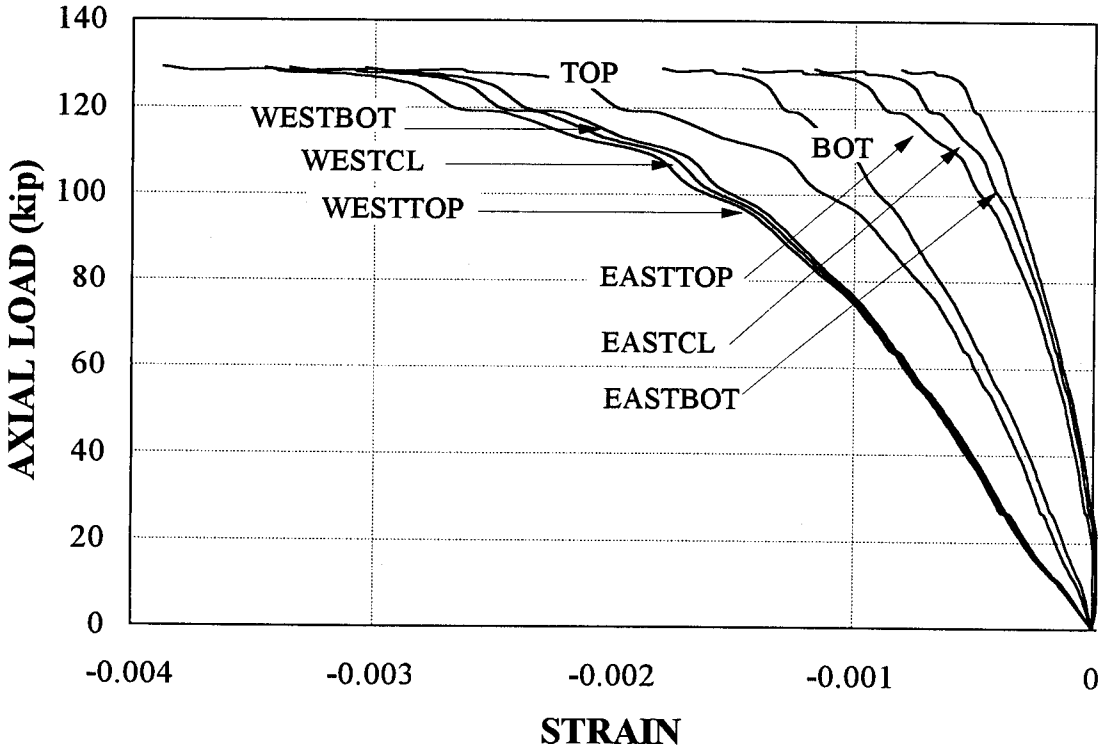

Figure 6.39 Axial load-strain plots for Specimen BC2

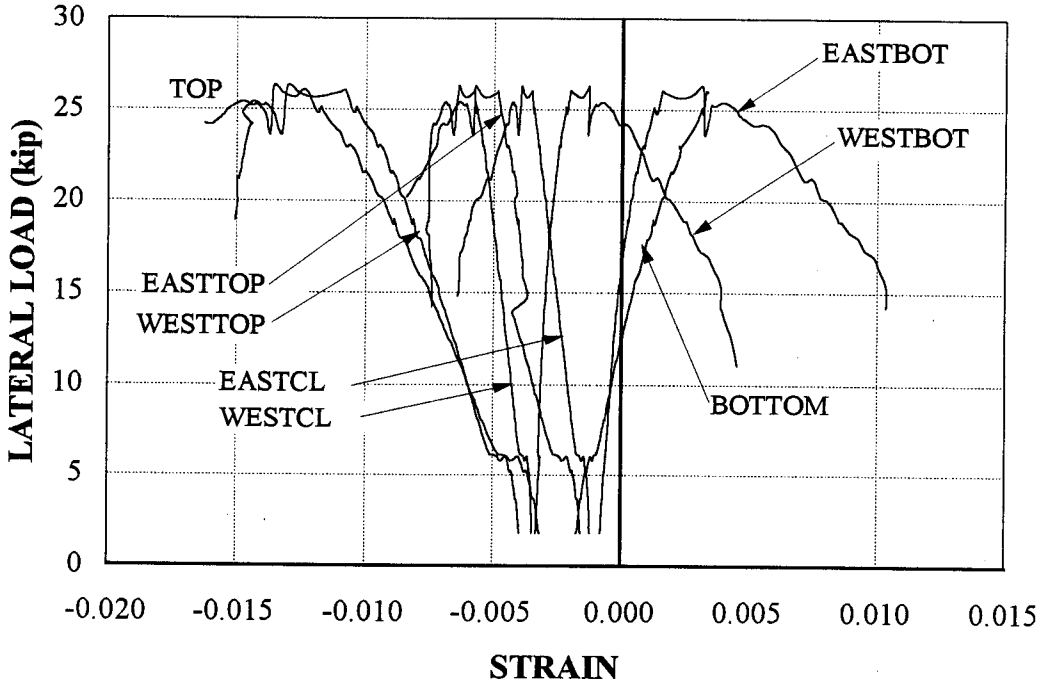

Figure 6.40 Lateral load-strain plots for Specimen BC2

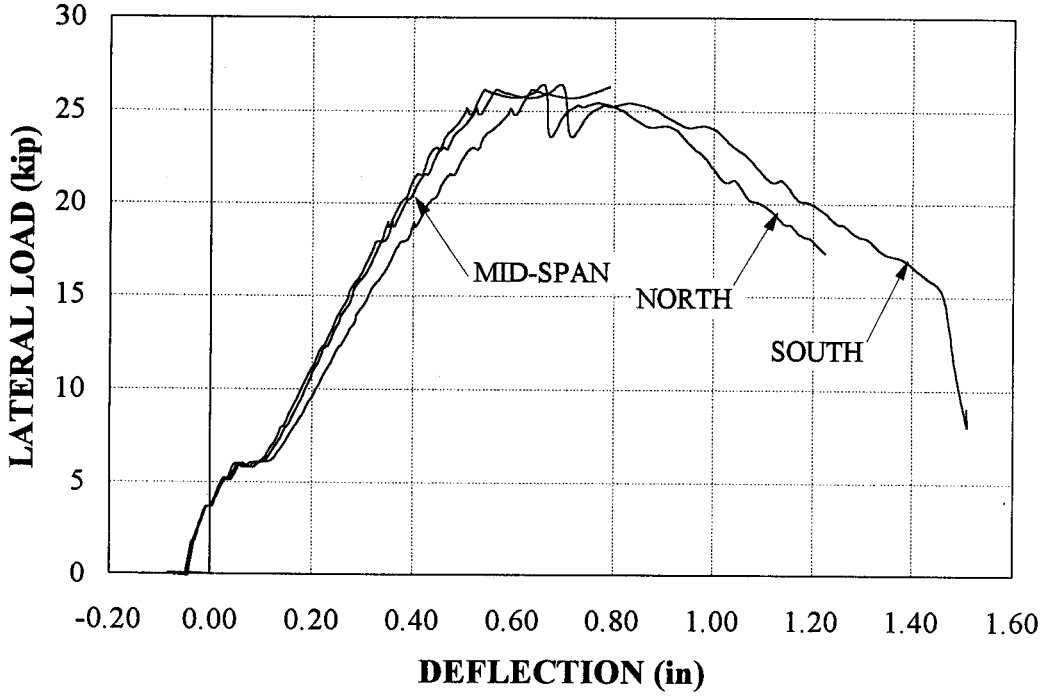

Figure 6.41 Load-deflection plot for Specimen BC2

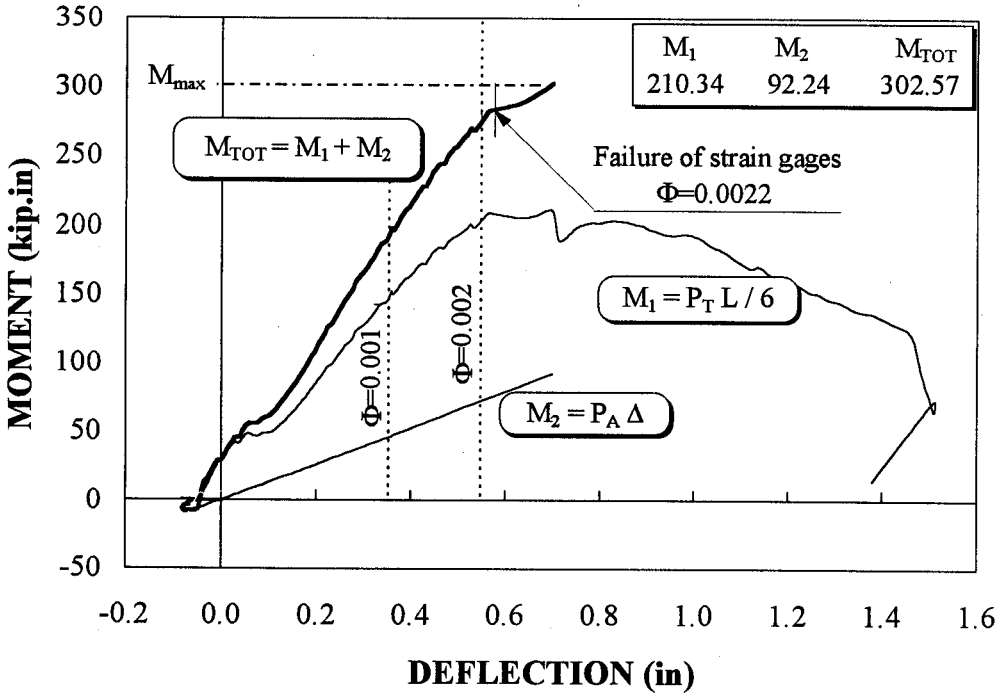

Figure 6.42 Moment-deflection-curvature plots for Specimen BC2

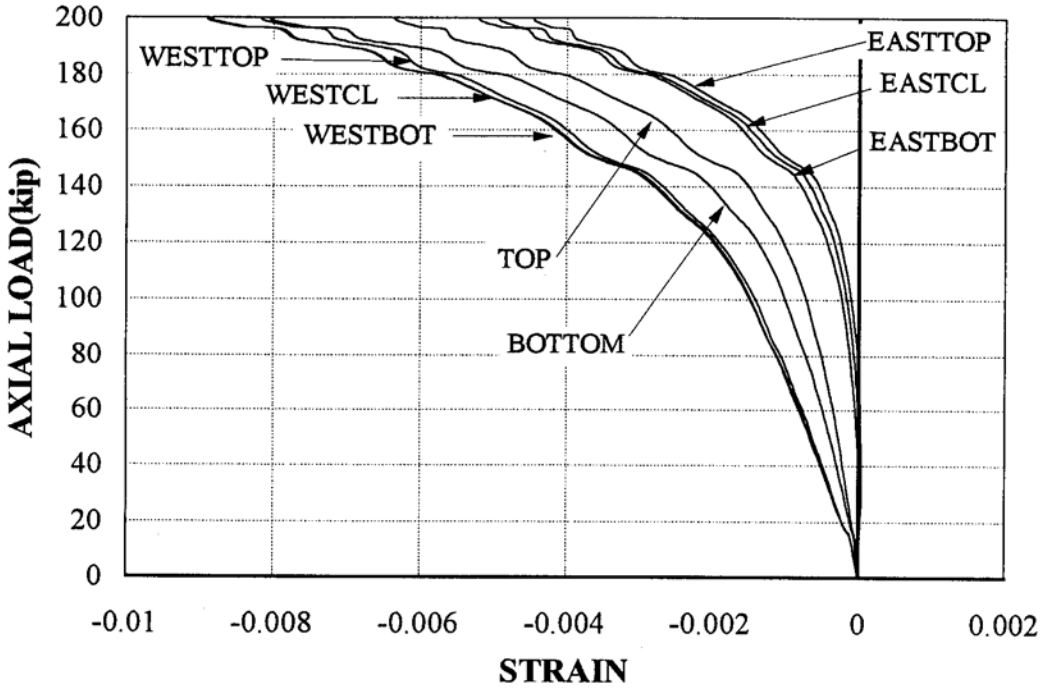

Figure 6.43 Axial load-strain plots for Specimen BC3

compression at the bottom side compared to the top side. The lateral load-strain curves shown in Figure 6.44, further verify the presence of the initial lateral eccentricity. It is to be noted that the west-bottom and east-bottom gage readings were not plotted due to their early failure. The high ultimate compressive strain at the top surface confirms a state of compression failure. Figure 6.45 displays the load-deflection curve at the mid-span. The initial camber is apparent. The moment-deflection-curvature plots are presented in Figure 6.46. The percentage of the secondary moment to the total moment is equal to 45%, which represents a rather high ratio. This is mainly attributed to the low stiffness of the tube in the longitudinal direction.

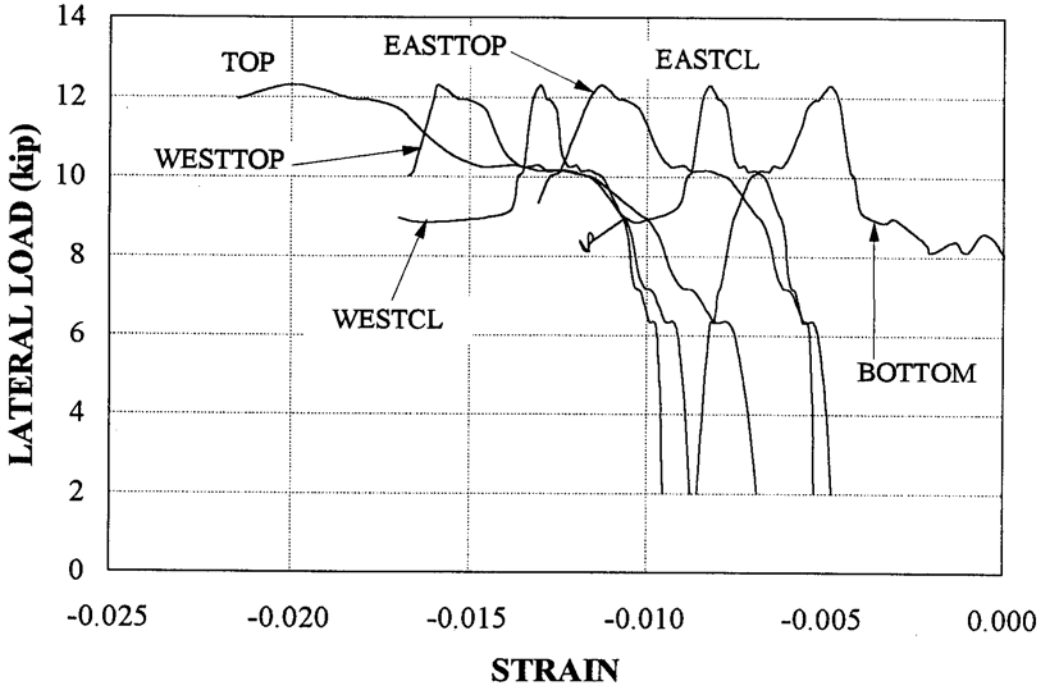

Figure 6.44 Lateral load-strain plots for Specimen BC3

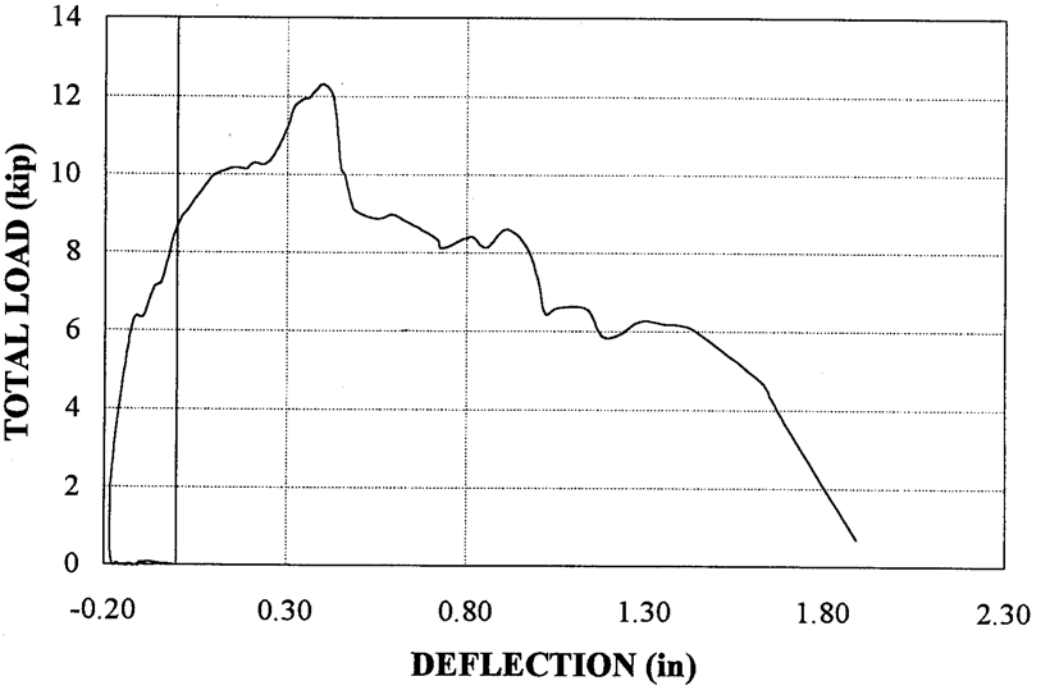

Figure 6.45 Load-deflection plot for Specimen BC3

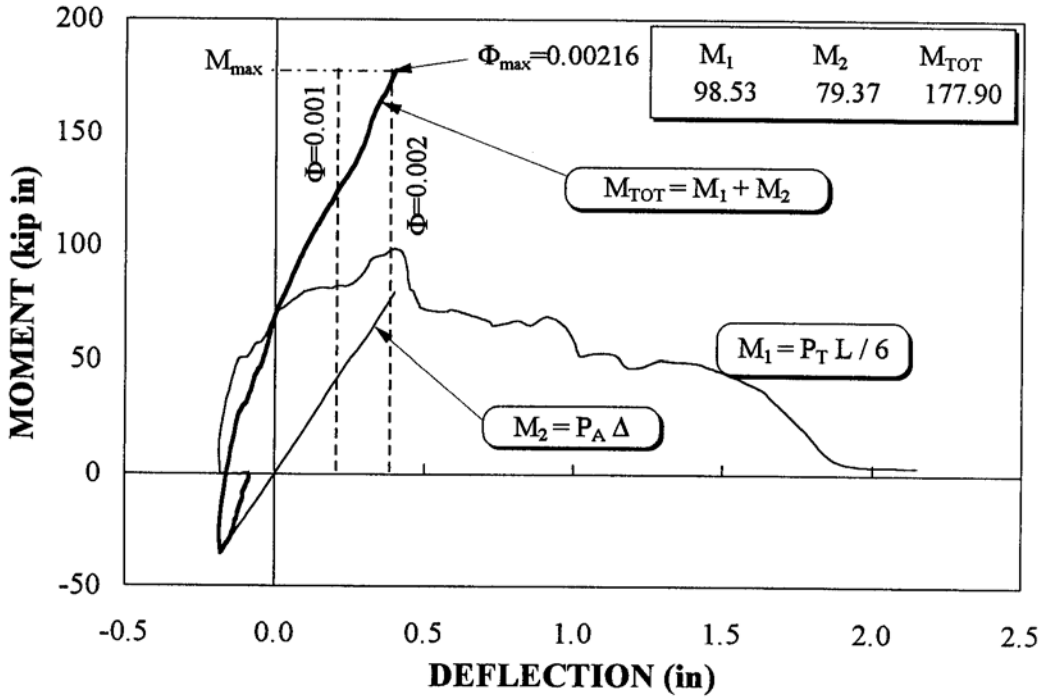

Figure 6.46 Moment-deflection-curvature plots for Specimen BC3

As an overview of the test results, Figure 6.47 provides the four experimental P-Δ curves for Specimens B, BC1, B C2, and B C3.

The results of beam-column tests establish the experimental interaction diagram of the square CFFT under study. This is presented and discussed in the next chapter along with a comparison with the conventional RC column.

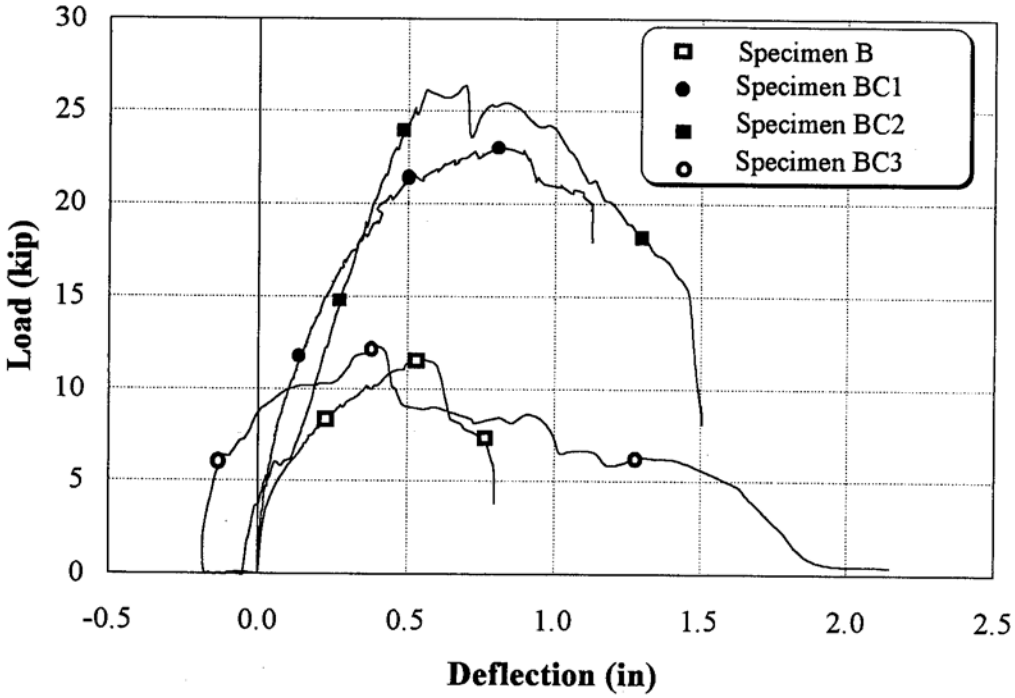

Figure 6.47 Combined load-deflection curves

7.

BEHAVIOR AND ANALYSIS OF SQUARE CFFT BEAM-COLUMNS

7.1 INTRODUCTION

In chapter 6, the beam column behavior of a square concrete-filled FRP tube was experimentally investigated. The tube provides perfect mechanical bond with the concrete core due to the projected internal ribs. The hoop fibers in the tube confine the concrete core, while also acting as shear reinforcement. The flexural reinforcement is primarily provided by the longitudinal unidirectional fiberglass woven roving. This novel composite column was tested under axial, flexural, and axial-flexural loadings, and an experimental force-moment interaction diagram was developed. In this chapter, the significance of those test results will be analyzed.

First, the experimental results are compared with the theoretical results of an equivalent conventional RC column used as a bench mark. Two aspects are considered in the comparison: the load-carrying capacity; and the ductility. For the first aspect, the circular CFFT is also included in the comparison. In general, it is shown that the confinement provided by the FRP tube improves both the capacity and the ductility of the column even under axial-flexural loading.

Second, the conventional beam theory is applied to the square CFFTs, in an attempt to develop a general design procedure. For this purpose, the mechanical properties of the FRP tube itself were determined experimentally, and then utilized in a fiber element model.

7.2 COMPARISON OF CFFT WITH CONVENTIONAL RC COLUMN

7.2.1 Load-Carrying Capacity

The first aspect of comparison is the load-carrying capacity. The comparison is performed for two loading schemes; the concentric loading, and the eccentric loading. For the former, both circular and square sections are included in the comparison, while for the latter, only the square section is considered.

7.2.1.1 Concentric loading

The column capacity under uniaxial compression is compared for two types of cross-sections; circular and square. For the circular sections, the CFFT has an inside diameter of 5.71", with a variable jacket thickness. No axial reinforcement was provided, since the FRP tube merely served as a hoop tension band, and, as such, did not contribute to the axial capacity. The axial capacity of an equivalent conventional RC column was calculated using the average outside diameter of the CFFT, taken as 5.88", the same unconfined strength of concrete core, and for the maximum allowable gross reinforcement ratios. The following ACI formula was used:

$$p_u = \left[0.85 f'_{co} + \rho_g \left(f_y - f'_{co}\right)\right] A_g \qquad (7.1)$$

where f'_{co} is the average unconfined strength of concrete, which was determined as 4.39 ksi, as the average of bend-points in the stress-strain diagrams of specimens of Series D (see Chapter 5), A_g is the gross cross-sectional area of the column, ρ_g is the gross reinforcement ratio, and f_y is the yield stress of steel which is taken as 60 ksi. The comparison is summarized in Table 7.1, where the capacity of the conventional RC column is calculated for an 8% steel reinforcement, which represents the maximum allowable reinforcement ratio according to ACI 318-95. The capacities of the CFFTs are the average of the experimental results of Series D for each of the three tube thicknesses (refer to Chapter 3**).**

Table 7.1 Axial load capacity of circular conventional RC column versus CFFT (kip)

RC Column	**CFFT**		
ρ_g = 8 %	t_j = 0.057"	t_j = 0.087"	t_j = 0.117"
222.0	227.7	300.8	362.7

The CFFT shows a superior capacity over the conventional RC column with an 8% gross reinforcement ratio. The strength enhancement is mainly attributed to the confinement effect of hoop fibers. Experiments by El-Echary (1997) have shown that circular CFFTs can resist eccentricities of up to 10% with a loss of capacity in the order of

17-18% for length to diameter ratios of 5:1. Since ACI 318-95 assumes a minimum eccentricity of 10% for tied columns and enforces a 20% reduction in nominal capacity of 2+ tied columns, the same reduction factor can be safely applied to CFFT columns.

The same comparison was performed for the square CFFTs which were discussed in Chapter 6. The column cross-sectional dimensions were 7" x 7" with a comer radius of 1.25". The unconfined strength of concrete was 2.72 ksi. In this case, the FRP tube included longitudinal fiber reinforcement in the form of unidirectional E-glass woven roving. The gross reinforcement ratio is about 5% of the gross cross-sectional area of the column (p_{gg}). However, the ultimate compressive strength $S_L^{(-)}$ of the reinforcement is around 20 ksi (manufacturer's data). In order to calculate an equivalent steel reinforcement ratio p_{ss}, the following formula is used (Fardis and Khalili 1982):

$$\rho_{gs} = \rho_{gg} \frac{S_L^{(-)}}{f_y} \tag{7.2}$$

where p_{ss} is the gross reinforcement ratio of glass. This results in a p. of 1.7 %. The conventional RC column capacity for this reinforcement ratio is only 162 kip versus an average capacity of 275 kip for the CFFTs. Again, the difference is attributed to the confinement effect, even though at a lesser degree than that of the circular sections (refer to Chapter 6).

7.2.1.2 Eccentric loading

In this section, the experimental thrust-moment interaction diagrams of CFFTs are compared with theoretical interaction diagrams for the conventional RC columns. The analytical interaction diagrams for conventional RC columns are calculated for gross longitudinal reinforcement ratios of 1% to 6% and minimum amount of lateral reinforcement required for tied RC columns (ACI 318-95). The confinement developed by the lateral reinforcement was also included in the analysis. For this purpose, a program was developed which uses the fiber element method to model the behavior of the conventional RC section. The analysis was based on the following assumptions:

1) Plane sections remain plane after bending. Therefore, a linear strain profile is assumed across the depth of the section.
2) Perfect bond exists between the steel rebars and the concrete. Therefore, strain in any steel rebar is the same as the strain in concrete at the level of the steel rebar.
3) Mander's model for unconfined concrete is used to express the stress-strain curve of the concrete cover in compression up to the strain of $2\epsilon_{co}$ (Mander et al. 1988), where ϵ_{co} is the strain corresponding to the peak strength of unconfined concrete, and is usually taken as 0.002. The descending branch is then followed by a straight line which reaches zero stress at a strain of $3\epsilon_{co}$, as shown in Figure 7.1. The stress-strain equation according to Mander's model is given by:

$$f_s = \frac{f'_{co}.x.r}{r-1+x^r} \tag{7.3}$$

where

$$x = \frac{\varepsilon_c}{\varepsilon_{co}} \tag{7.4}$$

$$r = \frac{E_c}{E_c - E_{\sec}} \tag{7.5}$$

$$E_{\sec} = \frac{f'_{co}}{\varepsilon_{co}} \tag{7.6}$$

and, E, is the initial modulus of elasticity of concrete and is given by (El-Tawil and Deierlein 1996):

$$E_c = 40{,}000\sqrt{f'_c} + 1.000.000 \qquad \text{(psi)} \tag{7.7}$$

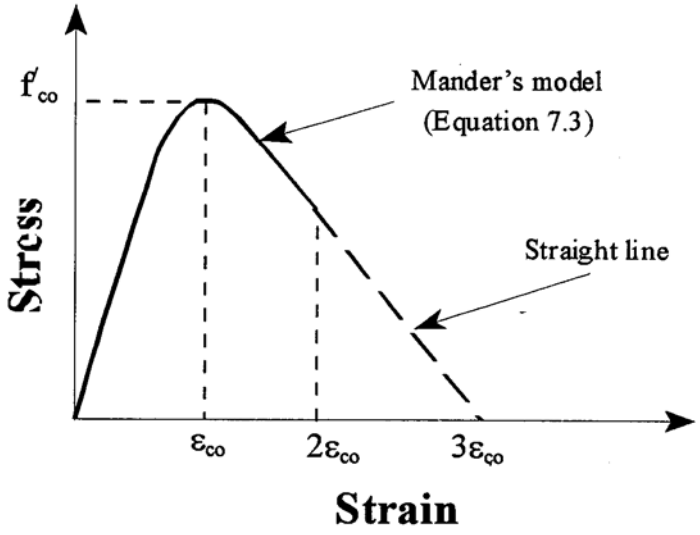

Figure 7.1 Stress-strain curve of concrete implemented in the model

4) Mander's confinement model (refer to Chapter 2) is used to develop the stress-strain curve of the concrete core in compression. An equivalent value of the confining pressure is calculated taking into account the spacing of the stirrups and the distribution of the longitudinal reinforcement (Mander et al. 1988).

5) The tension stiffening of concrete is included according to the model by Stevens et al. (1991) for both unconfined and confined concrete. A linear elastic relationship is assumed for tensile strains less than the cracking strain s_c, as shown in Figure 7.2. The modulus of elasticity is assumed to be the same as the one defined in Equation 7.7 for compression stresses. For strains larger than s,,,, the following equation applies:

$$f_g = f_{cu}\left[(1.0-\alpha)e^{-\lambda(\varepsilon_c-\varepsilon_{cr})}+\alpha\right] \tag{7.8}$$

where a is a parameter accounting for the effect of bar diameter and distribution, as

$$\alpha = C_t\frac{\rho_s}{d_b} \tag{7.9}$$

C_t is a constant coefficient with units of length, taken as 3 in. (Stevens et al. 1991), ρ_s is the reinforcement ratio and d_b is the bar diameter, and λ is given by

$$\lambda = \frac{270}{\sqrt{\alpha}} \tag{7.10}$$

and f_{cr} is the cracking stress of concrete given by

$$f_{cr} = 113\sqrt{f'_c}\ \text{(psi)} \tag{7.11}$$

and ϵ_{cr}, is the cracking strain as

$$E_{cr} = \frac{f_{cr}}{\varepsilon_c} \tag{7.12}$$

6) The reinforcement is placed in two equal layers on the tension and compression sides of the section.

7) An idealized elastic-perfectly-plastic stress-strain curve for steel is considered.

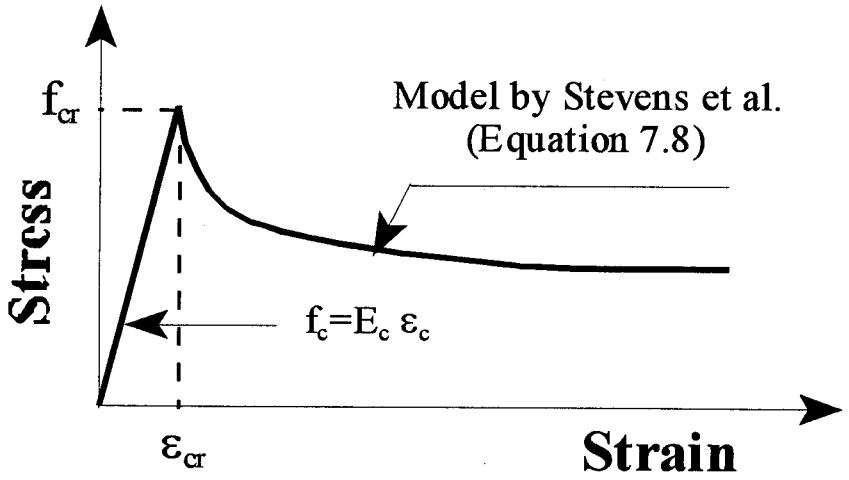

Figure 7.2 Tension stiffening model by Stevens et al. (1991)

Table 7.2 displays the experimental moments and forces for the CFFT specimens. Three different moments are reported for each of the beam-column specimens, $M_{1max.}$, M_2, and M_{TOT}, $M_{1max.}$ is the maximum primary moment produced by the applied lateral loads, M_2 is the corresponding secondary moment at the same section due to the P- Δ effect, where P is the axial load and Δ is the deflection at the midspan of the specimen, and M_{TOT} is the sum of the two moments, which represents the actual moment capacity of the section. The large P- Δ effect, which is evident from the large values of M_2, is primarily

attributed to the low stiffness of the FRP tube in the axial direction. It should be noted that the CFFT specimens were axially reinforced with a single sheet of E-glass woven roving, which as mentioned in the previous section, had an equivalent steel reinforcement ratio of only 1.7%.

Table 7.2 Experimental results of the long square CFFTs

Specimen	**P_{axial} (kip)**	**M_{1max} (kip.in)**	**M_2 (kip.in)**	**M_{TOT} (kip.in)**
C	230.60	-	-	-
B	-	92.10	-	92.10
BC I	33.75	184.90	24.40	209.20
BC2	135.00	210.30	92.20	302.60
B C3	200.00	98.50	79.40	177.90

By examining the comparative plots in Figure 7.3, it is evident that the square CUT has an enhanced performance in the compression failure region, and is comparable to a 6% conventional RC section. However, in the tension failure region, the strength is only comparable to a 1.2 % conventional RC section in pure flexure, which is slightly lower than the equivalent steel reinforcement ratio of 1.7%. The reason for the high capacity in compression is the partial confinement on the compression side, which results in higher ultimate strains. Moreover, the internal rib grid is very effective in load distribution and crack containment on the tension side of the section.

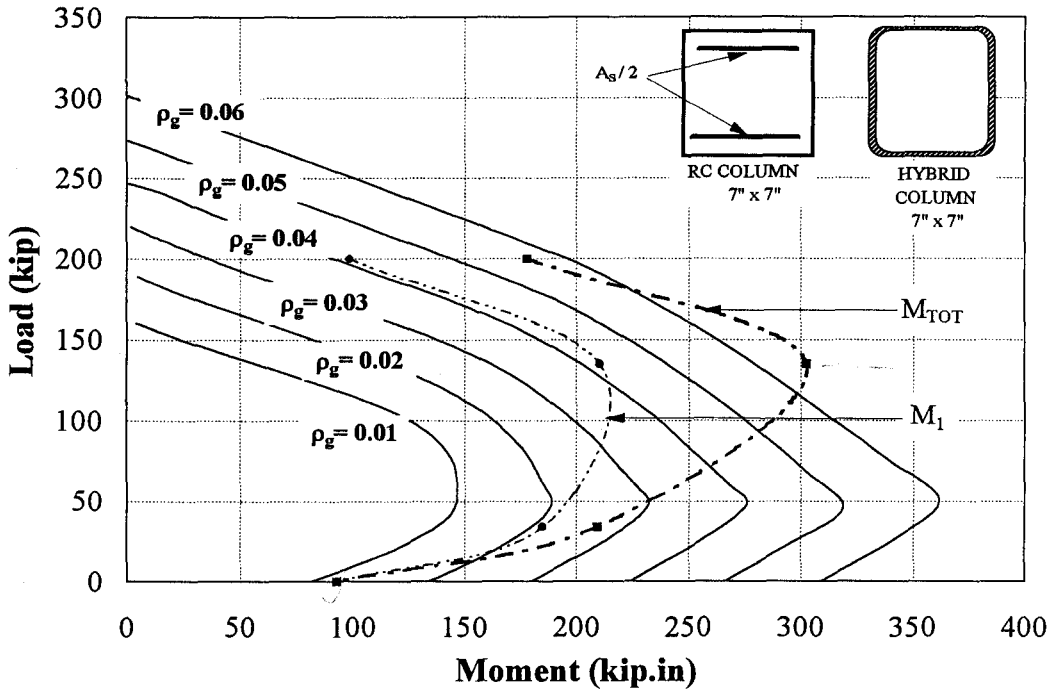

Figure 7.3 Interaction diagrams of CFFTs versus conventional RC columns

It can be concluded that CFFTs have significant load-carrying capacity due to the confinement effect. Another important issue is the ductility of the column, which is of great importance in seismic zones. This is discussed in the following section.

7.2.2 Deformations Under Lateral Loads

Ductility of a member, is defined as the ability to sustain inelastic deformations prior to collapse. Generally, ductility is measured by the ratio of the ultimate deformation of the member to that at the first yielding of steel reinforcement. Deformations can either represent curvature or deflection of the critical section, or rotation over a plastic hinge region. Therefore, the following measures of ductility can be introduced (Naaman et al. 1986):

$$\mu_{D=}\Phi_{u/}\,\Phi_y \tag{7.13}$$

$$\mu_{D=}\,\Delta_u\,/\,\Delta_y \tag{7.14}$$

$$\mu_{D=}\,\theta_u/\,\theta_y \tag{7.15}$$

where, μ_d is the ductility index, $\Phi_{u,}$ Δ_u and θ_u are the curvature, deflection, and rotation at the level of ultimate capacity, respectively, while Φ_y Δ_y and θ_y are the curvature, deflection, and rotation at yielding capacity, respectively. Park and Paulay (1975) suggest that for members with considerable post-peak descending branch, the ultimate capacity is taken as 80% of the peak capacity. These expressions of the ductility index are based on yielding of the reinforcement, and are, therefore, inappropriate for structural members reinforced by linearly-elastic materials, such as FRP. For this reason, four different measures of ductility and/or deformability are discussed in the present study. Three of these are considered for the comparison of RC and CFFT beam columns.

1) Toughness

Toughness is a measure of deformability of a system and is obtained by integrating the total area under the load-deflection curve (Smart and Jensen 1997). Yet, considerable amount of deformations prior to failure does not imply high ductility. The large deflections may be due to the low elastic modulus and the linear elastic response of the reinforcement, resulting in a large elastic energy stored in the system. The release of such energy at failure could be devastating.

2) Energy-Based Ductility

This is a ductility measure, which takes into account the inelastic energy absorbed during inelastic deformations and is appropriate for structures reinforced by non-yielding materials. This measure was proposed by Naaman and Jeong (1995), who applied it to concrete beams prestressed with FRP tendons. The energy-based index μ^*_D takes into account the elastic energy released at failure and is given by:

$$\mu^*_D = \frac{1}{2}\left(\frac{E_{tot}}{E_{el}} + 1\right) \tag{7.16}$$

where E_{tot} is the total absorbed energy, which is equal to the toughness of the specimen, and E_{el} is the elastic energy released at failure (see Figure 7.4). The elastic slope *s* at the failure point is the unloading slope at that point. However, if not available, it can be approximated as the weighted average of the two initial slopes s_I and s_Z of the load deflection curve. Here, it is noteworthy that for a steel section the ductility indexes μ^*_D and $,u_D$ (Equation 7.13) are equal.

Not knowing the unloading slope at failure for CFFT beam-columns, the proposed average slope was used. This was justified by the experimental results of uniaxial cyclic loading tests by Mirmiran and Shahawy (1997a). Figure 7.5 depicts the response of an unbonded circular 6" x 12" E-glass/polyester CFFT specimen subjected to three cycles of axial loading and unloading till failure. No substantial degradation of the unloading slope is evident neither in the axial nor in the lateral direction. The same observation was experimentally verified by Mastrapa (1997), who performed cyclic uniaxial compression

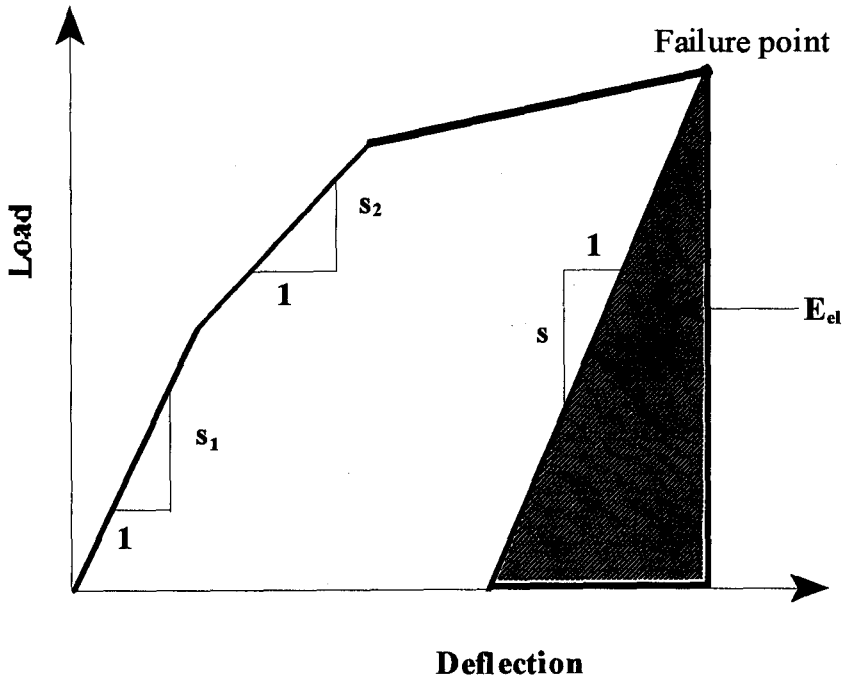

Figure 7.4 Elastic energy E_{el} released at failure (Naaman and Jeong 1995)

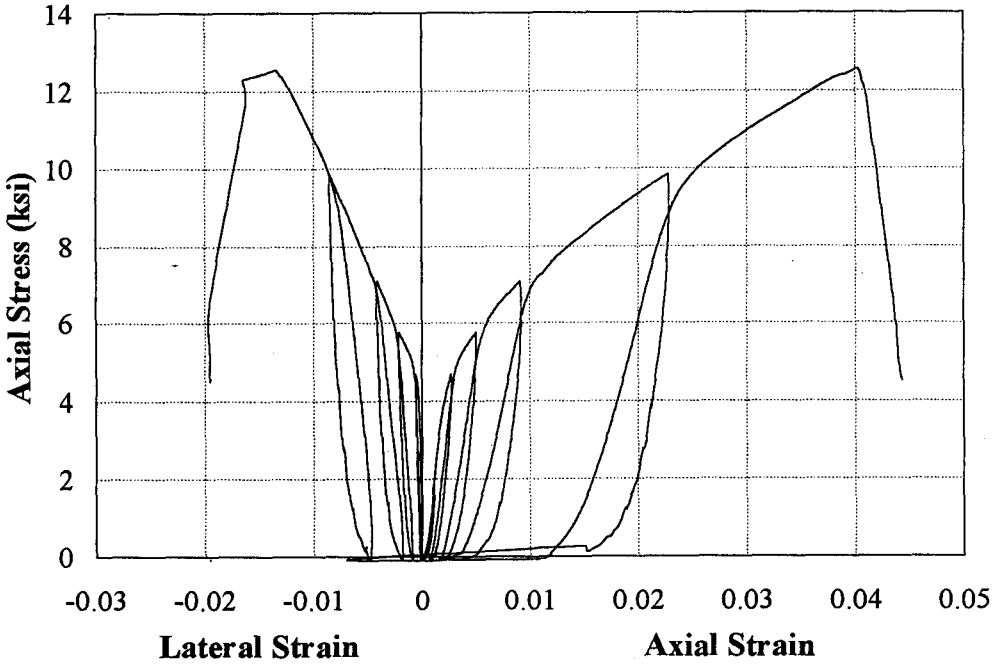

Figure 7.5 Cyclic response of unbonded circular CFFT in axial and lateral directions

tests on bonded circular 6" x 12" S-glass/polyester CFFT specimens. A sample of his test results is displayed in Figure 7.6. Again, no substantial reduction in stiffness is apparent till failure. These experiments strongly support the procedure proposed by Naaman and Jeong (1995).

3) Theoretical Yield Method

This method is applicable for beams with non-yielding reinforcement materials (Park 1989). The conventional ductility index (Equations 7.13-7.15) is applied, yet the yield deformation is determined graphically as the deformation at the intersection of the initial slope and the slope at the ultimate peak load of the load-deflection or the moment-curvature curves (Figure 7.7).

4) Visual Yield Method

This method is also proposed for beam-columns with non-yielding reinforcement materials. It is suggested to determine the point of first destress , i.e. yield deformation by visual inspection (e.g. white patches for CFFT) during the testing procedure and recording the deformation at that point as well as the ultimate deformation. These experimentally obtained values will be then substituted in the conventional ductility index formulae.

The first three methods were used to compare the deformability as well as the ductility of both the conventional RC and the CFFT beam columns. The fourth method, however, was not included since no visual yield deflection results for the RC beam-columns were available.

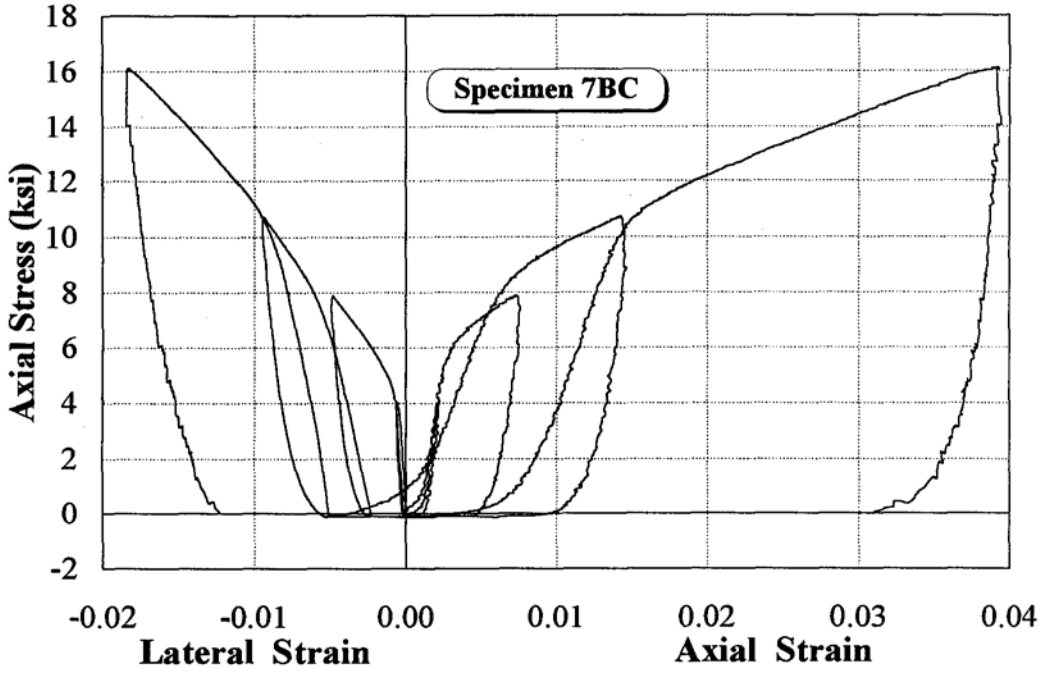

Figure 7.6 Cyclic response of bonded circular CFFT in axial and lateral directions

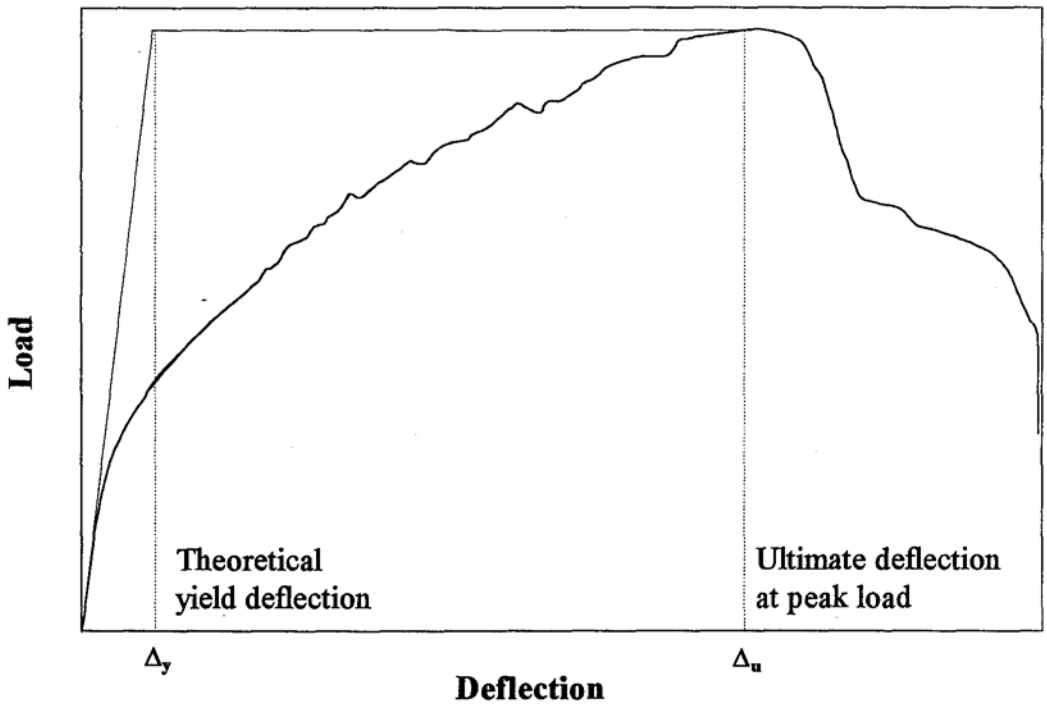

Figure 7.7 Schematic of the theoretical yield method

Theoretical P-Δ curves were developed for RC sections having the same peak moments as the CFFT specimens for the sake of comparison. These were developed using the same computer program explained in the previous section. The following steps were involved in generating these curves:

1) The steel reinforcement ratios were calculated that would result in the same primary peak moments M_{lpeak} as the CFFTs.
2) The moment-curvature (M-Φ) curves were generated using the computer program that was developed for the interaction diagrams.

The M-Φ curves were then used to generate the P-Δ curves by the conjugate beam method. In this method, the Φ-diagram is treated as the load on the conjugate beam, and the moment produced by this load at any point is set equal to the deflection at the corresponding point in the actual beam. The procedure was performed incrementally for each value of the actual moment, in order to construct the entire P-Δ curve.

The analytical P-Δ curves for RC columns along with the corresponding experimental curves for the CFFTs are displayed in Figures 7.8-7.11, for the four axial load levels. The deformability and ductility of both systems are compared in Table 7.3. It is apparent that the CFFTs, although more deformable, are less ductile than the conventional RC column. Improved ductility is obtained for higher levels of compression as compared to the ductility of RC columns. Accordingly, it may be concluded that the CUT in its present lay-up demonstrates acceptable behavior under compression control failure, yet less effective behavior for tension control failure. However, it should be also

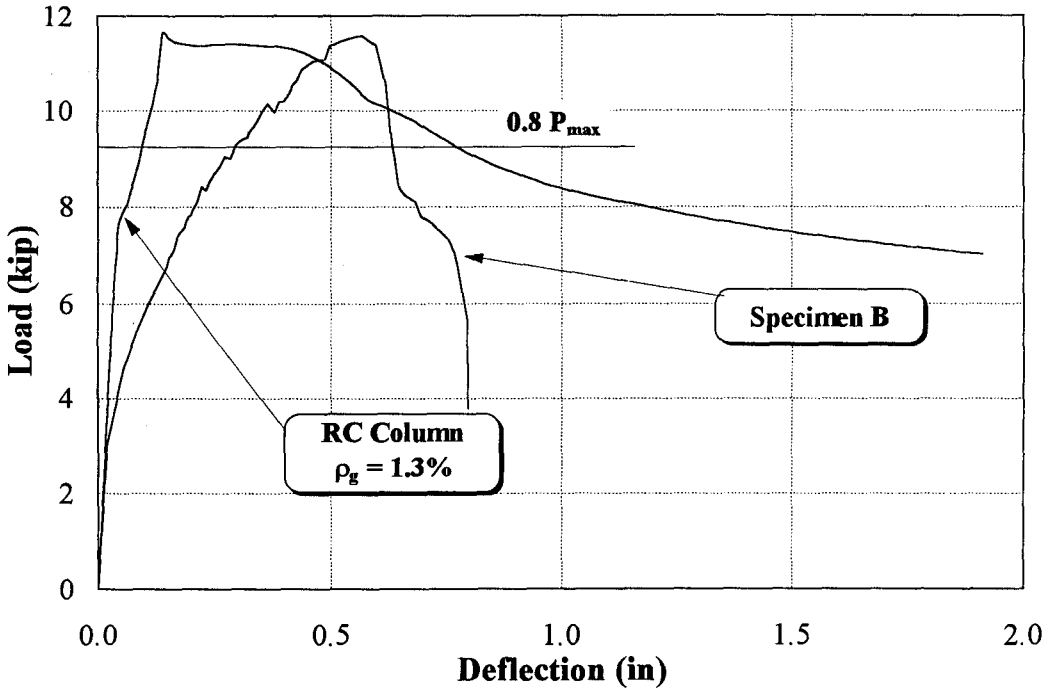

Figure 7.8 Load-deflection curves for Specimen B versus corresponding RC column

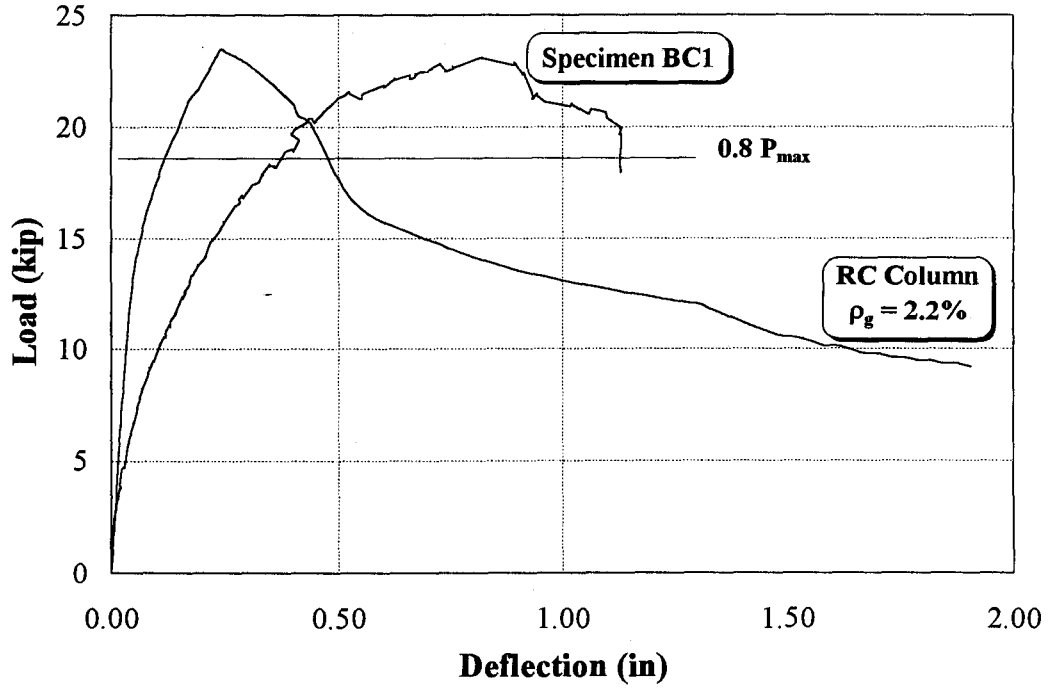

Figure 7.9 Load-deflection curves for Specimen BC1 versus corresponding RC column

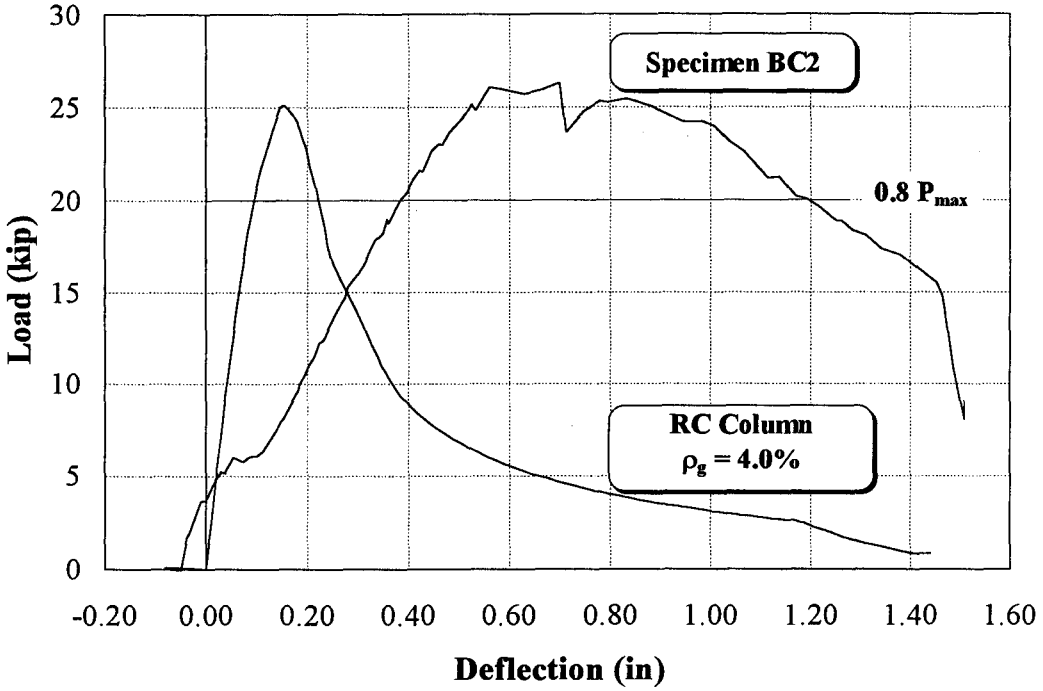

Figure 7.10 Load-deflection curves for Specimen BC2 versus corresponding RC column

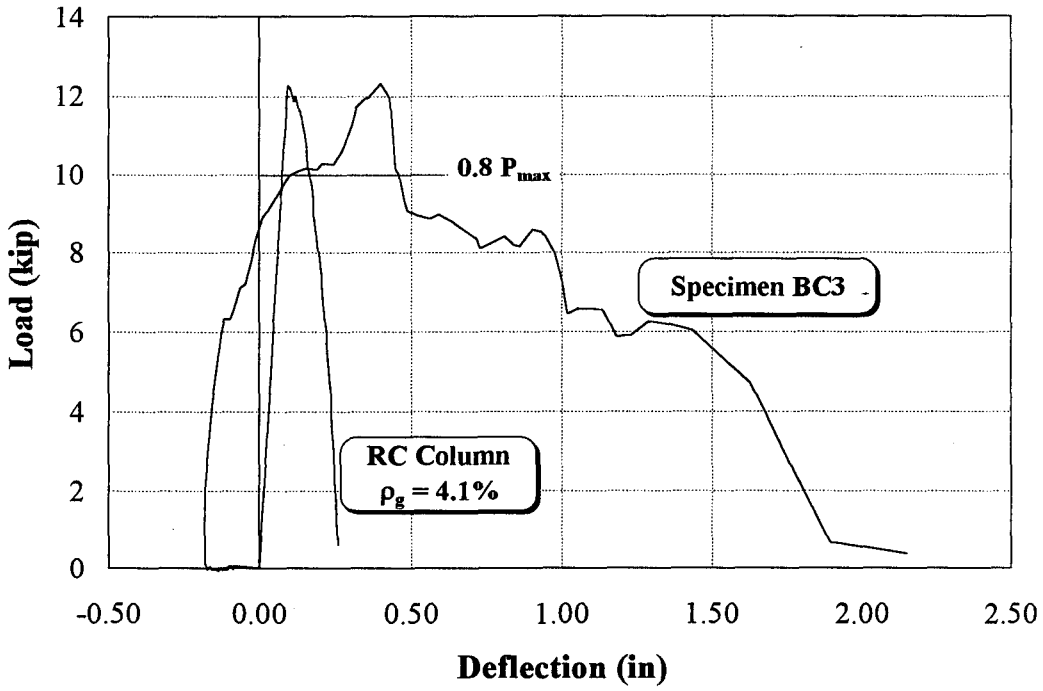

Figure 7.11 Load-deflection curves for Specimen BC3 versus corresponding RC column

Table 7.3 Toughness and ductility of the CFFT specimens and the equivalent RC sections

SPECIMEN	P_A/P_9	Equivalent steel ratio		Toughness (kip-in)		Energy-based method		Theoreticl yield method	
	(%)	ρ_{gg}(%)	ρ_{gs}(%)	CFFT	RC	CFFT	RC	CFFT	RC
B	0	1.7	1.3	5.51	7.6	3.65	17.99	10.24	13.12
BC1	11.03	1.7	2.2	21.00	9.1	2.59	5.71	4.73	6.88
BC2	48.87	1.7	4.0	22.56	3.84	2.64	2.27	2.16	2.64
BC3	73.42	1.7	4.1	6.00	1.39	2.36	2.42	1.43	2.34

made clear that the design of CFFT could be tailored according to the desired structural function. As mentioned earlier, the longitudinal reinforcement ratio provided in the square CFFT was quite low, which in turn resulted in a low strength in tension as well as a high secondary moment under combined lateral and axial loads. Nevertheless, the main advantage of the CFFT is the superior composite action between the concrete core and the FRP shell, which was created through the internal rib grid. Also, the confining action of the tube on the compression side and the crack closure on the tension side of the section are both very significant.

The proposed square CFFT was further investigated in order to arrive at an analysis and design procedure. The mechanical properties of the tube were determined and further implemented in the analysis procedure, as discussed in the following sections.

7.3 MECHANICAL PROPERTIES OF SQUARE FRP TUBE

The first step to analyze the square CFFT was to determine the mechanical properties of the "hybrid" FRP tube itself, which consists of three different components: the longitudinal and transversal polyester ribs, the longitudinal E-glass/polyester woven roving, and the E-glass/polyester filament winding (see Chapter 6). First, the mechanical properties of each component were established from the manufacturer's data and the tabulated data available in the literature. Using the computer program GENLAM (see Chapter 4), the overall strength and stiffness of the tube were established from the properties of its three components. However, due to uncertainty of the manufacturer's data and because of the hybrid nature of the tube which manifests itself by the interaction

between its various components, it was decided to conduct coupon tests of the entire tube cross section rather than relying on the results of the GENLAM program Since the strain gradient within the thickness of the tube is not significant, it was decided to conduct two sets of coupon tests: one for tensile properties of the tube, and another for its compressive properties.

7.3.1 Tensile Properties

In order to determine the tensile properties of the FRP tube, four 4" x 15" coupon specimens were cut off the sides of the tube. The coupons were cut from the middle of each side such that the central rib was centered in the middle of each specimen. All specimens were tabbed at both ends by four layers of unidirectional 24 oz E-glass woven roving attached with polyester resin (Figure 7.12). The tabs were added to serve as the gripping area and to avoid a premature local failure at the grips.

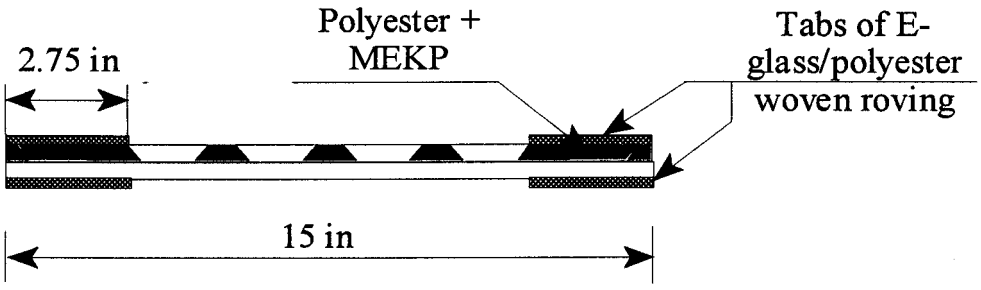

Figure 7.12 Tabbing of the tension specimens

Tests were conducted using a 550 kip MTS machine at the FDOT Structural Research Lab in Tallahassee, FL. All specimens were tested in pure tension at a displacement rate of 0.05 inch per minute according to ASTM D3039-95a. Each specimen was instrumented with two 60 mm strain gauges (PL 60) at its mid-height, one on each side. Additionally, two LVDTs were used to monitor the axial displacement of the specimen, again one on each side.

Figure 7.13 shows the location of the strain gauges on each side of the specimen. During the loading process the strain gauges failed before the specimen's failure, and thus did not record the full strain response. A horizontal crack usually formed prior to failure, which was primarily caused by the rupture of the longitudinal fibers. Figure 7.14 shows the specimens after failure.

Using the average cross-sectional area, the tensile stresses were calculated. Figure 7.15 depicts the stress-strain plots for the four tension specimens. There was some slippage at the grips which resulted in non-linearity of the response. Also, variation of the response among the four coupon tests may be attributed to the relative slippage at the grips. Specimen T1 shows the *stiffest* response, and hence the least slippage at the grip. A peak stress of 4.0 ksi and an ultimate strain of 2.3 % were recorded for Specimen T1. Using the initial stiffness of this specimen, a linear stress-strain model was proposed for the FRP tube in tension:

$$f_{j,} = 484.6\, \epsilon_1 \qquad (7.17)$$

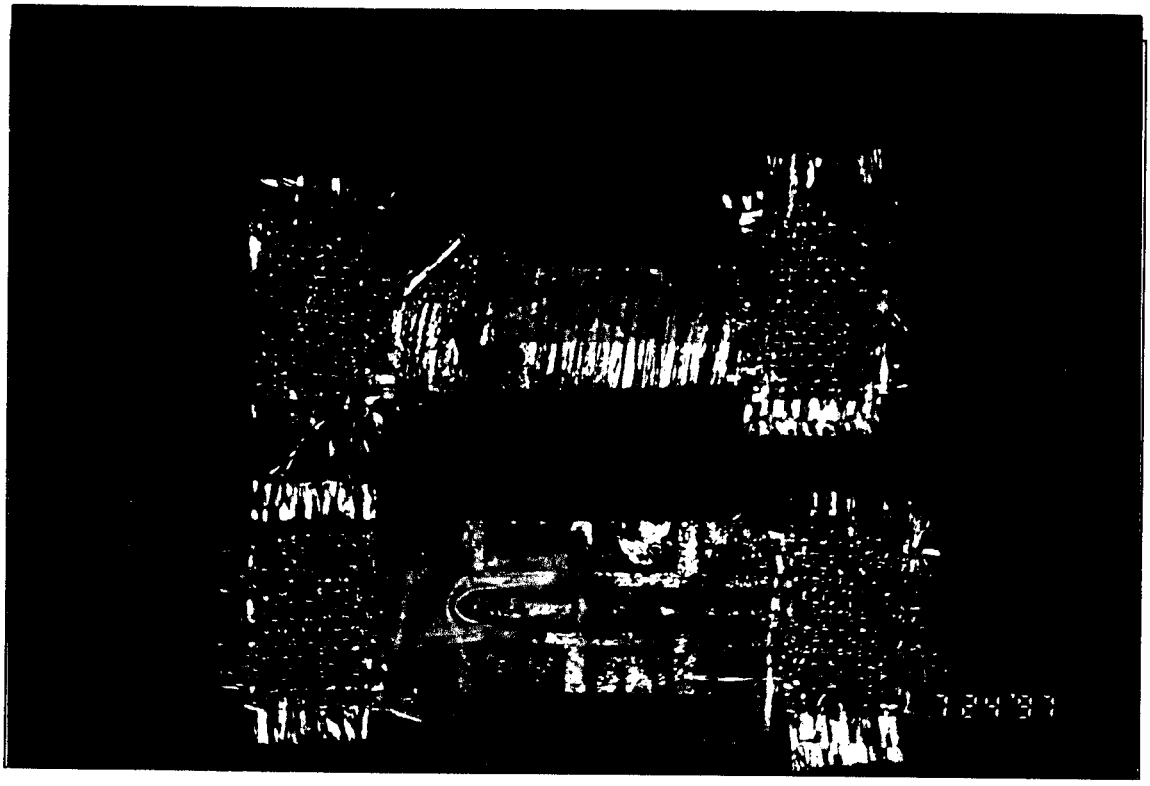

Figure 7.13 Specimens T1 and T3 before testing

Figure 7.14 Tension specimens after failure

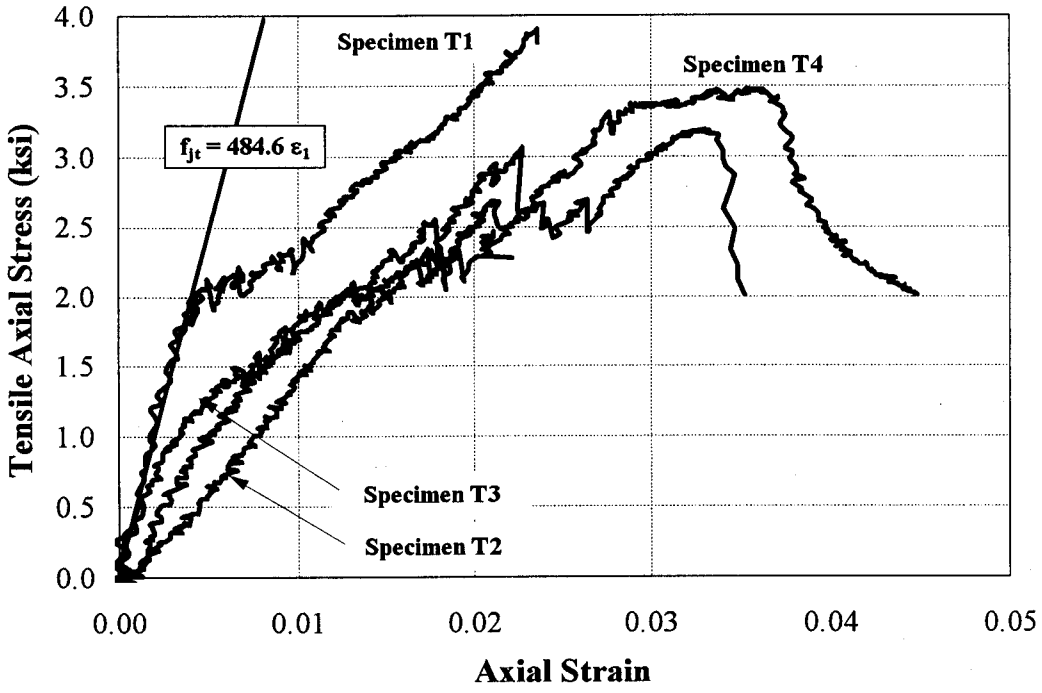

Figure 7.15 Stress-strain curves of the tension specimens

where, f_{jt} is the tensile stress in the tube, and ϵi is the longitudinal strain. Since beam-column tests had indicated strains of up to 2% in the tube, the corresponding ultimate strength was established at 9.7 ksi from Equation 7.17.

7.3.2 Compressive Properties

In order to determine the compressive properties of the FRP tube, four 5"-long section of the tube were tested under pure axial compression. Due to the hybrid structure of the tube, it was decided to test the full section of the tube rather than flat strips from the tube. The specimens were capped by $^1/4$"-thick flexible lead plates. Four LVDTs were used to measure the axial deformations. The specimens were tested using the 550 kip MTS

machine at a 0.05 in/min displacement rate (ASTM D 3410-95). Figure 7.16 shows specimen C1 before testing. Cracking noises heard during the loading process were attributed to the separation of the grid of internal ribs from the tube wall. White patches would then appear at the corners of the tube, followed by hoop cracks. The hoop cracks were generally initiated near the edges indicating regions of high stress concentrations.

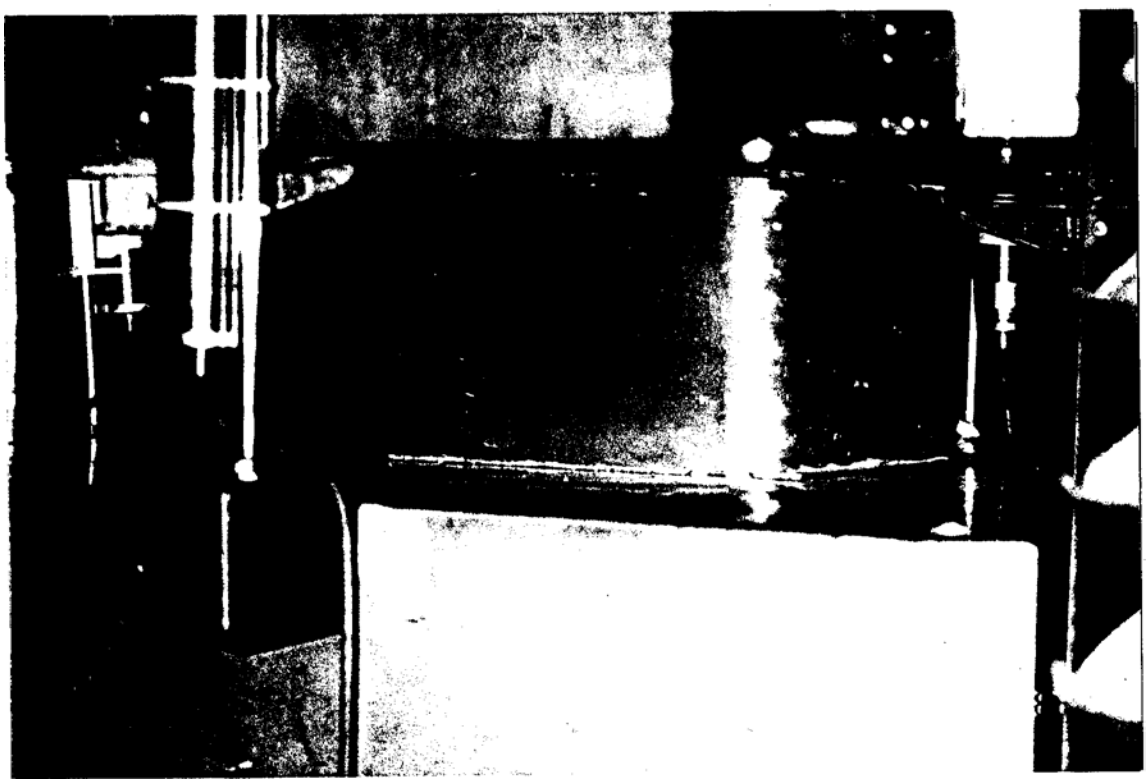

Figure 7.16 Specimen C1 before testing

It was noticed that the load would peak at some point, after which it would gradually drop until it would stabilize at a lower load level. The failure was, however, characterized by excessive deformations. Figure 7.17 shows three of the specimens after

failure. The separation of the internal grid, the hoop cracks, and the high stress concentration at the edges are apparent. The stress-strain curves for the four coupon specimens are shown in Figure 7.18. One general observation for all specimens is the low stiffness, which was mainly attributed to the separation of the internal grid due to lack of any lateral support. However, the lateral support is provided in the concrete-filled tube by the concrete core. Therefore, similar to the tension modeling, the highest initial slope was considered for a linear model, as follows:

$$f_{jc} = 551.96\ \epsilon_l \qquad (7.18)$$

where, f_{jc} is the compressive stress in the tube, and ϵ_l is the longitudinal strain. Again, based on the experimental results of the beam-column tests, an ultimate strain of 3.0 was assumed which would result in a compressive strength of 16.56 ksi.

7.4 ANALYTICAL MODELING

Earlier in this chapter, an experimental interaction diagram was presented for the square CFFTs. In this section, the conventional beam theory will be used to perform a sectional analysis of CFFTs, and to compare the analytical results with the experiments.

The analysis was performed by means of a modified version of the program developed for the RC section. The main assumptions involved in the analysis were: plane sections remain plane after bending, and perfect bond exists between the concrete core and the FRP tube. Experiments showed that the internal rib grid prevents any slippage between

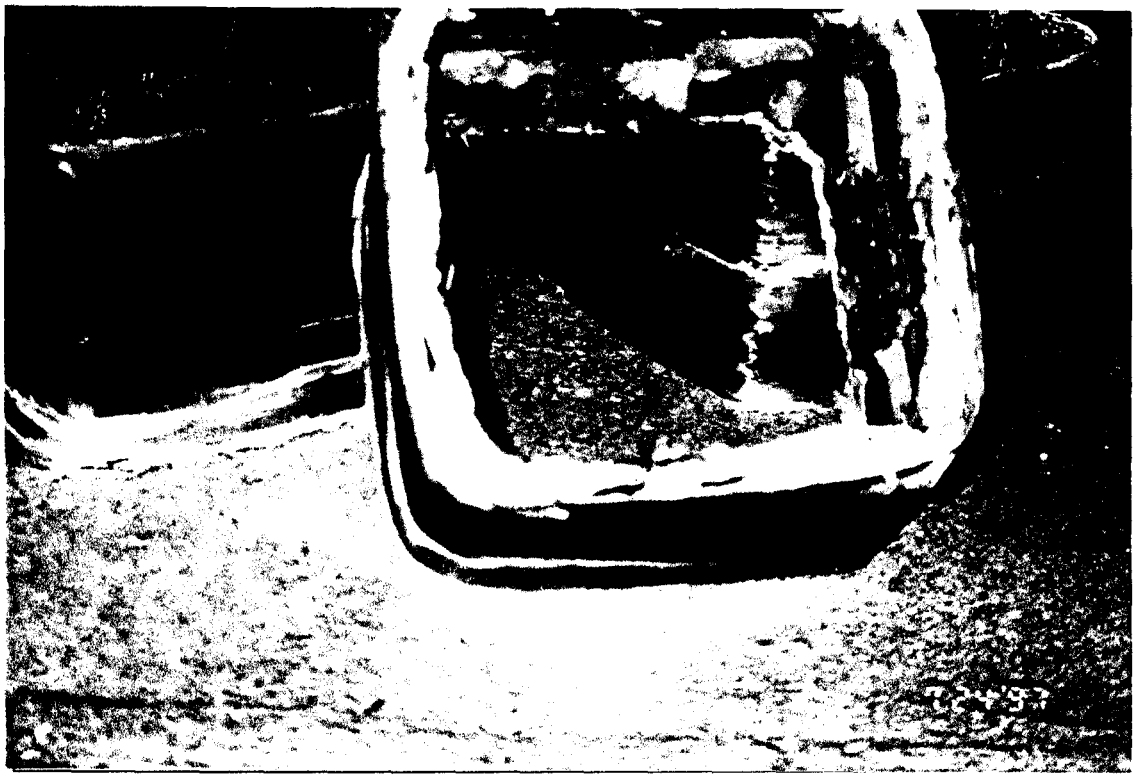

Figure 7.17 Compression specimens after failure

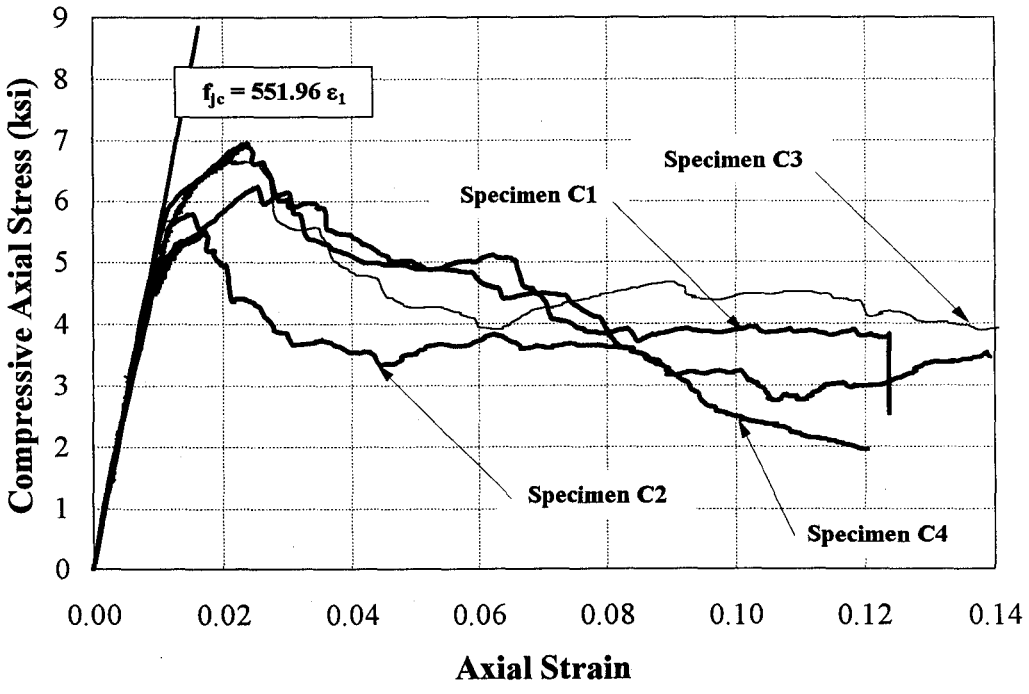

Figure 7.18 Stress-strain curves of the compression specimens

the two materials (see Chapter 6). The mechanical properties of the tube were determined from the coupon tests (Equations 7.17-7.18).

For tension stiffening in concrete, the model of Stevens et al. (1991) was replaced by the model of Vecchio and Collins (1986). The reason being that the model of Stevens et al. is more suitable for RC sections, since it takes into account the amount, size, distribution, and orientation of the reinforcing steel. While, the model of Vecchio and Collins is a simple function of the concrete cracking stress f_{cr} and the corresponding cracking strain ϵ_{cr}, which are taken as:

$$f_{cr} = 7.5\sqrt{f'_{co}} \tag{7.19}$$

$$\varepsilon_{cr} = \frac{f_{cr}}{E_c} \tag{7.20}$$

As shown in Figure 7.19, a linear elastic relationship is assumed for tensile strains less than E, Tensile modulus of elasticity is assumed to be the same as the initial compressive modulus of elasticity as:

$$E_c = 47.586\sqrt{f'_{co}} \qquad \text{(psi)} \tag{7.21}$$

For strains larger than e., the following equation applies:

$$f_c = \frac{f_{cr}}{1+\sqrt{200\varepsilon_c}} \tag{7.22}$$

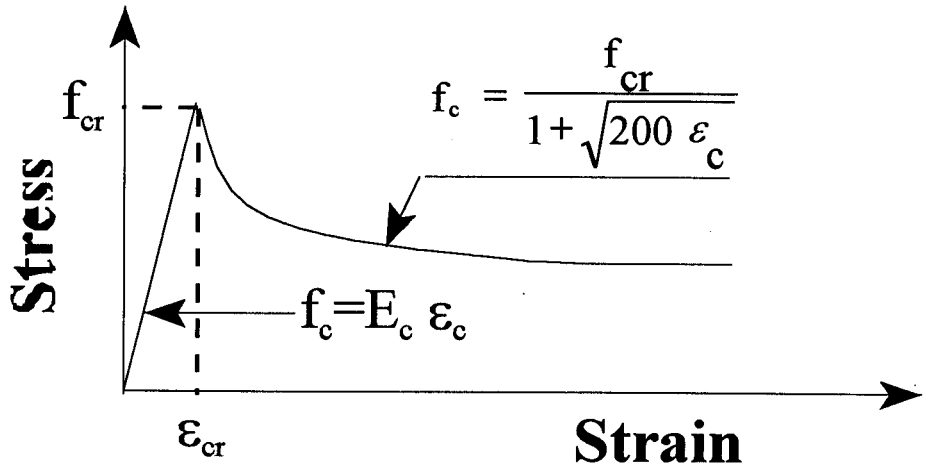

Figure 7.19 Tension stiffening model of Vecchio and Collins (1986)

The limiting ultimate tensile strain of the concrete was taken as large as 2.0%, to simulate the containment of the cracked concrete in tension. Strain gage results on the surface of the tube supported this assumption (refer to Chapter 6).

The stress-strain of concrete in compression was based on the proposed confinement model discussed in Chapter 5, which is a function of the initial slope E_1, the second slope E_2, the intercept stress f_o, and the curve-shape parameter *n,* in the following form:

$$f_c = \frac{(E_1 - E_2)\varepsilon_c}{\left[1+\left(\frac{(E_1 - E_2)\varepsilon_c}{f_o}\right)^n\right]^{\frac{1}{n}}} + E_2\varepsilon_c \qquad (7.23)$$

where the first slope E1 is taken as given in Equation 7.21, and the typical value of 1.5 is assigned to the curvature parameter n. In order to determine an appropriate value for E_2,

the amount of confinement developed in the compression side needs to be estimated first. An upper bound of 46.27 ksi was obtained for E_2 from the average of the experimental results of the short square CFFTs subjected to uniaxial compression (see Chapter 6). Based on studies by Rochette and Labossiere (1996), a lower bound of E_2=0 was also considered as an elastic-perfectly-plastic material with no strain hardening. In this case, the tube does not fully restrain the lateral expansion of concrete, but only contains the concrete to a lesser extent, not allowing a drop in stress. Similar results have been I, obtained by Ziara et al. (1995) for conventional RC beams with considerable transverse reinforcement.

The intercept stress f_o is obtained from E_2 and the geometry of the curve, as follows:

$$f_o = f'_{co} - E_2 \epsilon_{co} \tag{7.24}$$

where, E_{co} is the peak strain of plain concrete.

Using the upper-bound and lower-bound of E_2 along with the actual axial loads and the experimental top strains for each case, two analytical interaction diagrams were developed. Figure 7.20 shows the predicted and the experimental interaction curves.

The plots in Figure 7.20 suggest that the material properties obtained from the coupon tests are applicable. Good agreement is evident for the case of pure flexure (Point 1) for both values of E_2. Since the CFFT is axially under-reinforced, not much confinement is expected to develop on the compression side of the section in pure flexure.

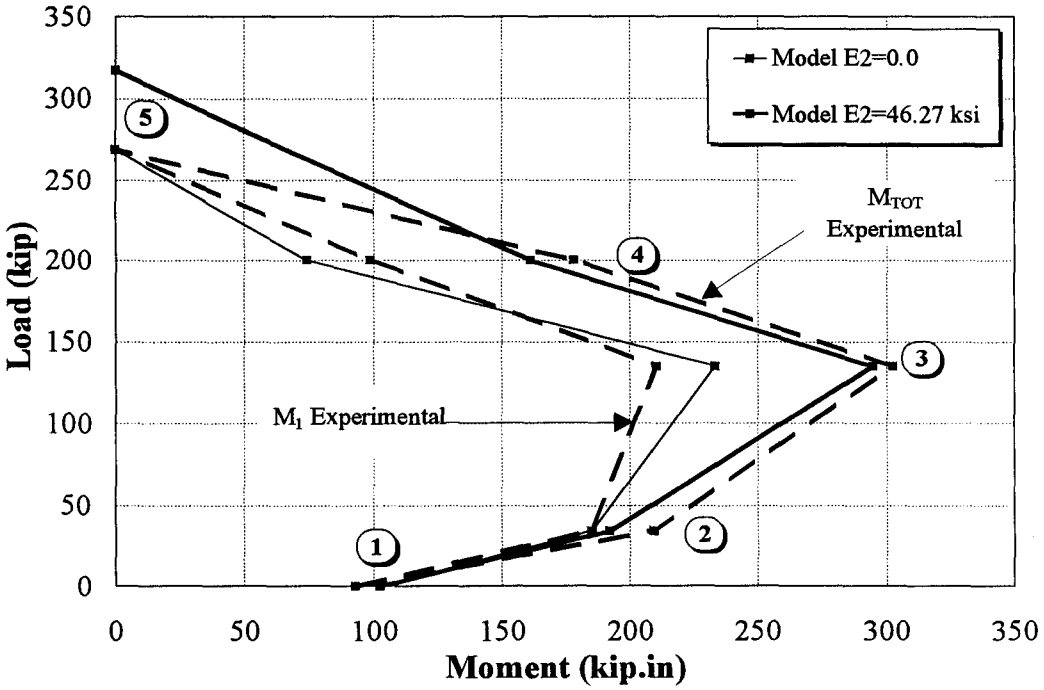

Figure 7.20 Comparison of experimental and analytical interaction diagrams

Also, the compression zone in the section is very shallow. Therefore, strain hardening of concrete does not affect the moment capacity of the section. On the other hand, the confinement effect is most pronounced for Specimen BC3 (Point 4) in the compression failure zone. For that specimen, the upper bound E_2 results in a much closer estimate of the moment capacity. Since the confinement effect increases with the increase in the axial load level, one may assume that the strain hardening of concrete, i.e., the second slope (E_2), is a function of P_i/P_o where P_i is the axial compressive load for specimen i, and P_o is the axial load capacity of the column.

The differences between the experimental and the predicted values are primarily attributed to the modeling of the tube wall as a single homogeneous layer, rather than a hybrid non-prismatic laminate. However, it can be concluded that the beam theory generally applies to the proposed CFFT. This facilitates its structural design, as discussed in the next section.

7.5 DESIGN ISSUES

According to the previous discussions, three major conclusions can be drawn:

1) The confinement provided by the tube improves both the load-carrying capacity and the ductility of the column.
2) The conventional beam theory can be used for the analysis and design of the CFFTs, provided that the mechanical bond between the tube and the concrete is fully developed.
3) The design of the FRP tube itself can be tailored to achieve the required strength and stiffness in the axial and transverse directions. The tube governs the flexural behavior as well as the level of confinement.

In order to design a CFFT, the following input data is needed:

1) The design loads: axial and/or flexural;
2) The shape of the column: circular or square; and
3) The strength of the concrete.

A preliminary design of the column should be carried out using different lay-ups. The mechanical properties of the tubes are usually provided by the manufacturer.

Otherwise, the procedure in Chapter 4 can be followed (using **GENLAM** program) to establish the required properties.

In case of circular CFFTs, the confinement model in Chapter 5 may be used directly to develop the full stress-strain curve of the column. Likewise, in the case of square CFFTs, the ultimate load may be determined using the program developed in the previous section. As far as the confinement is concerned, an elastic-perfectly-plastic stress strain curve (E_2 = 0.0) is proposed for the encased concrete, which provides a conservative solution.

It is important to note that both serviceability and ultimate limit states need to be checked for design of CFFTs. Deflections, secondary moments, slenderness and stiffness calculations are of great significance. For the ultimate design, the same load factors as prescribed by ACI may be used, since type of material should not affect the load calculations. As for the strength reduction factor, it seems appropriate to use a (Φ of 0.75 which is prescribed by ACI for spirally-reinforced columns. This, however, needs to be further investigated.

8.

SUMMARY, CONCLUSIONS, AND RECOMMENDATIONS

8.1 SUMMARY

The present study is a comprehensive experimental and analytical investigation of the concrete-filled FRP tubes. The main focus of the study is the confinement of the encased concrete under axial, and axial-flexural loads. An extended literature review was provided discussing the existing confinement models developed for steel-, and FRP-confined concrete columns and beam columns. Three series of uniaxial compression tests were conducted for circular short CFFTs, with a total of 54 specimens. The behavior of those specimens was investigated in the axial and hoop directions. Based on the test results, a new confinement model for FRP-confined concrete was proposed. The model consists of a simple polynomial equation, which predicts the stress-strain response of FRPconfined concrete columns in both the axial and lateral directions. The parameters of the model are basically functions of the material properties of both the FRP jacket and the concrete core. The proposed model was verified against the experimental results of the present study as well as those by other researchers. Good correlation was evident.

In order to obtain accurate material properties for the FRP jacket, a detailed mechanical analysis is required. A brief review of the mechanics of fiber composite was included, along with the application to the present filament-wound FRP tube. The properties of the FRP tube were also determined experimentally by means of the split-disk test.

The behavior of the CFFT beam column was also investigated. A square FRP tube was manufactured, which included longitudinal and transversal reinforcing fibers, as well as internal resin ribs. The function of the ribs was primarily to provide of the required bond between the FRP tube and the concrete core. Three short specimens, 7" x 7" x 12", were tested under uniaxial compression, along with five long specimens, 7" x 7" x 52", under different levels of axial-flexural loadings. The results of these tests constituted the force-moment interaction diagram of the proposed column. The test results were further compared with equivalent RC sections, with regard to the load-carrying capacity and the ductility of both mechanisms. The CFFT proved to have a superior behavior, especially in compression control region.

A sectional analysis was conducted for the square CFFT beam-column using the fiber element model. It was concluded that the conventional beam theory can be applied to CFFT. As a conclusion of the study, a step-by-step design procedure for CFFT was provided.

8.2 CONCLUSIONS

The findings of this research has been summarized in the following sections:

8.2.1 Circular CFFf Under Uniaxial Compression

1) The stress-strain response of FRP-confined concrete is bilinear in both the axial and lateral directions. The first slope of the response depends basically on the concrete core, while the stiffness of the FRP jacket is controls the second slope.

2) The bend point between the two slopes takes place at a stress level corresponding to the unconfined strength of the concrete core.

3) By plotting the volumetric strains, it was revealed that FRP jackets are capable of containing the encased concrete more efficiently than steel jackets. This is attributed to the fact the FRP is a linearly elastic material and does not have a yield. This was further confirmed by comparing the dilation characteristics of the FRP- and steel-confined concrete.

4) The confinement models calibrated for steel-confined concrete are not applicable to FRP-confined concrete.

5) In order to predict the response of FRP-confined concrete, a detailed mechanical analysis of the FRP jacket is required.

6) The proposed confinement model is capable of predicting the stress-strain responses in both the axial and lateral directions for different FRP materials.

7) The load-carrying capacity of the CFFT is considerably higher than the conventional RC column. The strength enhancement is primarily attributed to the confinement effect.

8.2.2 Square CFFT beam-columns

1) The internal resin ribs proved effective in preventing the slippage between concrete and the FRP. They also contributed to the load transfer between the tube and the concrete core, and to the crack containment on the tension side.

2) The failure of CFFT beam columns was ductile with much warning.

3) The confinement provided by the FRP tube improves both the load-carrying capacity and the ductility of the column.

4) CFFTs are superior to the corresponding RC sections as far as the load-carrying capacity is concerned.

5) The ductility of CFFT beam-columns is comparable to conventional RC sections in compression control region of the interaction diagram.

6) The conventional beam theory can be used for the analysis of the CFFTs, provided that the mechanical bond between the tube and the concrete is fully developed.

7) The design of the FRP tube itself can be tailored to achieve the required strength and stiffness in the axial and transverse directions. The tube governs the flexural behavior as well as the level of confinement.

8.3 RECOMMENDATIONS FOR FURTHER RESEARCH

The present study focused on the structural feasibility of CFFTs. Yet, a list of other related issues are recommended for further research:

1) Effect of cross section on the beam column behavior of CFFTs;

2) Serviceability issues such as deflections, required depth-to-span ratios, cracking, and vibrations (e.g. natural frequency of the system);

3) Stability issues such as slenderness of CFFT as beam columns;

4) Design criteria as related to the allowable stresses and/or strength reduction ` factors;

5) Implications of low stiffness of CFFTs (past the bend point on the stress-strain curve) on the design of CFFTs;

6) Feasibility of using CFFTs as over-reinforced beams which fail in compression,

7) Long term behavior and issues of creep, and fatigue;

8) Seismic performance of CFFT, especially from the point of view of ductility;

9) Connections of CFFT with other concrete members in the structure, and whether or not steel rebars are needed in the connections;

10) Durability and issues of corrosion due to glass-alkali reactions, ultraviolet rays, moisture intrusions, and effect of chemicals on the FRP tube;

11) Application issues such as vandalism, graphite, and painting;

12) Issues of skid resistance and abrasion when CFFTs are used as piles or pile splices;

13) Issues related to flammability and fire resistance both for bridges and building applications;

14) Impact of vehicles or ships for bridge piers or exterior building columns; 15) Drivability of CFFT piles; and

16) Contraction issues such as those encountered for precast or cast-in-place members**.**

Appendix A APPLICATION OF CONFINEMENT MODEL TO

SPECIMENS OF SERIES D

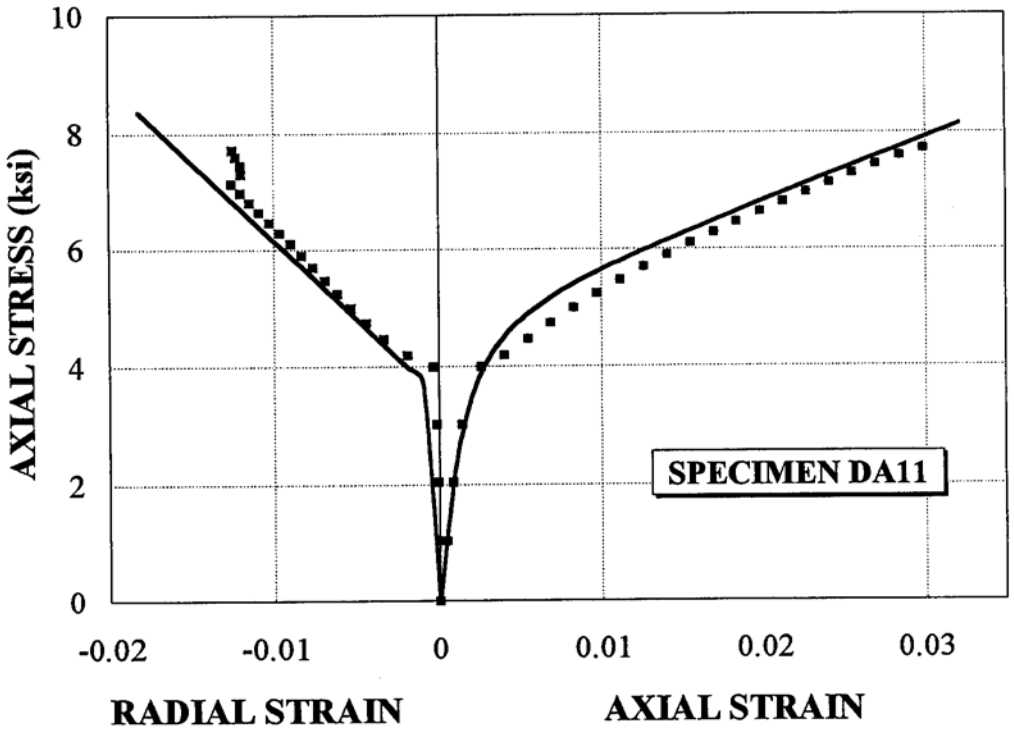

Figure A.1 Application of confinement model to Specimen DA11

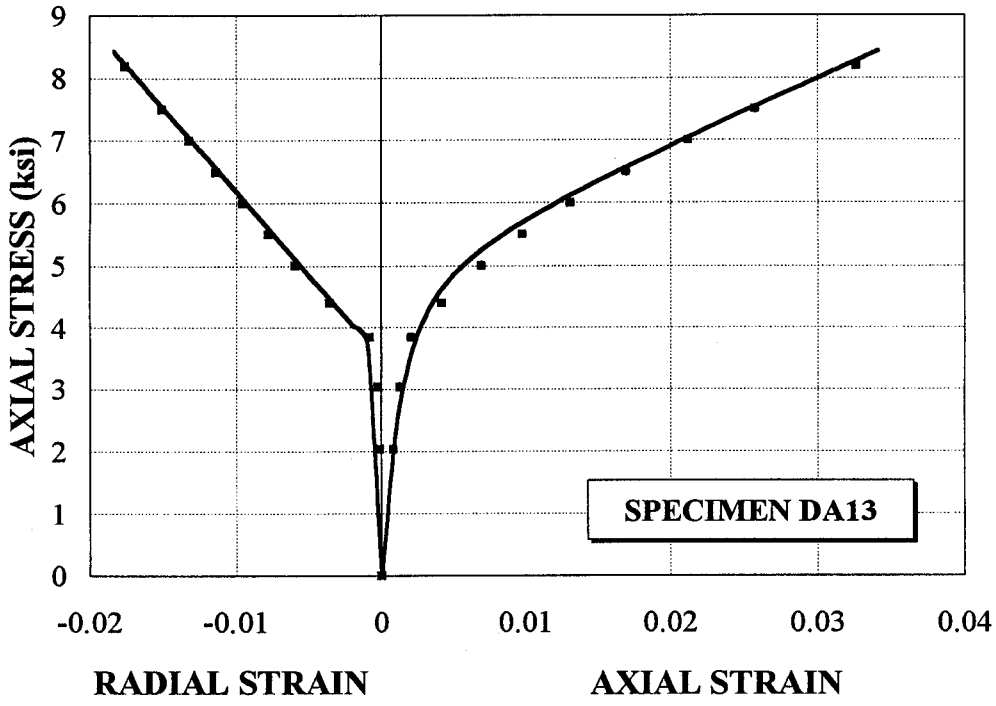

Figure A.2 Application of confinement model to Specimen DA13

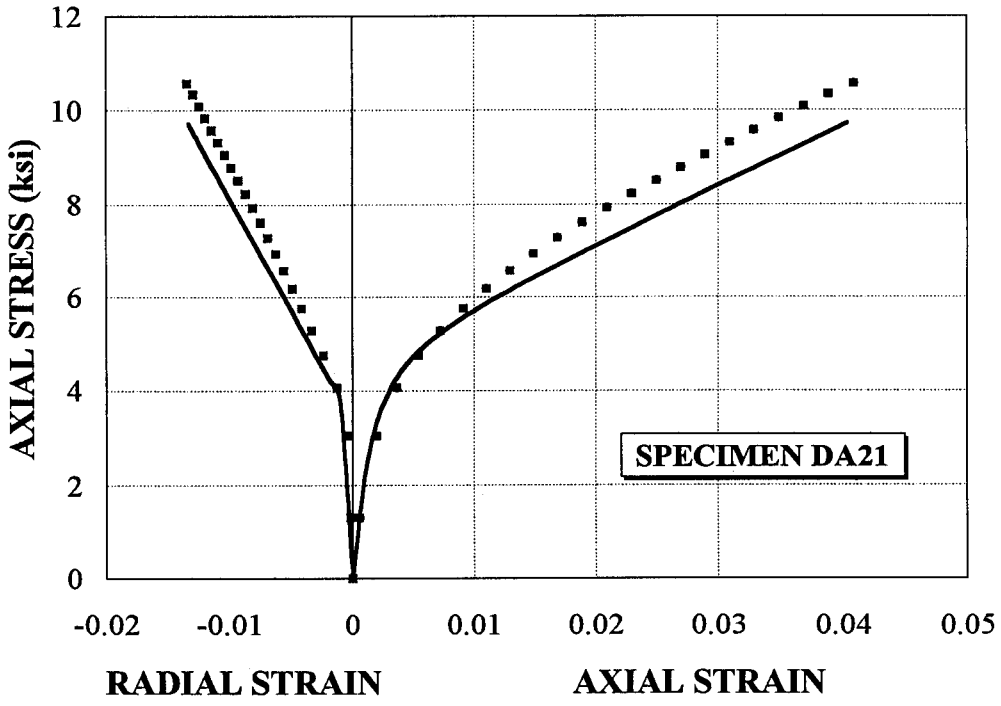

Figure A.3 Application of confinement model to Specimen DA21

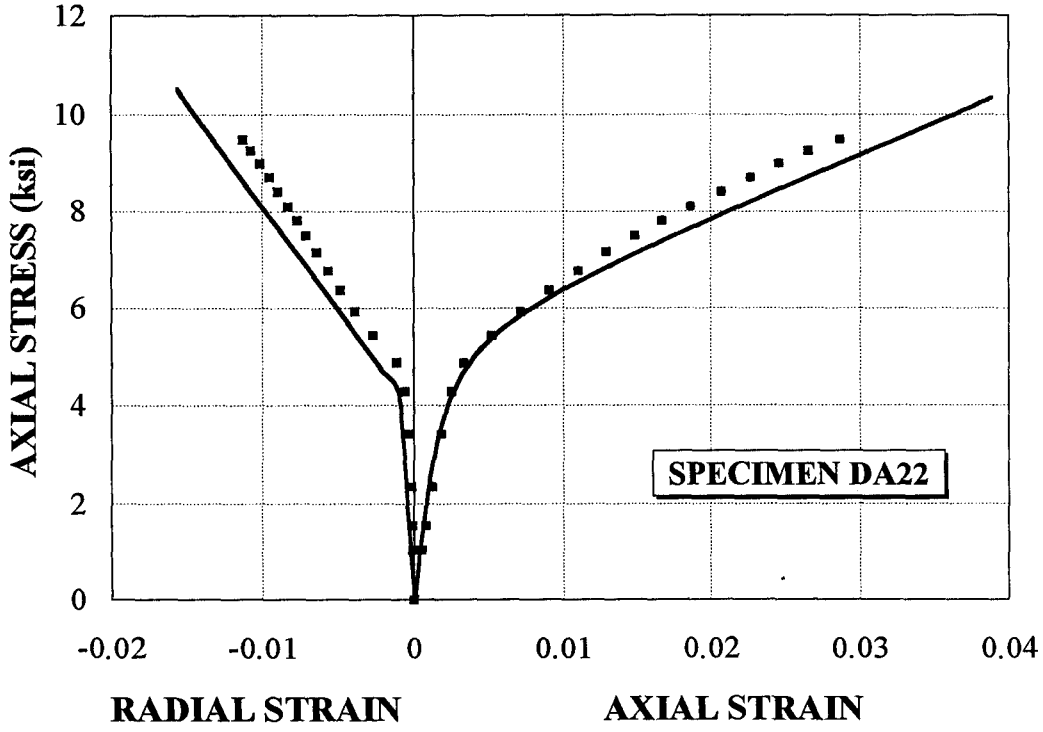

Figure A.4 Application of confinement model to Specimen DA22

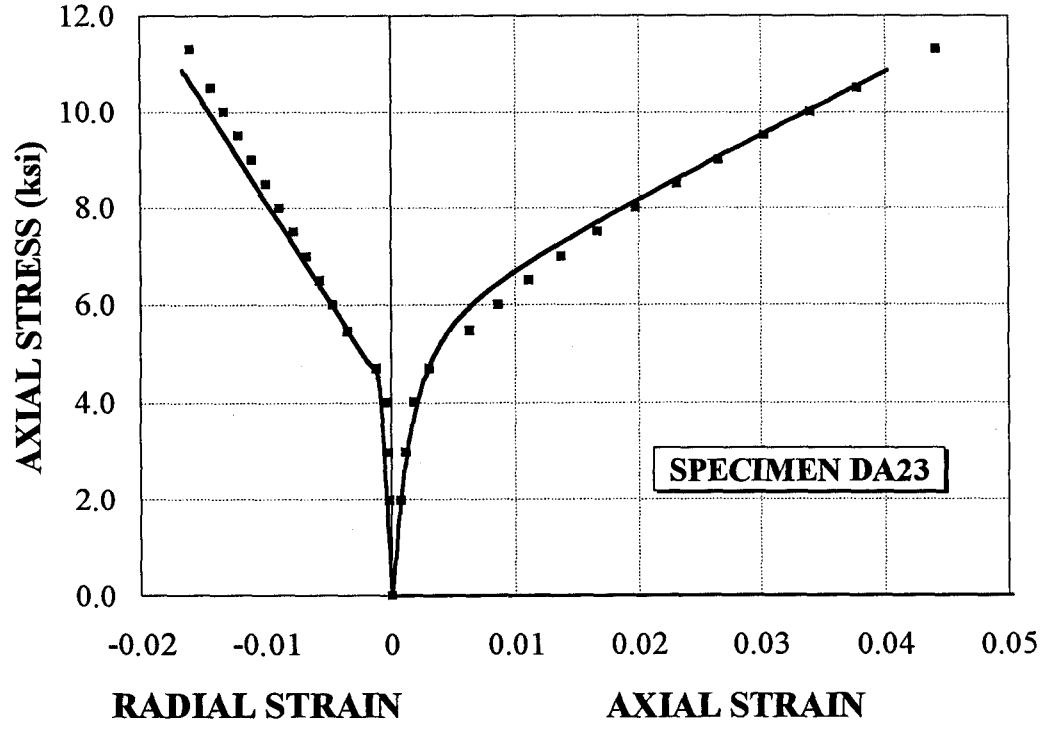

Figure A.5 Application of confinement model to Specimen DA23

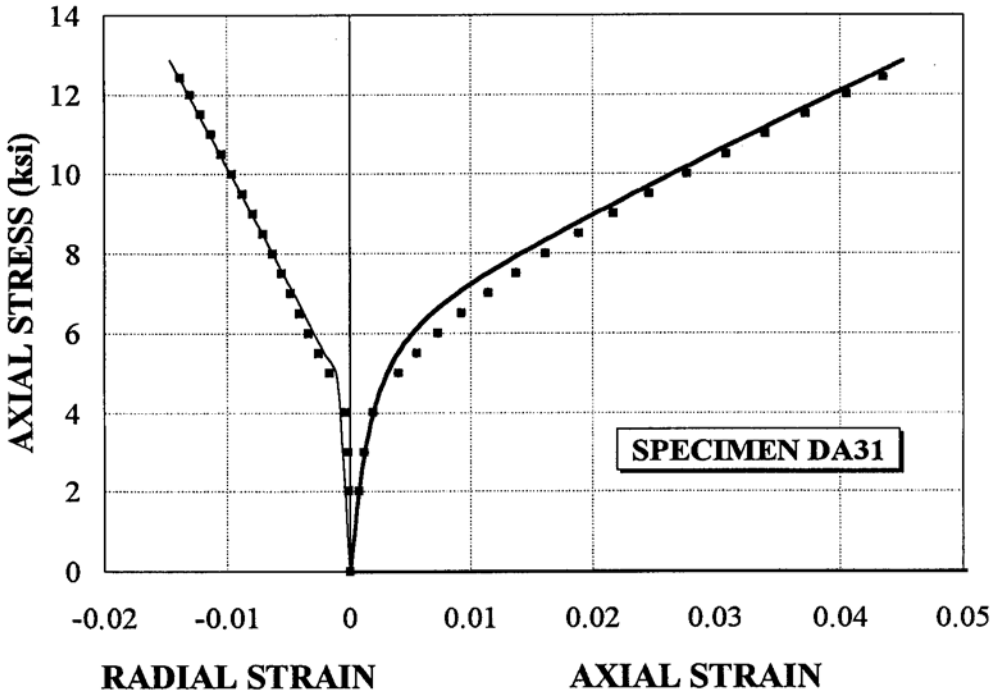

Figure A.6 Application of confinement model to Specimen DA31

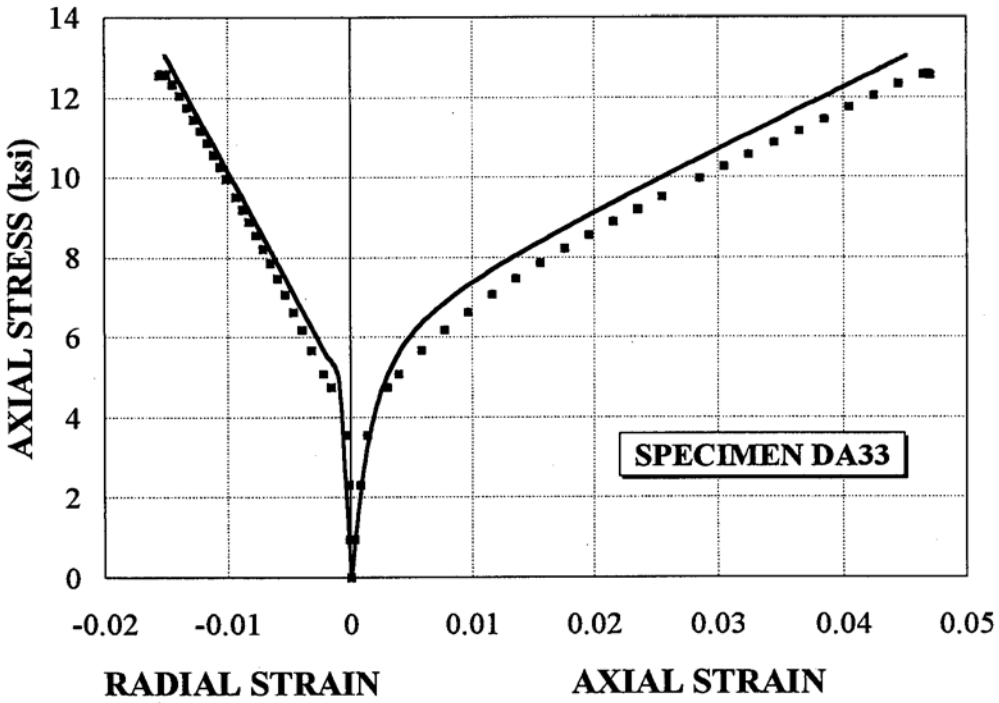

Figure A.7 Application of confinement model to Specimen DA33

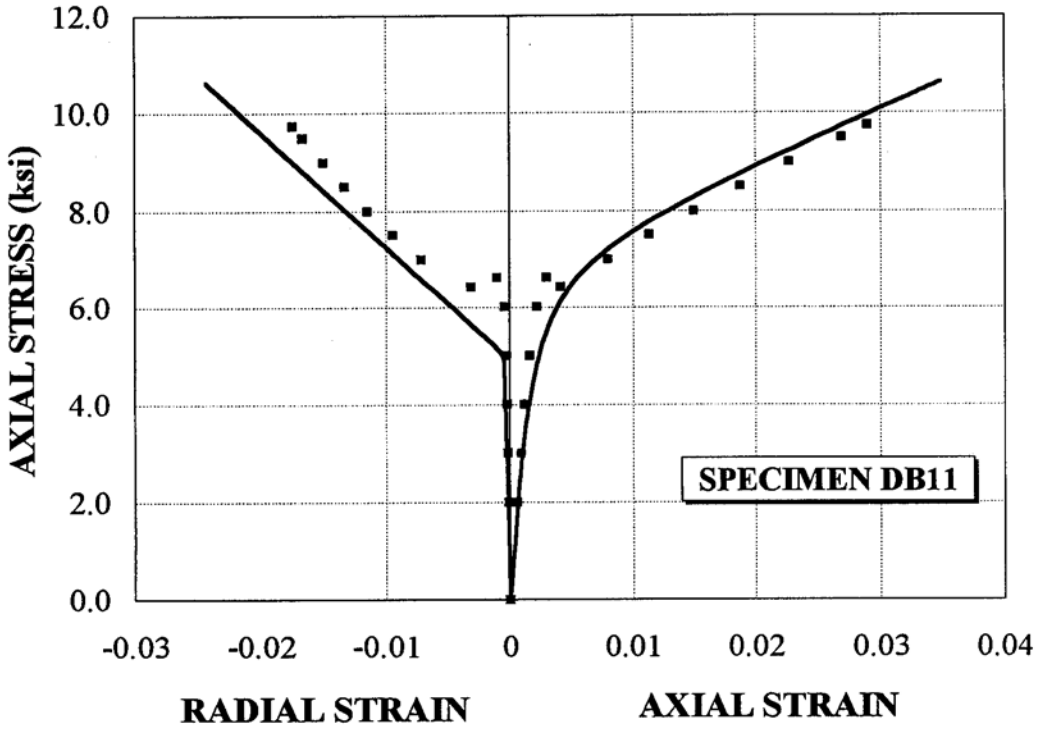

Figure A.8 Application of confinement model to Specimen DB11

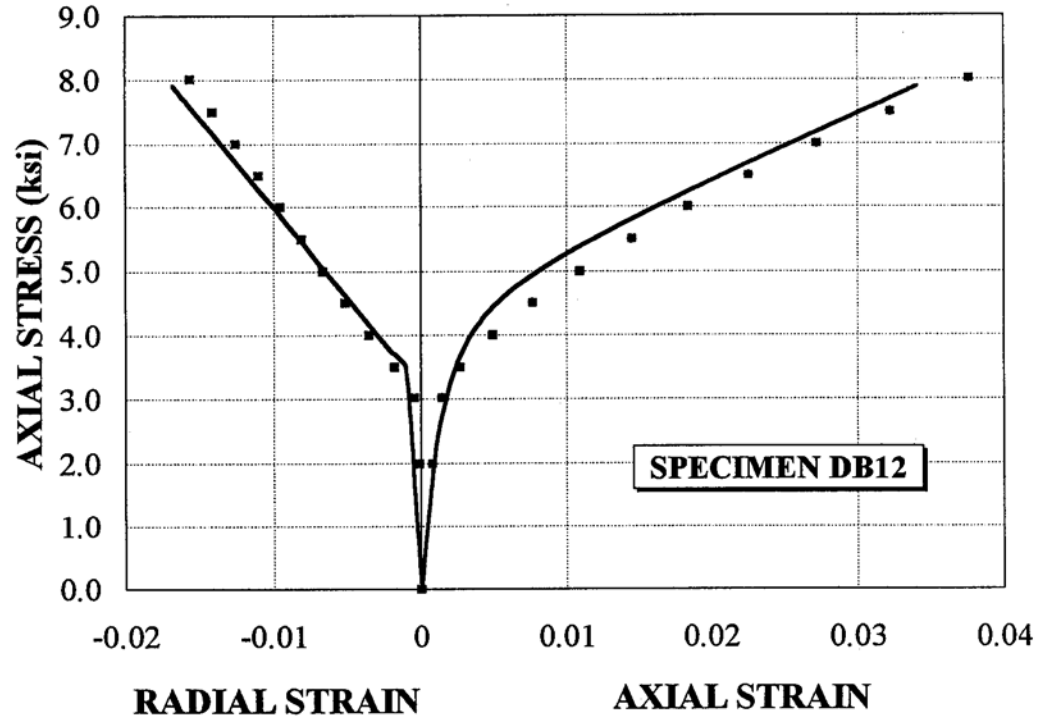

Figure A.9 Application of confinement model to Specimen DB12

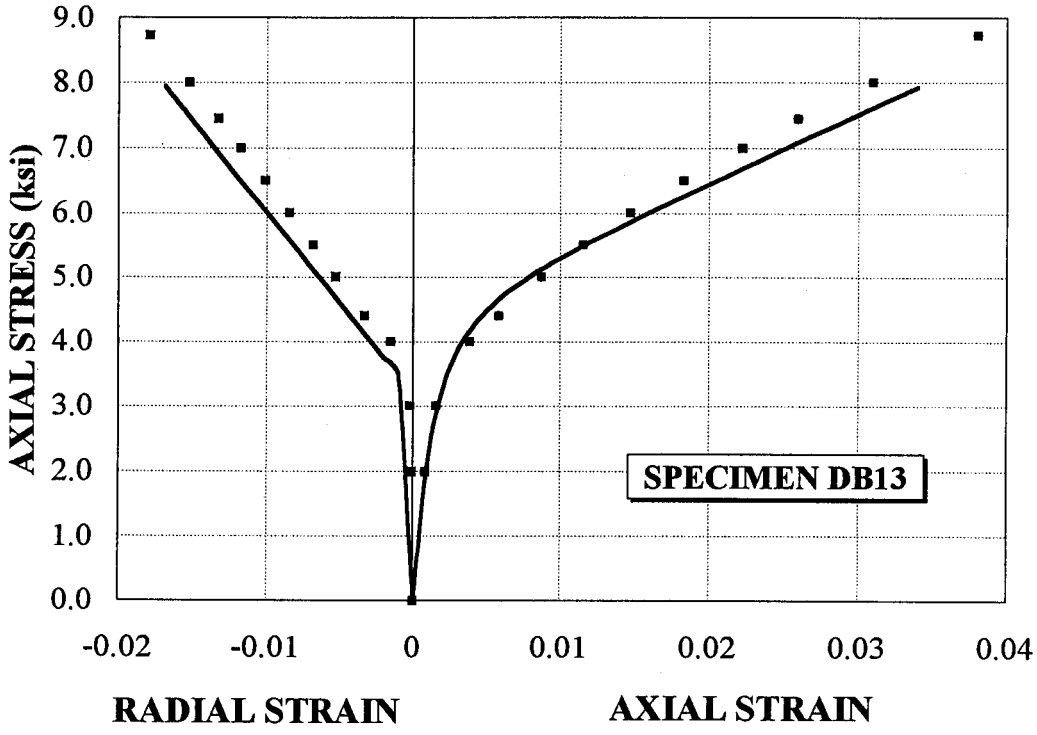

Figure A.10 Application of confinement model to Specimen DB13

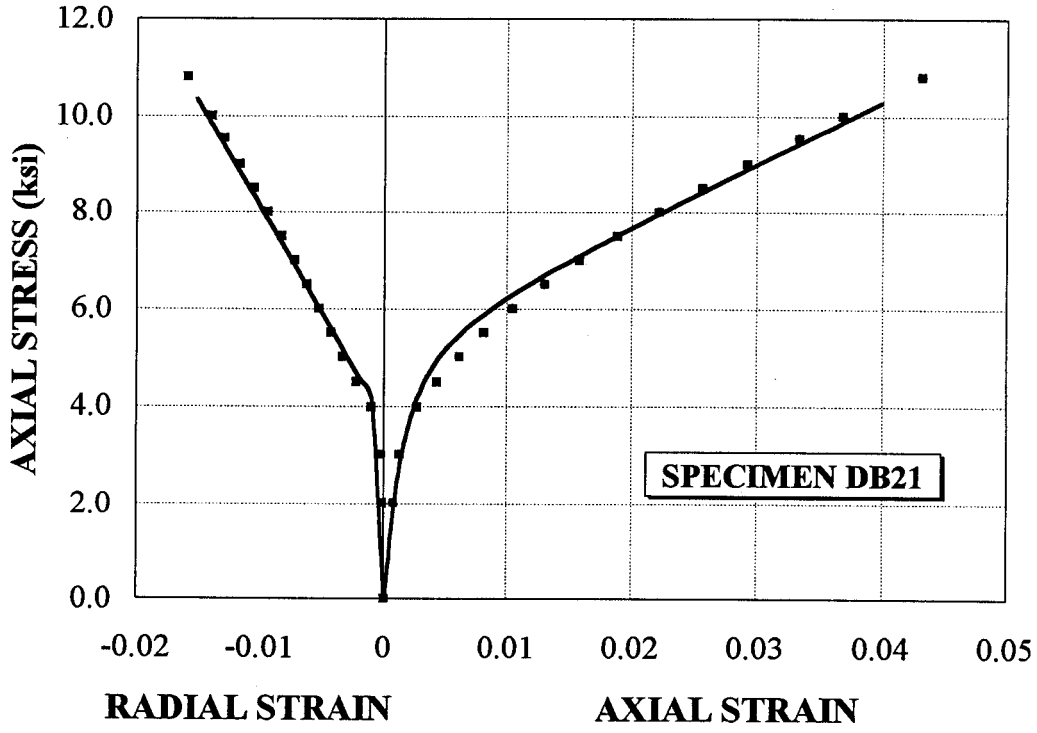

Figure A.11 Application of confinement model to Specimen DB21

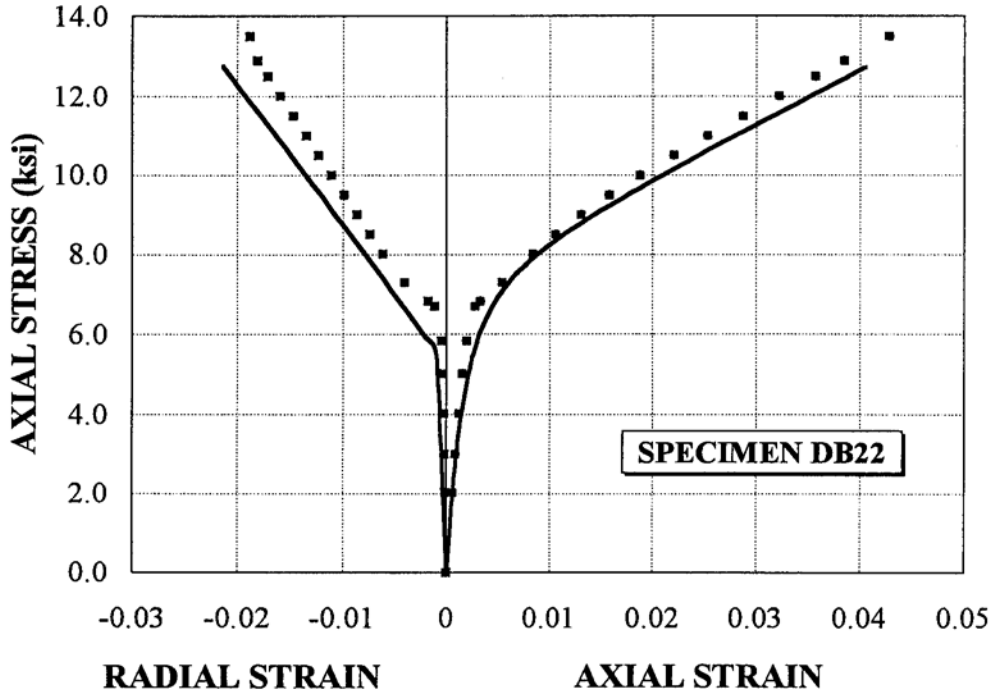

Figure A.12 Application of confinement model to Specimen DB22

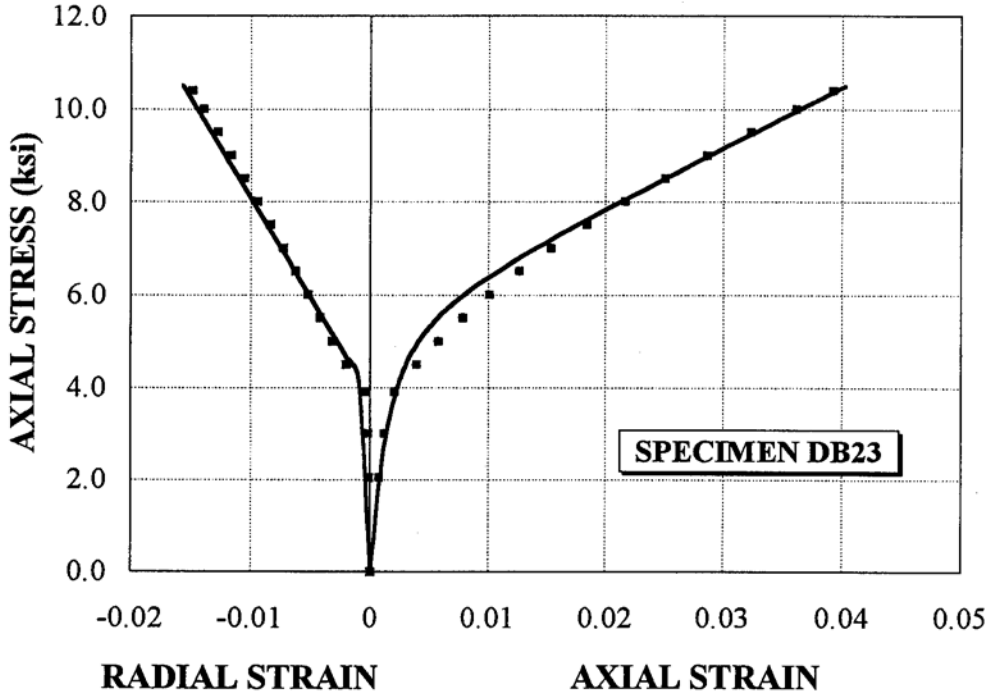

Figure A.13 Application of confinement model to Specimen DB23

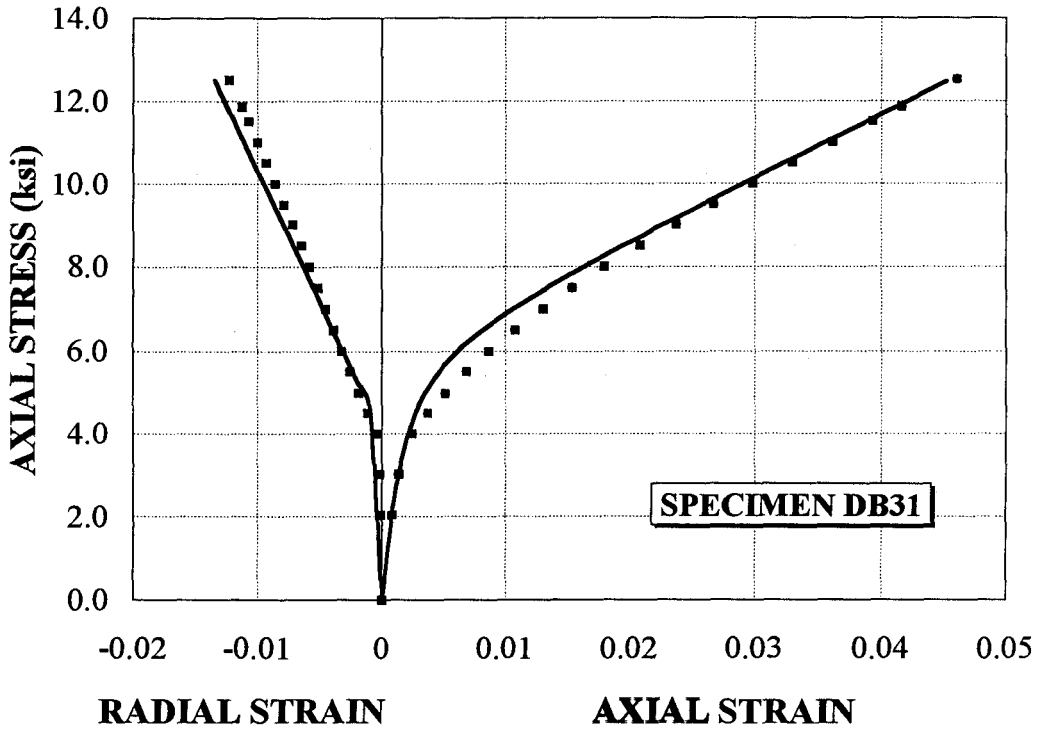

Figure A.14 Application of confinement model to Specimen DB31

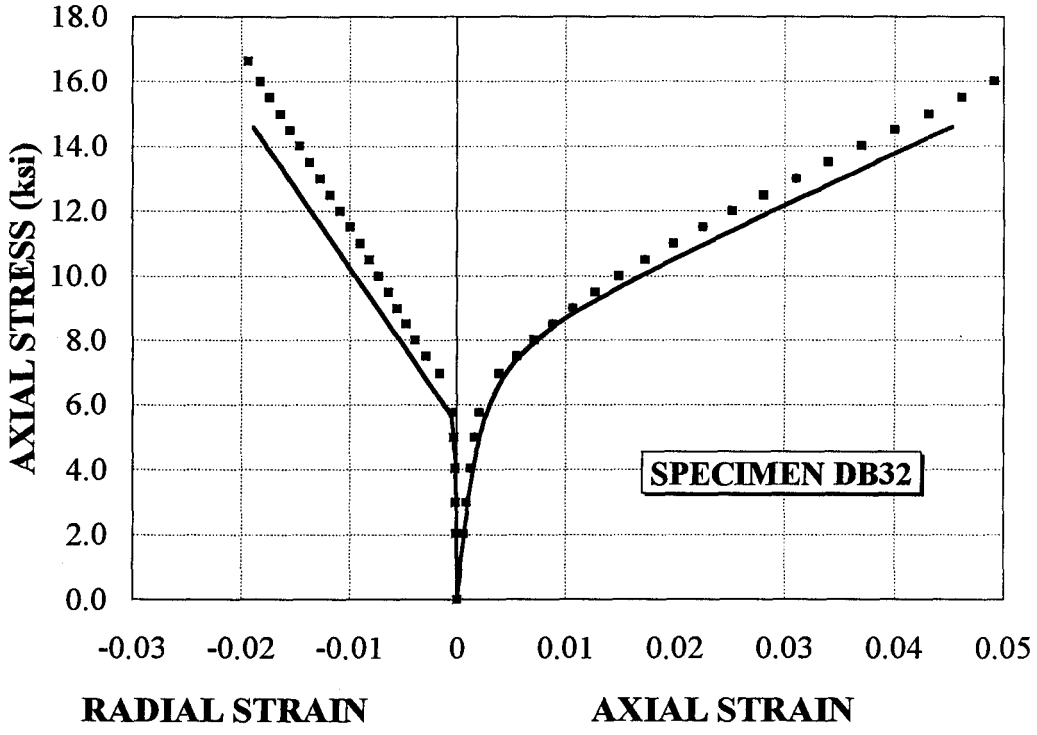

Figure A.15 Application of confinement model to Specimen DB32

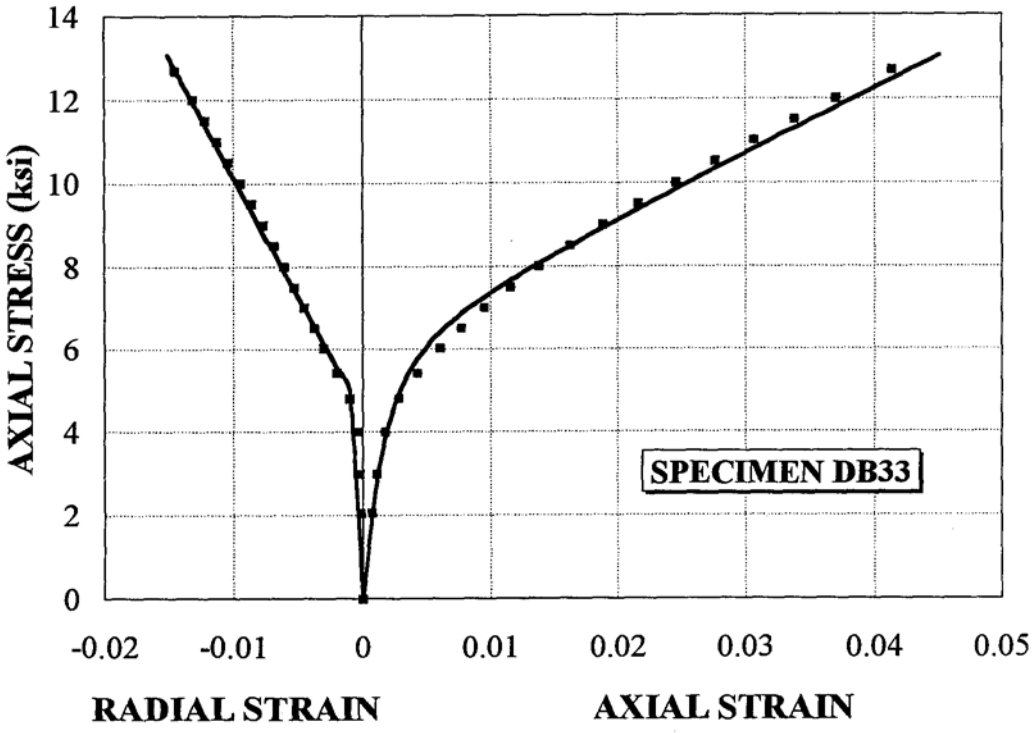

Figure A.16 Application of confinement model to Specimen DB33

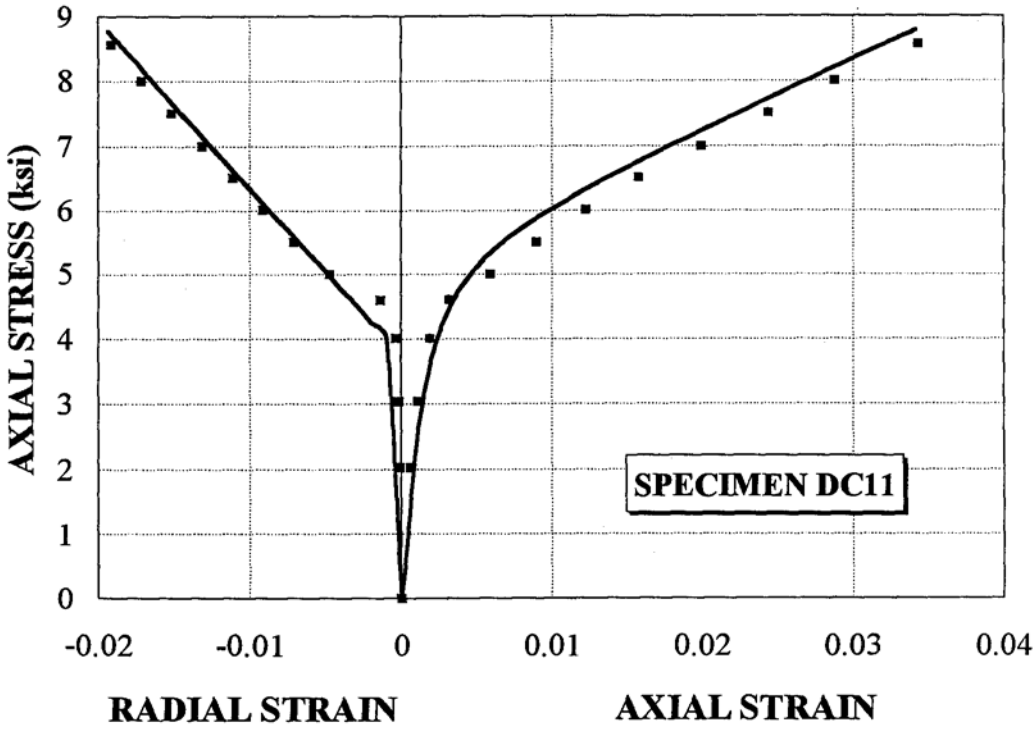

Figure A.17 Application of confinement model to Specimen DC11

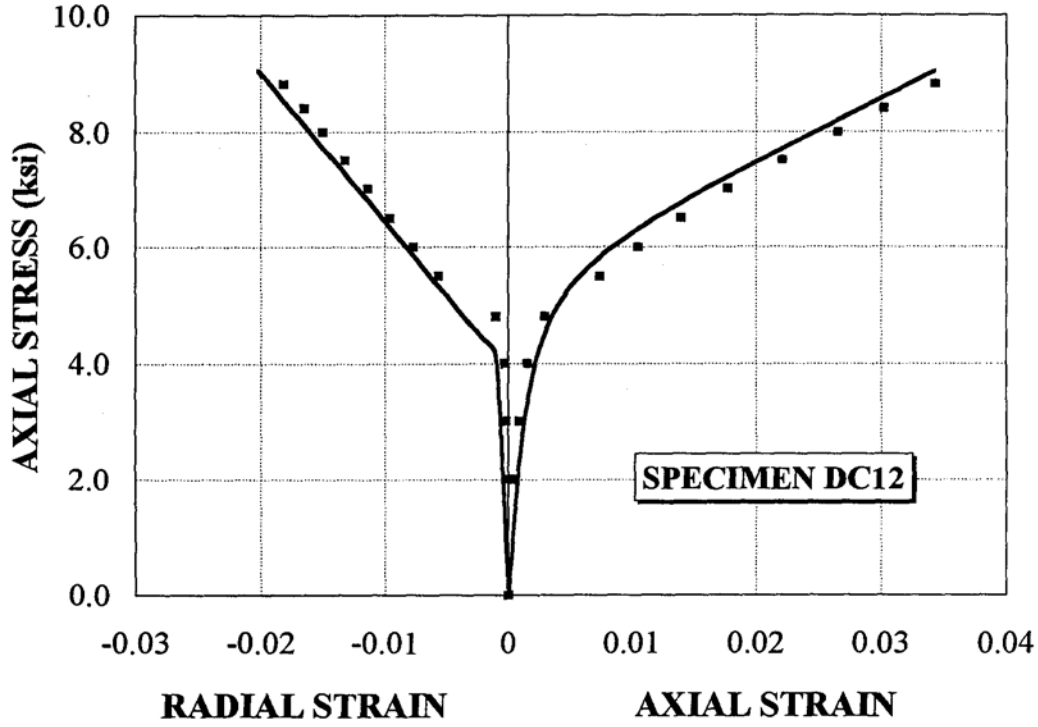

Figure A.18 Application of confinement model to Specimen DC12

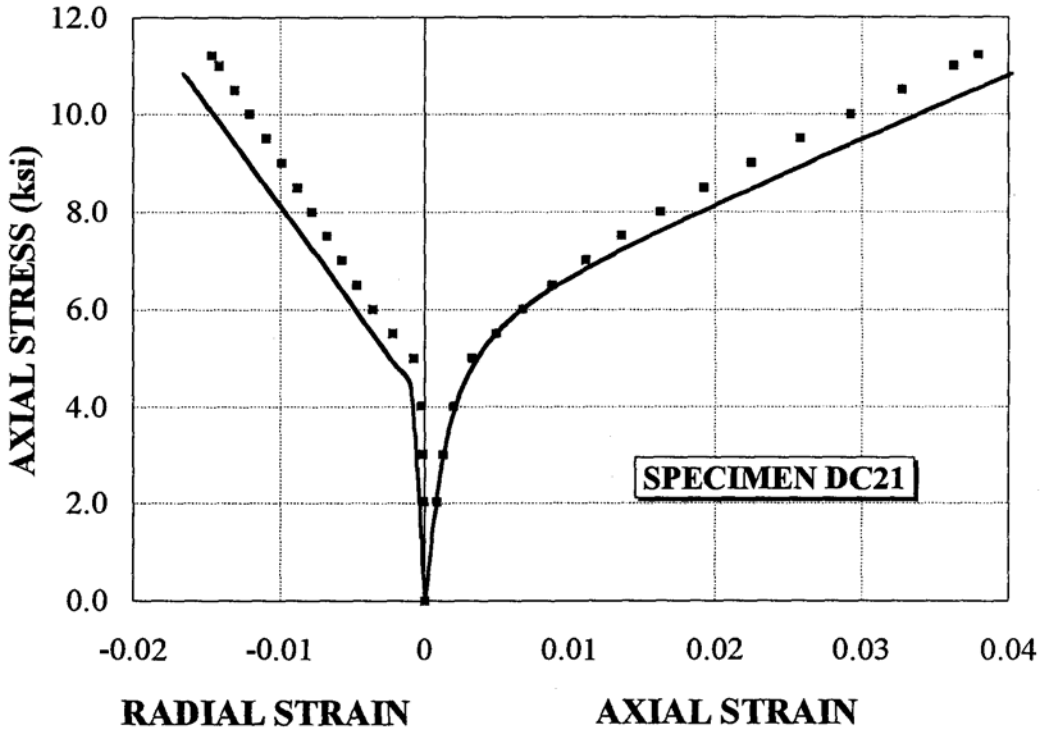

Figure A.19 Application of confinement model to Specimen DC21

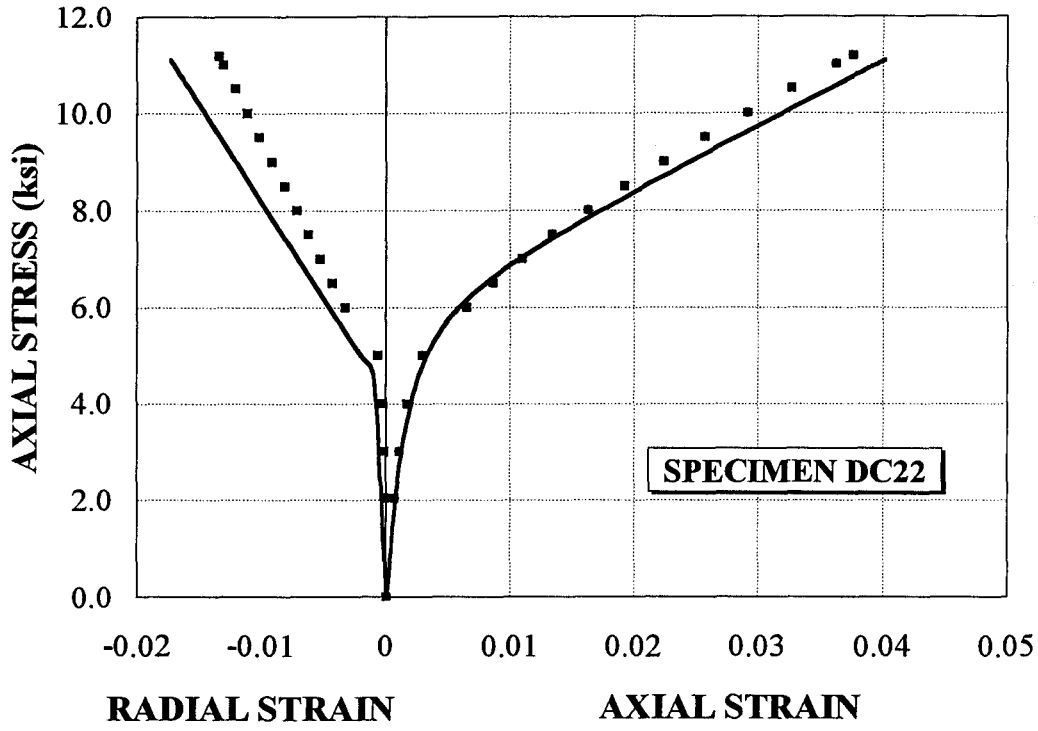

Figure A.20 Application of confinement model to Specimen DC22

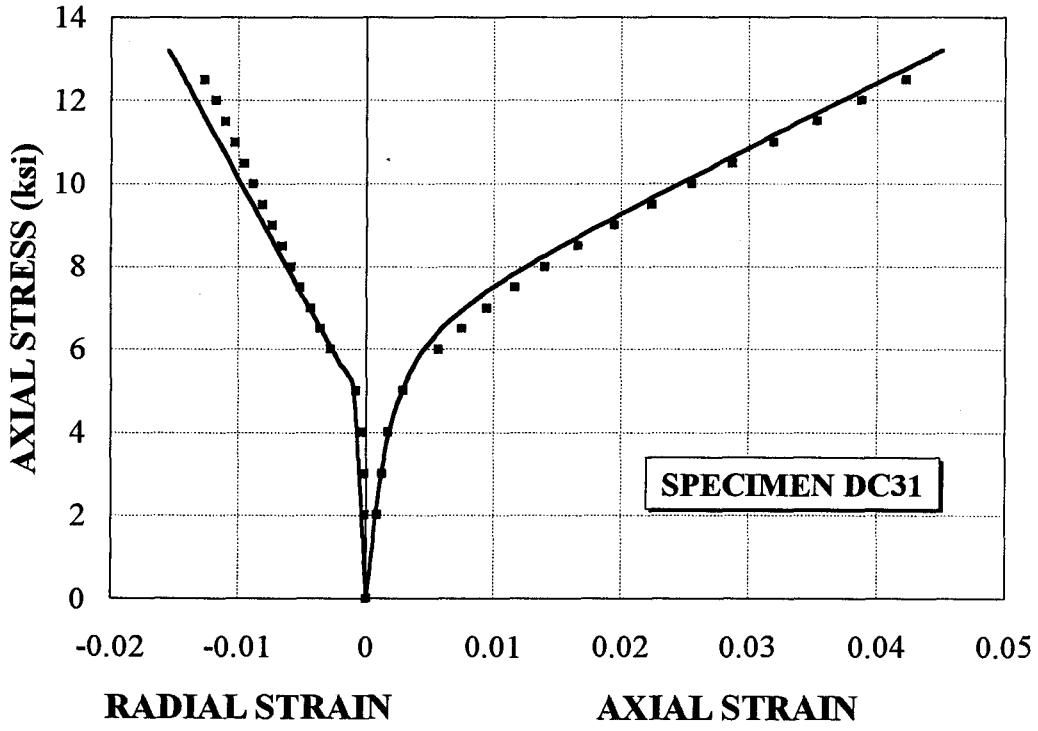

Figure A.21 Application of confinement model to Specimen DC31

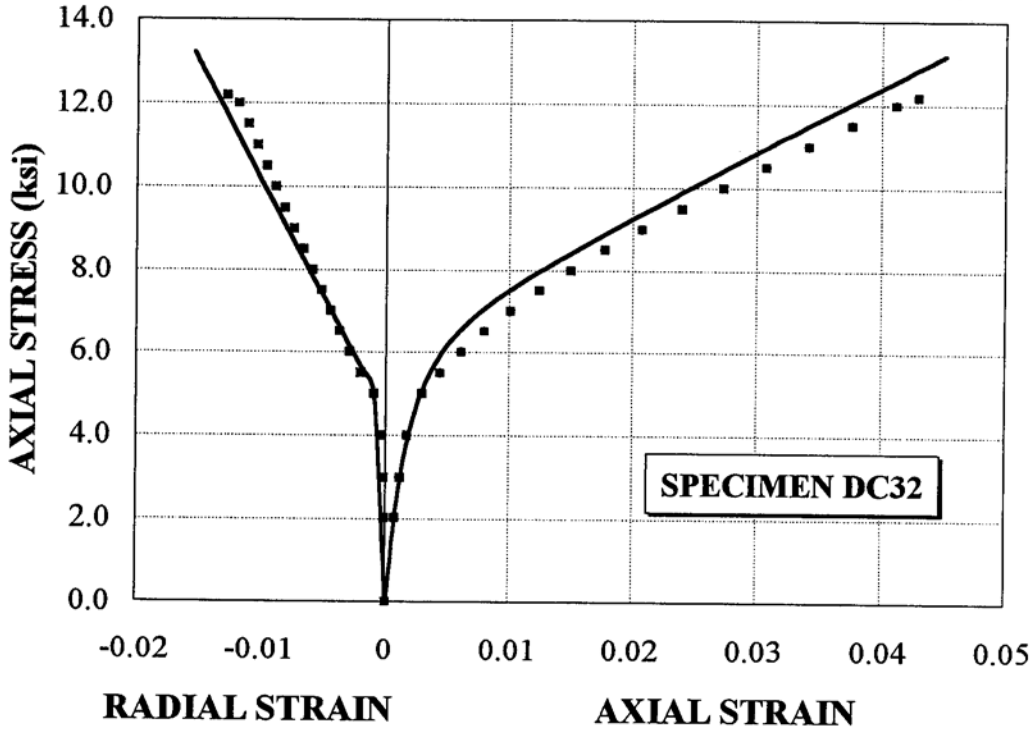

Figure A.22 Application of confinement model to Specimen DC32

Appendix B

RESULTS OF THE SPLIT-DISK TESTS

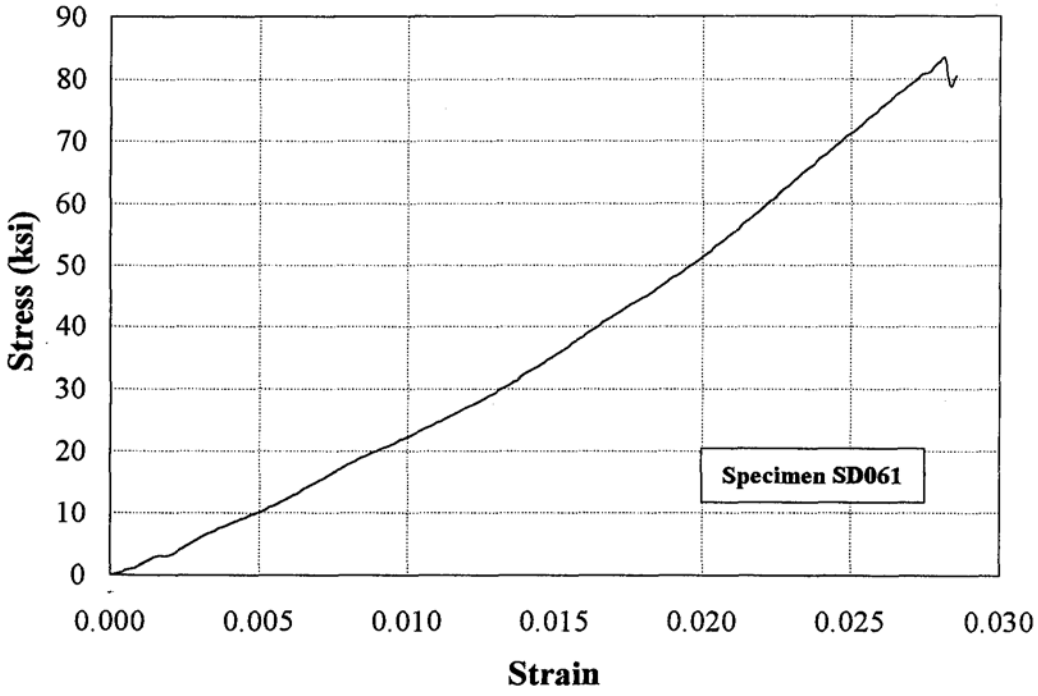

Figure B.1 Stress-strain curve of Specimen SD061

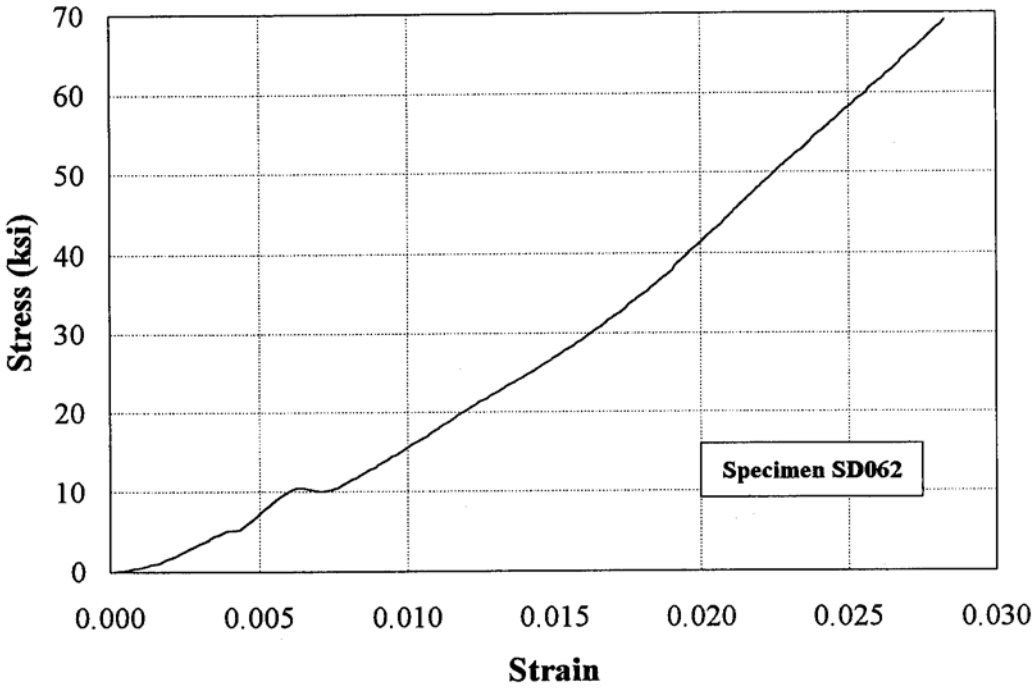

Figure B.2 Stress-strain curve of Specimen SD062

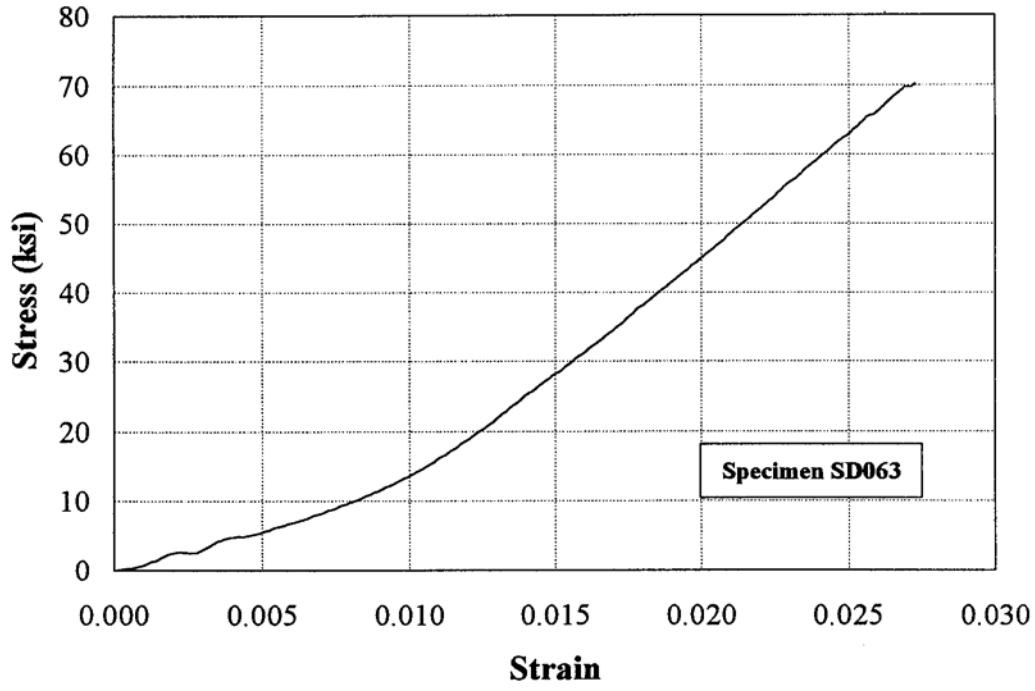

Figure B.3 Stress-strain curve of Specimen SD063

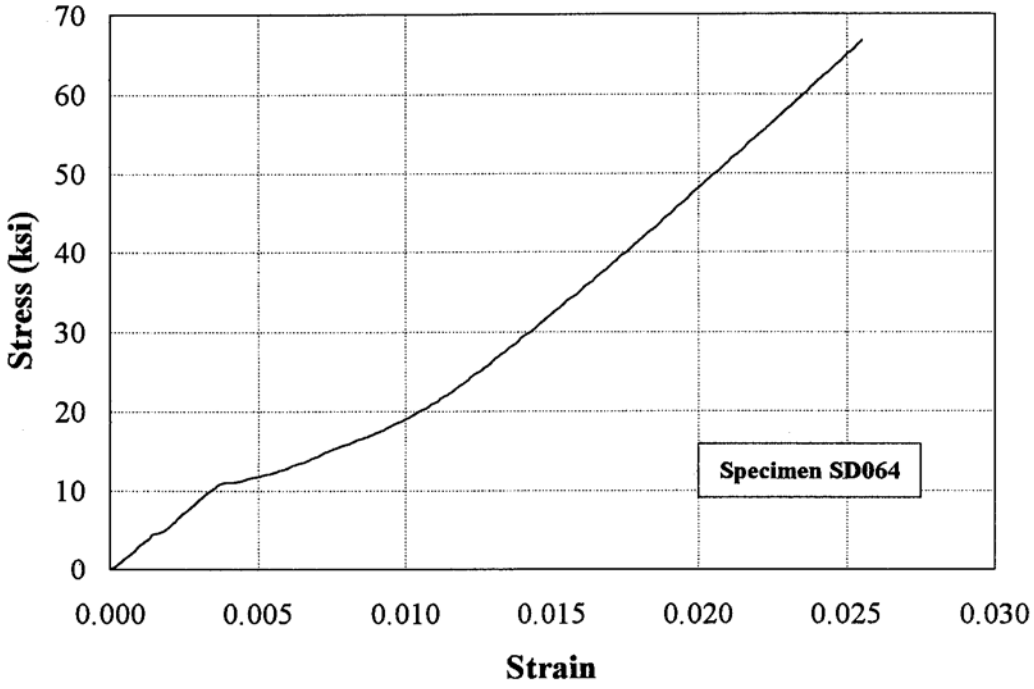

Figure B.4 Stress-strain curve of Specimen SD064

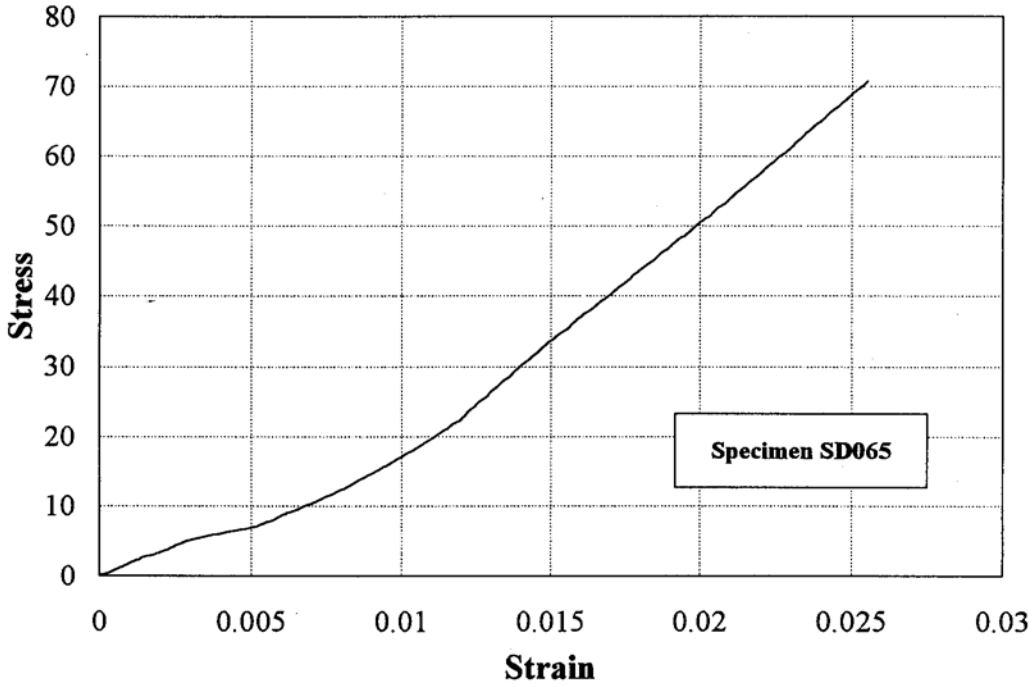

Figure B.5 Stress-strain curve of Specimen SD065

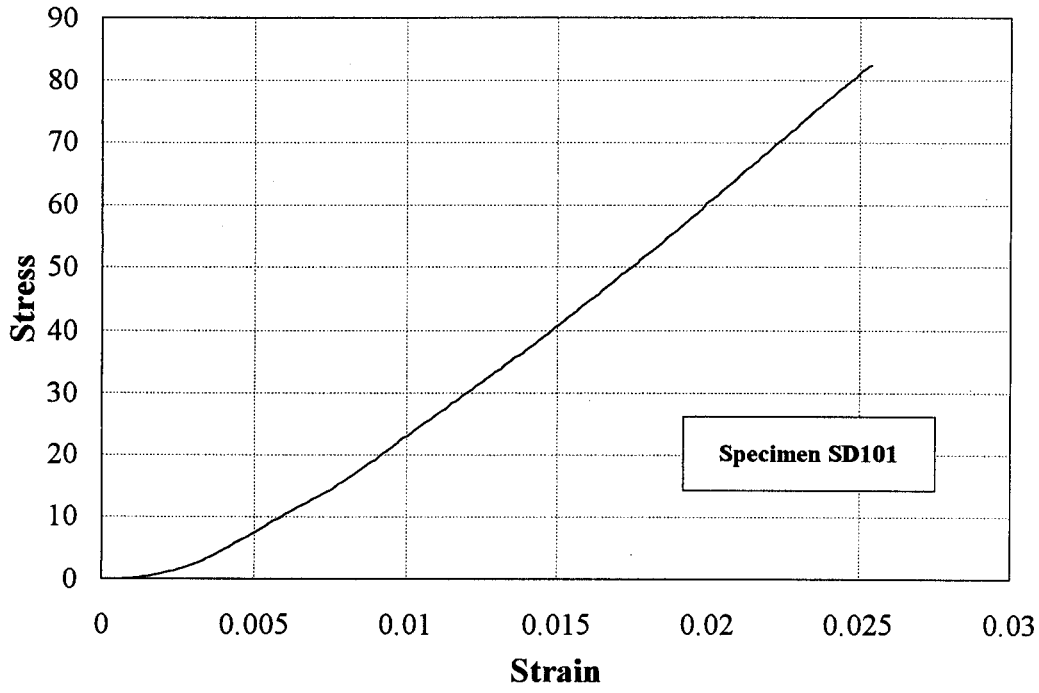

Figure B.6 Stress-strain curve of Specimen SD101

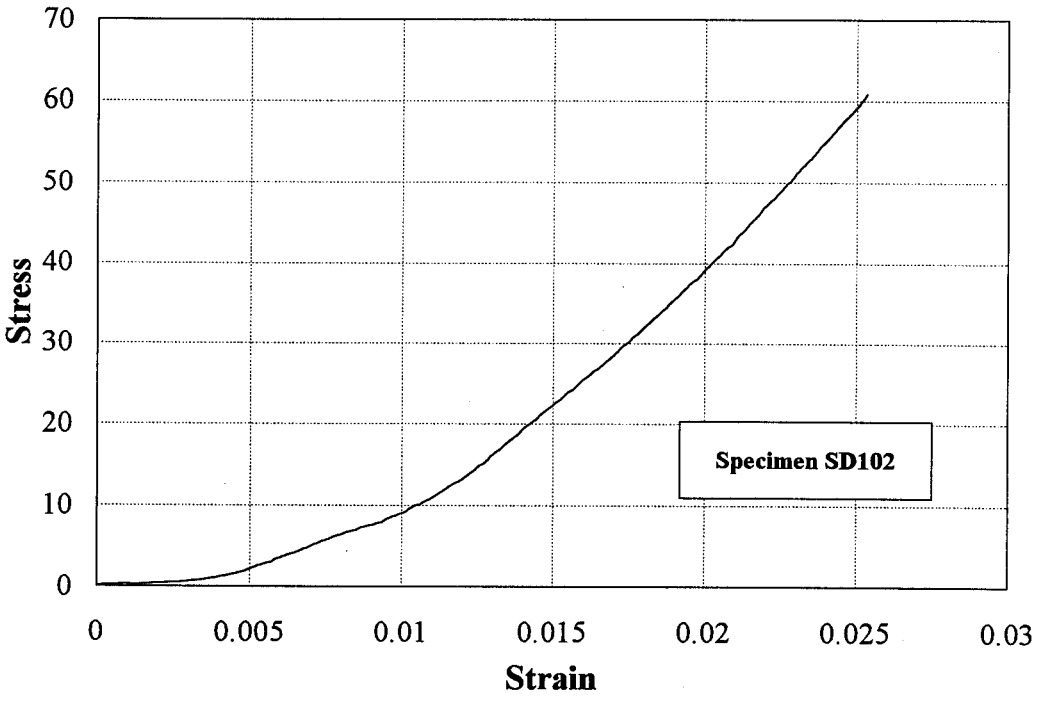

Figure B.7 Stress-strain curve of Specimen SD102

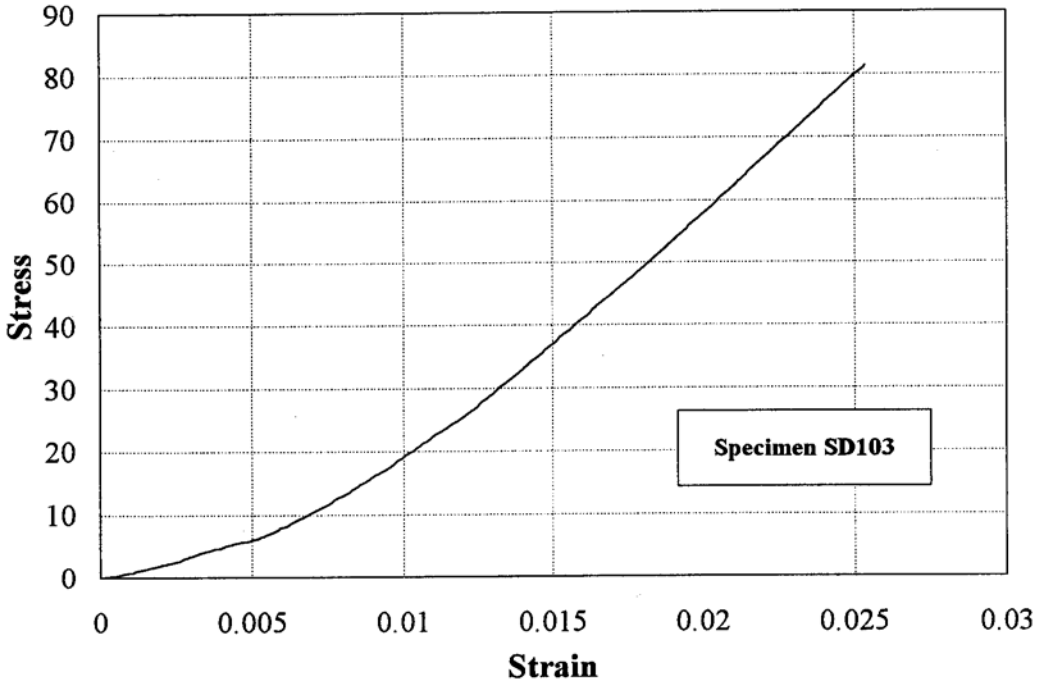

Figure B.8 Stress-strain curve of Specimen SD103

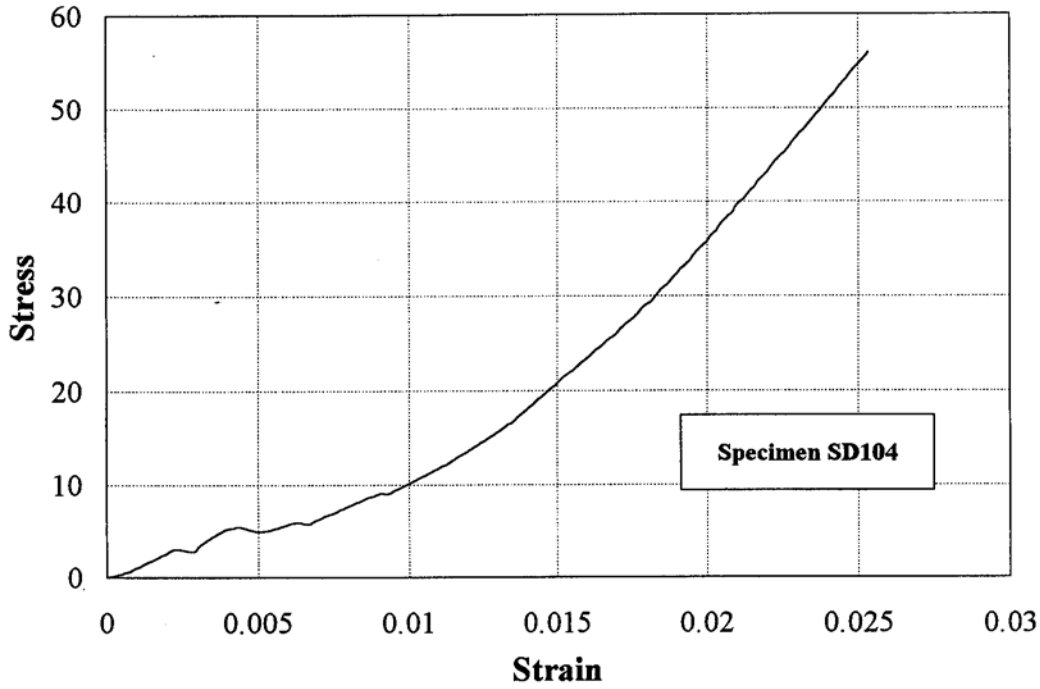

Figure B.9 Stress-strain curve of Specimen SD104

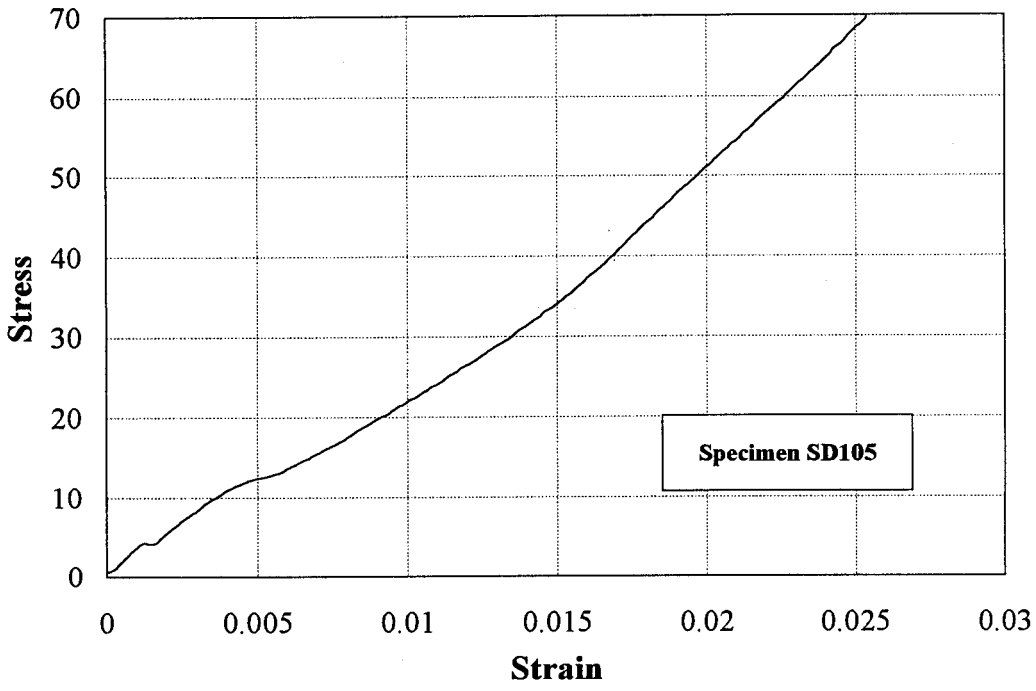

Figure B.10 Stress-strain curve of Specimen SD105

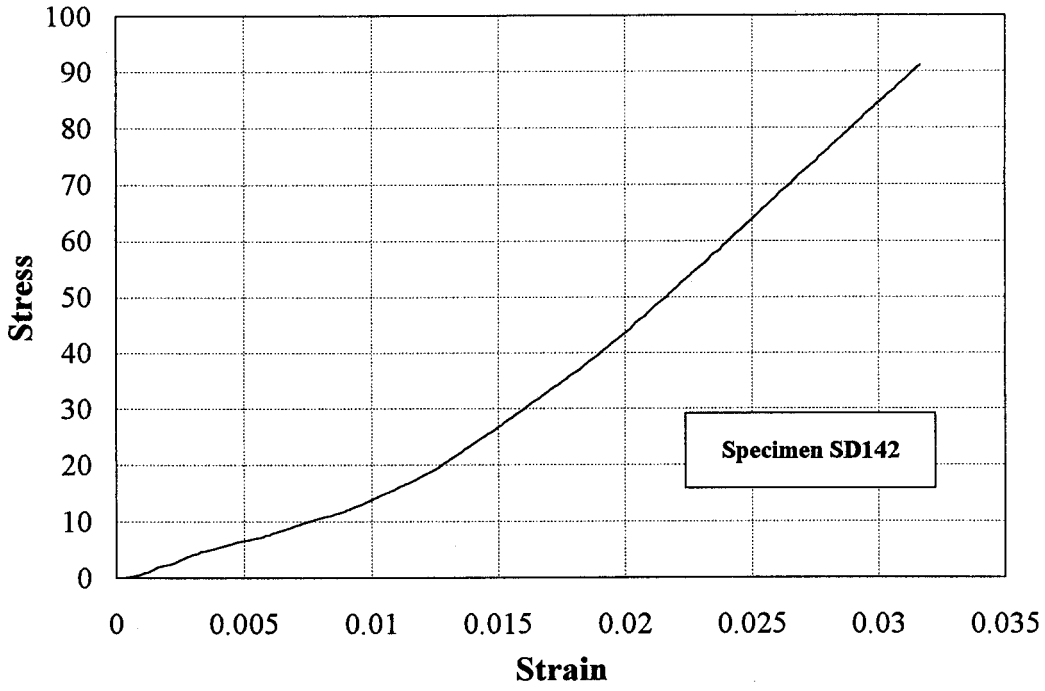

Figure B.11 Stress-strain curve of Specimen SD142

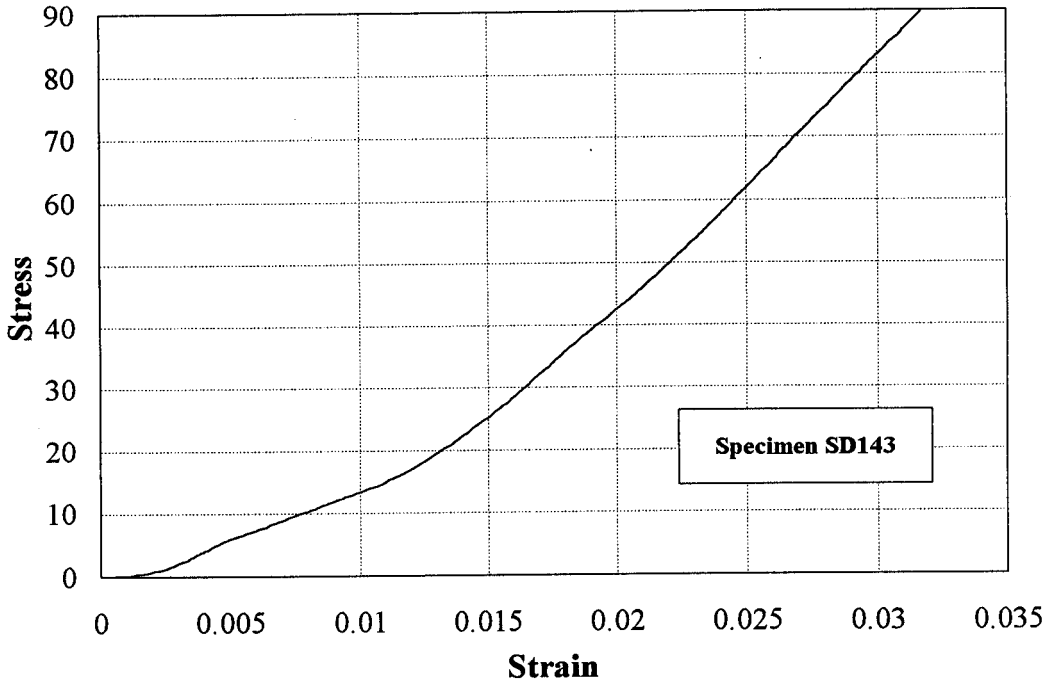

Figure B.12 Stress-strain curve of Specimen SD143

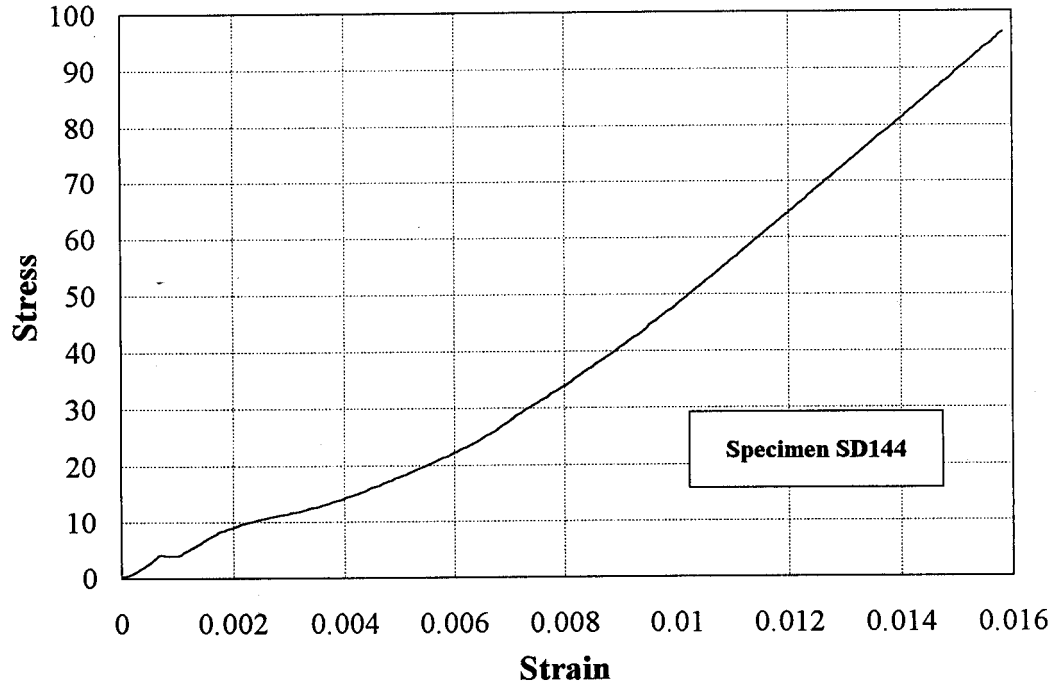

Figure B.13 Stress-strain curve of Specimen SD144

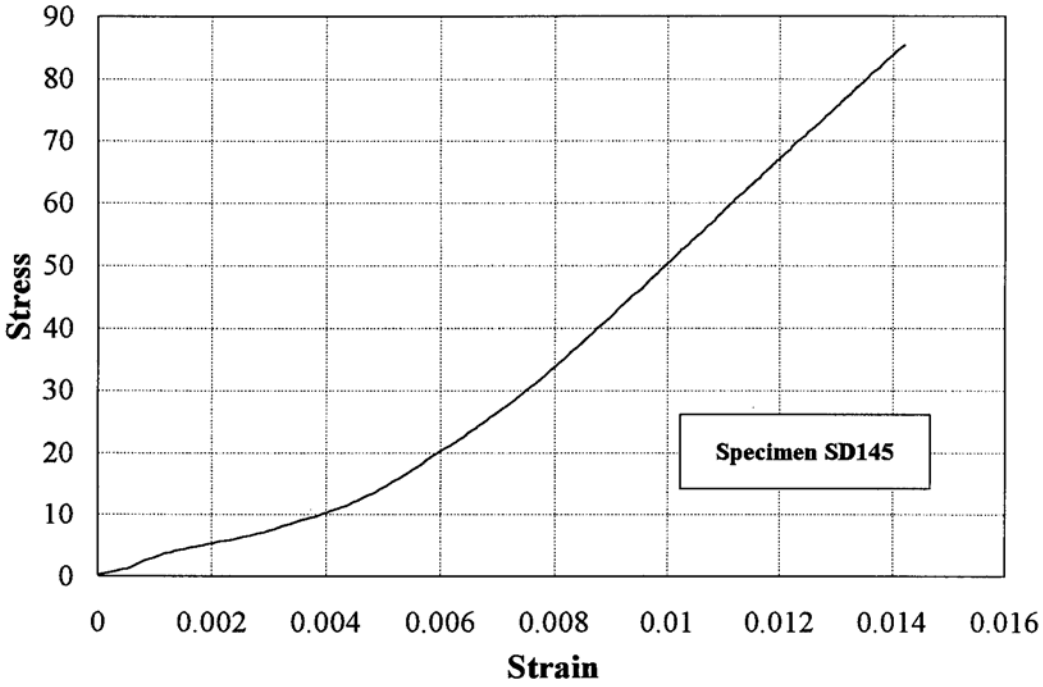

Figure B.14 Stress-strain curve of Specimen SD145

REFERENCES

ACI Committee 318. (1995). *Building code requirements for reinforced concrete.* ACI 318-95, American Concrete Institute, Detroit, MI.

Ahmad, S. H. (1981). "Properties of confined concrete under static and dynamic loads." *Ph.D. thesis,* Univ. of Illinois at Chicago Circle, Chicago, IL.

Ahmad, S. H., Khaloo, A. R, and Irshaid, A. (1991). `Behavior of concrete spirally confined by fiberglass filaments." *Mag. of Concrete Research,* 43 (156), 143-148.

Ahmad, S. H., and Shah, S. P. (1982a). "Complete triaxial stress-strain curves for concrete." *Proceedings,* ASCE, v. 108, ST4, 728-742.

Ahmad, S. H., and Shah, S. P. (1982b). "Stress-strain curves of concrete confined by spiral Reinforcement." ACI J, 79 (6), 484-490.

Almusallam, T. H., and Alsayed, S. H. (1995). "Stress-strain relationship of normal, high-strength and lightweight concrete." *Mag. of Concrete Research.,* 47 (170), 39-44.

ASTM (1991). "Standard test method for compressive properties of rigid plastics." ASTM *D-695,* American Society for Testing and Materials, Philadelphia, PA.

ASTM. (1992). "Apparent tensile strength of ring or tubular plastics and reinforced plastics by split disk method." ASTM *D-2290,* American Society for Testing and Materials, Philadelphia, PA.

ASTM. (1995). "Tensile properties of glass fiber strands, yarns, and rovings used in reinforced plastics." *ASTM D-2343,* American Society for Testing and Materials, Philadelphia, PA.

ASTM. (1995). "Tensile properties of polymer matrix composite materials." *ASTM D-3039,* American Society for Testing and Materials, Philadelphia, PA.

ASTM. (1995). "Compressive properties of polymer matrix composite materials with unsupported gage section by shear loading." *ASTMD-3410,* American Society for Testing and Materials, Philadelphia, PA.

Balmer, G. G. (1949). "Shearing Strength of Concrete under High Triaxial Stress. " U.S. *Bureau of Reclamation, Structural Research Lab,* Report No. SP-23, Denver, CO.

Bavarian, B., Shively, J., Ehrgott, R, and Di Julio, R. (1996). "External support of c concrete structures using composite materials." *Proc. 1st Int. Conf. Composites in Infrastructure,* Saadatmanesh, H., and Ehsani, M. R., (Ed.), Tucson, AZ., 917928.

Bert, C.W. (1975). "Experimental Characterization of Composites." *Composite Materials,* v.8 (2), Chamis, C. C. (Ed.), Academic Press, New York, NY.

Burdette, E. G., and Hilsdorl; H. K (1971). "Behavior of laterally reinforced concrete columns." *Proceedings,* ASCE, v. 97, ST2, pp. 587-602.

Cabrera, S. (1996). "Shear strength and seismic performance of concrete-filled FRP tubes." MS *thesis,* University of Central Florida, Orlando, FL.

Chai~ Y. H. (1991). "Steel jacketing of circular reinforced concrete bridge columns for enhanced flexural performance." *Ph.D. thesis,* University of California, San Diego, CA.

Chai, Y. H., Priestley, M. J. N., and Seible, F. (1991). "Seismic retrofit of circular bridge columns for enhanced flexural performance." *A CI Struct. J.,* 88 (5), 572-584.

Chai, Y. H., Priestley, M. J. N., and Seible, F. (1994). "Analytical model for steel jacketed RC circular bridge columns." J. *of Struct. Engr.,* ASCE, 120 (8), 2358-2375.

Chamis, C. C. (1987). "Simplified composite micromechanics equations for mechanical, thermal, and moisture-related properties." *Engineers.' Guide to Composite Materials,* Weeton, J. W., Peters, D. M., Thomas, K L., (Ed.), ASTM International, Materials Park, OH.

Chen, W. F. (1982). *Plasticity in reinforced concrete.* McGraw-Hill Book Co., New York, NY.

Chinn, J., and Zimmerman, R M. (1965). `Behavior of plain concrete under various triaxial compression loading conditions." *Technical Report No. WLTR-64-163,* Air Force Weapons Laboratory, NM.

Considere, A. (1903). "Resistance a la compression du beton arm6 et du beton frette." *Geiiie Civil.*

Daniali, S. (1992). "Investigation of the behavior of reinforced plastic columns with concrete core." *Materials: Performance and Prevention of Deficiencies and Failures,* Materials Engineering Congress, ASCE, New York, NY, 666-676.

Demers, M., and Neale, K W. (1994). "Strengthening of concrete columns with unidirectional composite sheets." *Developments in Short and Medium Span Bridge Engineering '94,* Mufti, A. A., Bakht, B., Jaeger, L. G., (Ed.), CSCE, 895- 905.

El-Dash, K M., and Ahmad, S. H. (1994) "A model for the stress-strain relationship of rectangular confined normal and high strength concrete columns." *Materials and Structures,* 27 (174), 572-579.

El Echary, H. (1997). "Length effect on concrete-filled FRP tubes using acoustic emission." MS *thesis,* University of Central Florida, Orlando, FL.

EI-Tawil, S. M., and Deierlein, G. G. (1996). "Fiber element analysis of composite beam column cross-sections." *Report No. 96-6,* Cornell University, Ithaca, NY.

Elwi, A. A., and Murray, D. W. (1979). "A 3D hypoelastic concrete constitutive Relationship." J. *of Engr. Mech. Div.,* ASCE, v. 105, No. EM4, 623-641.

Engineered material's handbook. (1987), v. 1: Composites, ASM International, Metals Park, OH.

Fardis, M. N., and Khalili, H. H. (1981). "Concrete encased in fiberglass-reinforced plastic." ACI J., 78 (6), 440-446.

Fardis, M. N., and Khalili, H. H. (1982). "FRP-encased concrete as a structural material." *Mag. of Concrete Research.,* 34 (121), 191-201.

Fyfe, E. R (1995). "Testing and field performance of the high strength fiber wrapping system." *Proc. Structures Congress XIII,* ASCE, Boston, MA, 603-606.

Gardner, N. J., and Jacobson, E. R. (1967). "Structural behavior of concrete filled steel tubes." ACI J., 64 (7), 404-413.

Gibson, R. F. (1994). *Principles of composite material mechanics.* McGraw-Hill, New York, NY.

Harmon, T., Slattery, K., and Ramakrishnan, S. (1995). "The effect of confinement stiffness on confined concrete." *Proceedings of the Second International RILEM Symposium (FRPRCS--2),* Taerwe, L., (Ed.), v. l, 584-592.

Harmon, T., Wang, H. (1996). "Behavior of composite confined concrete under cyclic loading." *Proceedings of the 41*^{s}` *International SAMPE Symposium,* 41 (2), 24-28.

Imran, I. (1994). "Applications of non-associated plasticity in modeling the mechanical response of concrete." *Ph.D. Dissertation,* University of Toronto, ON, Canada.

lyengar, K. T. S. R, Desayi~ R., and Reddy, K. N. (1970). "Stress-strain characteristics of concrete confined in steel binders." *Magazine of Concrete Research (London),* 22 (72),173-184.

Karbhari, V. M., and Eckel, D. A. (1993). "Effect of a cold-regions-type climate on the strengthening efficiency of composite wraps for columns." *Technical Report,* University of Delaware Center for Materials, Newark, DE.

Kargahi, M. (1995). "Fiber reinforced plastic (FRP) shell as external reinforcement for concrete columns." MS *thesis,* University of Central Florida, Orlando, FL.

Kloppel, Von K., and Goder, W. (1957). "Traglastversuche mit ausbetonierten Stahlrohren and Aufstellung einer Bemessungsformel." *Der Stahlbau (Berlin),* 26 (1).

Knowles, R B., and Park, R (1969). "Strength of concrete filled steel tubular columns." *ASCEJ. of the Struct. Div., v.* 95, ST12, 2565-2587.

Knowles, R B., and Park, R (1970). "Axial load design for concrete filled steel tubes." *ASCEJ. of the Struct. Div., v.* 96, ST 10, 2125-2153.

Kupfer, H., Hilsdorf; H. K., Riisch, H. (1969). "Behavior of concrete under biaxial stresses." *ACI J.,* 66 (8), 656-666.

Lahlou, K., Aitcin, P.C., and Chaallal, O. (1992). "Behavior of high-strength concrete under confined stresses." *Cement & Concrete Composites,* 14, 185-193.

Ligday, F. J., Kumar, S.V., GangaRao, H. V. S. (1996). "Creep of concrete beams with externally bonded carbon fiber tow sheets." *Adv. Composite Mater. in Bridges and Struct.,* El-Badry, M. M., (Ed.), CSCE, 513-518.

Liskey, K. (1991). "Structural applications of pultruded composite products." *Advanced Composite Materials in Civil Engineering Structures,* ASCE, 187.

Madas, P., and Elnashai, A. S. (1992). "A new passive confinement model for the analysis of concrete structures subjected to cyclic and transient dynamic loading." J. *Earthquake and Struct. Dynamics,* 21, 409-431.

Mallick, P. K. (1988) *Fiber-Reinforced Composites: Materials, Manufacturing, and Design,* Marcel Dekker, Inc., New York, NY.

Mander, J. B., Priestley, M. J. N., and Park, R. J. T. (1988). "Theoretical stress-strain model for confined concrete." J. *Struct. Engr.,* ASCE, 114 (8), 1804-1826.

Mastrapa, J. C. (1997). "Effect of bonded and unbonded construction on confinement with fiber composites." *MS thesis,* University of Central Florida, Orlando, FL.

Meier, U. (1996). "Composites for structural repair and retrofitting." Proc. *1st Int. Conf. Composites in Infrastructure,* Saadatmanesh, H., and Ehsani, M. R, (Ed.), Tucson, AZ., 1202-1216.

Mirmiran, A. (1997a). "Analytical and experimental investigation of reinforced concrete columns encased in fiberglass tubular jackets and use of fiber jacket for pile splicing." *Final Report Part I,* Contract No. B-9135, Florida Dept. of Transportation, Tallahassee, FL.

Mirmiran, A. (1997b). "Analytical and experimental investigation of reinforced concrete columns encased in fiberglass tubular jackets and use of fiber jacket for pile splicing." *Final Report Part* II, Contract No. B-9135, Florida Dept. of Transportation, Tallahassee, FL.

Mirmiran, A., and Shahawy, M. (1995). "A novel FRP-concrete composite construction for the infrastructure." Proc., *Struct. Congress* XIII, ASCE, Boston, MA, 1663-1666.

Mirmiran, A., and Shahawy, M. (1997a). "Behavior of concrete columns confined by fiber composites." *J. Struct. Engr.,* ASCE, 123 (5), 583-90.

Mirmiran, A., and Shahawy, M. (1997b). "Dilation characteristics of confined concrete." *Mech. of Cohesive Frictional Mater., An International J.,* 2 (3),237-249.

Monti, G., and Spoelstra, M.R (1997). "Fiber-section analysis of RC bridge piers retrofitted with FRP jackets." Proc. *Structures Congress XV Building to last,* ASCE, Portland, OR, 884-888.

Naaman, A. E., Harajli, M. H., and Wight, J. K. (1986). "Analysis of ductility in partially prestressed concrete flexural members." PCI J., 31 (3), 64-87.

Naaman, A. E., Jeong, S. M. (1995). "Structural ductility of concrete beams prestressed with FRP tendons." *Proceedings of the Second International RILEM Symposium (FRPRCS-2),* Taerwe, L.,(Ed.), v. l, 379-84.

Nanni, A., and Bradford, N. M. (1995). "FRP jacketed concrete under uniaxial compression." *Constr. &Bldg. Mater.,* 9 (2), 115-124.

Nanni, A., and Norris, M. (1995). "FRP jacketed concrete under flexure and combined flexure-compression" *Constr. &Bldg. Mater.,* 9 (5),273-281.

Nanni, A., and Norris, and Bradford, N. M. (1993). "Lateral confinement of concrete using FRP reinforcement." *Int'l Symposium, FRP Reinforcement for Concrete Structures,* Nanni, A., (Ed.), ACI SP-138, 193-209.

Newman, K., and Newman, J. B. (1971). "Failure theories and design criteria for plain concrete." Proc. *Int. Civil Engr. Mater. Conf. on Struct., Solid Mech. and Engr. Design,* Wiley Interscience, New York, NY, 936-995.

Orito, Y., Sato, T., Tanaka, N., and Watanabe, Y. (1987). "Study on the unbounded steel tube structure." Proc., *Int'l Conf. Composite Construction in Steel and Concrete,* ASCE, 786-804.

Pantazopoulou, S. J. (1995). "Role of expansion on mechanical behavior of concrete." *J. Struct. Engr.,* ASCE, 121 (12), 1795-1805.

Pantazopoulou, S. J., and Mills, R. H. (1995)."Microstructural aspects of the mechanical response of plain concrete." ACI *Materials J.,* 92 (6), 605-616.

Park, R (1989). "Evaluation of ductility of structures and structural assemblages for laboratory testing." *Bulletin of the New Zealand Society for Earthquake Engineering,* 22 (3), 155-166.

Park, R., and Paulay, T. (1975). *Reinforced concrete structures.* Wiley Interscience, New York, NY.

Pelvris, N., Triantafillou, T. C. (1994). "Time-dependent behavior of RC members strengthened with FRP laminates." *J of Struct. Engr.,* ASCE, 120 (3), 1016-1042.

Peters, S. T., Humphrey, W. D., and Foral, R. F. (1991). *Filament winding composite structure fabrication.* SAMPE, Covina, CA.

Picher, F. (1995). "Confinement de cylindres en beton par des composites carbone-epoxy unidirectionnels." *MS thesis,* University de Sherbrooke, Sherbrooke, Quebec, Canada.

Picher, F., Rochette, P., and Labossiere, P. (1996). "Confinement of concrete cylinders with CFRP." *Proc. 1st Int. Conf Composites in Infrastructure,* Saadatmanesh, H., and Ehsani, M. R., (Ed.), Tucson, AZ., 903-916.

Pico, O. (1997). "Confinement effectiveness of square FRP tubes in hybrid columns." MS *thesis,* University of Central Florida, Orlando, FL.

Popovics, S. (1973). "A numerical approach to the complete stress-strain curves for concrete." *Cement and Concrete Research,* 3 (5), 583-599.

Priestley, M. J. N., Seible, F., and Calvi, G. M. (1995). *Seismic Design and Retrofit of Bridges,* John Wiley & Sons, New York, NY.

Prion, H. G. L., and Boehme, J. (1994). `Beam column behavior of steel tubes filled with high strength concrete." *Canadian J. Civil Engr.,* 21 (2), 207-218.

Richard, R M., and Abbott, B. J. (1975). "Versatile elastic-plastic stress-strain formula." *J Engr. Mech.,* ASCE, 101 (4), 511-5.

Richart, F. E., Brandtzaeg, A., and Brown, R. L., (1928). "A Study of the Failure of Concrete under Combined Compressive Stresses." *Engineering Experiment Station Bulletin No. 185,* University of Illinois, Urbana, IL.

Richart, F. E., Brandtzaeg, A., and Brown, R L., (1929). "Failure of Plain and Spirally Reinforced Concrete in Compression. " *Engineering Experiment Station Bulletin* No. 190, University of Illinois, Urbana, IL.

Rochette, P. (1996). "Confinement de colonnes courtes en beton de section carree ou rectangulaire avec des materiaux composites." *MS thesis,* University de Sherbrooke, Sherbrooke, Quebec, Canada.

Rochette, P., and Labossiere, P. (1996). "A plasticity approach for concrete columns confined with composite materials." Adv. *Composite Mater. in Bridges and Struct.,* El-Badry, M. M.(Ed.), CSCE, 359-366.

Saadatmanesh, H., Ehsani, M. R, and Li, M. W. (1994). "Strength and Ductility of Concrete Columns Externally Reinforced with Fiber Composite Straps." ACI *Struct. J.,* 91 (4), 434-447.

Saatcioglu, M., and Razvi, S. R (1992). "Strength and ductility of confined concrete." *J. Struct. Engr.,* ASCE, 118 (6), 1590-1607.

Scherer, M. E. (1996). "Design optimization and behavior of concrete-filled FRP tubes." *MS thesis,* University of Central Florida, Orlando, FL.

Sheikh, S. A.(1982). "A comparative study of confinement models." ACI J., 79 (4), 296306.

Sheikh, S. A., and Uzurneri, S. M. (1980). "Strength and ductility of tied concrete columns." J. *Struct. Div.,* ASCE, 106 (5), 1079-1102.

Sheikh, S. A., and Yeh, C. (1986). "Flexural behavior of confined concrete columns." ACI J., 83 (3), 389-404.

Sheikh, S. A., and Yeh, C. (1992). "Analytical moment-curvature relations for tied concrete columns." J *of Struct. Engr.,* ASCE, 118 (2), 529-544.

Seible, F. (1996). "Advanced composite materials for bridges in the 21' century." *Adv. Composite Mater. in Bridges and Struct.,* El-Badry, M. M. (Ed.), CSCE, 17-30.

Smart, C. W., Jensen, D. W. (1997). "Flexure of concrete beams reinforced with advanced composite orthogrids."J. *ofAerospace Engr., 10 (1),* 7-15.

Soudki, K A., and Green, M. F. (1996). "Performance of CFRP retrofitted concrete columns at low temperatures." *Adv. Composite Mater. in Bridges and Struct.,* ElBadry, M. M.(Ed.), CSCE, 427-434.

Stevens, N. J., Uzumeri, S. M., Collins, M. P., and Will, G. T. (1991). "Constitutive model for reinforced concrete finite element analysis." *ACI Struct.* J, 88 (1), 49-59.

Tsai, S. W. (1988). *Composites Design.* Think Composites, Dayton, OR

Tsai~ S. W., and Wu, E. M. (1971). "A general theory of strength for anisotropic materials." J *of Composite Materials,* 5, 58-80.

Vecchio, F. J., and Collins, M. P. (1986). "The modified compression-field theory for reinforced concrete elements subjected to shear." ACI *Struct. J.,* 83 (2), 219-231.

William, K J., and Warnke, E. P. (1975). "Constitutive model for the triaxial behavior of concrete." *Proc., International Association for Bridge and Struct. Engr., v.* 19, 130.

Ziara, M. M., Haldane, D., and Kuttab, A. S. (1995). "Flexural behavior of beams with confinement." ACIStruct. J., 92 (1), 103-114.